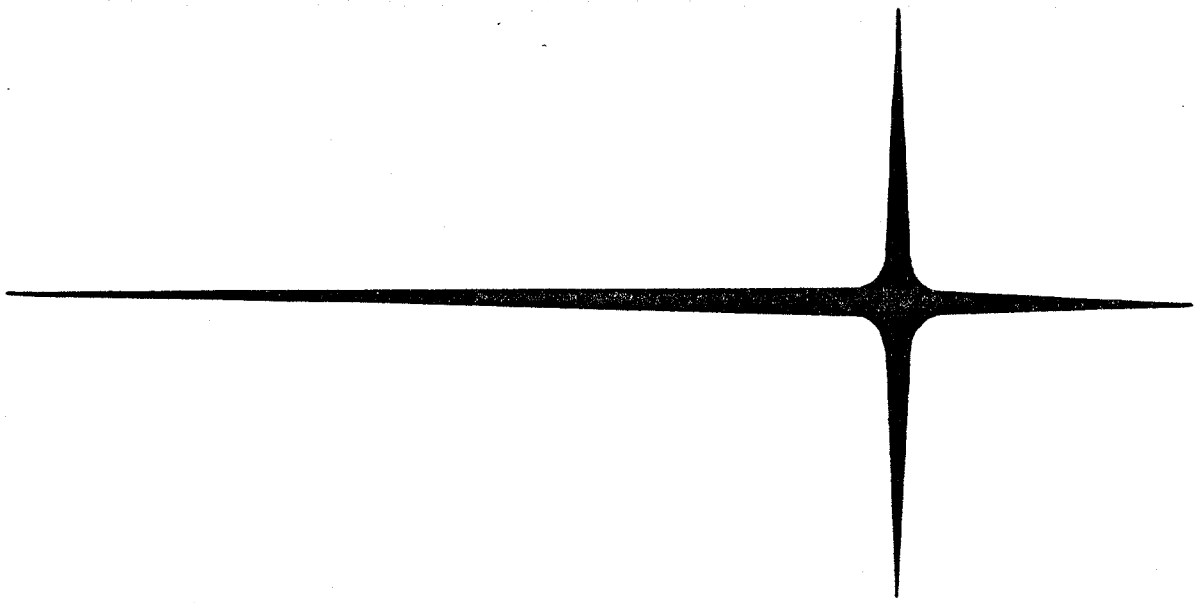

Optech Inc.

Final Report on a Study into the Feasibility of Constructing an Operational Sensor for Laser-Ultrasonic Remote Sensing of Oil Thickness (LURSOT)

Prepared For:
Environment Canada
c/o Scientific Authority
Chief, Emergencies Science Division
Conservation and Protection
Environmental Technology Centre
3439 River Road South
Gloucester, Ontario K1A 0H3

SSC File No.: 30SS.K2062-4-0015
Contract No: K2062-4-0015/01-SS

Prepared By:
Optech Incorporated
100 Wildcat Road
North York (Toronto), Ontario M3J 2Z9

Prepared By: _____ Date: Oct. 14/94

Approved By: _____ Date: OCT 14/94

Released By: _____ Date: Oct 14/94

Document No. 185frlursot

October 1994

TABLE OF CONTENTS

LIST OF FIGURES

Page

LIST OF TABLES

EXECUTIVE SUMMARY

Environment Canada, Esso Resources and a number of other government and industrial partners have over the past few years sponsored work on the development of a prototype system for the remote measurement of oil thickness on water. The technical approach of this work is based on a combination of laser radar and ultrasonic principles. The effort is aimed, ultimately, at providing the oil spill emergency response crews with a tool for more effective management of their clean-up efforts.

The work, thus far carried out primarily by researchers at the Industrial Materials Institute of the National Research Council of Canada, has successfully demonstrated in the laboratory environment the overall feasibility of the technique to measure oil thickness remotely. Optech's aim in the present study has been to assess the feasibility of obtaining a satisfactory performance, with sufficient reliability, from a LURSOT instrument in an airborne environment, and to evaluate the components of the existing LURSOT prototype with respect to the above criteria.

In general the results of this study have led to the following conclusions:

- The airborne environment affects the basic measurement technique in a manner not previously identified; the effect of this on the system design needs to be further analyzed before an optimized trade-off design is adopted.
- The current LURSOT design is not well-suited for airborne use.
- Further analysis, with possible development work, is required on the critical system components as well as on the operational configuration and the system integration.
- Eye-safety needs to be addressed and integrated into a system design or dismissed as a non-issue.

Specific recommendations detailing further required work, derived from the above conclusions, are summarized in the General Conclusions section. No cost estimate has yet been prepared. Optech is prepared to submit a proposal for the further work recommended, if desired.

1.0 INTRODUCTION

The Industrial Materials Institute (IMI) of the National Research Council of Canada has developed a non-destructive sensing technology for the inspection of opaque materials. This technique, termed laser-ultrasonics, uses an energetic laser pulse to initiate an ultrasonic shock wave in the target material. This ultrasonic wave travels through the medium scattering from internal defects or surfaces. By monitoring the minuscule vibrations at the surface of the material due to the initial laser pulse and the echoes from internal structures, the thickness and/or internal homogeneity of the sample material can be determined.

The monitoring of the surface movement is done using laser light. By detecting the small Doppler shifts in light reflected from the material surface as it vibrates, a time series of the ultrasonic pulse propagation in the material can be recorded. From this time series, information about the material can be derived for use in quality control or process control applications. Because the generation and sensing of the ultrasonic waves is done by laser light and its reflection, no direct contact between the laser-ultrasonic sensor and the material is required.

Recently, IMI was contracted by Environment Canada and Imperial Oil Resources Limited to investigate the possibility of using laser-ultrasonic techniques to remotely measure the thickness of oil on the sea surface. To be more specific, the laser-ultrasonic sensor would be mounted in an aircraft and measure the oil thickness as the aircraft flew over an oil spill.

For proof of principle demonstrations, IMI adapted a system designed for measuring steel sheets. Initially the system was tested in static tests in the laboratory; ultimately it was mounted in an aircraft for field trials. Despite promising results in a number of controlled laboratory tests, the system failed to make any oil thickness measurements during the test flights. At this point in the program, Environment Canada asked Optech Inc. to carry out a study of how to operate the sensor successfully from an airborne platform. For this study, Optech was to draw on their extensive expertise in the design and construction of airborne laser radar systems. This report presents the results of that study.

At the outset of this study, Optech personnel held meetings with IMI and Environment Canada personnel to review both the status of the system and the planned effort for the study. In our interaction with those involved in the project, it became clear that the statement of work for the study needed to be modified to include a more fundamental investigation of the suitability of the system components for the oil thickness measurement. For example, the lasers used to generate and monitor the ultrasonic waves were initially selected to measure steel in a controlled industrial environment. Since the hardware was available, it was simply adopted for the oil thickness work. In other words, no analysis of the most suitable laser sources for the generation and monitoring of the ultrasonic waves in the oil thickness case was done. Similarly, the detection system was adopted straight from the industrial system with little consideration of its ultimate operation in an aircraft. Thus, in addition to addressing the problem of operating this system in an aircraft, Optech was asked to perform a more detailed analysis of the entire system.

Overall, the application of the laser-ultrasonic technique to oil thickness measurement from an aircraft is an extremely challenging problem. We must take an instrument which operates by detecting very small high frequency surface motions and put it onto a platform that is subject to a wide vibrational spectrum. Additionally, the aircraft and the sea surface are in constant relative motion, thereby effectively removing any control over the measurement geometry. In this study we have examined the

effect of the dynamic nature of the airborne operation on the successful operation of the laser-ultrasonic oil sensing system, dubbed LURSOT.

1.1 Background

This section provides a brief description of the laser ultrasonic technique as applied to oil thickness measurements. A more detailed description of the technique can be obtained in the IMI report[1]. The principle of laser-ultrasonics is based on focusing a pulsed optical beam onto the surface of the oil sample. Due to local heating of the sample, an acoustic pulse is thermoelastically generated as the sample expands. The thermal expansion of the oil causes the surface to move upward sharply. The acoustic pulse that travels down the oil layer to the water substrate is partially reflected back to the oil surface. Once the reflected acoustic pulse reaches the oil surface, it causes an additional upward movement of the oil surface. The time lag between the echo and the initial surface displacement depends on the thickness of the oil layer and the acoustic velocity of oil.

The surface motion of the oil is detected by a second laser beam - the probe laser beam. The frequency of the probe laser beam is Doppler shifted upon reflecting from the oil surface which is undergoing motion due to laser-ultrasonic effect. The amount of frequency change is directly proportional to the instantaneous velocity of the oil surface. The frequency change of the probe laser beam will be detected by optical demodulation of the reflected light.

1.2 Approach

A block diagram of the Laser-Ultrasonic Remote Sensing of Oil Thickness system is illustrated in Figure 1. The system can be divided into many sub-systems, each of which has a unique function. In the current system design, key sub-systems include three different laser sources, the transmitter optics, a receiver system composed of the receiver telescope, the demodulation receiver and the trigger monitoring system detector, the signal capture system, and the post-detection signal processing system. The three lasers all serve a unique function. The generating laser provides energetic pulses which initiate the laser-ultrasonic interaction. The probe laser monitors the surface during the period of the laser-ultrasonic interaction to provide a return signal that carries the information about the surface motion. Finally, the triggering laser provides continuous illumination of the water surface. When the surface is oriented in the correct direction to allow the laser-ultrasonic measurement (i.e., perpendicular to the system line-of-sight), the specular reflection of the trigger laser is detected by the trigger detector. This results in the firing of the probe and generating lasers and the subsequent capture of the probe beam return signal.

The sensitivity of the LURSOT system depends on many factors. Strong laser-ultrasonic interaction between the oil sample and the incident optical pulse is required. The optical receiver should be able to collect as much of the backscattered energy of the probe laser beam as possible while minimizing the amount of background noise entering the system. The output of the demodulation receiver must be sensitive to the frequency change of the probe laser beam, and the post-detection signal processing algorithm must identify the pulses corresponding to the echo and initial surface displacement from the

[1] Marc Choquet and Jean-Pierre Monchalin, "Modeling of thermoelastic generation of ultrasound in oil upon water", Industrial Materials Institute, National Research Council of Canada,

waveform at the output of the optical receiver. In this study we have concentrated on issues associated with the optimization of the laser-ultrasonic interaction, the requirements of the generating laser and the probe laser, the requirements of the transmitter optics and the successful detection of the Doppler shifts in the return signal. To a lesser extent we have considered the post detection signal processing. We have examined the basic requirements of the oil thickness measurement under ideal conditions and then considered the additional requirements imposed by airborne operation of the system.

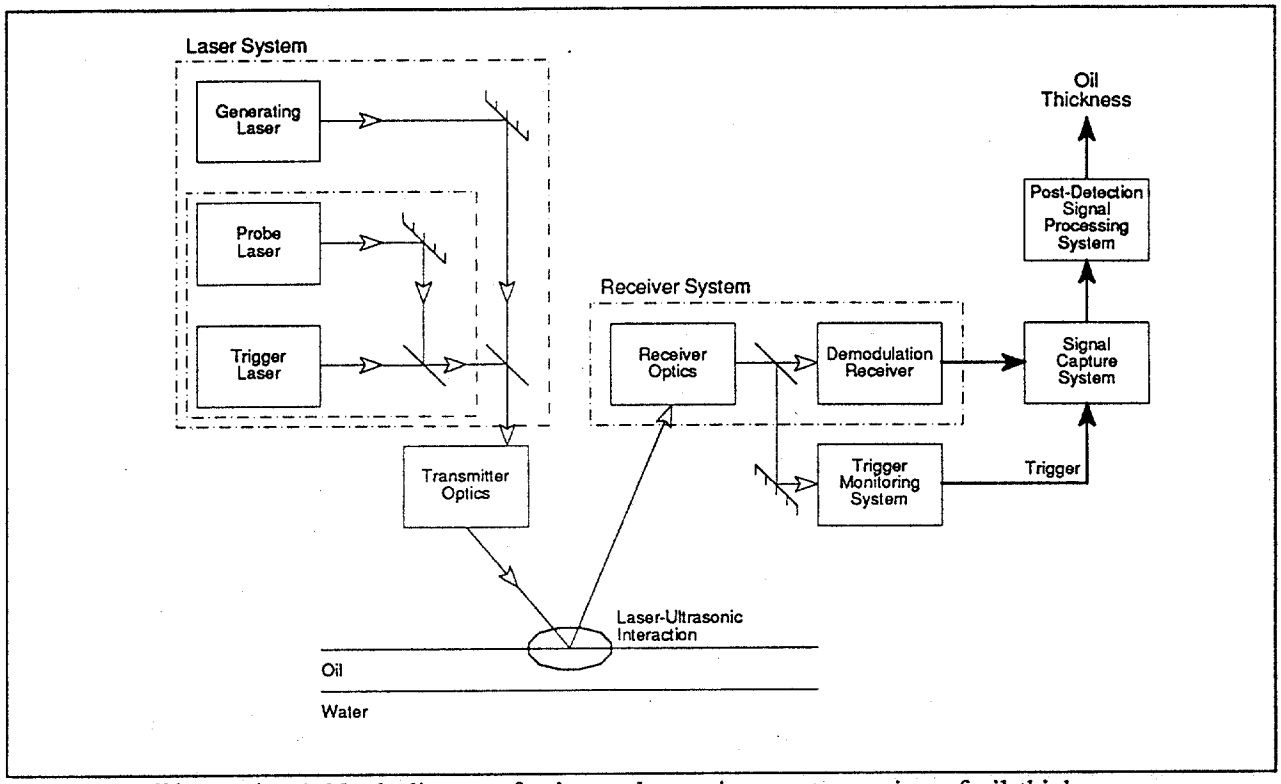

Figure 1 - A block diagram for laser-ultrasonic remote sensing of oil thickness

In order to provide a proper analysis of the LURSOT system, we had to understand in some detail the sensitivity of the laser-ultrasonic interaction and the optical demodulation of the probe laser returns. For this, we relied heavily on information supplied by IMI. IMI has developed a computer model to simulate the laser-ultrasonic interaction, and a copy of this model was provided to Optech. Using this computer model, the sensitivity of the laser-ultrasonic interaction to changes in the values of various measurement parameters has been studied and thus optimized. The measurement parameters include the spectral and temporal characteristics of the generating laser, and the physical properties of the oil and water. The results of this analysis are summarized in Section 2 of this report.

Section 3 of the report provides detailed evaluation of the requirements and possible solutions for the main system components. This includes the demodulation receiver, where a comparison of the demodulation technology with optical heterodyning and multiple-beam interferometers is briefly discussed. An analysis of the laser systems pulls together considerations of the requirements for optimal oil thickness measurement with those of eye-safety and operation of the system in an aircraft. Our analysis of the transmitter optics revealed a number of important issues that must be considered in their design. These are discussed at some length. Analysis of the receiver system indicates some considerations for the receiver optics configuration, the performance of certain key optical components within the receiver, the probable optical throughput for the receiver, and the expected performance of the receiver system as indicated by signal-to-noise estimations.

In initial discussions with Environment Canada, some concerns were expressed about the effect of surface topography on the ability of a LURSOT system to perform its measurements. This concern arises from the fact that LURSOT requires the surface to be oriented normal to its line-of-sight in order to make a successful measurement. Concern was expressed as to how often one might expect this fortuitous alignment to occur and whether conditions may exist when its frequency might be seriously reduced. Associated with these issues are questions about the effective size of the perpendicular patch of sea surface and the duration of this orientation. Although our ability to address these issues was limited by the sheer complexity of this problem, we provide our comments in Section 4.

In Section 5 we report on the results of our analysis of more general consideration regarding the fact that the LURSOT system must operate from a moving, vibrating platform over a surface which is in constant motion. We look at the sensitivity of the oil thickness measurement to aircraft vertical motion, aircraft vibration and sea surface motion. For this analysis, real altitude data of a DC-3 aircraft flying under normal flight conditions were studied. In particular, the distribution of the instantaneous vertical velocity of the aircraft was analyzed. The impact of the instantaneous vertical velocity of the aircraft on the performance of the demodulation receiver discussed. The vibrations within the aircraft were modeled as sinusoidal disturbances of different amplitudes and frequencies. The output of the demodulation receiver when the amplitude and frequency of the sinusoidal disturbances were varied was also evaluated. The significance of sea surface motion on the performance of the LURSOT system was investigated using the statistics of wave information recorded in the number of occurrences of characteristic wave height and peak period.

In Section 6 we provide a summary of the key issues to be considered before LURSOT can be successfully flown. In this section, we also provide our recommendations on what further work needs to be done in order to turn LURSOT into an operational system.

2.0 MODELING OF THE LASER-INDUCED SURFACE DISPLACEMENT

To optimize the laser-ultrasonic remote sensing of oil thickness, the generation and detection of the ultrasonic effect must be thoroughly understood. In this section, the results of our analysis of the interaction of the thermoelastic displacement of the oil surface with an incident optical pulse will be presented. The surface displacement of the oil sample was calculated numerically using the computer model developed by IMI. The computer model which is based on the mathematical description of the surface displacement expressed in the Laplace Transform domain will be briefly introduced. The mathematical relations are dependent on a number of parameters which describe the physical properties of the oil and water sample, and the characteristics of the generating laser. First, the values of the parameters that relate to the properties of the oil and water were varied one at a time about some nominal values. The resulting surface displacements were calculated for each case. The variability of the calculated surface displacement was investigated. These parameters related to the physical properties of the oil and water are uncontrollable parameters because their values depend on the type of oil and water and the conditions of the environment, not on the design of LURSOT. On the other hand, the parameters that describe the characteristics of the generating laser are controllable through selection of an appropriate laser. They can be chosen to give the best laser-ultrasonic interaction. Therefore, the wavelength of the generating laser was varied. The wavelengths that generated relatively large surface displacement were identified. Then, the surface displacement generated at selected wavelengths was calculated for the different types of oil that might be encountered in practice. From these results, the best wavelength(s) for the generating laser can be further refined by considering the sensitivity of the laser-ultrasonic interaction to oil type at these various wavelengths. The surface displacement was further examined by varying the risetime and pulse energy of the generating laser. The optimal choice of the risetime and pulse energy could then be obtained.

The IMI model provides calculation of the displacement of the oil surface due to the laser-ultrasonic interaction. The model however, does not provide the instantaneous velocity of the surface motion of the oil. It is well known that the amount of Doppler shifted in frequency is directly proportional to the velocity of a moving object, and it is this Doppler shift that the system measures. Furthermore, knowing the instantaneous velocity of the surface motion of the oil gives the frequency range over which the optical demodulation receiver needs to operate. An analytical description of the instantaneous velocity, not the displacement, of the initial surface displacement provides the link between the optimal generation of the thermoelastic displacement of the oil surface and the optimal detection of the probe laser beam by the optical demodulation receiver in laser-ultrasonic remote sensing of oil thickness. Hence, the analytical description of the initial surface displacement using Laplace Transforms has been developed to further extend the results obtained from the IMI model.

2.1 Modeling of the Thermoelastic Displacement

This section provides a review of the mathematical model used in the IMI computer model of the surface displacement. The thermoelastic displacement of the oil surface is obtained by solving the thermal and acoustic equations that relate the absorption of an incident optical beam to the thermal expansion of the oil and water resulting from the temperature variation at a given depth in the sample. It can be shown in Reference 1 that the Laplace Transform of the surface displacement is given by

$$U(0,s) = [U_1(s)\, e^{-k_1(s)L} + U_2(s) + \psi_1(s)]\, F(s) \qquad (1)$$

where

L is the thickness of the oil layer on water,
F(s) is the Laplace Transform of the normalized generating laser pulse shape f(t)

and

$U_1(s)$, $U_2(s)$, $\Psi_1(s)$ and $k_1(s)$ are complex functions of s, the peak power density, Φ_0 (W/m^2), of the generating laser at the surface and parameters related to the physical properties of oil and water.

The physical properties of oil and water are described by parameters such as the density ρ_i (kg/m^3), the specific heat C_i ($J/kg \cdot K$), the longitudinal sound velocity v_{longi} (m/s), the thermal expansion coefficient α_{Ti} ($°K^{-1}$) and the optical absorption coefficient α_i (m^{-1}). The subscript i is used to denote for oil and water by 1 and 2 respectively. It should be noted that the optical absorption coefficient of the sample is dependent on the wavelength of the generating laser. The characteristic of the pulsed generating laser can also be described by its risetime τ (s) and pulse energy E (J).

By taking the inverse Laplace Transform of U(0,s), the thermoelastic displacement of the oil surface can be calculated numerically. In our modeling, we first varied the values of the uncontrollable parameters. The resulting thermoelastic displacement of oil was studied for any variability of the magnitude and temporal response of the displacement when different types of oil and water are encountered in practice. Ideally, this variability should be of minimal magnitude such that the thermoelastic displacement of oil is independent of the type of oil being remotely sensed.

In this report, nominal values for the parameters describing the oil and water were used for the calculations of the thermoelastic displacement of oil unless some of them were changed intentionally to observe their effect on the displacement. These nominal values were obtained from IMI. The generating laser was initially assumed to be a 10 mJ pulsed CO_2 laser at wavelength 10.6 μm with a risetime of 100 ns and focused to a spot of 3 mm radius on the oil surface. The characteristics of this laser match closely the laser used in the prototype system built by IMI. The nominal parameters for oil and water are listed in Table 1.

Table 1: Nominal Parameters for Oil and Water

Parameter	Oil	Water
Density	800 kg/m^3	1000 kg/m^3
Specific Heat[2]	1000 $J/kg \cdot K$	4128 $J/kg \cdot K$
Longitudinal sound velocity	1300 m/s	1500 m/s
Thermal Expansion Coefficient	$1x10^{-4}$ $°C^{-1}$	$4.1x10^{-5}$ $°C^{-1}$
Optical Absorption Coefficient @λ = 10.6 μm	$1x10^{+4}$ m^{-1}	$1x10^{+5}$ m^{-1}

[2] Note that the values of the specific heat of oil and water used in the report "Modeling of thermoelastic generation of ultrasound in oil upon water", by Marc Choquet and Jean-Pierre Monchalin, Industrial Materials Institute, National Research Council of Canada, were four times smaller than the ones we used in this report.

In reality, the values of these parameters will be different for different types of oil and different environmental conditions.

Using the nominal parameters for oil and water, the thermoelastic displacement of a 1 mm thick oil layer was calculated and shown in Figure 2. Generally, the surface displacement shows a large step-like rise which resembles the integration of the generating laser pulse shape. The size of this step-like rise is referred to as the magnitude of the step. Typically, the magnitude of the step is of the order of 1 μm, which is considered to be useful. The time it takes for the surface displacement to rise from rest to 90% of the magnitude of the step is defined as the risetime of the initial surface displacement. Typical values of the risetime are 1-2 μs. The surface displacement also consists of a series of echoes, called the echo displacements, at periodic times corresponding to the two-way traveling time for the acoustic pulse between the oil/water interface and the surface of the oil layer. From Figure 2, it is seen that the echo displacement rides on top of the initial surface displacement. The peak of the echo displacement is the maximum displacement of the echo with reference to the magnitude of the step of the surface displacement.

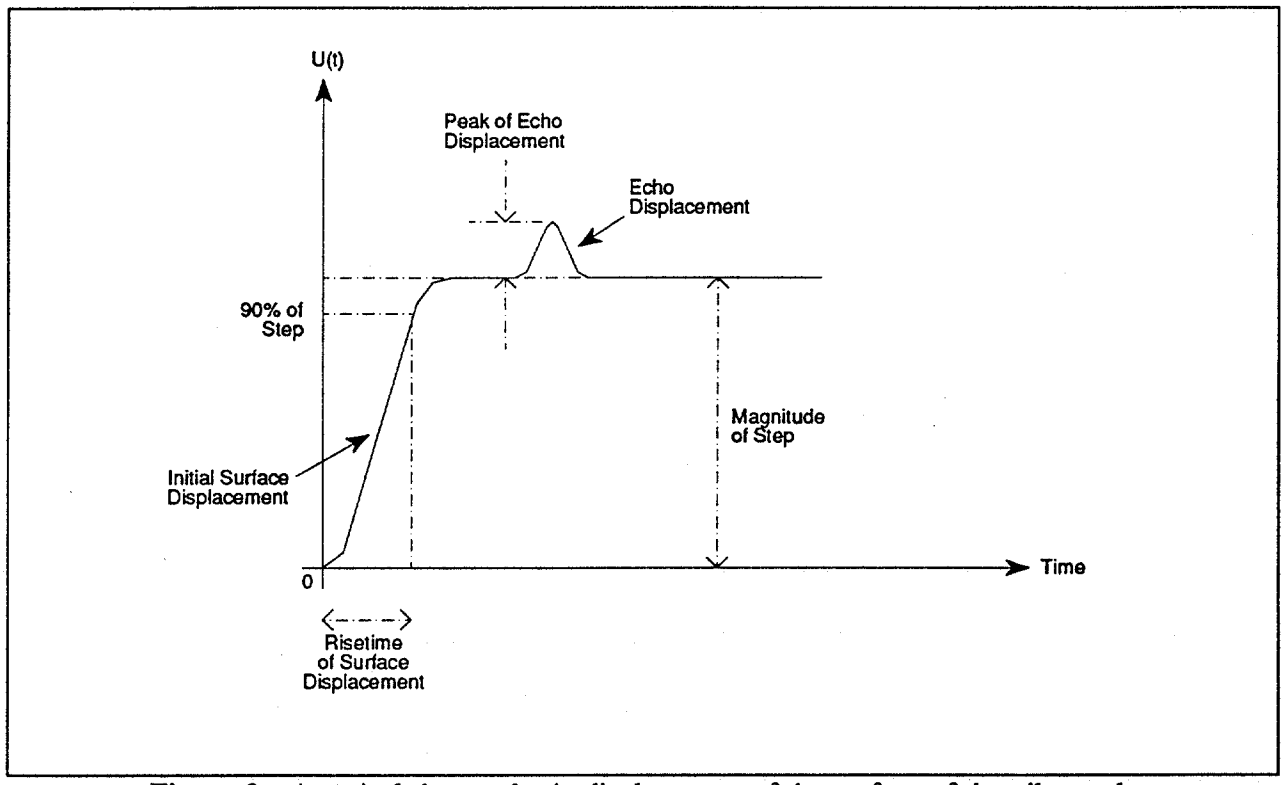

Figure 2 - A typical thermoelastic displacement of the surface of the oil sample

The first derivative, that is the instantaneous velocity, of the surface displacement for the case shown in Figure 2 is illustrated in Figure 3. From Figure 3, the instantaneous velocity of the surface displacement shows two pulses. The first pulse, which resembles the pulse shape of the generating laser, indicates the velocity of the initial surface displacement. The location of the second pulse depends on the arrival time of the acoustic echo. Note that the shape of the two pulses is different and the initial surface displacement has larger instantaneous velocities than that of the echo displacement.

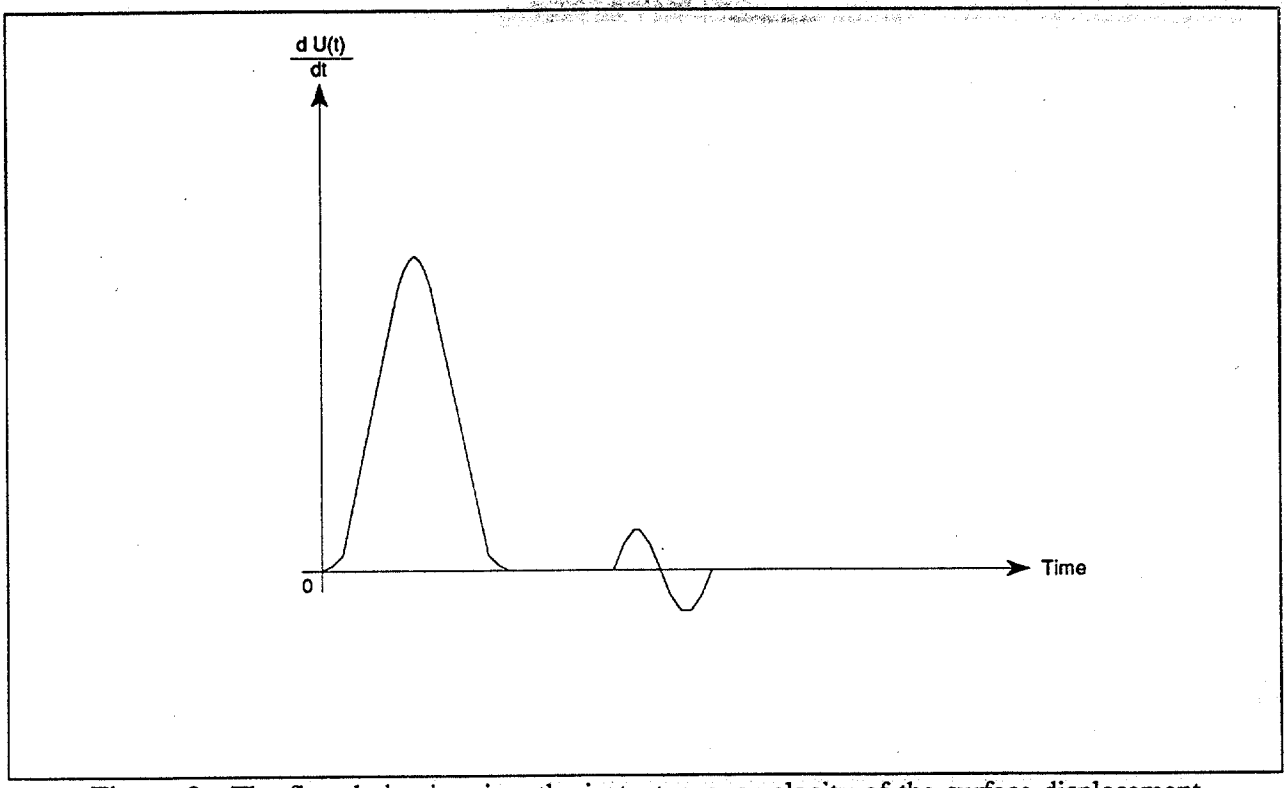

Figure 3 - The first derivative, i.e., the instantaneous velocity of the surface displacement

An efficient laser-ultrasonic interaction between the oil sample with the incident optical pulse is one in which the magnitude of the step of the surface displacement is large. In addition, we also look for a good temporal response of the thermoelastic displacement as characterized by a short risetime of the initial surface displacement, and large peak value of the echo displacement. Good temporal responses are required such that the echo displacement can be easily distinguished from the initial surface displacement. In other words, a slow risetime on the initial displacement can allow this to blend into the echo displacement, making it difficult to identify the echo. The detection of the initial surface displacement and the echo displacement is accomplished by detecting the Doppler shift of the reflected light. This Doppler shift is related to the instantaneous velocity of the surface motion, not the displacement. Therefore, it is really the velocity that is an important characteristic of the surface response. Thus in the following results, we are looking for large surface displacements and fast risetimes which combine to give large instantaneous velocities.

As a first step in the investigation, the physical parameters of oil were varied one at a time about the nominal values. The values of the physical parameters used in the calculations were five times larger and five times smaller than the nominal values. This was done arbitrarily as the purpose of the investigation in this section was to see how sensitive the thermoelastic displacement of the oil would be to each of the parameters in question. This range of values does not necessarily represent the realistic values for various oils. In Section 2.3, the results of calculations using more realistic values for the absorption coefficient of twelve types of oil are presented.

Figure 4 shows the calculated surface displacement for different values of the specific heat of oil. The results of Figure 4 indicate that the temporal response of the thermoelastic displacement is not affected by changes in the specific heat of oil. However, the magnitude of the thermoelastic displacement is inversely proportional to the specific heat of oil. This is because more heat energy is needed to increase the temperature of the oil sample when the specific heat of oil is larger. Note that since IMI has used a value for the specific heat that is four times smaller than our nominal value, they obtain a

surface displacement that is four times larger. This means that our calculations of the displacement are more conservative than those of IMI in the sense that if there is an error in our values, we will be underestimating the response.

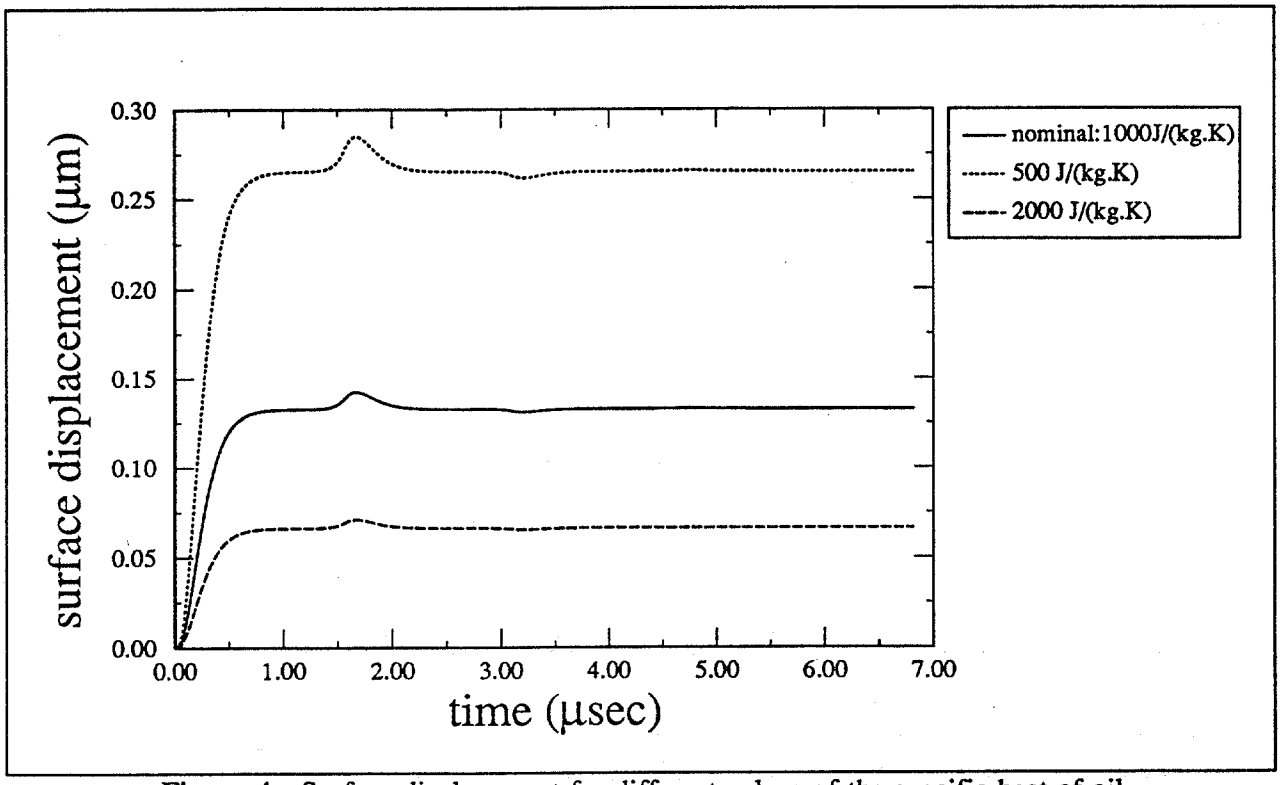

Figure 4 - Surface displacement for different values of the specific heat of oil

Figure 5 presents the results for different longitudinal sound velocities in oil. There is little effect on the initial surface displacement. There may be a slight dependence on the risetime of the initial surface displacement. There is however a strong effect on the time of arrival and magnitude of the echo pulses. The results show that the arrival time of the echoes increases as the longitudinal sound velocity is reduced. This is entirely expected. Also, the peak of the echoes depends very strongly on the longitudinal velocity. This dependence can be explained by recognizing that the magnitude of the echo from the oil/water interface depends on the mismatch of the acoustic impedance. The greater the difference between the acoustic velocity in water (1500 m/s) and that of the oil, the larger the magnitude of the echo. In terms of providing optimal response for the oil thickness measurements, the case with a longitudinal velocity of 1000 m/s is excellent as it provides a good separation between the echo and the initial surface step and the echo is very strong.

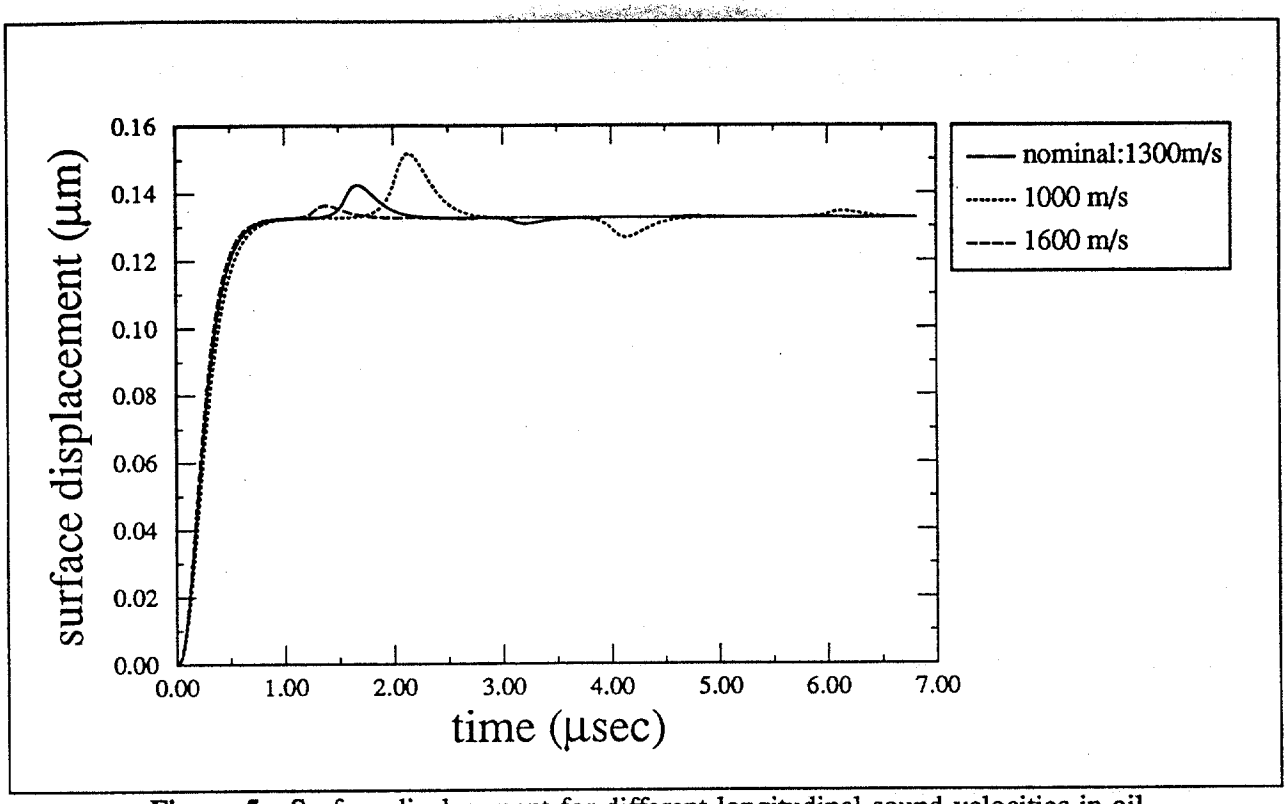

Figure 5 - Surface displacement for different longitudinal sound velocities in oil

In Figure 6, the results for different thermal expansion coefficients of oil are similar to that of the specific heat but the effect is reversed. That is, for large values of the thermal expansion coefficient, the magnitude of the thermoelastic displacement is increased. This can be explained by the fact that for large thermal expansion coefficients of oil, the volume of the heated oil sample will expand more. Consequently, the displacement of the oil surface is larger.

As the optical absorption coefficient of oil was varied, the risetime of the step was affected as shown in Figure 7. For small optical absorption coefficients of oil, as the step rises so slowly, the first echo merges with this initial surface displacement. The results in Figure 7 also show that for large optical absorption coefficients of oil, the peak of the echoes diminishes significantly. Although the strength of optical absorption of the oil and water depends on its type, it is also wavelength dependent. Consequently, the absorption coefficient of the oil can be considered as a controllable parameter by choosing the wavelength of the generating laser. Ideally we want to find a laser wavelength with which the oil sample has an absorption coefficient that produces a fast initial step in the surface displacement but is not so strong that the magnitude of the echo suffers. This issue is addressed in considerable detail in Section 2.3.

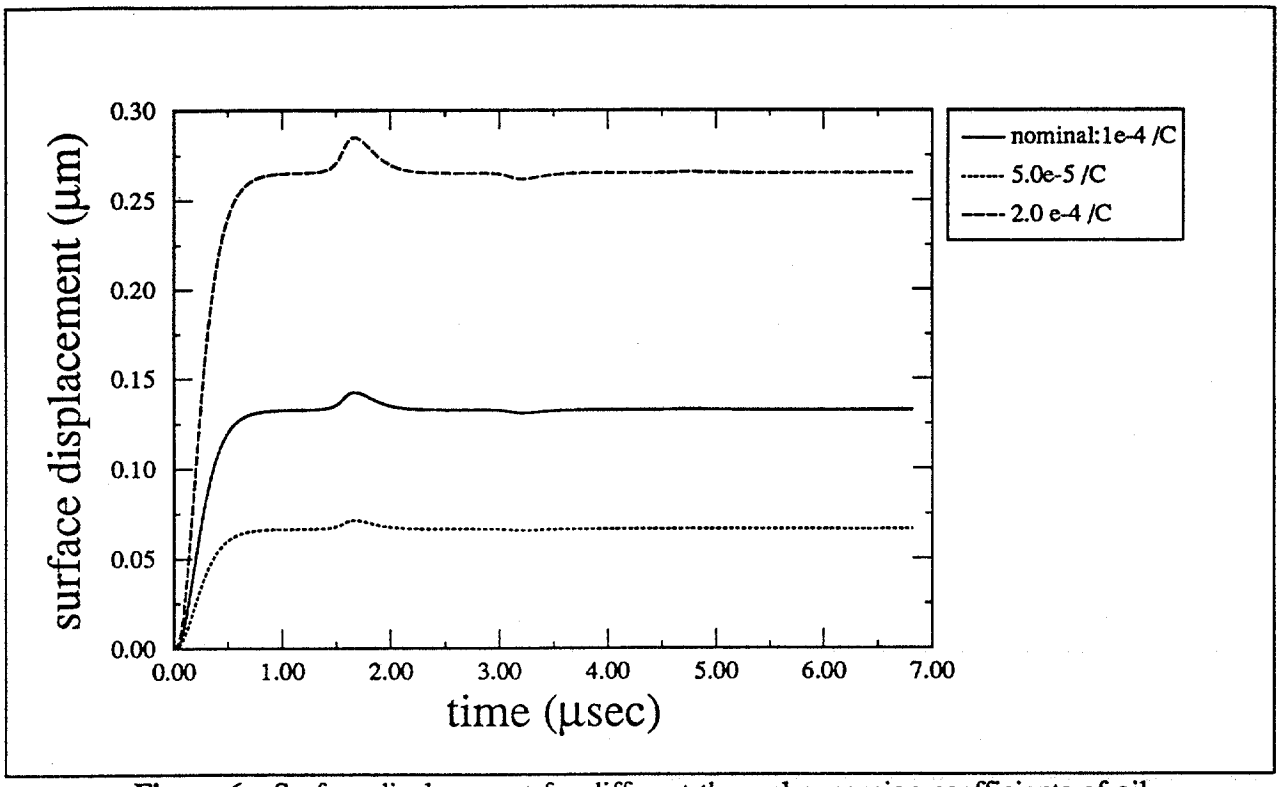

Figure 6 - Surface displacement for different thermal expansion coefficients of oil

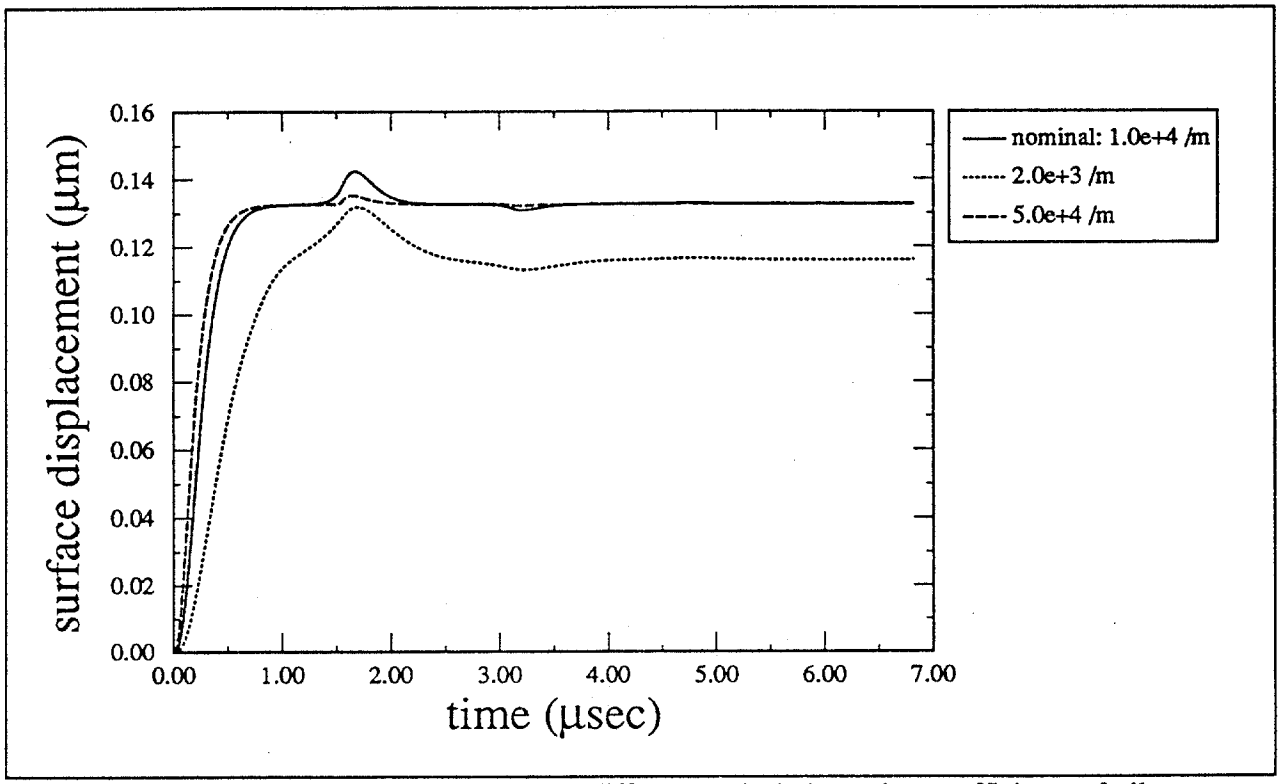

Figure 7 - Surface displacement for different optical absorption coefficients of oil

Figure 8 presents the results for different risetimes of the generating laser pulse. As can be seen from Figure 8, the risetime of the step is directly proportional to the risetime of the generating laser pulse, while the magnitude of the step is not affected at all. Note also that for short pulse risetime, the shape of the echo is narrower and the peak is larger. The pulse risetime is another parameter associated with the generating laser and thus we do have some control over it. In general, a shorter pulse appears to provide a much faster oil response. This dependence is examined in more detail in Section 2.4.

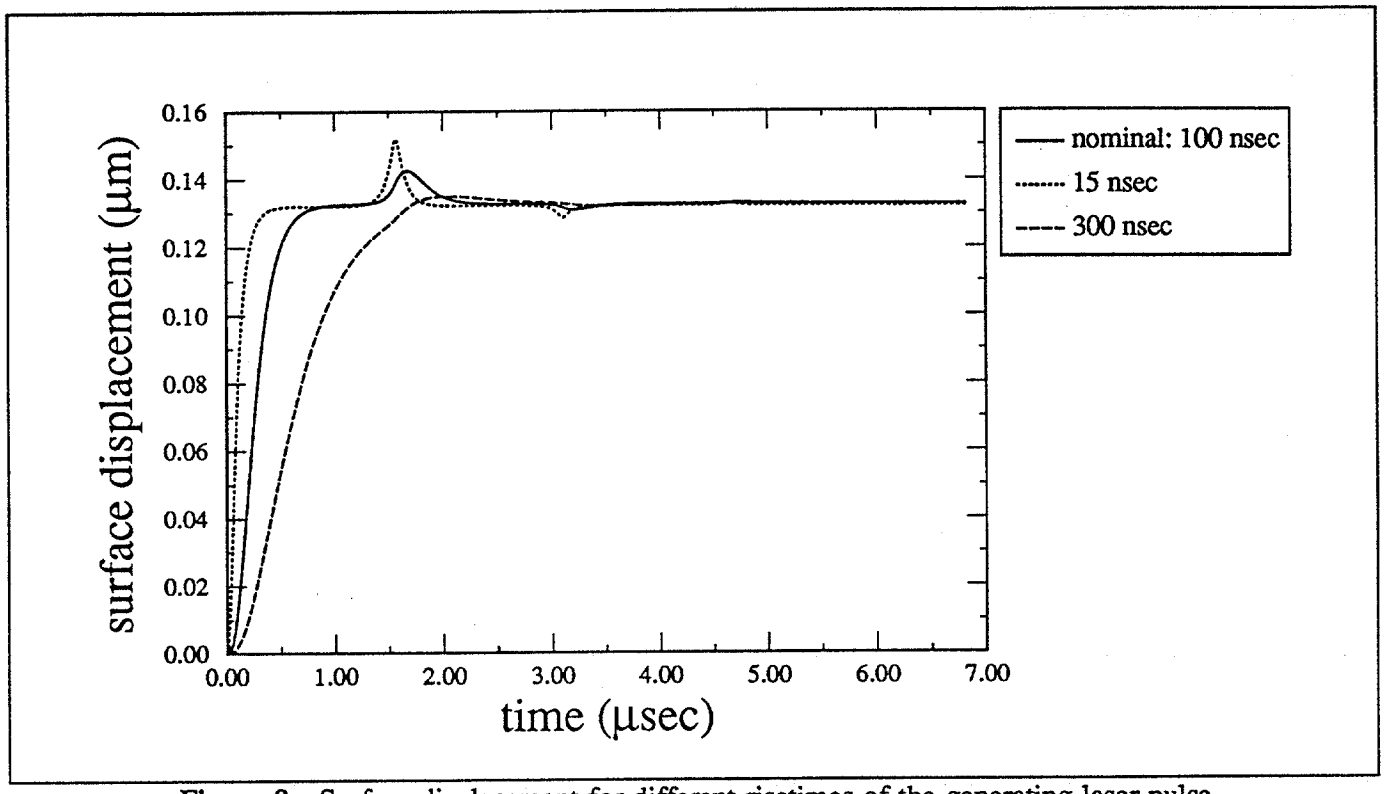

Figure 8 - Surface displacement for different risetimes of the generating laser pulse

The results for different thicknesses of the oil layer are shown in Figure 9. As one might expect, the arrival time of the echoes is linearly proportional to the thickness of the oil layer. For very thin oil layers, the first echo merges with the initial surface displacement. This places restrictions on the minimum measurable oil thickness. Additionally, the magnitude of the step is slightly reduced and hence decreases the sensitivity in measuring the oil thickness.

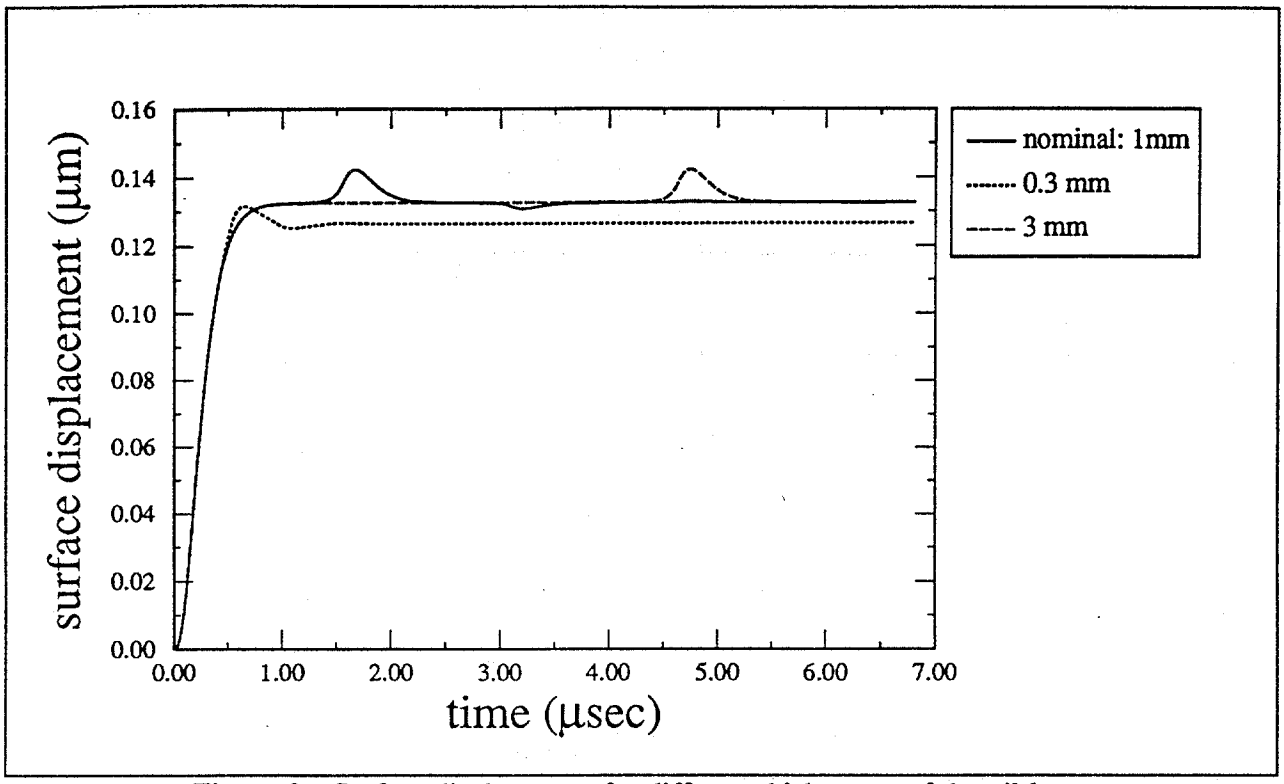

Figure 9 - Surface displacement for different thicknesses of the oil layer

From the above results, the thermoelastic displacement of oil on water depends on parameters that are related to the physical properties of the oil and water sample, and the characteristics of the pulsed generating laser. In particular, the risetime and the magnitude of the step and the peak value of the echoes are of importance in measuring the thickness of the oil layer. Although the values of the parameters were varied arbitrarily in this section, the results did reveal the variations and the dependence of the thermoelastic displacement of the oil surface with respect to the parameter under investigation. In later sections, realistic values of the uncontrollable parameters will be used. The next stage of our study involved changing the controllable parameters to find the optimum thermoelastic displacement. Optimum thermoelastic displacement is obtained by choosing the proper characteristics of the pulsed generating laser that yield the most efficient and sensitive thermoelastic response while minimizing the dependence of oil type.

2.2 Sensitivity to Different Generating Laser Wavelengths

As an initial look at the wavelength dependence, Figures 10-14 show the thermoelastic displacement of the oil when the wavelength of the 10 mJ pulsed generating laser of 100 ns risetime was varied from 0.2 μm to 2.6 μm. As before, a 1 mm thick oil layer is used in this calculation. For each wavelength under consideration, the corresponding optical absorption coefficient of oil and water was used. A plot of the absorption coefficients of a typical crude oil at wavelengths from 0.2 μm to 2.6 μm is shown in Figure 15. As shown in Figure 10 and Figure 11, the thermoelastic displacement diminishes rapidly as the wavelength is increased from 0.3 μm to 1.1 μm. It can be observed that the thermoelastic displacement has good response only at wavelengths between 0.2 μm and 0.3 μm. As the wavelength increases beyond 1.2 μm to 1.6 μm in Figure 12, the magnitude of the thermoelastic displacement improves but the temporal response is very poor. The echo can barely be observed. Figure 13 shows that the thermoelastic displacement is better at the wavelength of 1.7 μm. However, the magnitude of

the thermoelastic displacement is still poor for wavelengths between 1.8 μm to 2.2 μm, although the temporal response is significantly better than the results in Figure 12. Finally, the thermoelastic displacement shown in Figure 14 for wavelengths between 2.3 μm to 2.6 μm are significantly improved. In fact, the results for wavelengths of 2.3 μm and 2.4 μm are comparable to the wavelength of 10.6 μm that IMI had used for their system. From these results, four useful wavelengths or wavelength regions of the generating laser can be identified. These are the 0.2-0.3 μm, 1.7 μm, 2.3 μm and 10.6 μm regions. It can be readily observed that these wavelength regions correspond to strong oil absorption coefficients as shown in Figure 15.

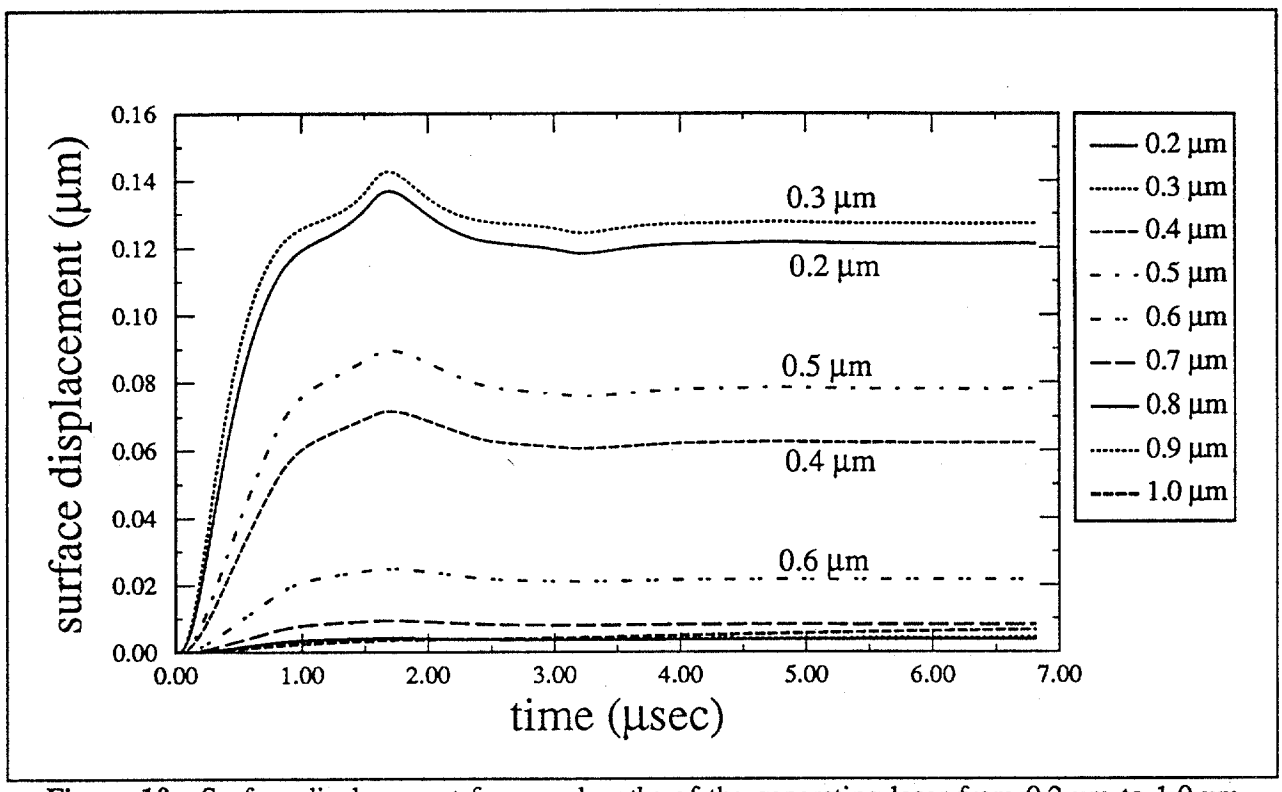

Figure 10 - Surface displacement for wavelengths of the generating laser from 0.2 μm to 1.0 μm

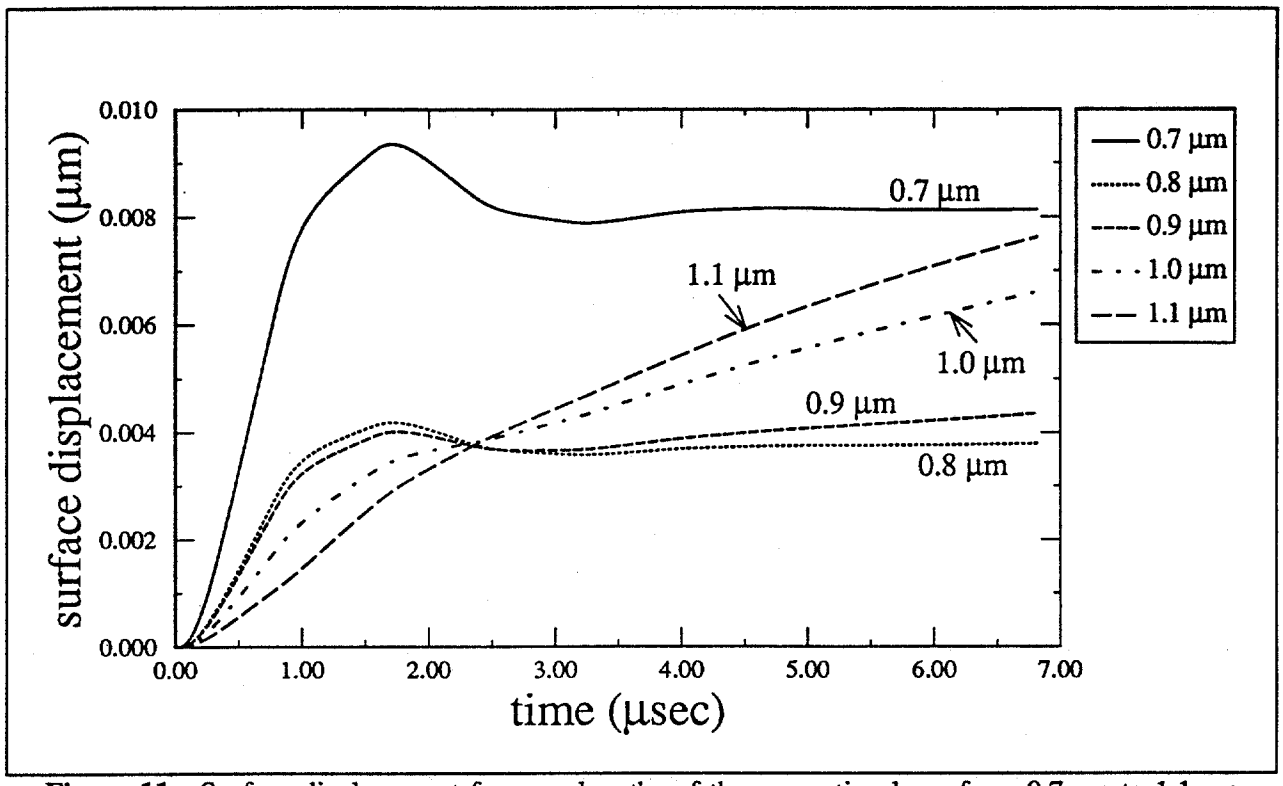

Figure 11 - Surface displacement for wavelengths of the generating laser from 0.7 μm to 1.1 μm

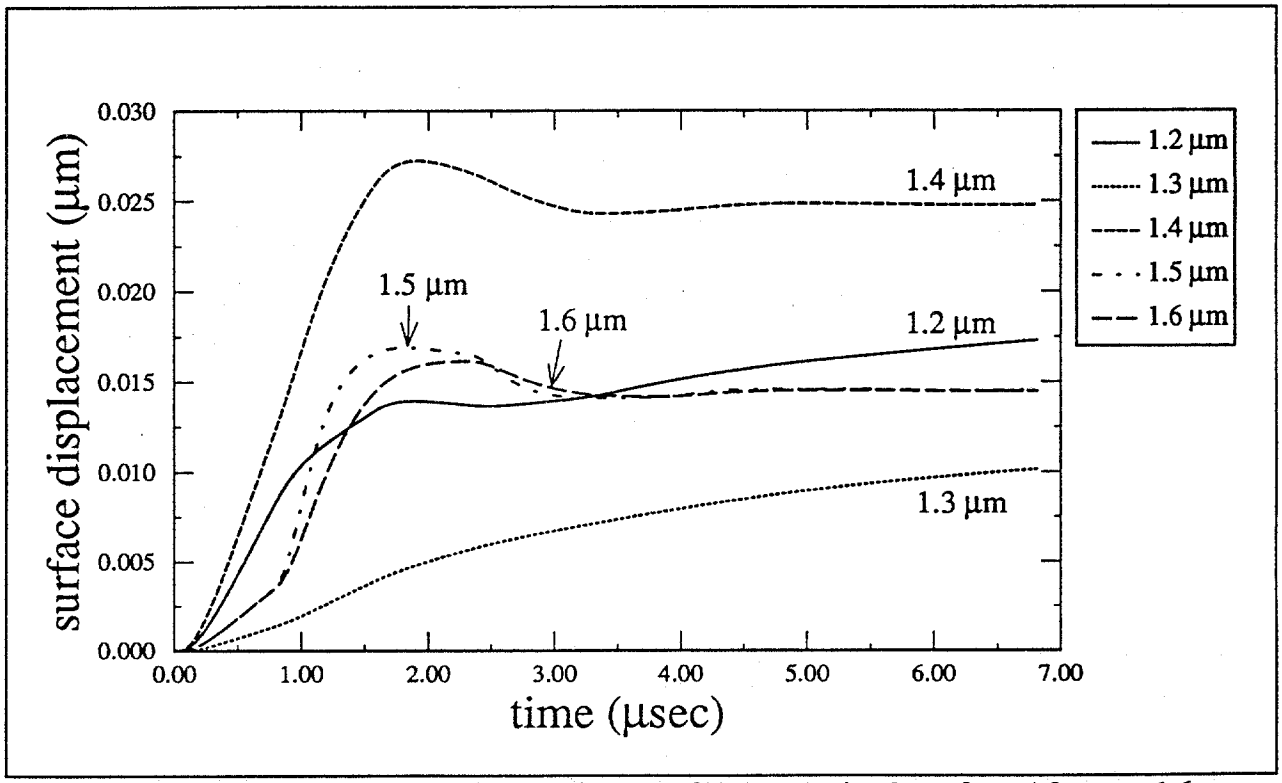

Figure 12 - Surface displacement for wavelengths of the generating laser from 1.2 μm to 1.6 μm

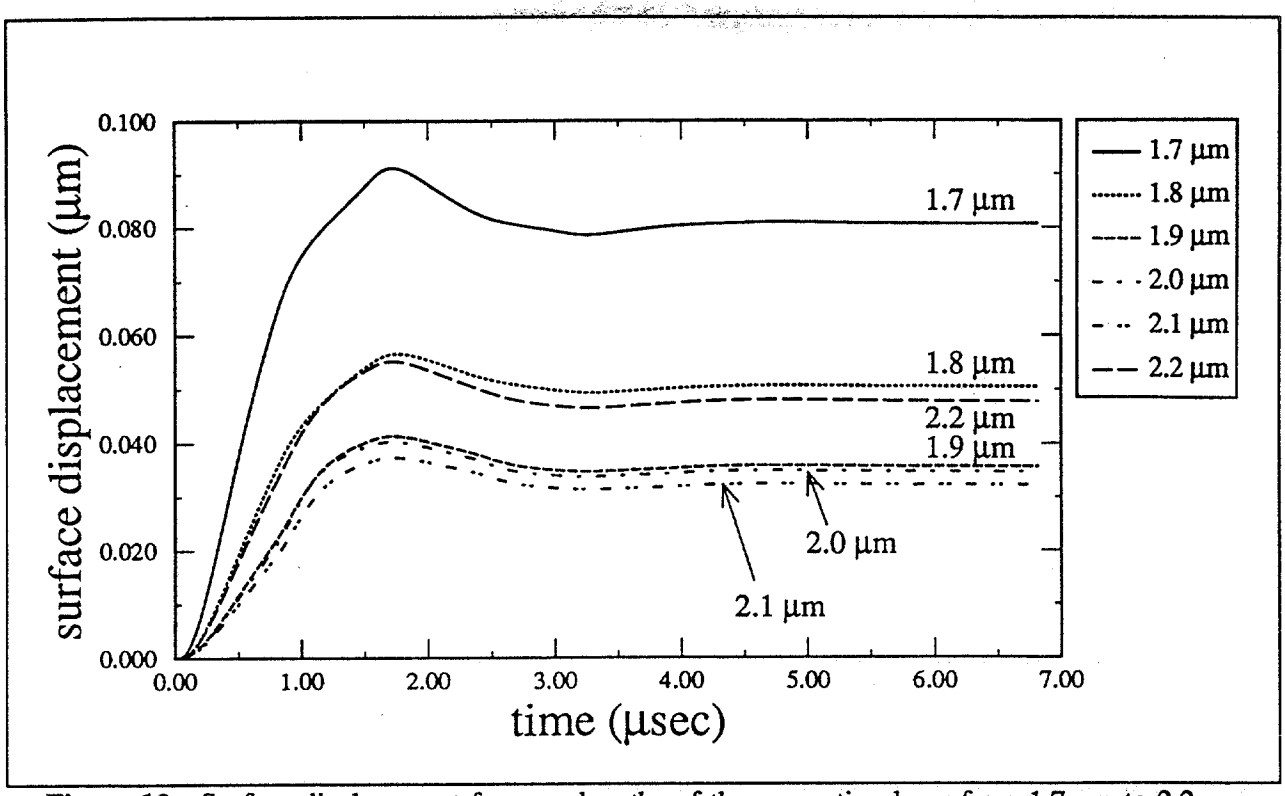

Figure 13 - Surface displacement for wavelengths of the generating laser from 1.7 μm to 2.2 μm

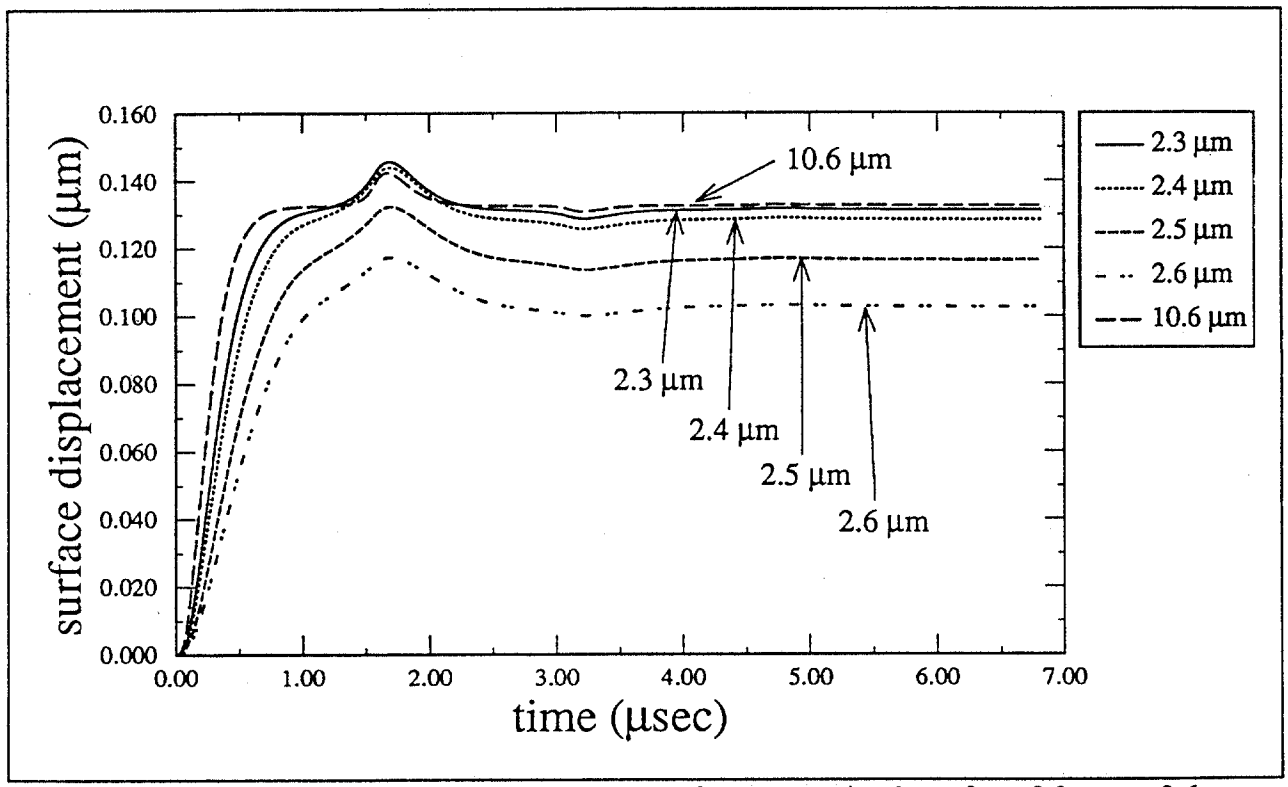

Figure 14 - Surface displacement for wavelengths of the generating laser from 2.3 μm to 2.6 μm

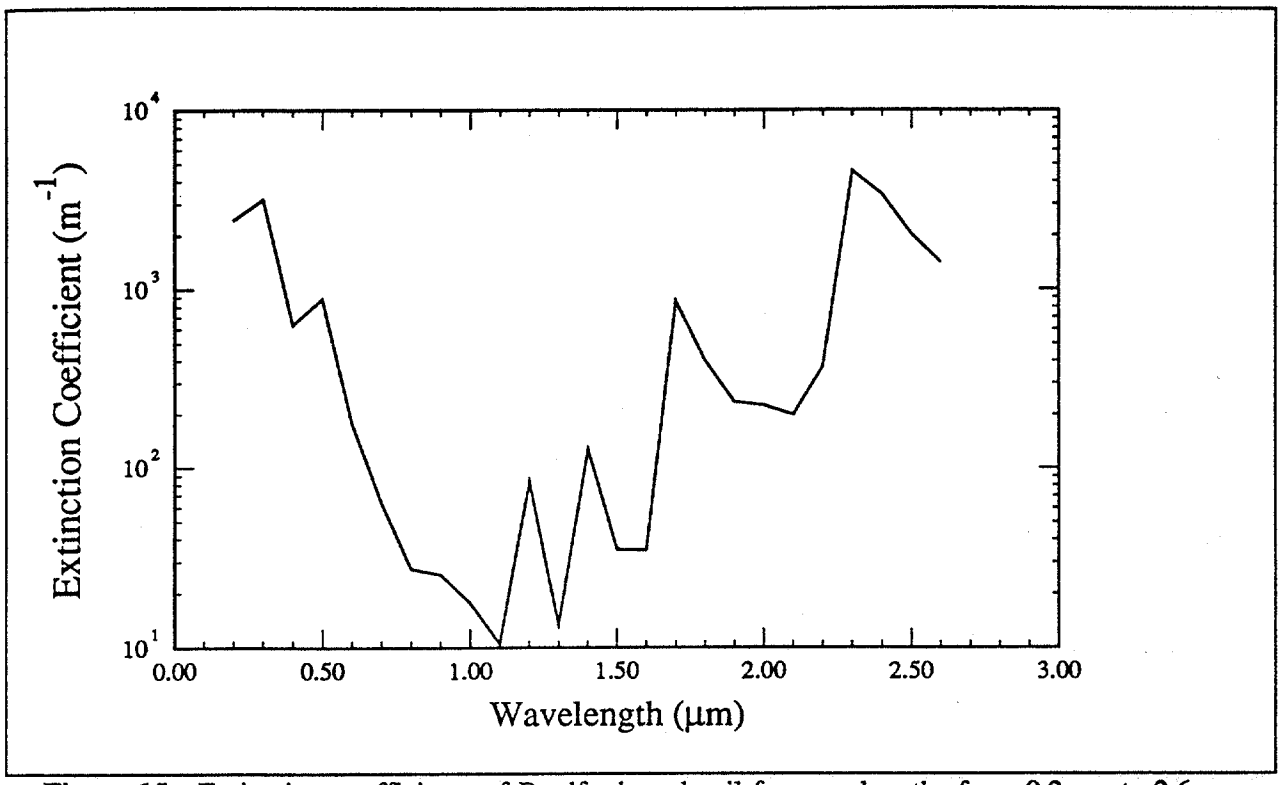

Figure 15 - Extinction coefficients of Bradford crude oil for wavelengths from 0.2 μm to 2.6 μm

2.3 Variability with Respect to Oil Type

In this section, the variability of the thermoelastic displacement in various types of oil was studied for the above four wavelengths. In this case, twelve different types of oil were considered.[3] The maximum, minimum and averaged optical absorption coefficients at each of the four wavelengths were used for the thermoelastic displacement calculation. For the wavelength at 0.3 μm, the optical absorption coefficients of only five types of oil were available. The range of optical absorption coefficients for the four wavelengths are summarized in Table 2 and plotted in Figure 16.

[3] R. Horvath, W.L. Morgan, R. Spellicy, "Measurements Program for Oil-slick Characteristics", U.S. Coast Guard Tech. Rep. AD-758 591, Feb. 1970.

Table 2: Optical Absorption Coefficient of Oil

Wavelength	Optical Absorption Coefficient (m^{-1}) Minimum	Maximum	Range of Optical Absorption Coefficient (m^{-1})	Variability of Thermoelastic Displacement
0.3 μm	$2.7x10^3$	$4.3x10^4$	$4.03x10^4$	moderate
1.7 μm	$8.6x10^2$	$1.7x10^3$	$8.40x10^2$	most
2.3 μm	$4.0x10^3$	$5.8x10^3$	$1.80x10^3$	least
10.6 μm	$2.6x10^3$	$6.3x10^3$	$3.70x10^3$	moderate

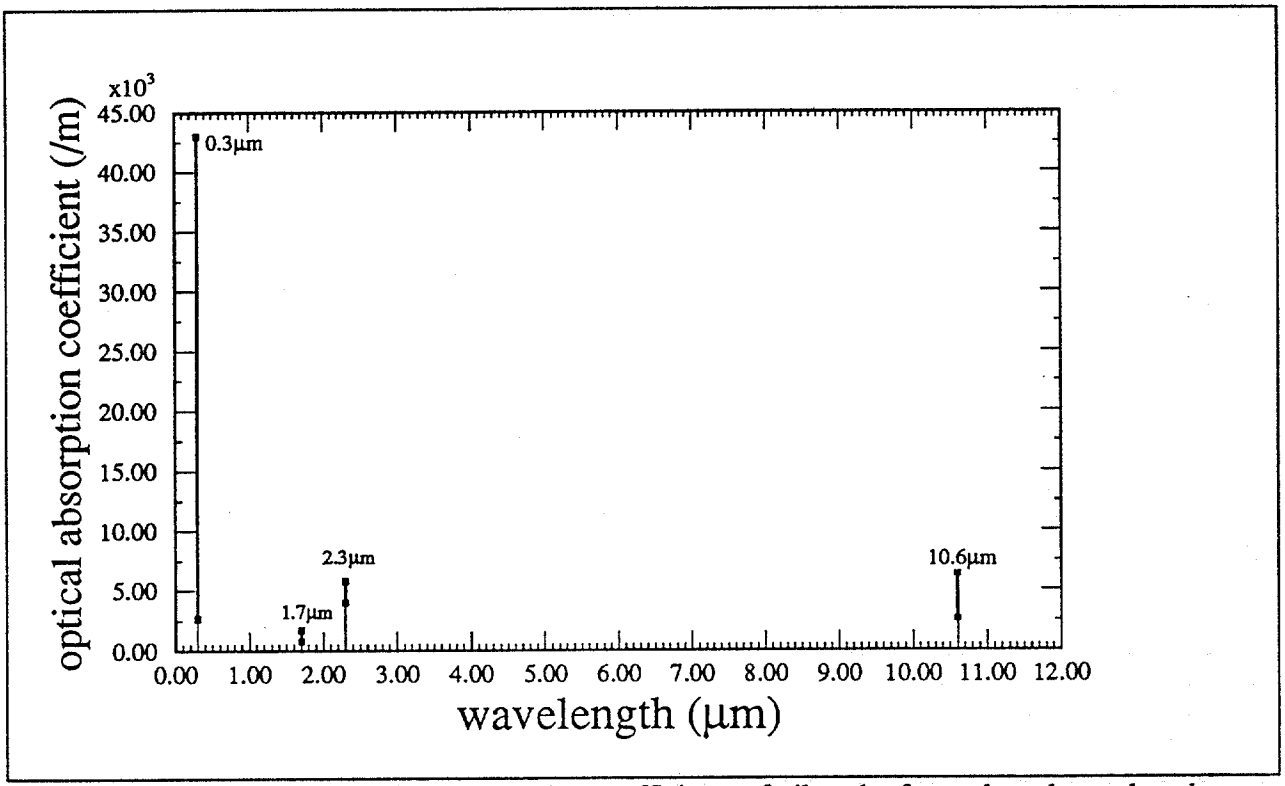

Figure 16 - Values of optical absorption coefficients of oil at the four selected wavelengths

At the wavelength of 0.3 μm, the values and the range of the optical absorption coefficient are the largest among the four wavelengths. The thermoelastic displacements shown in Figure 17 show that the variability is small when the optical absorption coefficients are relatively large. However, it can also be observed that the peak of the echo is significantly reduced for large values of the optical absorption coefficient. The thermoelastic displacements shown in Figure 18 for the wavelength of 1.7 μm show large variability even though the optical absorption coefficient has the smallest range. However, these values are also the smallest. The results for a wavelength of 2.3 μm in Figure 19 show little variation of the thermoelastic displacement for the range of values for the optical absorption coefficient. The echo returns are essentially unchanged. In Figure 20, the results for the wavelength at 10.6 μm are similar to that of 0.3 μm except that the peak of the echo is now maintained almost constant.

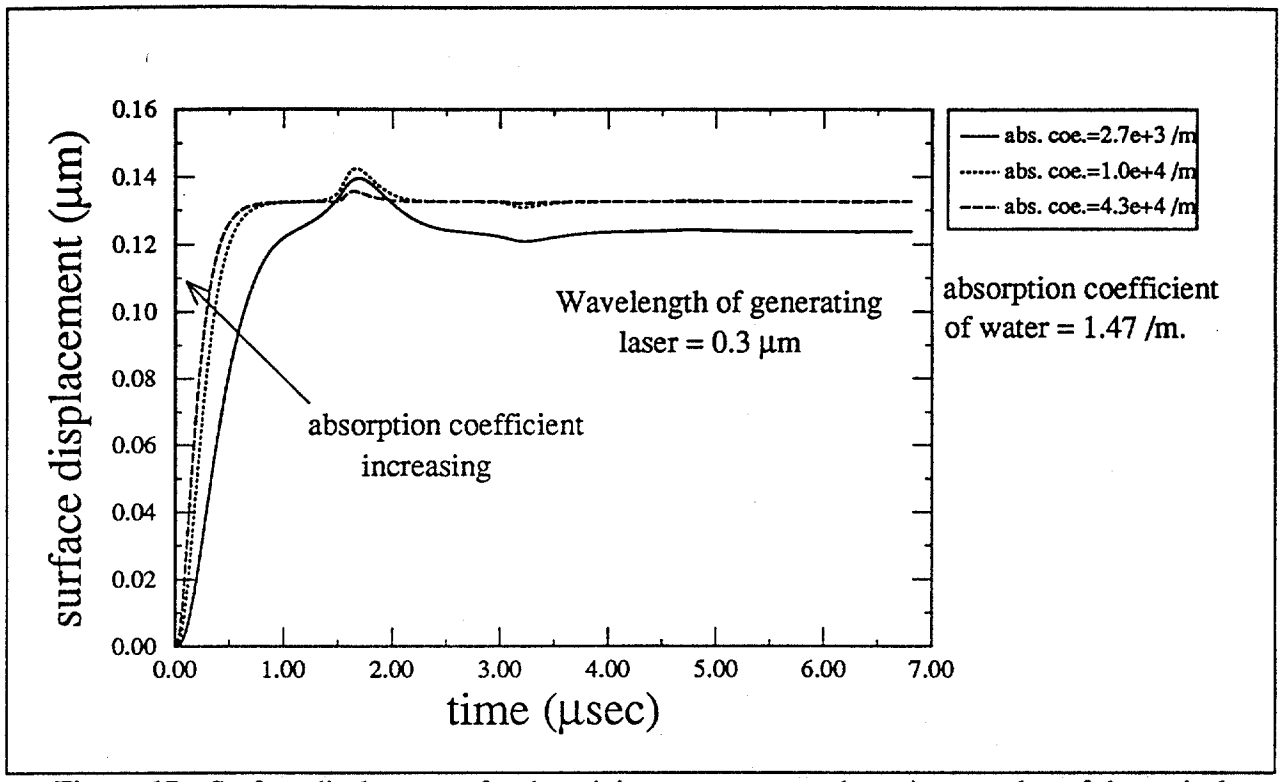

Figure 17 - Surface displacement for the minimum, average and maximum value of the optical absorption coefficient at the wavelength of 0.3 μm

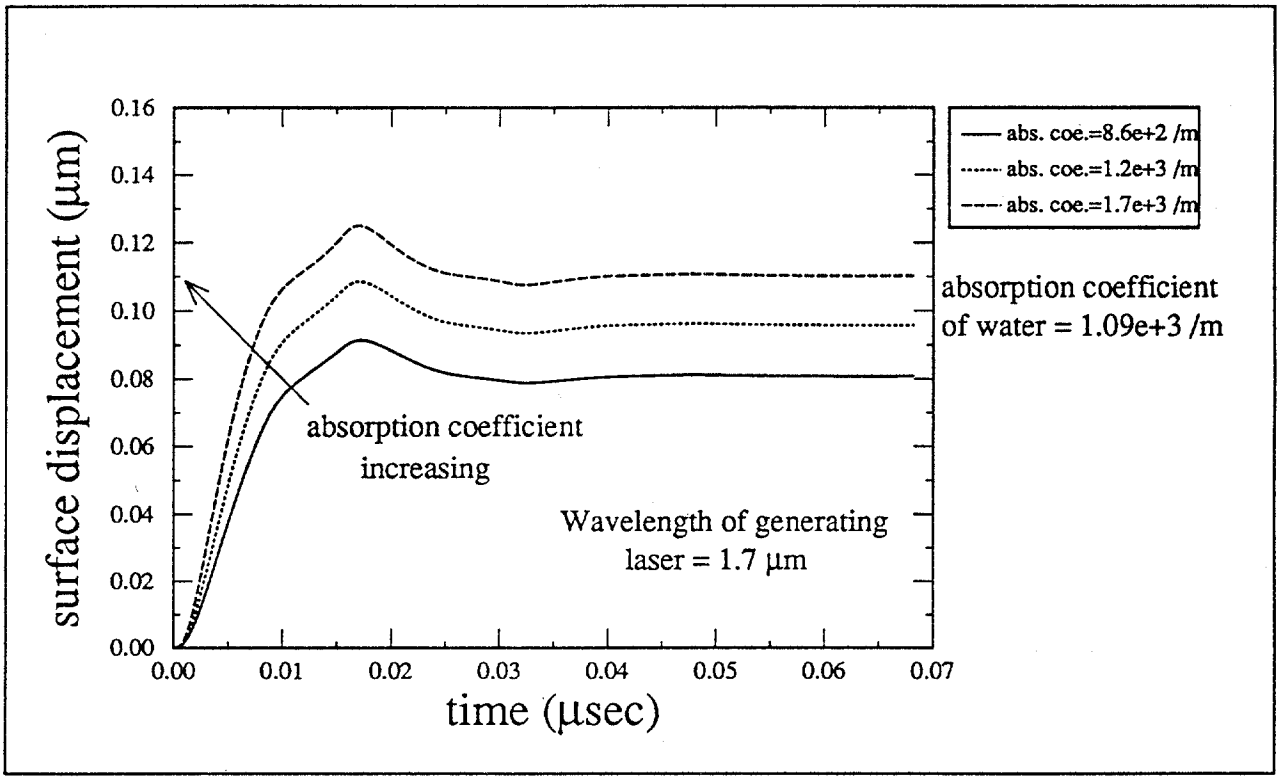

Figure 18 - Surface displacement for the minimum, average and maximum value of the optical absorption coefficient at the wavelength of 1.7 μm

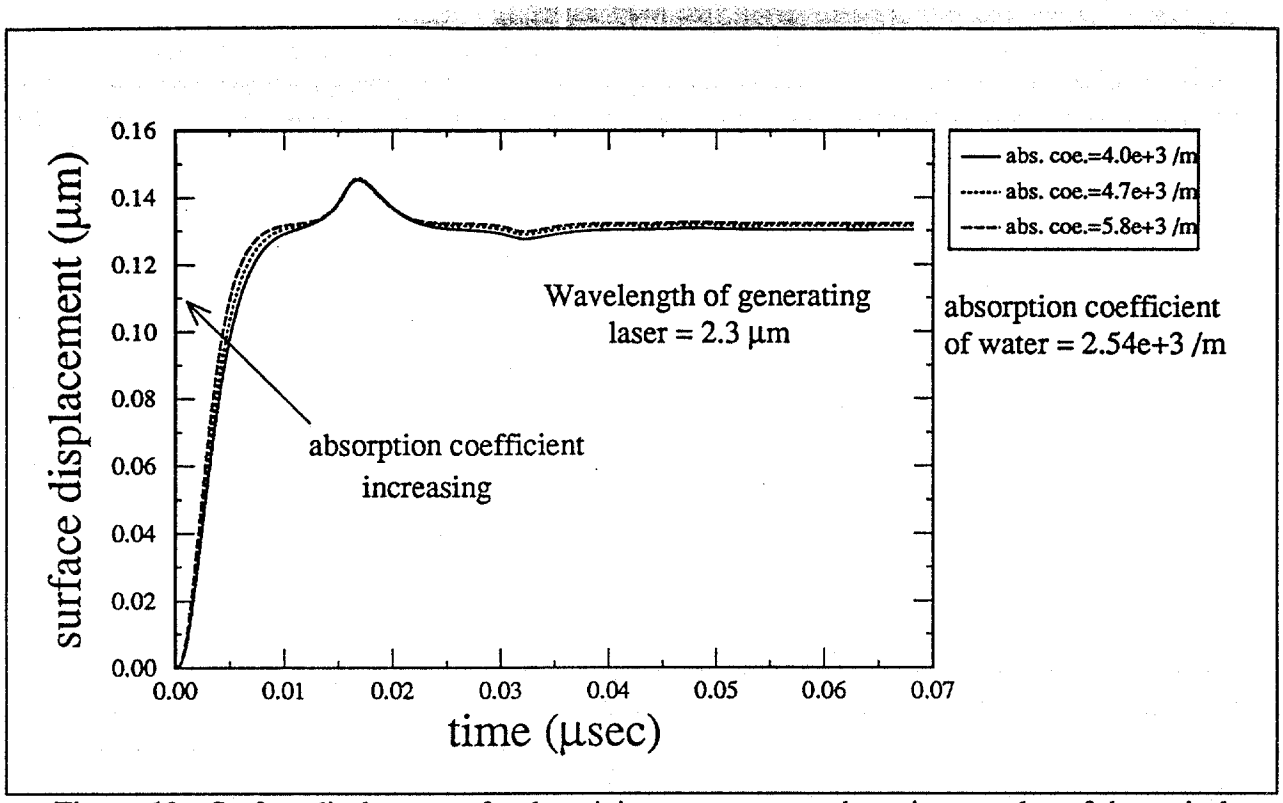

Figure 19 - Surface displacement for the minimum, average and maximum value of the optical absorption coefficient at the wavelength of 2.3 μm

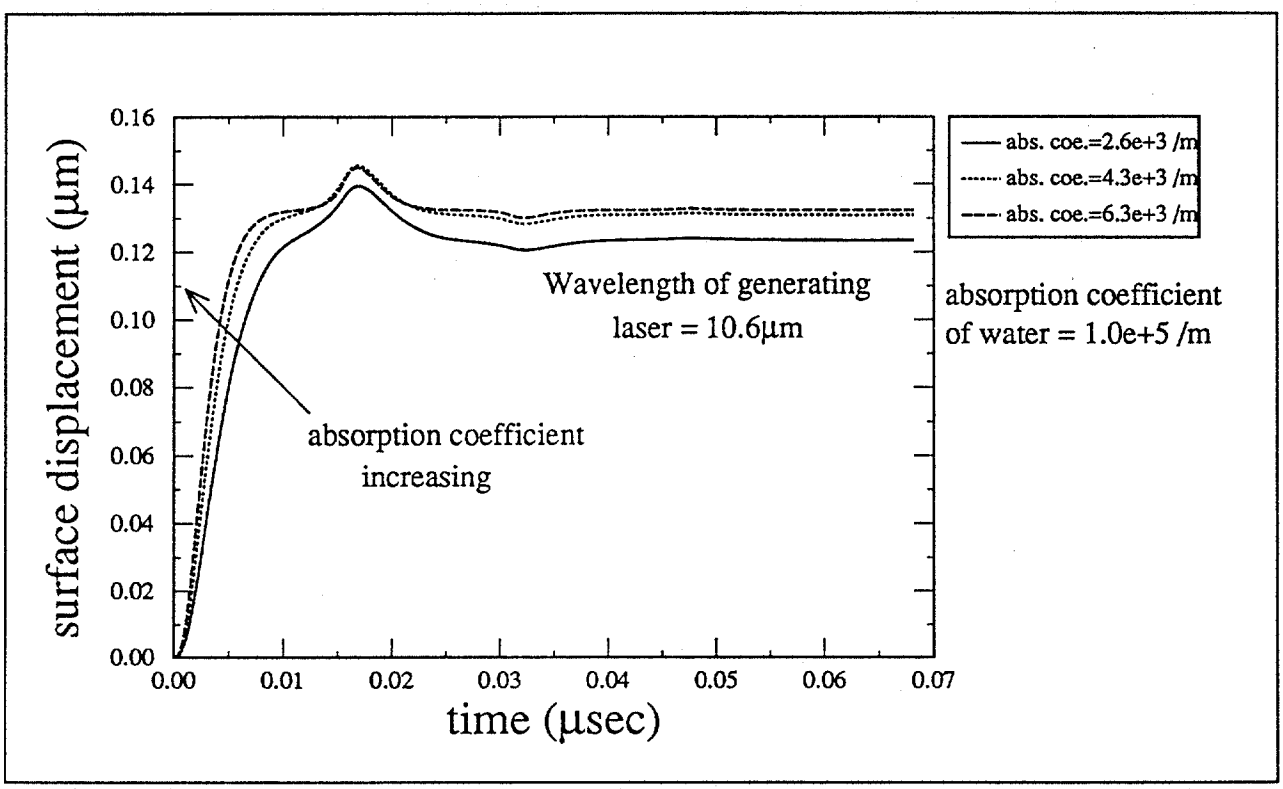

Figure 20 - Surface displacement for the minimum, average and maximum value of the optical absorption coefficient at the wavelength of 10.6 μm

In summary, our examination of the wavelength dependence of the laser-ultrasonic response suggests that there are 3 or 4 preferred wavelength regions for the generating laser. Of the four wavelength regions examined in detail, 2.3 μm appears to be the best choice since the laser-ultrasonic response is both strong and independent of oil type. The results also show that the responses at 0.3 μm and 10.6 μm are very similar. Finally, there is a great deal of variability at 1.7 μm for the different oils. This makes this wavelength less desirable although, as we will discuss in later sections, there are other reasons to consider this wavelength.

2.4 Sensitivity to Generating Laser Risetime and Energy

The results obtained from the IMI computer model suggested that the wavelength of the pulsed generating laser at 2.3 μm or 10.6 μm could generate optimum thermoelastic displacement. We now look at the effect of changing the risetime and energy of the pulsed generating laser with the wavelength chosen to be 10.6 μm. The reason for this choice is mainly because this wavelength is used for the system built by IMI.

In the previous calculations we have only used that portion of the IMI model that calculated the surface displacement. For the analysis of the risetime and energy, we use the model of the demodulation receiver to examine how changes in these two parameters affect the demodulation receiver output. In this modeling, the Doppler shifted probe laser beam was assumed to be optically demodulated by a 1 m confocal Fabry-Perot Interferometer (c-FPI) of finesse 10, the same optical demodulation technique used in the current LURSOT design. The transmission response of the c-FPI is determined by the degree to which the frequency of the reflected probe laser light matches the bandpass of the c-FPI. Optimal transmission will occur if the return frequency falls near the center of this bandpass. For optimal detection of the Doppler shifted return, the c-FPI is tuned such that the unshifted frequency of the probe laser falls on one side of the transmission curve. At this point, the transmission versus frequency has a very large slope, so small changes in frequency will result in large changes in the c-FPI transmission.

Sample input and output signals of the receiver are illustrated in Figure 21. The output of the receiver is almost directly proportional to the instantaneous velocity of the oil surface. A typical waveform of the output of the c-FPI consists of a surface pulse and the echo pulses which correspond to the initial surface displacement and echo displacements respectively. Obviously, a large magnitude of the output surface pulse and the echo pulses is needed to identify them more accurately.

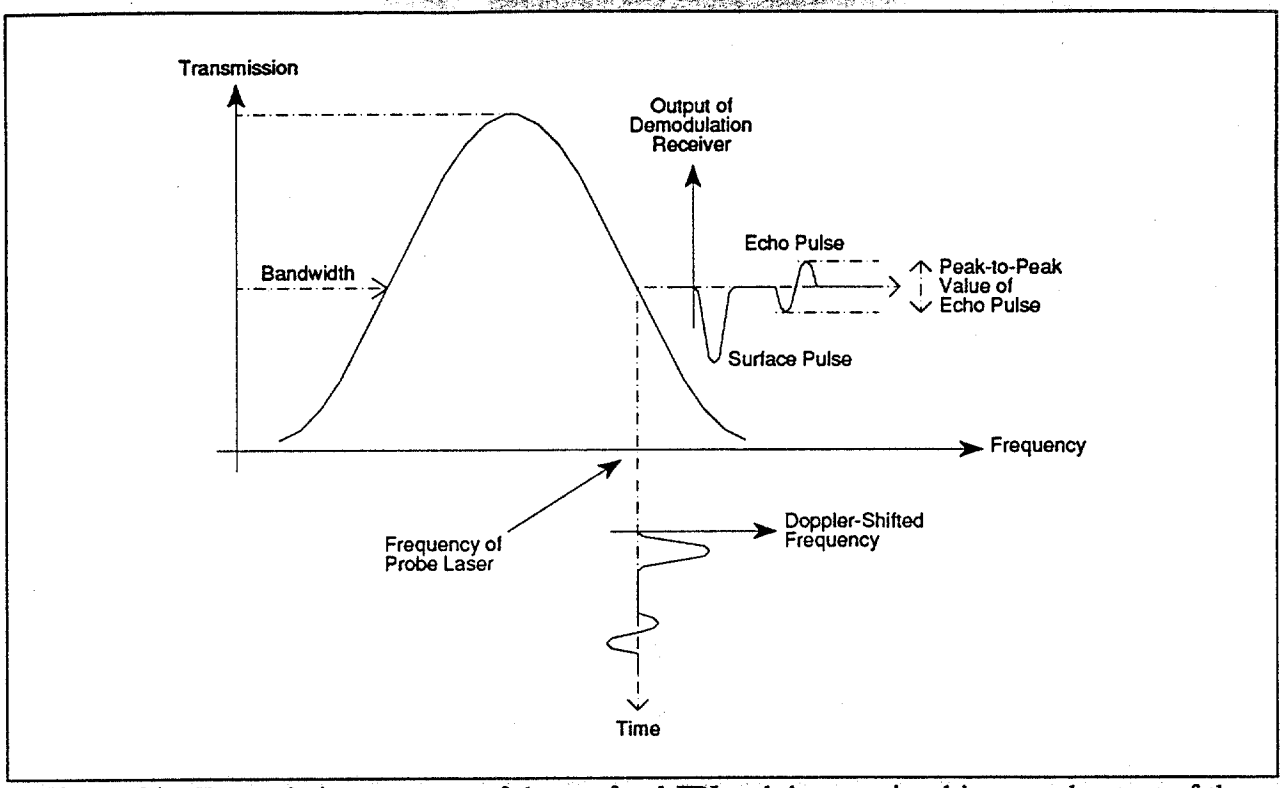

Figure 21 - Transmission response of the confocal FPI and the associated input and output of the demodulation receiver

First, the risetime of the pulsed generating laser was varied from 10 ns to 250 ns. From the calculations, the risetime of the initial surface displacement and the peak of the first echo displacement were evaluated. At the output of the c-FPI, the peak value of the surface pulse and the peak-to-peak value of the first echo pulse were also of interest. This is because the magnitude of these two output pulses determines the probability of identification of the pulses in the subsequent analysis to determine the oil thickness. These results are shown in Figures 22-25 respectively. Figure 22 shows that the risetime of the surface displacement is directly proportional to the risetime of the generating laser pulse. A shorter risetime for the initial surface displacement is preferred because the optical demodulation technique is sensitive to the rate of change, that is, the instantaneous velocity, of the thermoelastic displacement. Figure 23 shows that the larger the risetime of the pulsed generating laser is, the smaller the peak of the echo displacement will be. Also, a shorter generating laser pulse improves the capability of the system to measure thin oil layers, as the initial surface displacement and the sharper echo displacement can be distinguished more easily.

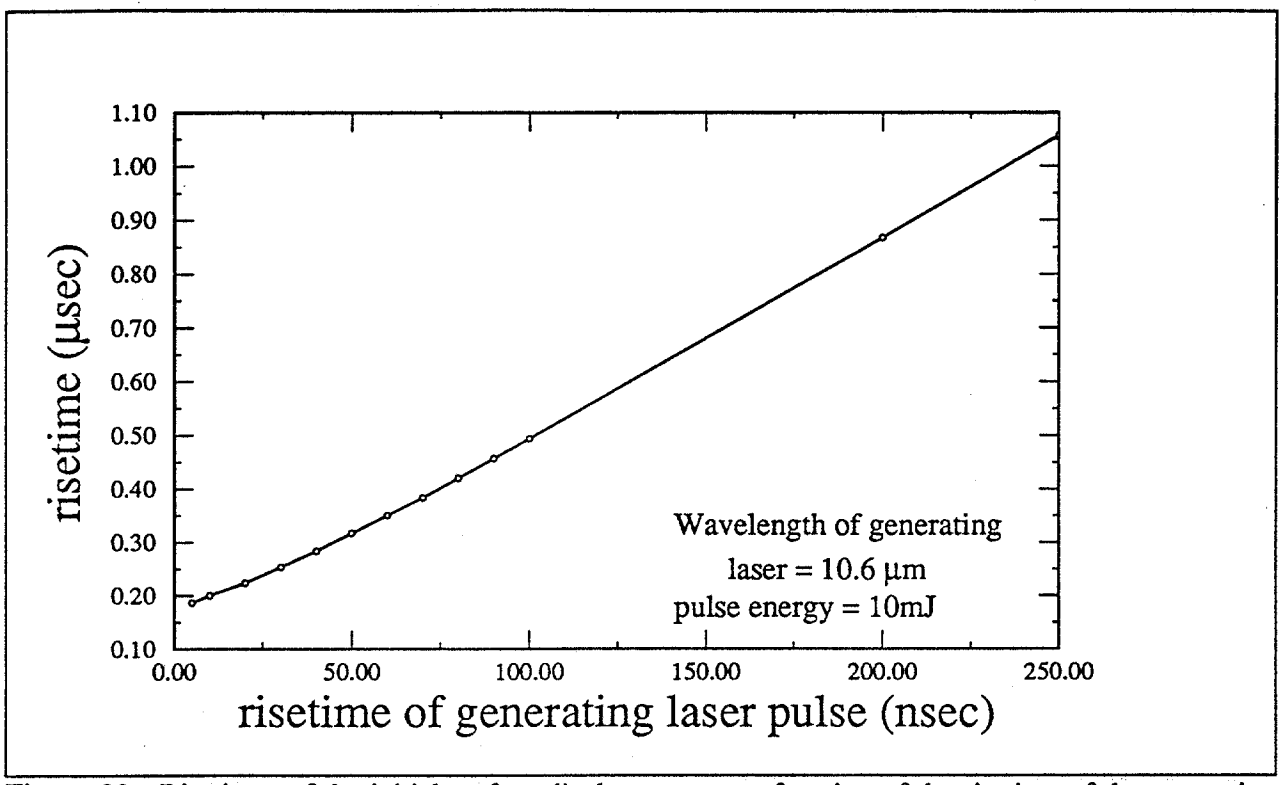

Figure 22 - Risetimes of the initial surface displacement as a function of the risetime of the generating laser pulse

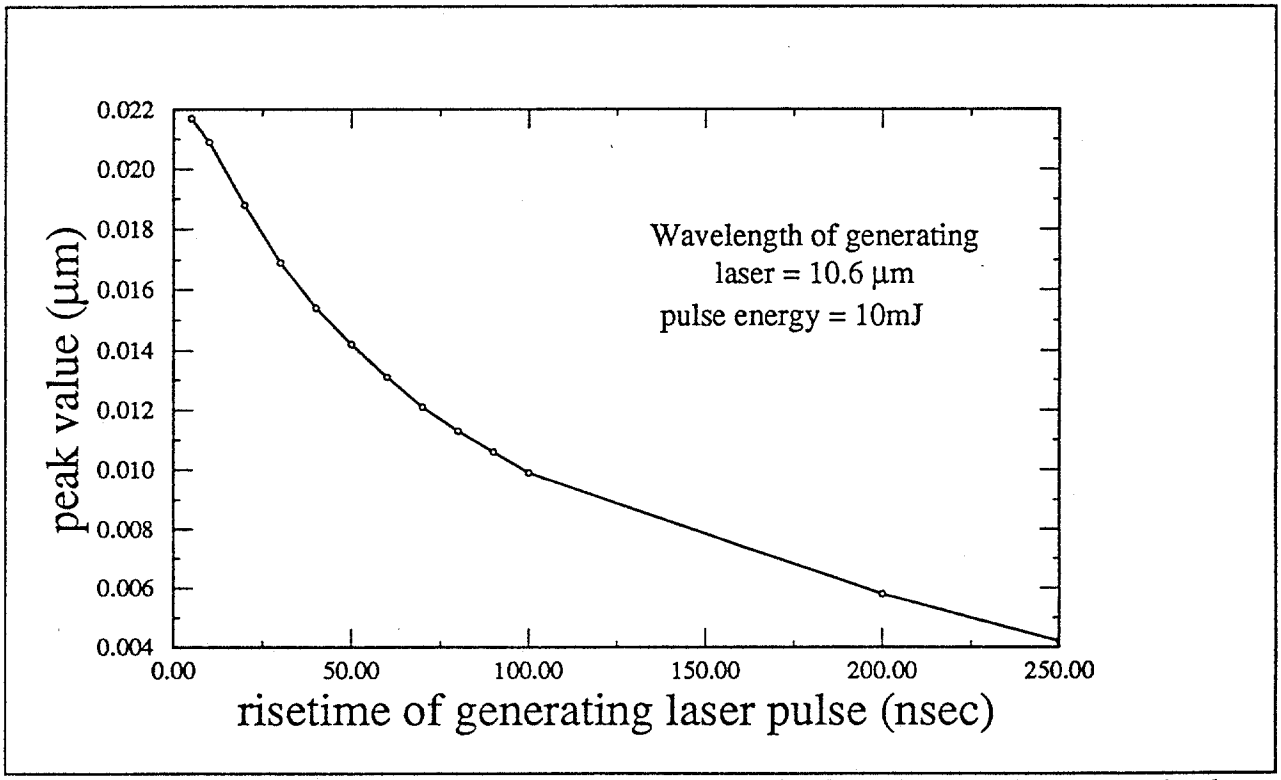

Figure 23 - Peak values of the echo displacement as a function of the risetime of the generating laser pulse

At the output of the c-FPI, the peak value of the surface pulse is inversely proportional to the risetime of the pulsed generating laser as shown in Figure 24. A similar result is observed for the peak-to-peak value of the echo pulse at the output of the c-FPI, as indicated by Figure 25. These results clearly demonstrate that a short risetime for the pulsed generating laser is preferred. Ideally, the generating laser pulse risetime should be of the order of 10 ns. This is considerably shorter than the risetime available from the CO_2 laser used in the current LURSOT design.

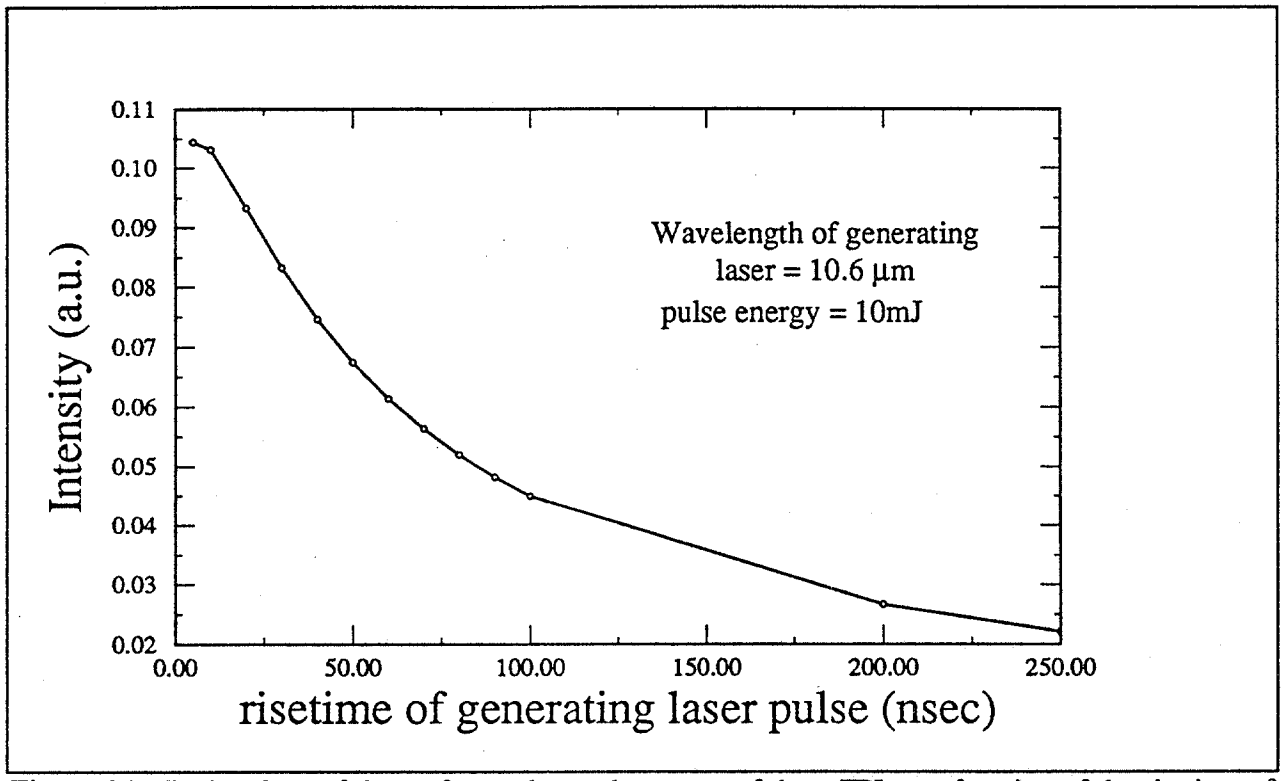

Figure 24 - Peak values of the surface pulse at the output of the c-FPI as a function of the risetime of the generating laser pulse

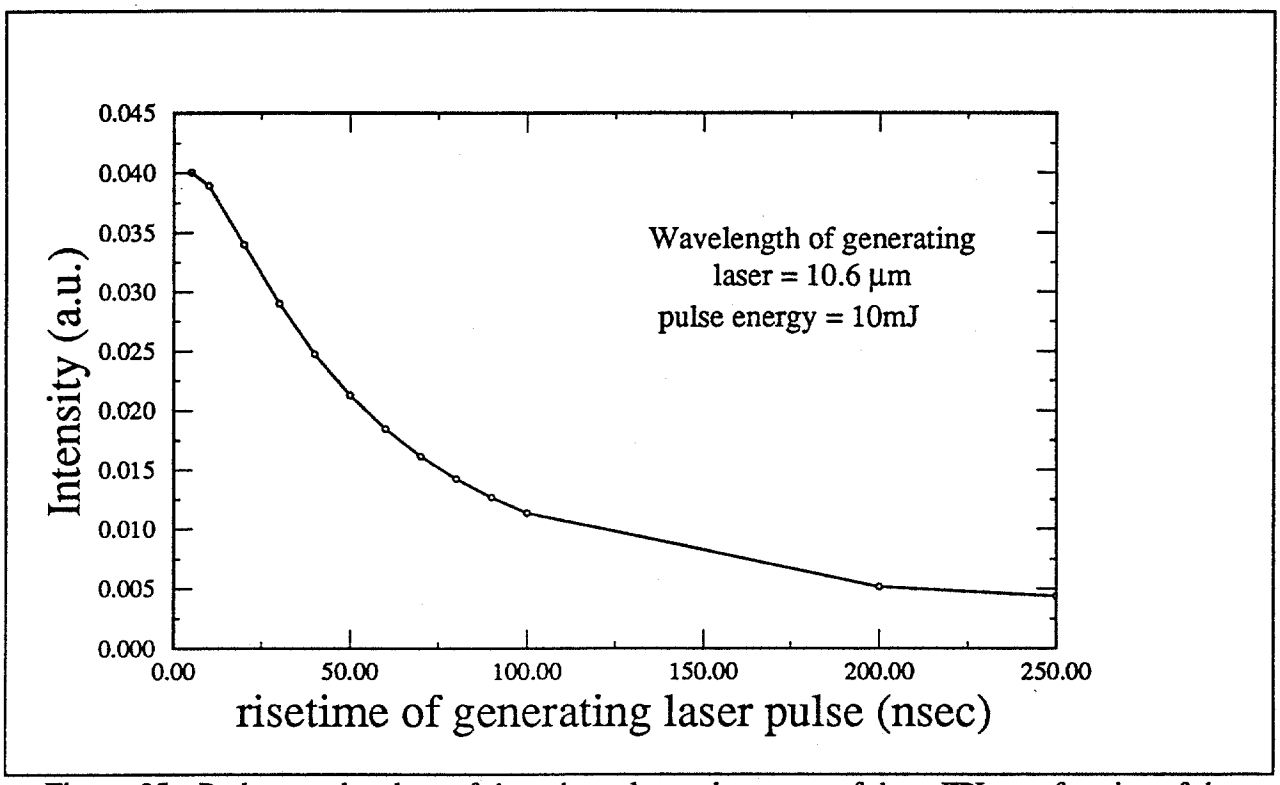

Figure 25 - Peak-to-peak values of the echo pulse at the output of the c-FPI as a function of the risetime of the generating laser pulse

We now examine the effect of changing the pulse energy. For these calculations we assumed a pulse risetime of 10 ns. As the pulse energy was varied from 1 mJ to 200 mJ, the results in Figure 26 and Figure 27 show that the magnitude of the step of the surface displacement and the peak of the echo displacement are directly proportional to the pulse energy of the laser. The large magnitude of the step of the laser-ultrasonic displacement implies the instantaneous velocity of the initial surface displacement is larger. Figure 28 and Figure 29 show that for lower (< 50 mJ) pulse energies, the peak of the surface pulse and the peak-to-peak value of the echo pulse at the output of the c-FPI are also linearly proportional to the pulse energy. Note, however, that the peak of the surface pulse will saturate at lower laser pulse energies than the peak-to-peak value of the echo pulse. Despite this, since it is more difficult to identify the echo pulse because of its smaller magnitude, it may be desirable to increase the pulse energy to get a larger peak-to-peak value of the echo pulse even though there is no gain in the peak value of the surface pulse.

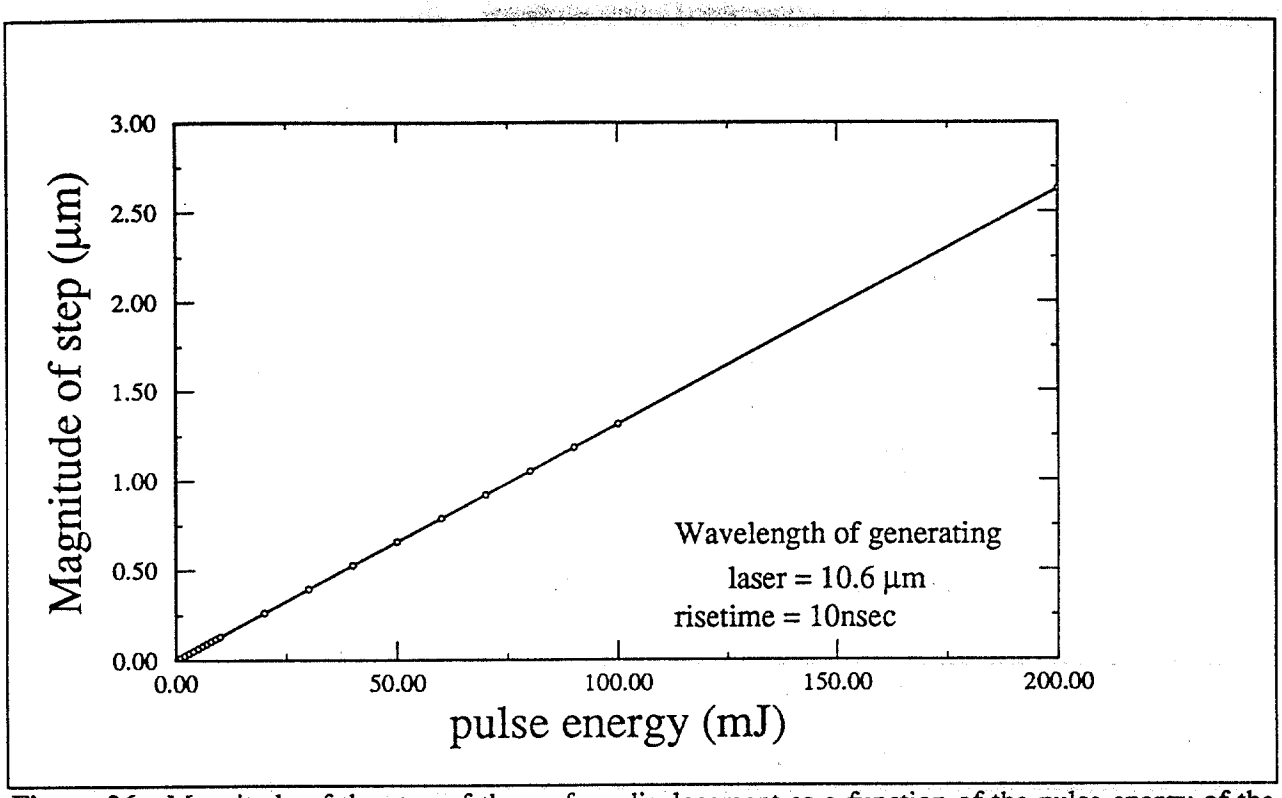

Figure 26 - Magnitude of the step of the surface displacement as a function of the pulse energy of the generating laser

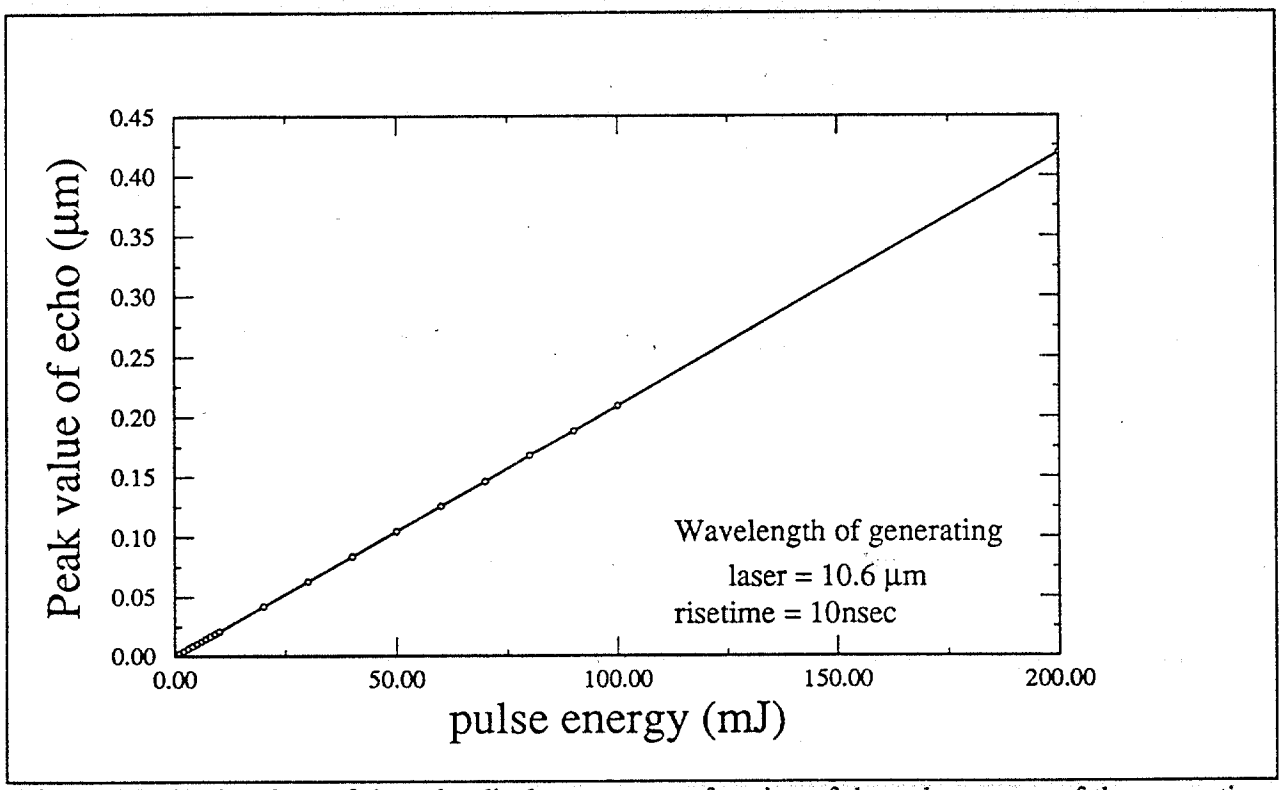

Figure 27 - Peak values of the echo displacement as a function of the pulse energy of the generating laser

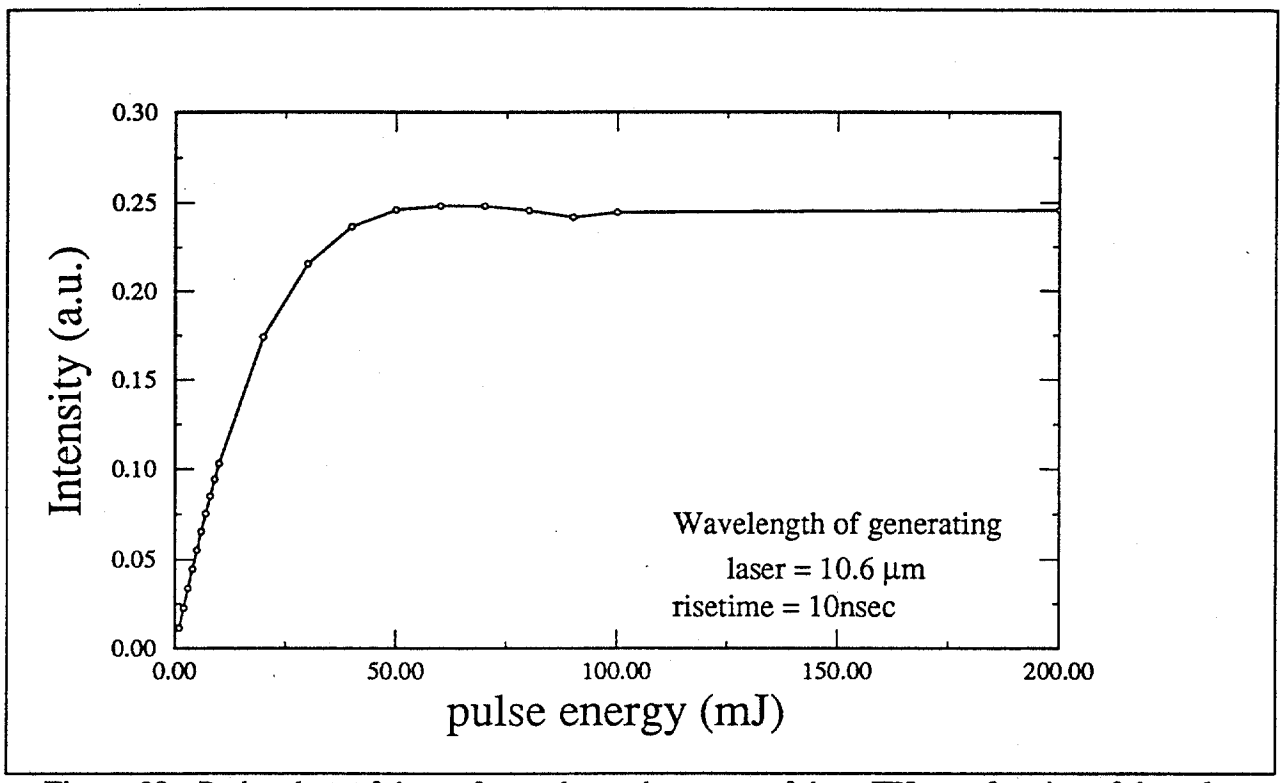

Figure 28 - Peak values of the surface pulse at the output of the c-FPI as a function of the pulse energy of the generating laser

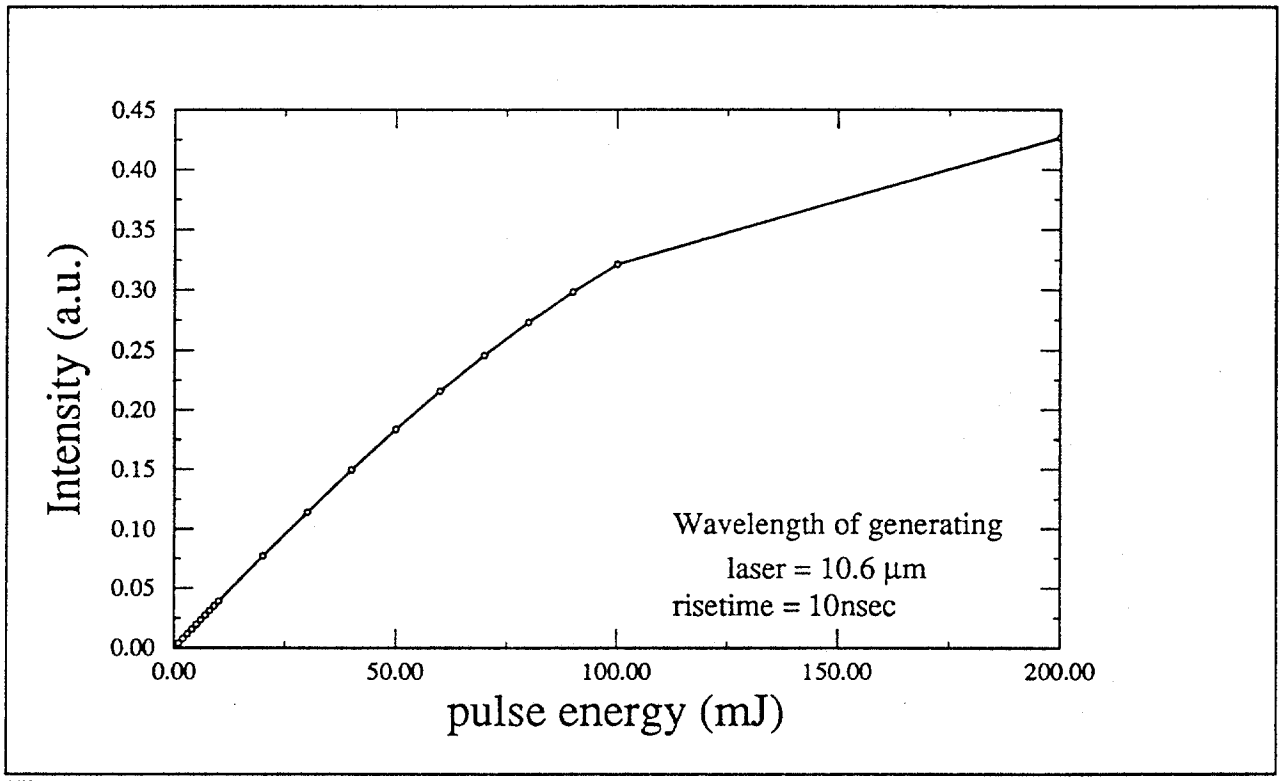

Figure 29 - Peak-to-peak values of the echo pulse at the output of the c-FPI as a function of the pulse energy of the generating laser

2.5 Analysis of the Instantaneous Velocity of the Initial Surface Displacement

In the above sections, we have used the IMI model to examine the dependence of the laser-ultrasonic measurement on the characteristics of the oil and the generating laser. In this section, we look at what the model can tell us about the demodulation receiver and probe laser. Unfortunately, the IMI model does not take the analysis far enough since it does not calculate the instantaneous velocity of the oil surface. As a result, the initial surface displacement of the oil sample is calculated analytically in this section. From this, the instantaneous velocity of the oil surface can be evaluated. Since the Doppler shifted frequency of the probe laser beam is directly proportional to the instantaneous velocity of the oil surface, the frequency modulation of the probe laser beam is thus obtained from the instantaneous velocity of the oil surface. Based on the frequency modulation of the probe laser beam, the requirements of the demodulation receiver can be defined and examined.

Equation (1) for the Laplace Transform of the thermoelastic displacement is a very complex function of the characteristics of the pulsed generating laser and the physical properties of the oil and water samples. From the numerical calculations, it has been observed that the initial surface displacement possesses a larger instantaneous velocity than that of the echo displacement. As the amount of Doppler shifted frequency induced on the probe laser is linearly proportional to the instantaneous velocity of the thermoelastic displacement, the largest instantaneous velocity expected under various operating conditions will determine the optical bandwidth of the optical demodulation receiver. Therefore, the analytical description of the initial surface displacement provides insight on how the demodulation receiver should be designed. However, directly solving Equation (1) analytically to obtain the thermoelastic displacement is not possible. Since the initial surface displacement is of more interest, the analytical description of it would be very useful. Equation (1) can be significantly simplified if the thickness of the oil layer is assumed to be infinite. In this situation, the echoes will arrive at a time which is infinitely long. Therefore, the solution to Equation (1) will consist of only the initial surface displacement. Hence, putting L equal to ∞, the Laplace Transform of the thermoelastic displacement becomes

$$U(0,s) = \frac{-3\nu_{long}\alpha\alpha_T}{\rho C s(s+\nu_{long}\alpha)} \Phi_o F(s) \qquad (2)$$

where Φ_0 (W/m^2) is the peak power density of the pulsed generating laser at the surface of oil, and is given by

$$\Phi_o = \frac{P}{r^2\pi} \qquad (3)$$

where P (W) is the peak power of the pulsed generating laser and r is the radius of the generating laser spot on the oil surface.

The physical parameters shown in Equation (2) are those of the oil. A typical normalized pulse shape of the generating laser is of the form

$$f(t) = \frac{t}{\tau} e^{1-\frac{t}{\tau}} \tag{4}$$

where τ is defined as the risetime of the pulse.

The Laplace Transform of this normalized pulse is

$$F(s) = \frac{e\tau}{(1+\tau s)^2} \tag{5}$$

As a result, the product Φ_0 F(s) is related to the pulse energy E of the generating laser as

$$\Phi_o F(s) = \frac{E}{r^2\pi(1+\tau s)^2} \tag{6}$$

where the pulse energy E is given by

$$E = Pe\tau \tag{7}$$

Obviously, the expressions shown in Equation (2) and Equation (6) are much simpler now and the inverse Laplace Transform is hence given by

$$u(t) = \frac{-3\nu_{long}\alpha\alpha_T E}{\rho C r^2\pi} \left\{ \frac{1}{\nu_{long}\alpha} - \frac{1}{\nu_{long}\alpha(\nu_{long}\alpha\tau-1)^2} e^{-\nu_{long}\alpha t} \right. \tag{8}$$

$$\left. + \frac{\tau(2-\nu_{long}\alpha\tau)}{(\nu_{long}\alpha\tau-1)^2} e^{-\frac{t}{\tau}} - \frac{1}{(\nu_{long}\alpha\tau-1)} t\, e^{-\frac{t}{\tau}} \right\}$$

A plot of the thermoelastic displacement using Equation (8) with the nominal parameters in Table 1 is shown in Figure 30. Two curves are shown in this plot, corresponding to different generating laser characteristics. In one case we assumed a CO_2 generating laser having a wavelength of 10.6 μm and a pulse risetime of 100 ns. In the second case, we assumed a 2.3 μm laser having a 10 ns risetime. In both cases we have assumed that the energy density on the oil surface is the same. Clearly, the resulting displacement does not consist of any echoes, and the initial surface displacement within the first 1 microsecond and the magnitude of the step are identical to results shown in previous figures using the computer model. We once again see the strong influence of the laser pulse risetime on the surface response. The magnitude of the step can be analytically obtained from Equation (8) as time tends to infinity.

$$u(\infty) = \frac{-3\alpha_T E}{\rho C r^2\pi} \tag{9}$$

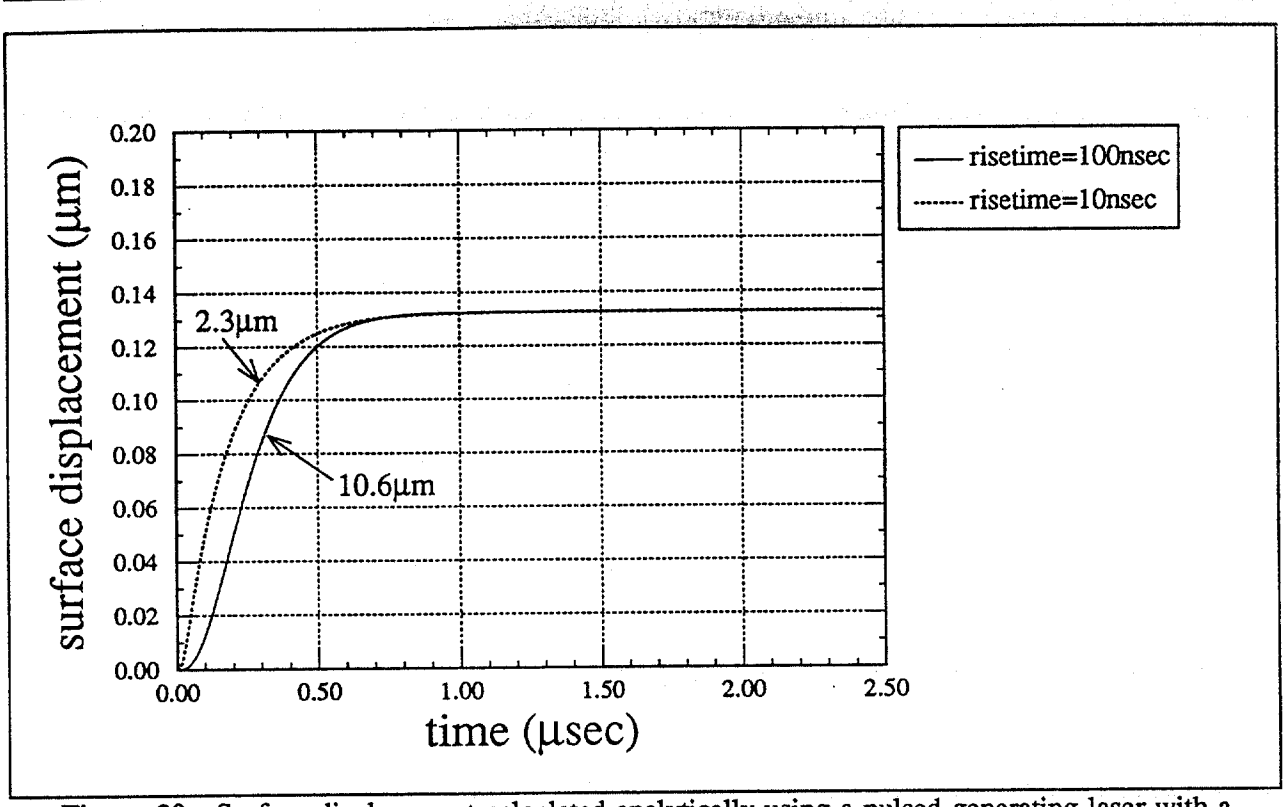

Figure 30 - Surface displacement calculated analytically using a pulsed generating laser with a risetime of 100 ns at 10.6 μm and 10 ns at 2.3 μm

Interestingly from Equation (9), the magnitude of the step is shown to be linearly proportional to the thermal expansion coefficient of the oil and the pulse energy of the generating laser, and inversely proportional to the density and specific heat of the oil. This observation has already been demonstrated using the computer model. The magnitude of the step is also inversely proportional to the radius of the focused generating laser spot on the oil surface. Consequently, larger power density on the surface of the oil sample yields a larger step of the thermoelastic displacement of oil.

As was already mentioned, the optical demodulation technique is sensitive to the instantaneous velocity of the thermoelastic displacement. The instantaneous velocity of the initial surface displacement v(t) can be obtained by taking the derivative of Equation (8). Therefore,

$$v(t) = \frac{-3v_{long}\alpha\alpha_T E}{\rho C r^2 \pi (v_{long}\alpha\tau - 1)} \left\{ \frac{t}{\tau} e^{-\frac{t}{\tau}} + \frac{1}{(v_{long}\alpha\tau - 1)} \left[e^{-v_{long}\alpha t} - e^{-\frac{t}{\tau}} \right] \right\} \qquad (10)$$

Once the instantaneous velocity of the thermoelastic displacement is known, the amount of Doppler shifted frequency induced on the probe laser beam with wavelength λ_p can be evaluated by

$$Doppler\ frequency = -\frac{2\ v(t)}{\lambda_p} \qquad (11)$$

Obviously, the Doppler shifted frequency induced on the probe laser is directly proportional to the instantaneous velocity of the surface displacement of the oil and inversely proportional to the

wavelength of the probe laser. Figure 31 shows the instantaneous velocity of the initial surface displacement for the two generating lasers. The corresponding Doppler shifted frequencies are shown in Figure 32. From Figure 31, it can be observed that the maximum instantaneous velocity of the initial surface displacement is strongly dependent on the generating pulse risetime. For the 100 ns and 10 ns cases, the maximum velocity is on the order of 0.4 m/s and 0.6 m/s respectively. Any disturbances whose velocity is also of this order of magnitude will definitely affect the performance of the system in measuring the thickness of the oil layer. Figure 32 shows that the maximum Doppler shifted frequency is of the order of megahertz assuming that the wavelength of the probe laser beam is at 1.06 μm. For the current LURSOT system, the bandwidth of the demodulation receiver is about 7.5 MHz. This may be larger than the bandwidth required to demodulate the laser-ultrasonic signal, which has a maximum frequency change of about 0.75 MHz as shown in Figure 32. Therefore, the demodulation receiver of the existing LURSOT system might not be optimally designed. The bandwidth of the demodulation receiver must be designed with the same order of magnitude as the maximum Doppler shifted frequency of the probe laser beam for sensitive detection of the thermoelastic displacement of the oil surface.

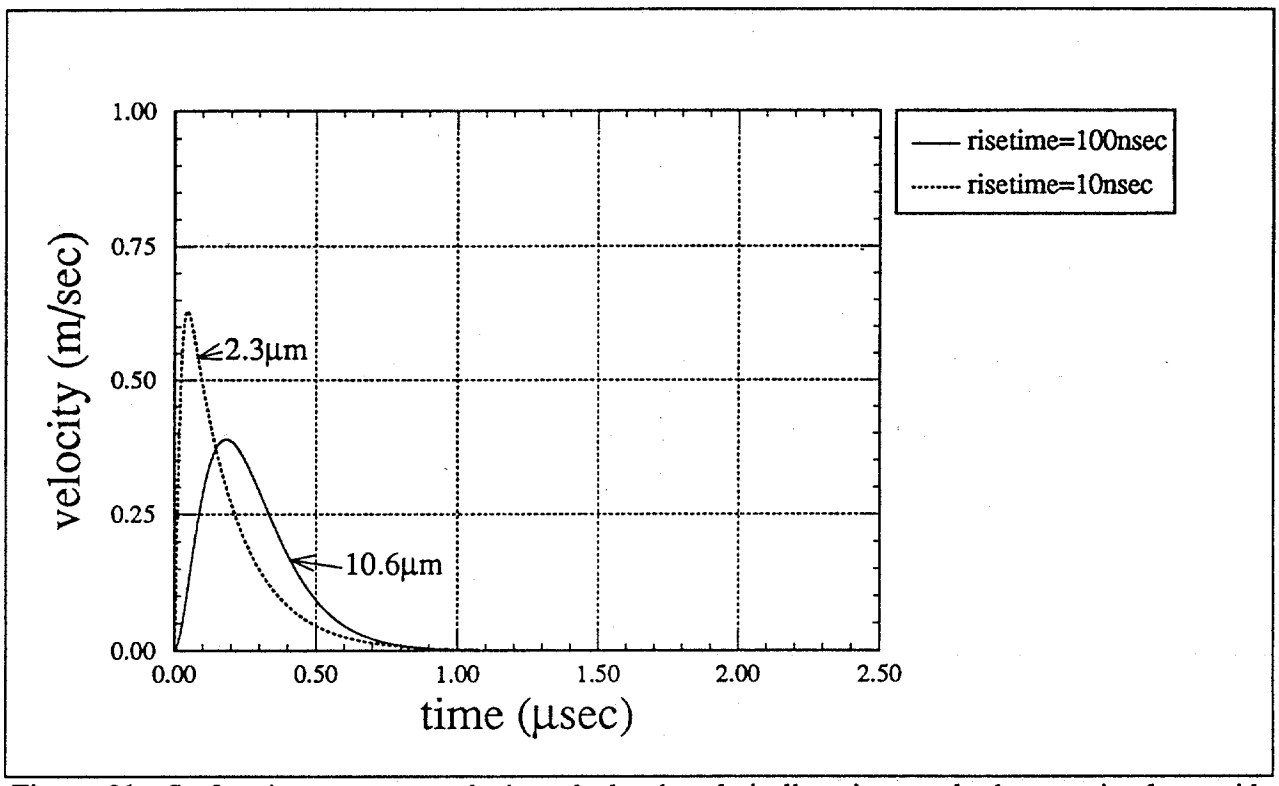

Figure 31 - Surface instantaneous velocity calculated analytically using a pulsed generating laser with a risetime of 100 ns at 10.6 μm and 10 ns at 2.3 μm

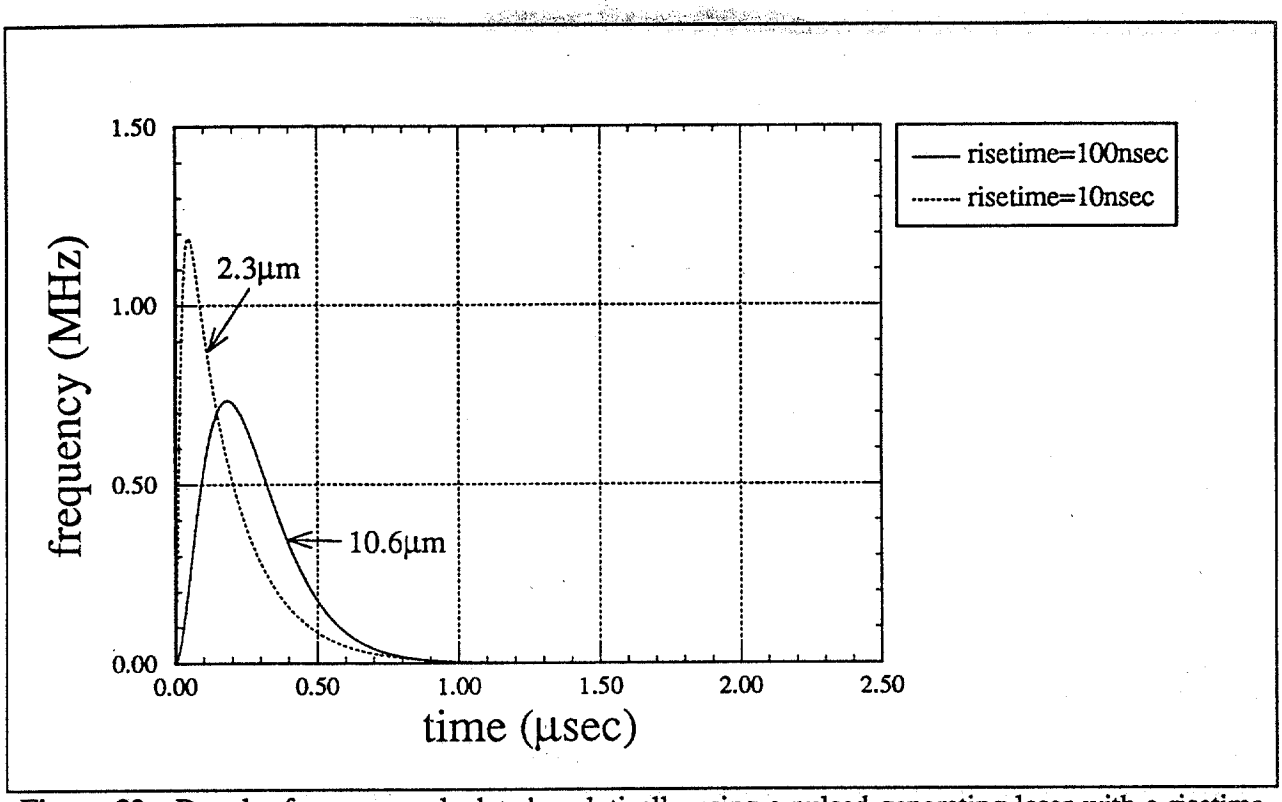

Figure 32 - Doppler frequency calculated analytically using a pulsed generating laser with a risetime of 100 ns at 10.6 μm and 10 ns at 2.3 μm

2.6 Conclusions

The use of the IMI model has provided us with the ability to closely examine the relationships between the generation and measurement of the ultrasonic waves and the characteristics of the oil, the generating laser, the probe laser and the demodulation receiver. The principal outcome of this modeling is the realization that although IMI has been able to demonstrate successful measurement in the laboratory using a CO_2 generating laser, this may not be the best choice. We have identified four potentially useful wavelength regions which will produce equivalent or better laser-ultrasonic interaction in the oils. Furthermore, when the importance of pulse risetime and pulse energy are considered along with our *a priori* knowledge of what is available from various laser sources, we expect that considerable improvement in the sensitivity of a LURSOT device may be possible. In the next section, we explore in more detail the components of the LURSOT system with respect to currently available technologies.

3.0 SENSOR SYSTEM INVESTIGATIONS

In this section we examine the requirements and possible solutions for the major system components. We have examined the demodulation receiver and addressed the question of whether the c-FPI is the best method for this application. For the laser systems, we have looked at both the generating and probe laser requirements and possible commercially available laser systems to satisfy these requirements. This section has a lengthy discussion of the various trade-offs associated with the lasers, including their performance, eye-safety, availability, reliability, development required and degree of technical risk. There are also discussions of the problems associated with the focusing of laser beams to small spot diameters at long distances, the optics required to perform these tasks, and the implications of these issues for the system design. Finally, this section addresses the receiver optics configuration, the optical throughput of the receiver and the expected performance and performance trade-offs associated with components of the receiver optics, in particular the design of the confocal Fabry-Perot Interferometer.

3.1 Demodulation Receiver Technology

During the study we have looked at various optical techniques that can be used to demodulate the probe laser. These include techniques such as optical heterodyning/homodyning and interferometry. The advantages and disadvantages of the various demodulation techniques are briefly discussed in this section. Since we had to limit the effort spent on this activity, it is by no means exhaustive and there may be techniques unknown to us that would satisfy the LURSOT demodulation requirements.
In the following discussion, it will be argued that frequency demodulation using a confocal Fabry-Perot Interferometer is better than the other approaches considered. The sensitivity of the frequency demodulation will be analyzed. Since most optical techniques require critical alignment of the optical components, they are very sensitive to mechanical and acoustical vibrations and temperature change of the environment. For the laser-ultrasonic system considered, the optical receiver must be mechanically and acoustically isolated from the vibrations and acoustic noise inside the aircraft. Even with this isolation, we expect that some active compensation will be required to deal with residual vibrations. Thus, in this section we also address the difficulty of compensating the c-FPI for the effects of vibration and noise.

3.1.1 Demodulation Technology Comparison

In optical heterodyning/homodyning techniques, the backscattered probe laser beam is mixed with a reference laser beam. If the frequencies of the probe laser beam and the reference beam are identical, the demodulation receiver is a homodyne receiver. Otherwise, it is a heterodyne receiver. Doppler shifted return frequencies are mixed with the reference beam, generating a beating of the return signal which is related to the difference between the reference and return beams. Heterodyning/homodyning is, however, a complex technique with a number of inherent problems. The field-of-view of the heterodyne/homodyne receiver is diffraction limited. Therefore, the backscattered probe laser beam and the reference laser beam must be aligned within this diffraction limited field-of-view at the photodetector. This will be very difficult to maintain in airborne applications as the vibrations inside the aircraft will disturb the alignment between the two beams. The sensitivity of heterodyning/homodyning receivers is also significantly reduced due to the speckle effect. The speckle

effect occurs when the oil surface is optically rough. When such a surface is illuminated by the probe laser beam, the intensity of the backscattered light is found to vary randomly with position. Finally, heterodyning/homodyning techniques rely on the coherency of the probe laser beam and hence their sensitivity can also be reduced by turbulence in the atmosphere.

Interferometry can be classified into techniques based on two-beam interference, such as in a Michelson Interferometer, or on multiple-beam interference, such as in the planar/confocal Fabry-Perot Interferometer such as used in the current system. In general, the demodulation technique based on interferometry is preferred over the heterodyning/homodyning technique because of a better demodulation sensitivity and a less stringent requirement for optical alignment.

The following summarizes the advantages/disadvantages of laser demodulation by a confocal Fabry-Perot Interferometer compared to the Michelson Interferometer:

Advantages

- High frequency discrimination sensitivity because of its narrow bandwidth.
- Insensitive to small change of tilt or orientation of the plates as all the emerging beams overlap after two round trips within the cavity.
- Larger light collection efficiency.
- Output signal is proportional to the Doppler frequency, which is the signal of interest.
- Less problem with surface flatness because of spherical surfaces.
- The interferometer is less bulky because the Michelson Interferometer normally requires a large path length difference.

Disadvantages

- Difficult to stabilize the operating point because of narrow bandwidth.
- Difficult to perform analysis because of the multiple beam interference.
- Spherical aberration limits the etendue of the interferometer.
- Devices are not adaptable to varied applications as the bandwidth is fixed once the length of the cavity is decided.

Overall, based on our analysis, the c-FPI appears to be the best approach for the LURSOT application.

3.1.2 Demodulation Receiver Sensitivity Analysis

In this section, the sensitivity of the frequency demodulation using a confocal Fabry-Perot Interferometer is investigated. Since one of the slopes of the transmission response of the c-FPI is used as an frequency discriminator, the derivative of the transmission response of the c-FPI will be evaluated. This provides a measure of the sensitivity of the c-FPI to changes in return frequency. The magnitude of the derivative and its dependence on the finesse and the cavity length of the c-FPI will be demonstrated.

The transmission response $I_T(\nu)$ of a c-FPI due to an electric field of frequency ν is given by

$$I_T(\nu) = 2\,\frac{T^2}{(1-R^2)^2}\,A(\varphi) \tag{12}$$

where R and T are the reflectivity and transmittance of the c-FPI. It has been assumed that the absorption of the partially transmitting surfaces is zero. $A(\varphi)$ is the well known Airy function whose value depends on the phase term φ and the finesse F.

$$A(\varphi) = \frac{1}{1+\frac{4F^2}{\pi^2}\sin^2(\frac{\varphi}{2})} \tag{13}$$

The phase φ can be expressed as

$$\varphi = \frac{2\pi}{F}\,[\frac{(\nu - \nu_0)}{B} + \mathit{offset}] \tag{14}$$

where B is the bandwidth, which is defined as the full width at half maximum of the transmission response. The transmitted probe laser beam frequency is ν_0 and the frequency of the backscattered probe laser beam is ν. Therefore, $(\nu - \nu_0)$ is the amount of Doppler shifted frequency. The parameter "offset" in Equation (14) is defined as the frequency of the operating point from the peak on the transmission response normalized by the bandwidth. The cavity length of the c-FPI is chosen to satisfy the bandwidth requirement and to lock the operating point with offset on the transmission response for a given value of the finesse.

Figure 33 shows the transmission response of a c-FPI with a bandwidth of 7.49481 MHz for various combinations of the cavity length and the finesse. The results show that when the bandwidth is specified, the product of the cavity length and finesse is also fixed.

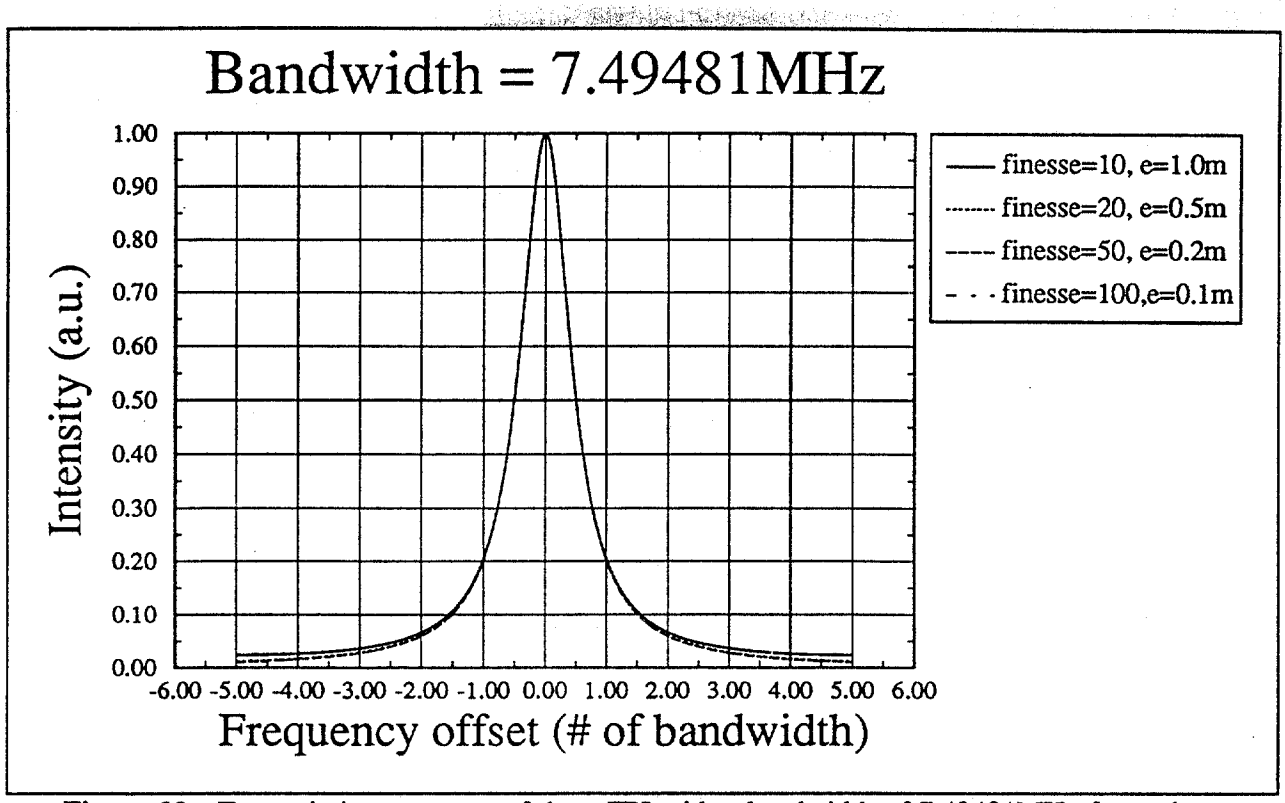

Figure 33 - Transmission response of the c-FPI with a bandwidth of 7.49481MHz for various combinations of the cavity length and the finesse

The c-FPI is normally operated on one side of the transmission response such that the frequency of the transmitted probe laser sits at the 50% transmission point. As the frequency of the probe laser beam is Doppler shifted, the output intensity of the c-FPI will vary depending on the sign and magnitude of the Doppler shifted frequency. In effect, the transmission response of the c-FPI near the 50% transmission works as a frequency discriminator. The sensitivity of this frequency discrimination depends on the slope of the nominal operating point at the transmission response. Therefore, the derivative of the transmission response of the c-FPI will indicate the frequency range over which the c-FPI has good frequency discriminating capability. That is, a large slope produces a higher sensitivity to the frequency shift. This is also useful in analyzing the overall sensitivity of the whole system. Taking the derivative of the transmission response of the c-FPI in Equation (13) with respect to the frequency of the backscattered probe laser beam ν gives

$$\frac{\partial A(\nu)}{\partial \nu} = -A^2(\nu)\left[\frac{4F}{B\pi}\right]\sin\varphi \qquad (15)$$

The derivative shown in Equation (15) is plotted in Figure 34 and Figure 35 for various finesse and cavity lengths of the c-FPI respectively. In Figure 34, the cavity length of the c-FPI is set to 1 m. In Figure 35, the finesse is set to 10. From these results, we can see that high finesse and long cavity length of the c-FPI are preferred. However, since the product of these two parameters is fixed once we settle on a bandwidth, there is a trade-off to be made between these two. In general, a longer cavity is more difficult to keep aligned and it is more difficult to couple the collected backscatter light into it. On the other hand, a high finesse requires higher quality reflecting surfaces and coatings.

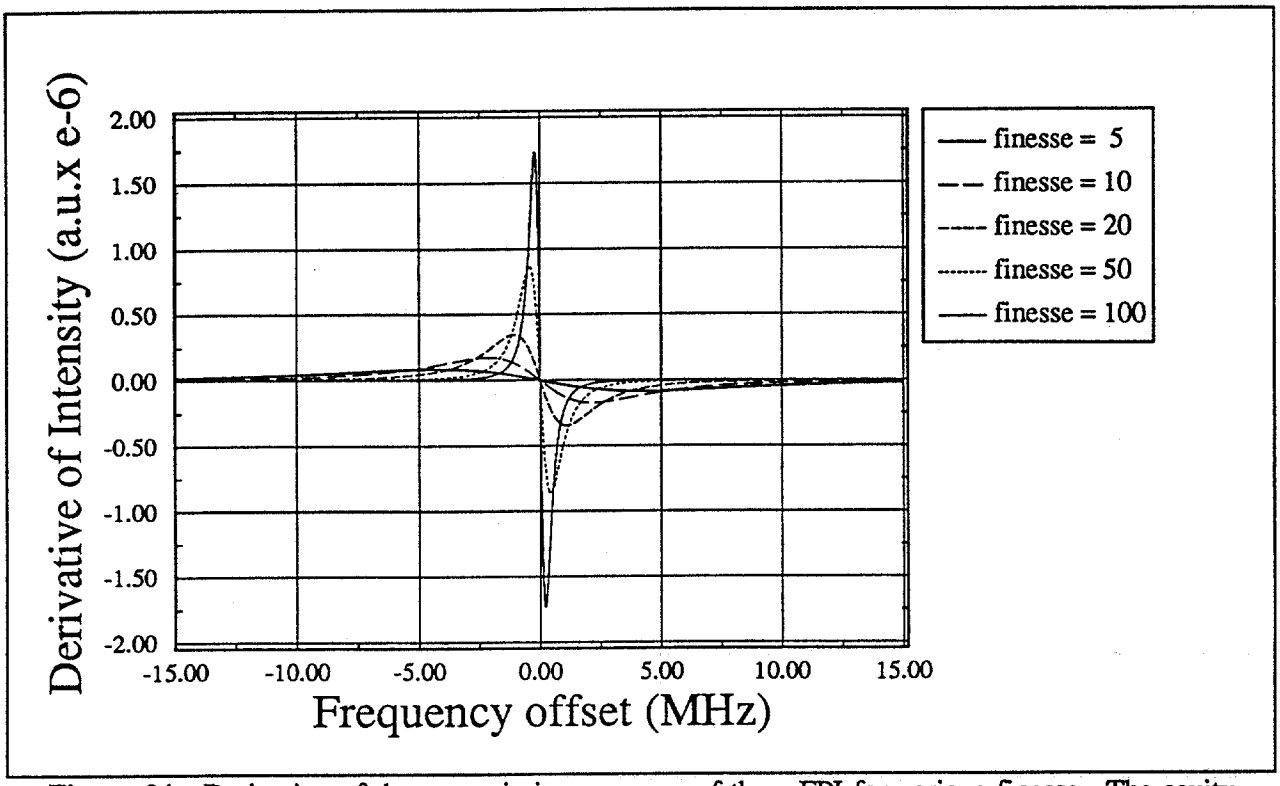

Figure 34 - Derivative of the transmission response of the c-FPI for various finesse. The cavity length is 1 m.

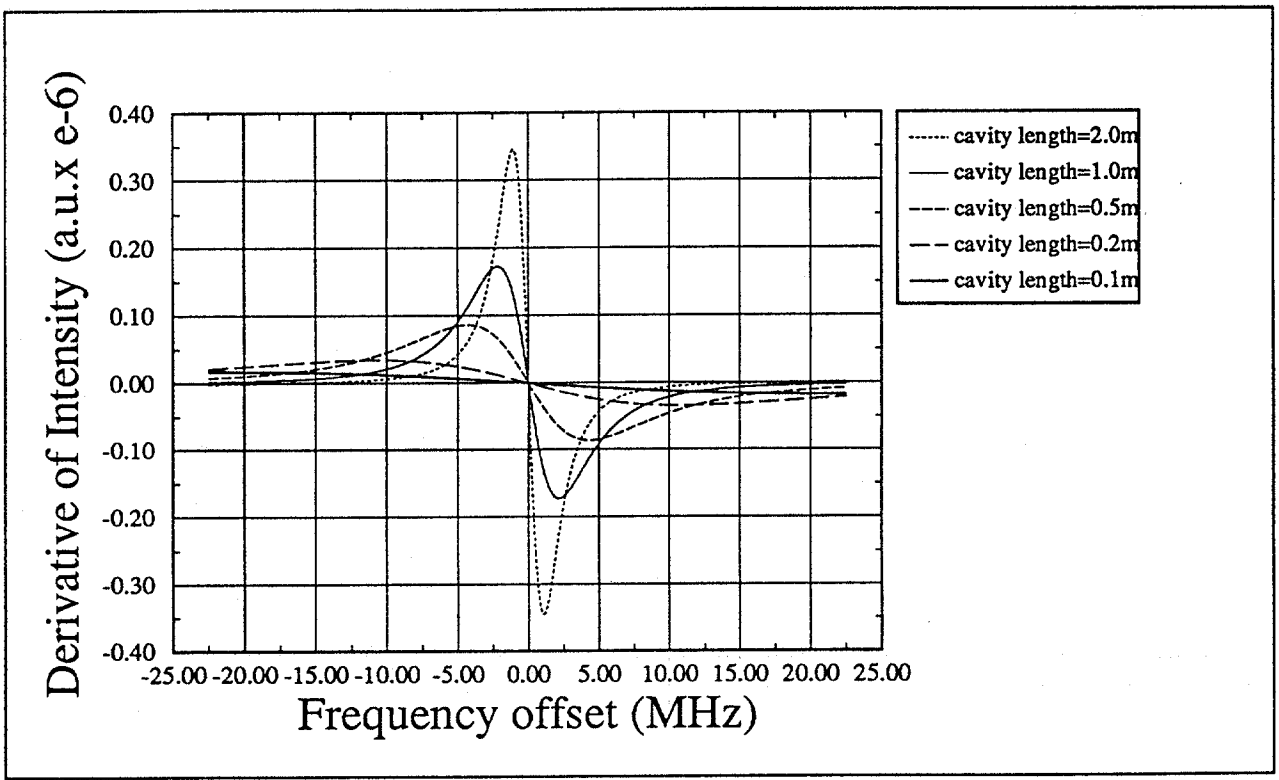

Figure 35 - Derivative of the transmission response of the c-FPI for various cavity lengths. The finesse is 10.

Also, the results in Figure 34 and Figure 35 show that the frequency range over which the derivative is large and the maximum magnitude of the derivative are inversely related to each other. Hence, the c-FPI should be designed to provide the best frequency discriminating capability while its bandwidth should be just large enough to cover the largest Doppler shifted frequency expected. Additionally, we have to be careful that in designing the system to produce good initial surface response, we do not widen the bandwidth of the receiver so much that it becomes less sensitive to the echo pulse.

3.1.3 Cavity Locking Methodology

One of the greatest uncertainties associated with the operation of the current LURSOT system in the aircraft is the ability of the feedback system in the c-FPI to compensate for vibration and acoustic noise. Without adequate compensation, the system will never be able to operate in the aircraft environment. In this study we have reviewed literature on active feedback systems for FPI applications. We could not actually find references to similar applications, so we have drawn on examples of feedback systems in other quite different applications. Additionally, an evaluation of the existing feedback system in LURSOT was not possible as details of this system were considered to be confidential.

Current Feedback System

For LURSOT, the probe laser frequency must be locked to the 50% transmission of a confocal Fabry-Perot Interferometer. Within the time span of the literature survey, no reports on stabilizing a c-FPI in the airborne environment were found. Perhaps, the stability of the c-FPI is not a problem for space-borne, ground-based, industrial or laboratory environments. From conversations with Marc Choquet of UltraOptec Inc., the feedback control loop to stabilize the c-FPI contains proprietary information and the feedback electronics were custom-made to implement the control design. As a result, no details of the design of the feedback loop are available and hence no comparison can be made with other stabilizing techniques. However, Choquet did provide the following information regarding their feedback system:

- The design of their feedback loop was based on monitoring the input and output intensity of the c-FPI using two photodetectors.
- The same feedback loop was used for the laboratory system and the airborne system.
- The feedback loop was able to lock the probe laser frequency at the desired operating point of the c-FPI for the laboratory system, but the c-FPI was placed on a vibration isolating table.
- The design of the feedback loop was meant to eliminate the drift of the probe laser frequency due to low frequency thermal effect on the probe laser up to 100 Hz.
- The performance of the feedback loop was not extensively tested on its performance.
- Choquet believed the real reason why the c-FPI was unable to lock during the airborne tests was poor mechanical and acoustical isolation of the c-FPI. He believed the feedback loop should be able to eliminate low frequency noise up to 100 Hz, and proper mechanical and acoustical isolation would eliminate noises from 100 Hz to 100 kHz.

Feedback Control of Cavity Length of c-FPI

For proper demodulation of the probe laser beam, the cavity length of the c-FPI must be accurately set to within a few hundredths of the probe laser wavelength. The cavity length of the c-FPI must then be accurately maintained in the presence of vibrations and acoustic noise inside the aircraft. It is extremely important to mechanically and acoustically isolate the c-FPI and to design a feedback control loop to correct for any residual noise or vibration. However, in order to properly design this feedback control, a detailed analysis of the effect the mechanical and acoustical noise of the aircraft has on the demodulation receiver must be done. Without such knowledge, the detrimental effects cannot be properly compensated and corrected.

The transmission and reflection characteristics of the Fabry-Perot Interferometer (FPI), planar and confocal, depend mainly on two parameters: the finesse and the phase lag between two successive beams which are part of the multiple beams that are summed to give the characteristic of the interferometer. The finesse of the FPI is a function of the reflectivity of the two mirrors that make up the device. Under normal conditions, the finesse can be considered constant. On the other hand, the phase lag between two successive beams can be fluctuating rapidly due to:

- Changes of the frequency of the laser caused by thermal instability of the laser
- Changes of the cavity length caused by mechanical and acoustical vibrations
- Changes of the index of refraction of the medium of the interferometer.

As an example, consider the use of a FPI to stabilize the frequency of a laser. In this case, the cavity length and index of refraction of the medium must be kept constant at all times. Normally, a short cavity length solid etalon is used. The frequency of the laser is locked to the FPI. In general, the locking technique can be classified into two categories: locking to the peak of the response of the FPI, and locking to the point of the response of the FPI near which the slope is maximum. In locking to the peak of the response of the FPI, the frequency of the laser is modulated slightly at a known frequency. If the frequency of the laser is properly locked to the FPI, the output of the FPI at the same modulating frequency would be zero. This technique has good sensitivity because of the synchronous demodulation of the frequency error signal. However, this method does require the modulation of the frequency of the laser and the subsequent synchronous demodulation of the frequency error signal. As a result, locking to the peak transmission can be quite complex. To lock the frequency of the laser at the maximum slope of the response of the FPI, the input beam is normally split into two paths. The FPI is contained in one path. The beam in the second path is detected by a second photodetector whose output gives the input intensity of the laser in front of the FPI. The output of the FPI is compared with the scaled output in the second photodetector. When the frequency of the laser is locked to the FPI, the difference between the output of the FPI and the scaled output in the second photodetector would be zero. Any changes in the frequency of the laser would then result in substantial changes in the transmission of the FPI. The relative strength of the transmitted signal would indicate the direction of the frequency change. This technique is very simple but it is sensitive to any difference in the characteristic of the two photodetectors.

For spectroscopy applications, the cavity length or the index of refraction of planar FPI is normally scanned linearly during the measurement period. If a long measurement period is required, the planar FPI must be kept as parallel as possible during the measurement period. Early work on FPIs had concentrated on devising control schemes to keep the planar FPI parallel. Such techniques include:

- Using auxiliary light sources and an additional reference interferometer
- Using capacitance micrometers for controlling parallelism and spacing of the mirror plates
- Using a strong spectral component of the scattered light to control the mirror distance of the FPI during the measurement
- Monitoring the change in position of the fringes as the cavity length varies.

All servo-controlled planar FPIs designed to maintain parallelism and constant spacing contain three piezoelectric transducers or voice coil drivers.

The following discussion concentrates on issues to be aware of in designing a feedback control system to stabilize the c-FPI in the aircraft environment.

As part of an electro-mechanical stabilization feedback loop, one of the mirrors of the c-FPI is mounted on a piezoelectric pusher. The feedback loop provides an electrical signal to the piezoelectric pusher to adjust the cavity length of the c-FPI in the presence of vibrations and acoustic noise. The cavity length must be adjusted accurately to within $\lambda/200$ of the nominal value. The elements comprising the electro-mechanical feedback loop are discussed below and their arrangement shown in the block diagram in Figure 36.

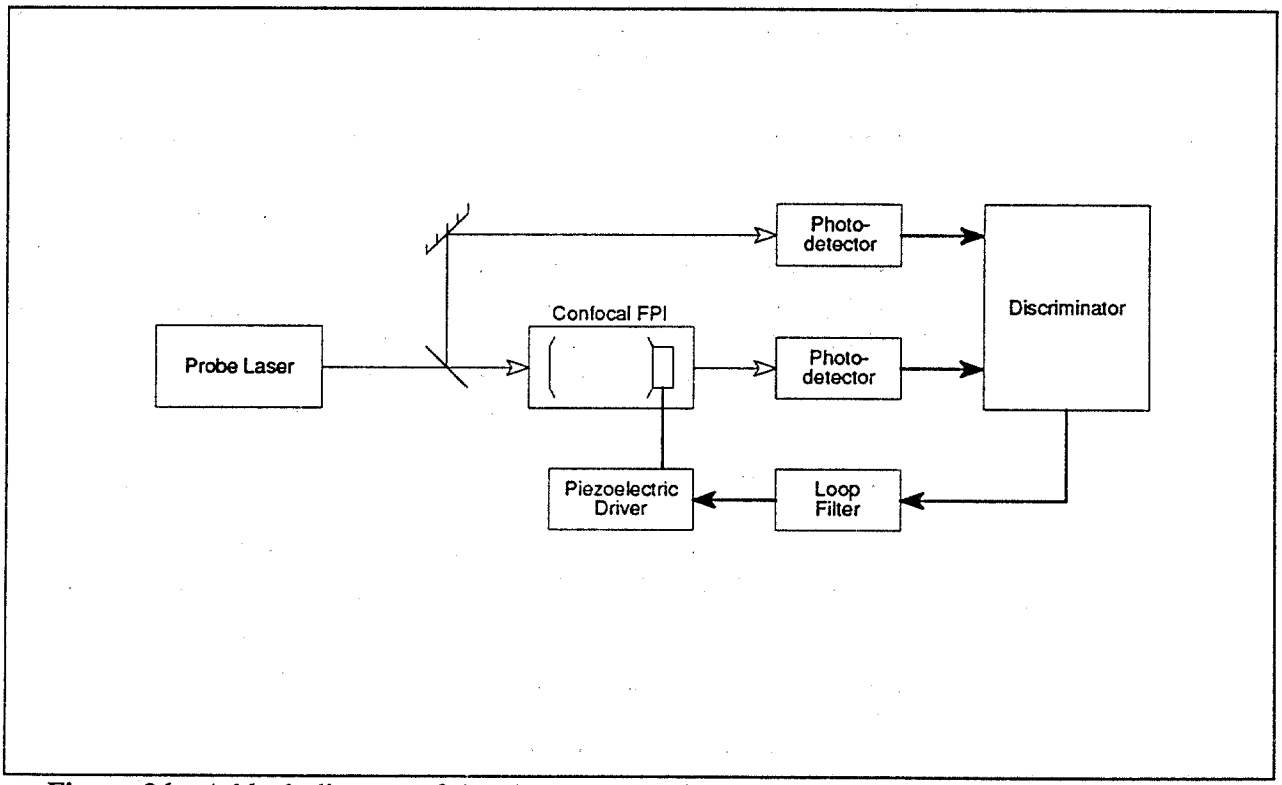

Figure 36 - A block diagram of the electro-mechanical stabilization feedback loop for the c-FPI

Probe Laser

- The frequency of the probe laser must be kept constant within a small fraction of the bandwidth of the c-FPI. The effect of temperature within the aircraft on the stability of the probe laser frequency must be understood and consequently minimized.

Piezoelectric Pusher

- The temperature sensitivity of the voltage expansion coefficient of the piezoelectric pusher material must be known.
- Nonlinear behavior of the material must be compensated.

Loop Filter

- The design of the loop filter must be subject to knowledge of the aircraft vibrational and acoustical noise spectrum.
- **Stability vs Sensitivity**: Higher loop gain decreases fluctuation of the cavity length but cannot be increased above a certain limit because of some delay in the feedback loop. The feedback loop can oscillate when the loop gain exceeds a certain value.

Confocal Fabry-Perot Interferometer

- The variations of index of refraction in the air gap due to pressure and temperature changes must be kept minimal.

Mirror Mounting

- For high frequency cavity length adjustments, the ultimate frequency obtainable is limited by the inertia of the interferometer plate and the stiffness of the mount.

The proper isolation of the c-FPI and the design of the cavity control loop require a knowledge of the acoustic and vibration noise inside the cabin of the aircraft. Moreover, the characteristics, properties and limitations of the various components that made up the electro-mechanical stabilization feedback loop as shown in Figure 36 must be well understood. The feedback control of the cavity length of the c-FPI is deemed to be crucial for the success of LURSOT.

3.2 Laser Systems

In the previous section we saw that there are specific wavelengths or wavelength regions that for a variety of reasons will perform better for the ultrasonic pulse generation. We also saw that for the detection of the Doppler shift at the oil surface, shorter probe laser wavelengths are preferred. In this section we use the results of the modeling study to specify laser systems for use as the generating laser or as the probe laser. So far the modeling has considered only the strength of the interaction of the laser pulses with the oil surface as a function of laser wavelength, pulse energy and pulse length. In this section we also consider such issues as eye-safety, laser availability, ruggedness, reliability and technical risk. Ultimately this presents us with a number of performance/risk trade-offs that must be considered in subsequent work on the LURSOT program.

3.2.1 Eye-Safety Considerations

Eye-safety of the LURSOT system is of great importance since the intended use of the system requires flight over oil spills where surface clean-up crews will be active. However, LURSOT presents a particularly difficult eye-safety problem since in order for the system to operate effectively, the laser pulses must be tightly focused onto the water surface. This is quite different from most lidar systems where the output beam is expanded and allowed to diverge to provide minimal eye-hazard to distant observers. Moreover, the system has two, even three, independent laser sources whose combined effect can increase the eye-hazard level.

For the generating laser, we have identified the wavelengths of 10.6, 2.3, 1.7 and 0.3 μm as having the best ultrasonic-generating characteristics. The best pulse energy range is 10 to 50 mJ while the pulse risetime should be short, ideally 10 to 15 ns. The current LURSOT system uses 10.6 μm for the generating laser, with a pulse energy of 10 mJ and pulse risetime of 100 ns. Since we appear to have a number of options for the generating laser wavelength, in this section we examine these potential sources in terms of eye-safety.

For the probe laser, a long pulse YAG laser is used. It may also be possible to use a cw laser for this function. As a result, for our eye-safety analysis we consider both pulsed and cw cases for the probe laser. The probe laser has a less specific wavelength requirement than the generating laser. The wavelength should be short, on the order of 1.0 μm or less. In the pulsed case, the pulse length must be long enough to bracket the time during which the surface response occurs, on the order of 50 μs. The probe beam energy need not be large, 2 μJ should be adequate.

An additional important parameter in the eye-safety calculations is the spot size of the laser beam as this determines the overall intensity. For the purposes of the eye-hazard evaluation, we generally assume that the spot sizes for the generating and probe laser will be 1 cm diameter at the water surface. The only exception to this is the 10.6 μm generating laser, which we expect will have a minimum spot size of about 2.5 cm diameter.

To determine what level of laser output power/energy is eye-safe, we have adopted the guidelines of the American National Standards Institute [American National Standards Institute , ANSI z136.1-1993, American National Standard for Safe Use of Lasers, (New York, 1993)]. Compliance with these guidelines is sufficient for operating a particular laser system within Canada; however, if operation within the United States is required then the particular laser system must also comply with the guidelines of the FDA/CDRH (Federal Laser Product Performance Standard, 21 CFR Part 1040), and if operation in other parts of the world is required then it must comply with the IEC standards (IEC

Standard on Radiation Safety of Laser Products, Equipment Classification Requirements and Users' Guide, Publications 825-1984 and 825-1990). Compliance with these other guidelines was not addressed in this study.

The evaluation of eye-safe laser power and energy levels for this application requires us to make some assumptions regarding the likely scenario whereby an observer would be irradiated by a laser beam from an overhead aircraft. As such we assume that the aircraft overflies an observer at an altitude of 100 m and a minimum speed of 100 knots (50 m/s). At an expected measurement rate of a few hertz, this means that an observer on the ground can only be exposed to a single laser pulse. In the case of a cw laser, the exposure will be relatively short, also reducing the hazard level. It is further assumed that the laser beam is nadir-directed (i.e., pointing vertically downwards from the aircraft), and that the beam is focused to a specific spot size where it then impinges directly on the observer's unaided eye (i.e., no binoculars or other optical aids). For simplicity in this preliminary analysis, we have assumed that only a single laser beam would be incident on the eye of the observer. In practice this would not be the case, since at least two and perhaps three coincident laser beams, at up to three different wavelengths and pulse durations, may strike the observer's eye simultaneously. However, for the purposes of this analysis we have tried not to overly complicate the situation.

3.2.2 Generating Laser

3.2.2.1 Eye-Safety Analysis

Figure 37 illustrates the maximum eye-safe laser pulse energy for relatively short laser pulse lengths (10, 30 and 100 ns), as might be utilized for the laser-ultrasonic generating laser. Immediately obvious is the tremendous range of eye-safe pulse energies over the spectral interval shown, 180 nm to 3.0 μm. There are approximately 6 orders of magnitude difference in eye-safe pulse energy between 400 nm and 1.5 μm. Beyond 3.0 μm out to 10.6 μm the eye-safe pulse energy remains approximately constant.

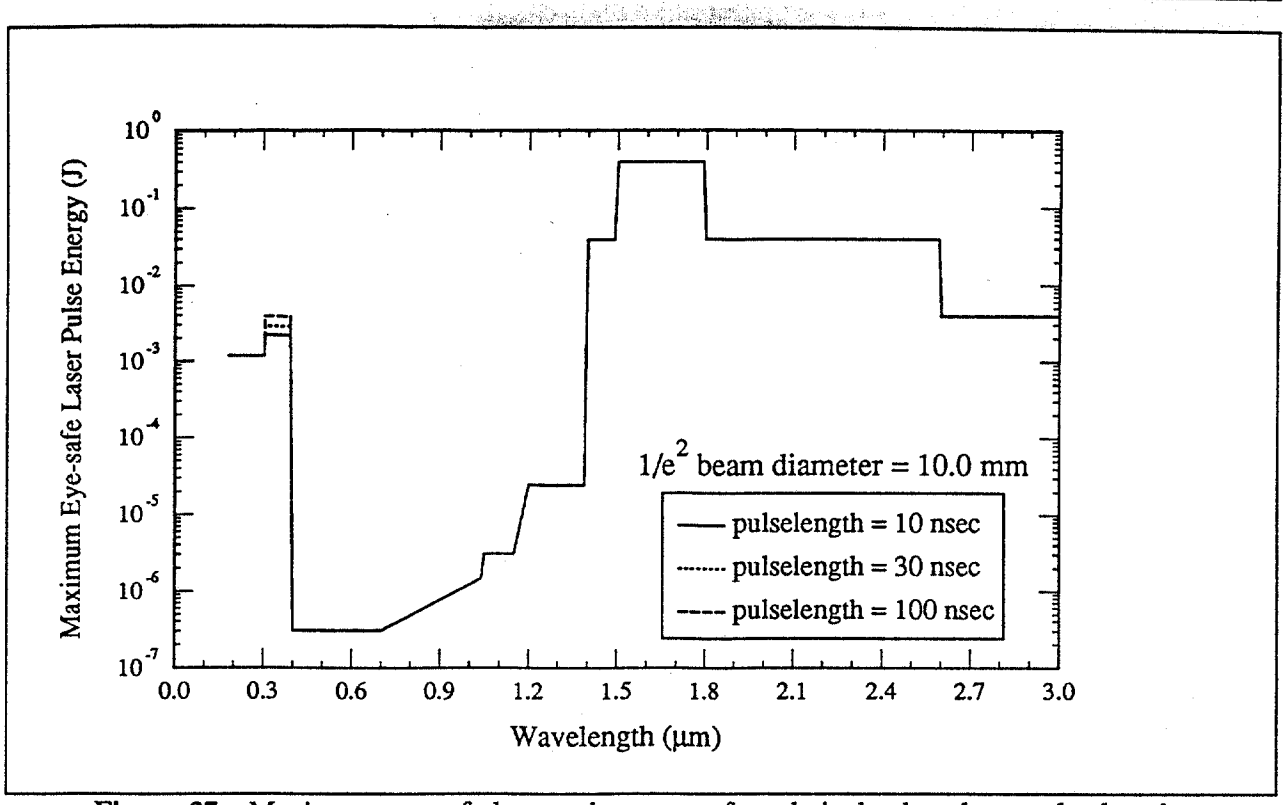

Figure 37 - Maximum eye-safe laser pulse energy for relatively short laser pulse lengths

The safest wavelength interval, usually referred to as the "eye-safe spectral region", extends from 1.5 μm to 1.8 μm. For the case shown where the $1/e^2$ beam diameter is 1.0 cm, about 400 mJ of pulse energy remains eye-safe to an observer. This includes the wavelength of 1.7 μm, which is one of our preferred generating laser wavelengths. The allowed energy in this wavelength region is well in excess of the energies required for either the generating or probe laser.

The next most eye-safe spectral regions are 1.4 μm to 1.5 μm and 1.8 μm to 2.6 μm, which allow similar levels of maximum laser pulse energy (about 40 mJ, or 10% of the values in the best eye-safe spectral region). This again is in excess of the required pulse energy for the generating laser and encompasses the wavelength of 2.3 μm.

The spectral range from 2.6 μm to greater than 10.6 μm represents the third-best choice for eye-safety, where about 4 mJ of pulse energy is eye-safe. It is in this region that the current LURSOT generating laser operates at a pulse energy of 10 mJ. Reducing the energy of this laser to 4 mJ will greatly reduce the current system performance.

The fourth-best eye-safe region extends from about 305 nm to 390 nm, where between 2 and 4 mJ of pulse energy remains eye-safe, followed by the region from 180 to 300 nm, where about 1 mJ of pulse energy is eye-safe. This encompasses our fourth preferred wavelength for the generating laser. These eye-safe pulse energies in this region are very restrictive.

The most dangerous spectral region is the "retinal hazard region" (about 400 nm to 1.4 μm). The least eye-safe portion of this region is at the visible wavelengths between 400 nm and 700 nm, where only about 0.3 μJ of pulse energy can be considered eye-safe. This value increases essentially logarithmically over the range from 700 nm to 1.2 μm, and then holds constant between 1.2 and 1.4 μm where only about 25 μJ of pulse energy is eye-safe. These energy levels are far below the requirements for the generating laser.

Assuming a laser spot size of 1 cm purely for the purposes of comparison, the 1.7 μm wavelength has by far the largest eye-safe level of our preferred wavelengths of 0.3, 1.7, 2.3 and 10.6 μm. For the wavelength of 2.3 μm, an energy of 40 mJ is allowed. This is about right for optimal laser-ultrasonic generation. For a wavelength of 10.6 μm, a 1 cm spot size would limit the pulse energy to about 4 mJ, as indicated by our eye-safety analysis. In the current LURSOT system, a 10 mJ energy is used with a claimed 6 mm spot diameter (see Section 3.3.2 for a discussion of the feasibility of focusing laser beams at large distances). This puts the current system about a factor of 10 above the eye-safe level. Making the current generating laser eye-safe will therefore require a reduction in energy density at the surface by a factor 10. This in turn will seriously reduce the strength of the laser-ultrasonic interaction. Finally, our fourth wavelength region between 0.2 and 0.3 μm has a similarly restrictive eye-safe level, allowing only 2 to 4 mJ pulse energies. Here again, making a system operating in this wavelength region eye-safe will seriously reduce the laser-ultrasonic interaction.

The impact that these eye-safe levels have on the generating laser function is illustrated in Figure 38 where the calculated surface displacement is plotted as a function of time. Because of their very restrictive eye-safe levels, the displacements generated by the 0.3 μm and 10.6 μm generating lasers are very small. The 1.7 μm displacement is calculated assuming a 20 mJ pulse energy since this is the practical limit for existing laser systems. The surface response at this wavelength is considerably larger than that for the 0.3 μm and 10.6 μm cases but the initial surface displacement runs into the echo displacement. This could lead to serious problems in extracting the oil thickness from the probe laser signal. Finally, the 2.3 μm case allows a good energy level (we used 20 mJ in this calculation) and provides a very sharply defined echo and initial surface displacement.

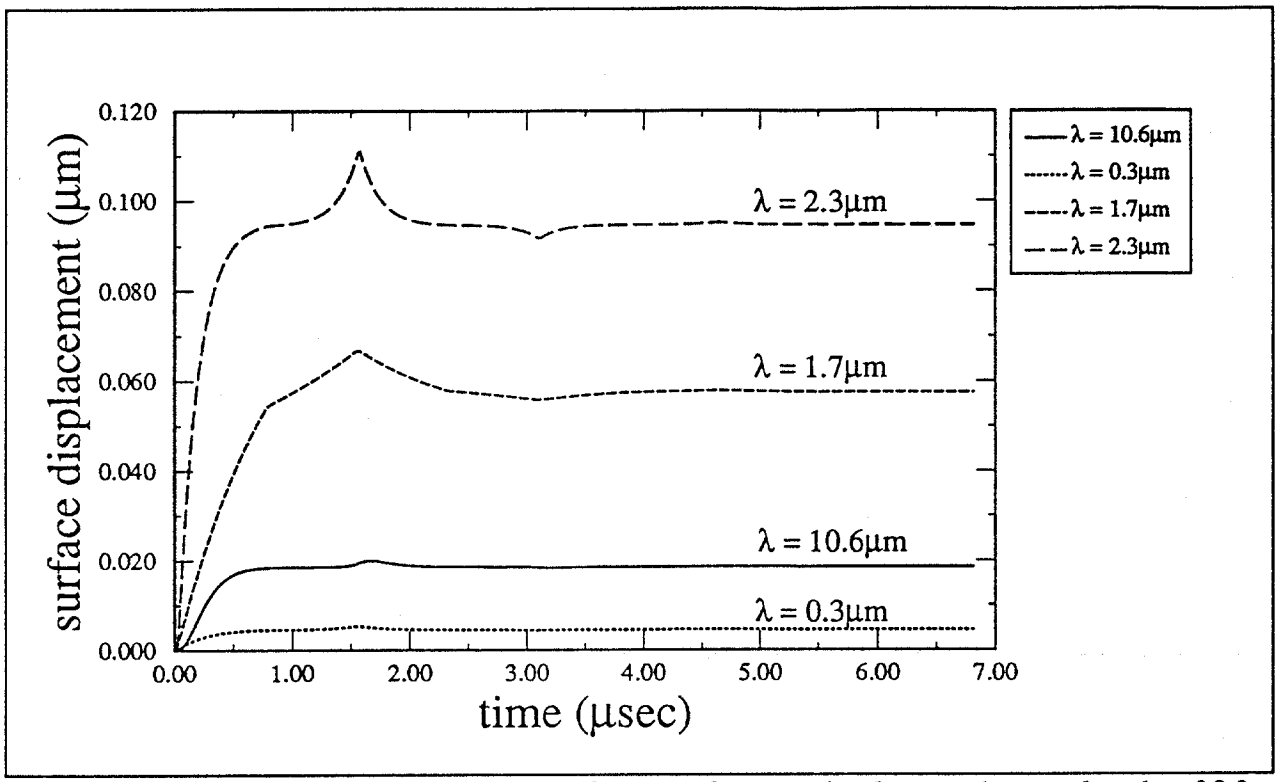

Figure 38 - Calculated surface displacement for eye-safe generating laser at the wavelengths of 0.3 μm, 1.7 μm, 2.3 μm and 10.6 μm

In Figure 39, the velocity of the initial surface displacement is plotted as a function of time for the four different wavelengths. Since it is the velocity of the surface which induces the Doppler shift that is to be measured by the probe laser, it is important that the generating laser produce as large a velocity as possible. In Figure 39 we see that the velocities induced by the eye-safe levels of the 0.3 and 10.6 μm laser pulses are very low. Such small velocities will not be detectable using the current LURSOT receiver design. On the other hand, the velocities produced at 2.3 μm are almost an order of magnitude larger and closely match those being generated by the existing prototype system.

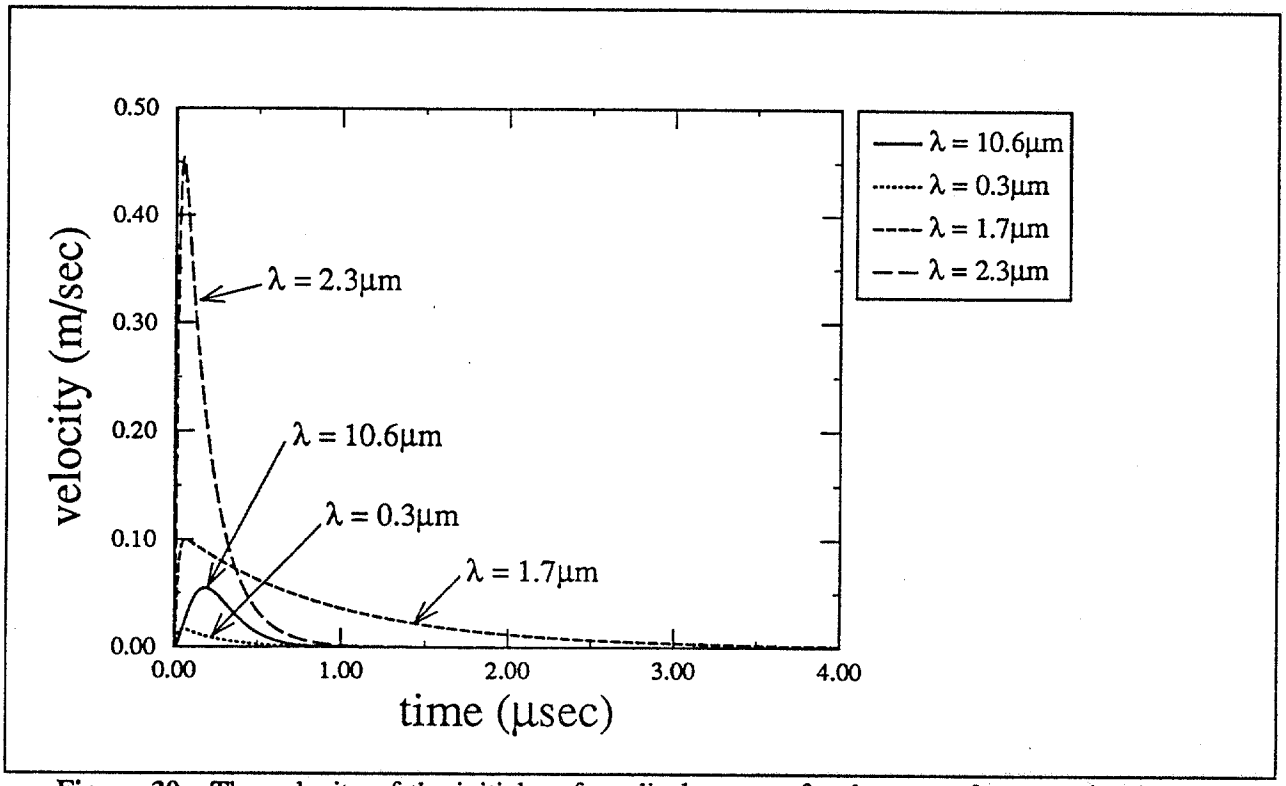

Figure 39 - The velocity of the initial surface displacement for the eye-safe generating laser at wavelengths of 0.3 μm, 1.7 μm, 2.3 μm and 10.6 μm

For the generating laser, if it is to be eye-safe at the water surface, we are forced to operate at a wavelength of 2.3 μm. This is the only wavelength where an eye-safe pulse energy will generate an ultrasonic wave of the required intensity. In order to obtain useful performance at the other wavelengths we will require a substantial relaxation of the eye-safety requirements. For example, if we could ensure that the system would not fire while personnel are directly under the aircraft, we need only be concerned about the hazard created by the reflected pulse. Moreover, the reflected pulse energy will be greatly reduced by absorption at the water surface and will be directed back toward the aircraft. In this case, we need only consider the eye-safe levels of the reflected pulse at the aircraft. This would allow considerably higher pulse energies, and consideration of generating lasers operating at 0.3 and 10.6 μm is again possible.

3.2.2.2 Generating Laser Requirements

The requirements for the generating laser are listed in Table 3. This table provides a list of key parameter values as well as comments on why particular values were chosen. The important considerations for each of these parameters will be discussed in the following paragraphs.

Wavelength: We have already examined the question of what wavelengths would be best in terms of their ability to generate a strong laser-ultrasonic interaction and in terms of eye-safety. Ideally, we want a laser operating near 2.3 μm. If an appropriate laser source for this wavelength exists, then we would recommend that the LURSOT system be redesigned around this laser. If this is not the case, and the eye-safety requirements can be relaxed, sources operating at the other three promising wavelength regions can be considered.

Spectral Bandwidth: Based on the information that we have on the absorption spectrum of typical oils, the wavelength dependence is a relatively smooth function lacking any sharp fine structure. This being the case, the spectral bandwidth of the generating laser can be very wide (up to several nanometers wide).

Center Wavelength Stability: Once again, since the absorption coefficient of the oil is not strongly wavelength dependent, some movement of the center wavelength will not be a problem. In general, it should be equal to or less than the laser spectral bandwidth. This ensures that, pulse to pulse, the effective oil absorption coefficient seen by the laser pulse does not change. In this case, we have somewhat arbitrarily assigned the center wavelength stability a value equal to 40% of the spectral bandwidth.

Pulse Length: The pulse length (and therefore risetime) is a critical parameter for the generating laser. Our analysis has shown that there is a strong correlation between the pulse risetime and the speed of the oil surface response. In general, we want the risetime of the pulse to be short, less than 100 ns.

Pulse Energy: This is another parameter which is critical to the laser-ultrasonic interaction. Our analysis has shown that pulse energies in the 10 to 50 mJ range will generate a good surface response.

Energy Stability: The pulse-to-pulse energy stability from the laser is not critical as long as it represents a small fraction of the actual output. We have arbitrarily assumed a pulse-to-pulse stability of ±15% here, since this is in our experience a typical performance level achievable by pulsed lasers.

Pulse Repetition Rate: Unlike many other remote sensing applications involving lasers where the pulse repetition frequency is constant, the triggering rate for the generating laser in this application is aperiodic. This comes about since the system only fires the generating laser when the water surface is perpendicular to the instrument line-of-sight. This aperiodic firing does not pose a problem for most gas lasers. However, this can be a problem for many solid state lasers. These devices generate a lot of heat in the laser medium each time they are fired. Generally, in fixed repetition rate systems, the laser material reaches a thermal equilibrium under which it is designed to have optimum output. Under aperiodic operation, the laser medium can experience uneven heating which in turn can cause thermal lensing in the material. This effect can ruin the stability of the laser and, in the case of high energy lasers, can result in the generation of localized concentrations of laser energy that can damage the laser optics. This problem will be particularly bad for flashlamp-pumped systems. For this reason, where possible, we consider laser diode-pumped systems, which are far more efficient systems and have much less severe thermal problems.

Hold-off Time: The laser hold-off time is usually defined as the time interval between the receipt of an external electrical trigger pulse and the emission of the resulting optical laser pulse. In the LURSOT application, a very short window of opportunity exists once the correct orientation of the sea surface is detected. This duration of this window is highly variable. IMI quotes an average duration of about 250 μs. We wish to use as little of this time as possible in initiating the laser firing. Ideally, we would like this time to be zero, but realistically we can expect hold-off times up to 150 μs. We have adopted a figure of less than 100 μs for the hold-off time specification as we expect that the longer the hold-off time, the fewer successful measurement will be possible.

Spot Size, Spatial Mode and Beam Divergence: All of these parameters affect the ability of the system to provide a small spot on the sea surface. These will be discussed in some detail in Section 3.3. For now we require the laser to operate in a single mode (TEM_{00}) in order to provide an output beam with a Gaussian intensity profile.

Beam Pointing Stability: We consider this to be a critical parameter. One of the key requirements of the LURSOT system is that the generating and probe laser beams be overlapped on the sea surface. Assuming an aircraft altitude of 100 m, a beam pointing stability of ±50 μrad implies that the laser spot may wander about its nominal position by ±0.5 cm. For laser spot sizes on the order of 1 cm, this is a maximum allowable wander.

Temperature, Vibration: These environmental parameters are very important as most commercially available laser systems are not designed for the kind of environment that will be presented to the LURSOT system. A standard temperature range for a solid state laser is 5-30°C. Temperatures lower than 5°C become problematic as there is a possibility that the water coolant in the laser might freeze. Other low temperature coolants could potentially be used, thus extending the temperature range at the low temperature limit, but there are also problems of material compatibility which can occur. For vibration, the only reliable way to ensure that a laser system will operate properly is to test it.

Size, Weight and Power Requirements: We recognize that since LURSOT is an airborne system, all of these characteristics of the system must be minimized.

Table 3: Generating Laser Specifications

Laser Property	Specification	Comments
Wavelength	near-UV, near-IR or far-IR	fixed, tunability unnecessary
Spectral Bandwidth	≤ 5 nm	not critical
Center Wavelength Stability	≤ 2 nm	not critical, but less than spec. band.
Pulse Length	≤ 100 ns	preferably no long tail; definitely no multi-pulsing
Pulse Energy	10-50 mJ	more is better
Pulse Energy Stability	±15 %	not critical
Repetition Rate	variable 10 Hz max.	ability to "fire on demand" is IMPORTANT without changing properties of optical pulse
Hold-off Time	≤ 100 µs	min. time between external trigger pulse and generation of optical pulse is VERY IMPORTANT
Spot Size	negotiable	ability to focus laser pulse to a small spot at ~ 100 m distance is CRITICAL
Spatial Mode	near-Gaussian preferred	
Beam Divergence	negotiable	
Longitudinal Mode	negotiable	not critical
Beam Pointing Stability	±50 µrad	less is better
Temperature Range	5-30°C	do not reject lasers solely for this reason
Vibrational Environment	severe	laser to be aircraft mounted; do not reject solely for this reason
Size, Weight & Configuration	negotiable	as light/compact as possible
Power Requirements	negotiable	as economical as possible
Development Considerations	negotiable	commercially-avail. sources preferred

3.2.2.3 Generating Laser Evaluation

The LURSOT system currently uses a CO_2 laser as the generating laser. As we have seen from our eye-safety analysis, the 10.6 μm wavelength of the CO_2 laser is not a good choice if the generating laser is to be eye-safe at the water surface. Additionally, we have seen from our modeling of the laser-ultrasonic interaction that the long pulse of the CO_2 laser results in a slower surface response than would be generated by a shorter pulse system. Our modeling identifies the wavelengths of 0.3 μm, 1.7 μm and 2.3 μm as being potentially better than 10.6 μm in terms of the strength of the laser-ultrasonic interaction and, with the exception of the UV wavelengths, having better eye-safety. We thus examined the availability of laser sources capable of providing these wavelengths.

UV Wavelengths (300 nm)

Our modeling demonstrated that this wavelength has strong oil absorption, which leads to good ultrasonic generation. Our eye-safety analysis, however, showed that a UV generating laser is only feasible if the eye-safe limits are substantially relaxed. In terms of laser sources, there are a number of mature laser systems that can provide short-pulse output in the UV region. These are discussed in the following.

There is a wide range of laser systems that can be used to generate output in the UV spectral region. This includes excimer lasers which have fundamental output at a few specific wavelengths in the UV; solid state IR lasers such as Nd:YAG and Nd:YLF which through frequency conversion (harmonic generation) can produce UV output at fixed wavelengths; and tunable solid state lasers such as Ti:Sapphire and Alexandrite which through harmonic generation can provide a tunable range of wavelengths in the UV. All of these sources can provide high pulse energies in well-collimated beams with pulse risetimes on the order of 10 ns.

The solid state laser systems are available in two designs: flashlamp-pumped and laser diode-pumped. The flashlamp-pumped designs provide higher pulse energy at low repetition rates while the diode-pumped systems provide lower pulse energies at very high repetition rates. Both designs may have difficulty in providing stable output when fired aperiodically, although the thermal effects in the diode-pumped systems will be much less severe than in the flashlamp-pumped case. The diode-pumped lasers are rapidly evolving with rising pulse energies and decreasing prices. Unfortunately, these lasers are not yet capable of delivering the several millijoules of pulse energy at frequency tripled output that is required for the LURSOT generating laser. For this reason we consider only flashlamp-pumped solid state lasers in the rest of this discussion on the generating laser.

Excimer lasers, on the other hand, do not have these thermal problems as their lasing medium is a gas and they are basically single-pass devices. That is, all laser energy is dumped in a single pass of the cavity so inhomogeneities and hot spots in the beam do not build up to damaging levels.

Table 4 provides a summary of the capabilities of a number of laser systems capable of providing UV output. The critical consideration is the ability of the laser to operate aperiodically. All of the entries in this table that are designated as *Questionable* refer to uncertainty about the ability of the laser system to operate stably in a fire-on-command mode. For all but the excimer lasers, frequency tripling is required. Typically, the crystals used for this process are temperature and alignment sensitive, making airborne operation much more difficult.

Table 4: Comparison of Possible Generating Lasers for UV Operation

Laser Type	Excimer XeCl/KrF	YAG/YLF Tripled	Ti:Sapphire Tripled	Alexandrite Tripled
Wavelength (nm)	308/248	355/349	235 - 300	240 - 270
Spectral Bandwidth (nm)	0.25	0.3	0.3	0.5
Pulse Energy (mJ)	1 - 200	1 - 100	5 - 10	10 - 100
Pulse Energy Stability	Good	Questionable	Questionable	Questionable
Pulse Length (ns)	~10	6 - 20	≤ 10	20 - 30
Pulse Repetition Rate (Hz)	0 - 300	1 - 20	1 - 20	1 - 20
Hold-off Time (μs)	~ 0.05	~ 150	≥ 150	unknown
Spot Size, Spatial Mode	good	very good	very good	very good
Beam Pointing Stability	excellent	Questionable	Questionable	Questionable
Fire on Command	Yes	Questionable	Questionable	Questionable
Sensitivity to Temperature	Low	Moderate	High	Moderate
Prior Airborne Use	Yes	Yes	No	No
Size, Weight, Power	Moderate	Low	High	High

Based on the above considerations, the fact that it is relatively insensitive to temperature and vibration, and its virtually instantaneous emission on command, we would recommend the use of the excimer laser if a UV source for the generating laser is to be used. An additional significant advantage of this approach is the fact that Environment Canada is already flying an excimer laser in its LEAF system. Thus the operating procedures and technical familiarity with the laser source already exist.

In particular, there are now available so-called miniature excimer lasers (MINex) from Lambda-Physik. This laser weighs only 100 lbs, is air cooled and requires only 1 kW of electrical power. Pulse energies at 308 nm are 15 mJ. At this energy level the laser-ultrasonic response of the oil will be about half that of the current system. We can expect to see improvements in this miniature laser pulse energy if the product proves successful.

1.7 μm Laser Sources

The 1.7 μm wavelength has the best eye-safe levels of our four selected wavelengths although there is some concern about the fact that our model predicts poor resolution between the initial surface displacement and the echo displacement. An examination of available laser sources for 1.7 μm reveals that the choice is very limited. There are no established laser sources that can emit this wavelength directly. The Co:MgF_2 laser is tunable between 1.75 μm and 2.5 μm, just missing our target wavelength. There is enough difference in the laser-ultrasonic response at 1.7 μm and 1.75 μm to eliminate this laser.

This wavelength can also be accessed by frequency shifting the output of solid state lasers (Ti:Sapphire, Alexandrite). The frequency shifting would use either OPO technology or Raman shifting. The Raman shifting is a well-characterized method, being very simple and reliable. It does require a gas cell filled with high pressure hydrogen or deuterium (potentially explosive gases), for which flight-worthiness approval must be specially authorized; however, this has been done. It is also worth noting that calculations have been performed to indicate that the amount of hydrogen or deuterium necessary to fill a Raman conversion cell does not lead to a serious safety concern. The OPO technology is rapidly emerging as a significant laser technology and may soon provide a reliable 1.7 μm source. As of now, however, this technology is very immature and as a result there would be considerable technical risk associated with attempting to operate such a system in an aircraft.

To summarize, 1.7 μm is not a straightforward wavelength to generate. Systems to do this will be large and energy-inefficient and will use sources that have no track record in aircraft usage.

2.3 μm Laser Source

Of the three wavelength regions we have identified as being good alternatives to 10.6 μm, the 2.3 μm region offered the best combination of laser-ultrasonic interaction and insensitivity to changes in oil type as well as having good eye-safe energy levels. Unfortunately, the choice of sources for this wavelength is as limited as was the case for 1.7 μm. We have only the Co:MgF_2 laser, Alexandrite pumping a hydrogen Raman cell and the OPOs pumped by solid state lasers (YAG/YLF).

This wavelength is at the far tuning range for current commercial OPO systems. Considerable technical risk is associated with these systems as this is a new, emerging technology. Commercial systems are designed to provide broadband wavelength tuning. Such large, complex optical systems not perform well in the aircraft environment. LURSOT will require a custom OPO development in which ruggedization and stability would be the primary goals. Some work may also be required to reduce the hold-off time of the system as the OPO is pumped by a solid state laser which itself has a long hold-off time. Finally, because we are dealing with a solid state pump laser, there may be problems associated with the aperiodic operation of the system.

The above concerns also apply to the Co:MgF_2 laser. The Co:MgF_2 laser is pumped by a YAG laser emitting at 1.3 μm. Output pulses of 20 mJ are possible with pulse lengths on the order of 50 ns. This pulse length is considerably longer than we would like and will reduce the effectiveness of this laser.

Finally, the Alexandrite-pumped Raman cell will provide 2.3 μm output using off-the-shelf systems but this would be a very large system. The output energy of this system would be limited to about 10 mJ. Once again, since the pumping laser is a solid state laser, our concerns about hold-off time and aperiodic operation also apply.

To summarize, a considerably more detailed study of the characteristics of existing OPO, Alexandrite and Co:MgF_2 lasers is required before any decision is made to change the generating laser to this wavelength.

3.2.2.4 Generating Laser Summary

It has already been demonstrated that a CO_2 laser can produce efficient laser-ultrasonic interactions. Except for eye-safety concerns, the existing generating laser used in the LURSOT system is perfectly adequate. We would like to see shorter risetimes on the laser pulses, but the risetime of a CO_2 laser is fixed by its gas mixture and there is little that can be done to modify it. If the current pulse energy can be tolerated from an eye-safety point of view, we see no reason to change to a 2.3 μm or 1.7 μm source. There do, however, remain a number of advantages to the excimer laser that bear further investigation. Primary among these is the ability of the excimer laser to deliver the pulse energy in a very small spot within a very short time (10 ns).

If eye-safety at the water surface is required, then we are forced to find a 2.3 μm laser source capable of satisfying all of the generating laser requirements. This will require further investigation followed in all likelihood by a laser development program. Such a program would be expensive and time consuming. Thus the requirement for eye-safety is a key issue in determining the future of the LURSOT system.

3.2.3 Probe Laser

3.2.3.1 Eye-Safety Analysis

The probe laser will either be a long pulse system or a cw system. For these, the eye-safe levels will be slightly different from those calculated for the generating laser. For the probe laser, we have to be very careful with the specification of the eye-safe level. In this case we have a long duration pulse or a cw beam that has long enough duration on the water surface that wave motion could direct the laser reflection in virtually any direction. In this case, then, it is important that the probe laser energy be eye-safe at the water surface.

Figure 40 illustrates the maximum eye-safe laser pulse energy for longer laser pulse lengths (50 μs, 100 μs and 250 μs). As with the results shown in Figure 37, the data represent a $1/e^2$ beam diameter of 1.0 cm. A comparison of the results presented in Figures 37 and 40 shows that the general characteristics of the corresponding curves in each of the two graphs are quite similar.

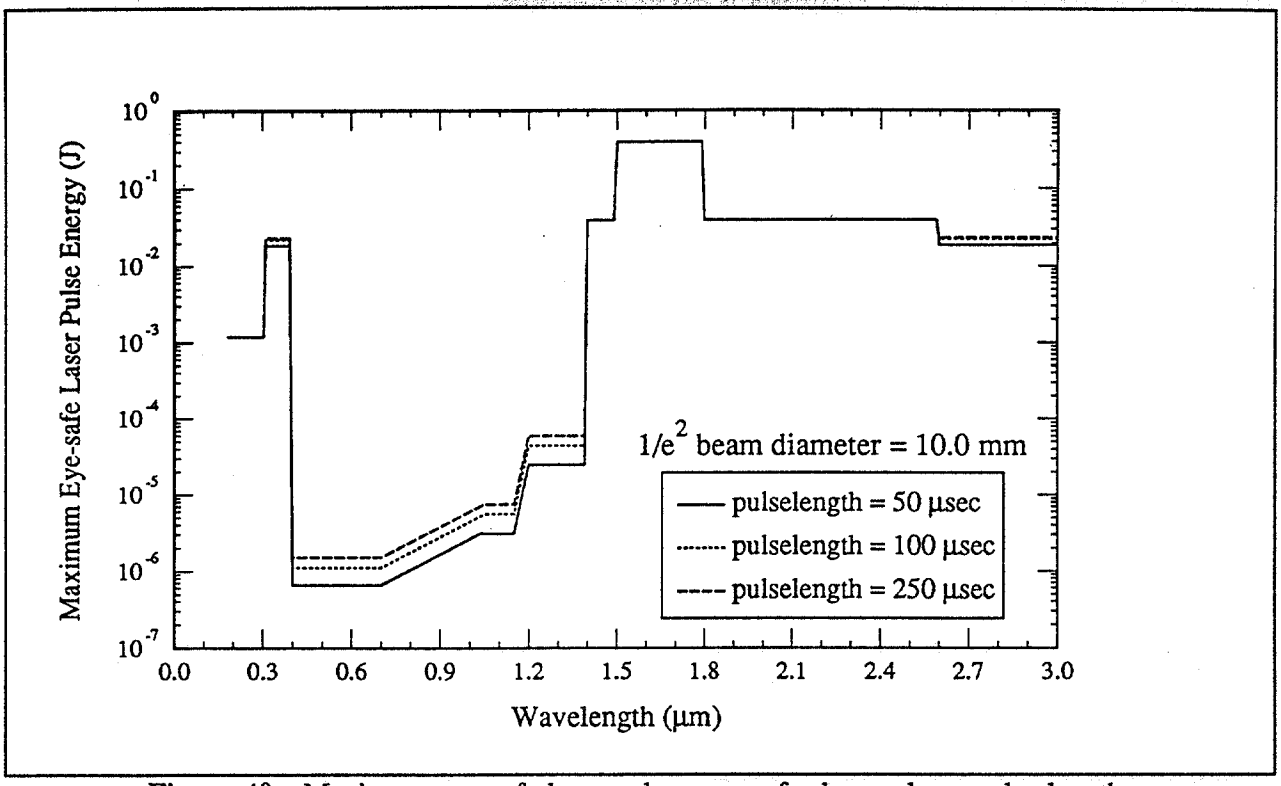

Figure 40 - Maximum eye-safe laser pulse energy for longer laser pulse lengths

In the retinal hazard region, the longer laser pulse lengths allow the use of additional pulse energy between 400 nm and 1.05 μm. However, the gains in eye-safe pulse energy are not large (between a factor of 2 and 5, depending on the increase in pulse length), and they occur in a spectral region where the eye-safe laser pulse energy is very low. In the visible region, pulse energies must be less than 1 μJ, too low for use as the probe laser. At 1.06 μm, the allowed pulse energy has increased to about 2 μJ which may be just enough for the probe laser. Above 1.2 μm, the allowed pulse energies increase substantially and any of these longer wavelengths would satisfy the energy requirements of the probe laser. Finally, at wavelengths below 0.4 μm, pulse energies in the tens of millijoules are allowed, so these wavelengths could also be considered for the probe laser.

The primary purpose of the probe laser is to illuminate the oil surface during the entire surface displacement period. Any variation in the probe laser intensity or optical frequency during this period acts to obscure the measurement of the true surface displacement. By nature then, a pulsed source used for the probe laser is itself a compromise, since it is difficult or impossible to produce laser pulses whose intensity cuts on sharply, remains constant over an extended interval and then drops sharply to define the end of the pulse. For this reason alone, a cw laser represents an attractive alternative to the long-pulse laser when used for a probe source.

Figure 41 illustrates the maximum eye-safe laser power for a cw laser whose beam sweeps across the eye of an observer at 50 m/s. The calculations for this case were also done assuming $1/e^2$ beam diameter values of 3.0 mm, 10.0 mm and 30.0 mm. The characteristic of the curves shown in Figure 41 is by now familiar, being very similar to that shown for the pulsed laser cases.

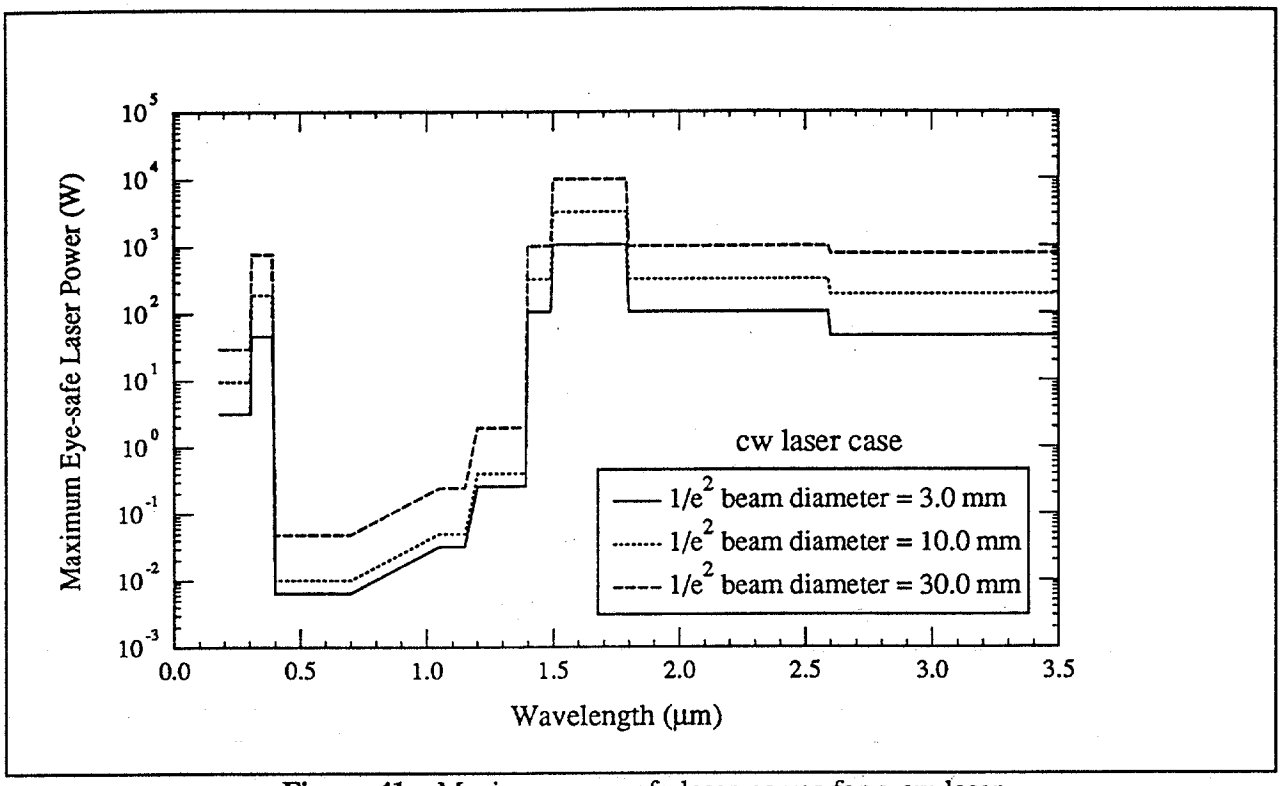

Figure 41 - Maximum eye-safe laser power for a cw laser

The best eye-safe spectral region allows laser power values up to the kilowatt range or more, depending on the extent to which the beam is spread (i.e., the beam diameter). Our system modeling suggests that cw powers on the order of several tens of milliwatts are sufficient to provide good return signals. For eye-safe laser power values of 10 mW, we need to only exclude the visible region between 0.4 and 0.7 μm. All other wavelength regions have substantially higher eye-safe power levels.

In summary, for a pulsed system, assuming a 50 μs pulse duration and laser spot size on the sea surface of 1.0 cm diameter, eye-safe operation in the visible region (400 to 700 nm) which requires pulse energies less than 1 μJ is out of the question. System sensitivity will also be marginal in the region from 700 nm to 1.2 μm. This forces us to look to wavelengths in the 1.2 μm to 1.8 μm region or once again at shorter wavelengths, below 400 nm. For the cw case, powers of 10 mW appear to be adequate and this power level is eye-safe at all wavelengths except the visible region. Thus in general, for either the pulsed or cw probe laser case, we are not limited by eye-safety considerations in the type of laser chosen.

3.2.3.2 Probe Laser Requirements

The probe laser requirements are quite different from those of the generating laser. The requirements for a pulsed system are listed in Table 5. In this case, high pulse energy is not required but very narrow spectral bandwidth with good stability is of primary importance. This is required to ensure that the receiver can detect the small Doppler shifts in the reflected laser frequency due to the motion of the oil surface. Also, in this case, we require longer laser pulses. As was the case with the generating laser, the pointing stability of the probe laser as well as the ability to fire on command are important requirements for this laser. The specific requirements are discussed in the following paragraphs.

Wavelength: The actual wavelength of the probe beam is not a critical parameter. Ideally it will be short; 1 μm is perfectly acceptable in terms of the ability of the system to detect the surface motion. One additional consideration is that the beam would be best not to penetrate into the water volume. This would only be a problem in the visible region of the spectrum and so we want to avoid that region. Additionally, eye-safety considerations push the wavelength into regions below 0.4 μm or above 1.0 μm.

Spectral Bandwidth, Center Wavelength Stability: These are critical parameters since the detection of the surface motion depends on detecting very small Doppler induced wavelength shifts in the reflected laser energy. The detection is made easier if the spectral bandwidth is kept small. This bandwidth must be considerably less than the expected frequency shifts to be detected in order not to lose sensitivity. Since we expect our maximum frequency shifts to be on the order of 1 MHz, we have adopted a probe laser spectral bandwidth of < 200 kHz. For center wavelength stability we specify half the spectral bandwidth or < 100 kHz.

Pulse Length: The requirements for illuminating the target during the entire duration of the surface displacement event place a lower limit on the pulse duration. Given a nominal acoustic velocity of 1300 m/s in oil, we would need a pulse length of at least 5 μs to measure oil layers up to 3 mm thick. Thicker oil layers would require proportionally longer pulse lengths. However, the temporal characteristics of the probe pulse are also of great importance. Any variation in the pulse intensity during the time interval corresponding to the surface displacement acts directly on the demodulation receiver output signal and will result in erroneous surface motions. To ensure that we will have a sufficiently long portion of the pulse that has constant intensity, we have arbitrarily doubled the required duration. Furthermore, if we assume that we want the ability to measure 15 mm thick oil layers, the pulse duration must be 50 μs, as specified in Table 5.

Pulse Energy: The return signal from the oil surface is due to a specular reflection. This means that the return beam will be collimated and relatively intense. For this reason, very little energy is required for the probe laser pulse. Assuming a reasonably flat oil surface, we estimate that a strong return signal will be obtained if the probe laser pulse energy is 0.01 μJ or better. There is however, much uncertainty about the flatness of the oil surface and even slight curvature of the surface could introduce large losses to the return beam. For this reason we overspecify the probe laser pulse energy at 2 μJ.

Energy Stability: The pulse-to-pulse energy stability from the laser is not critical, as long as it represents a small fraction of the actual output. We have arbitrarily assumed a pulse-to-pulse stability of ± 15% as was done for the generating laser.

The rest of the required parameters are specified the same as for the generating laser. The one exception is the longitudinal mode structure which for the probe laser must be designed to be a single longitudinal mode. This ensures that the laser output frequency is as close to single frequency as possible.

Table 5: Pulsed Probe Laser Specifications

Laser Property	Specification	Comments
Wavelength	0.35 to 3.0 μm	fixed, tunability unnecessary
Spectral Bandwidth	≤ 300 kHz	CRITICAL for maximum sensitivity
Center Wavelength Stability	≤ 100 kHz short-term	CRITICAL for maximum sensitivity
Pulse Length	> 50 μs	temporal intensity distribution as smooth as possible
Pulse Energy	> 2 μJ	more is better; scales up with increasing pulse length; more in IR
Pulse Energy Stability	±15 %	not critical
Repetition Rate	variable 10 Hz max.	ability to "fire on demand" is IMPORTANT without changing properties of optical pulse
Hold-off Time	≤ 50 μs	min. time between external trigger pulse and generation of optical pulse is VERY IMPORTANT
Spot Size	negotiable	ability to focus laser pulse to a small spot at ~ 100 m distance is CRITICAL
Spatial Mode	near-Gaussian preferred	
Beam Divergence	negotiable	
Longitudinal Mode	SLM	this is CRITICAL to achieve a near-"single frequency" source
Beam Pointing Stability	±50 μrad	less is better
Temperature Range	5-30°C	do not reject lasers solely for this reason
Vibrational Environment	severe	laser to be aircraft mounted; do not reject solely for this reason
Size, Weight & Configuration	negotiable	as light/compact as possible
Power Requirements	negotiable	as economical as possible
Development Considerations	negotiable	commercially-avail. sources preferred

For the cw probe laser, we still have the tight requirements on the spectral characteristics of the laser. We no longer have specifications for pulse length or fire-on-command since the laser by definition is running continuously. Also, the output of the laser is now expressed in terms of power rather than pulse energy. A 10 mW output power is quite modest for cw systems. Except for these differences, all specifications for the cw laser are the same as for the pulsed probe laser. The requirements for the cw probe laser are listed in Table 6.

Table 6: CW Probe Laser Specifications

Laser Property	Specification	Comments
Wavelength	0.35 to 3.0 μm	fixed, tunability unnecessary
Spectral Bandwidth	≤ 300 kHz	CRITICAL for maximum sensitivity
Center Wavelength Stability	≤ 100 kHz short-term	CRITICAL for maximum sensitivity
Output Power	> 10 mW	more is better; more in IR
Spot Size	negotiable	ability to focus laser pulse to a small spot at ~ 100 m distance is CRITICAL
Spatial Mode	near-Gaussian preferred	
Beam Divergence	negotiable	
Longitudinal Mode	SLM	this is CRITICAL to achieve a near-"single frequency" source
Beam Pointing Stability	±50 μrad	less is better
Temperature Range	5-30°C	do not reject lasers solely for this reason
Vibrational Environment	severe	laser to be aircraft mounted; do not reject solely for this reason
Size, Weight & Configuration	negotiable	as light/compact as possible
Power Requirements	negotiable	as economical as possible
Development Considerations	negotiable	commercially-avail. sources preferred

3.2.3.3 Probe Laser Evaluation

In this discussion, we consider both pulsed and cw systems. The difficulty for pulsed systems is the need for long duration pulses and ultrahigh spectral purity. Neither of these features is generally available in commercial systems. On the other hand, cw systems look very attractive as they avoid all of the problems associated with pulsed systems as well as providing the surface orientation laser in the same package.

The current long pulse YAG laser has demonstrated the ability to do the job of the probe laser in controlled tests. This laser satisfies all of the requirements for the probe laser except that its output pulse energy of about 0.3 mJ is not eye-safe at the water surface. This could be remedied in a number of ways. The output energy could be reduced to the eye-safe level of 2 μJ. This could be done by simply splitting off a portion of the pulse energy before it leaves the aircraft. Alternatively, this laser could be used to pump a Raman cell or OPO, effectively shifting the wavelength into the eye-safe region around 1.5 μm. A Raman cell would produce long duration pulses at 1.54 μm at an energy of about 60 μJ, as long as the beam could be focused tightly enough within the Raman cell to successfully use the potential 20% conversion efficiency. The Raman cell has the advantage of being a rugged, alignment insensitive device. Low repetition rate and aperiodic operation do not present a problem for the Raman cell. Furthermore, the Raman cell will retain the narrow spectral bandwidth of the pump laser. An OPO could also be used to shift the probe laser wavelength but these devices are very alignment sensitive and would not retain the narrow bandwidth of the pump laser. In order to ensure a narrow linewidth on the output of the OPO, a second seed laser is required. As one can appreciate, this approach rapidly becomes quite complex.

Of the above options to render the probe laser eye-safe, we recommend that the Raman cell be used. This could be retrofitted to the existing probe laser with minimal effort.

There are a number of cw lasers available with the required characteristics. These include diode-pumped solid state lasers based on Nd:YAG operating at 1.064 μm, Nd:YVO_4 (vanadate) also operating at 1.064 μm and Er:glass operating from 1.53 to 1.565 μm. Table 7 lists the key probe laser requirements along with the specifications for these cw lasers.

Table 7: Possible CW Probe Lasers

Parameter	Requirement	Micracor Nd:YAG/YVO	Micracor Er:glass	Amoco Er:glass
Wavelength	> 1 μm	1.064 μm	1.535 μm	1.530-1.565 μm
Spectral Bandwidth	< 300 kHz	< 10 kHz	< 10 kHz	< 50 kHz
Frequency Stability	< 100 kHz	<30 kHz in 1 ms	<30 kHz in 1 ms	500 kHz in 1 s
Pulse Length	50 μs	cw	cw	cw
Power	10 mW	25-35 mW TEM_{00}	20 mW TEM_{00}	50 mW TEM_{00}
Longitudinal Mode	SLM	SLM	SLM	SLM
Size: Head/ Power Supply	small	1.75" x 1.25" x 0.75"	1.75" x 1.25" x 0.75"	8"x 2.4"x 2.6" 4"x 10"x 9"

From the data in Table 7, one can see that these miniature cw lasers from Micracor satisfy all of our requirements while being extremely small packages.

3.2.3.4 Probe Laser Summary

The potential use of cw diode-pumped solid state lasers for the probe beam should be further investigated. Based on our analysis, it appears that these tiny cw lasers can perform the probe laser function at least as well as the current pulsed system while having the advantages of size and reliability. In addition, these cw lasers allow for continuous tuning of the Fabry-Perot receiver to the laser wavelength by splitting a portion of the probe laser output through the Fabry-Perot Interferometer. Also, this cw laser could also serve the function of the surface orientation monitor.

3.3 Transmitter Optics

Many applications involving the use of lasers for remote sensing do so with the intent to interrogate an area (or volume) of the medium under investigation which is significantly larger than the laser beam size. Thus, beam spot size is not a critical parameter in determining the performance of those systems. The LURSOT sensor is unique in this respect since the laser beams must be focused down to small spots at the oil surface. Since the altitude of the aircraft used as the sensor platform is by necessity quite large (at least 100 m), the laser beams must be focused over quite long distances. In addition to the difficulty of focusing the beams onto the oil surface, we have to consider the fact that the system can consist of up to three different laser beams, each having its own unique wavelength, size and initial divergence. The transmitter optics have to combine these beams co-linearly and maintain this alignment under the influences of vibration and temperature changes. A misalignment of any of the beams by a few millimeters on the oil surface will seriously decrease the sensitivity of the system. These place quite stringent limitations on the design of the transmitter optics.

3.3.1 Transmitter Optics Requirements

On detailed examination, the transmitter optics become a critical element of the LURSOT system and may in fact be one of the primary reasons for the poor results in the airborne tests. As mentioned above, these optics have to be able to deliver up to three laser beams to a tight spot on the oil surface. This involves collimating and combining of the beams from the different laser sources. The optics to combine the beams must be designed to withstand the vibrational and temperature environments in the aircraft such that co-linearity of the beams is maintained at all times. Once combined, the optics must provide focusing, possibly over a wide range of wavelengths. Finally, a general requirement is that the probe beam spot on the oil should be smaller than the spot size of the generating beam. This is to ensure that the probe beam reacts to the center of the interaction region where the laser-ultrasonic interaction will be most pronounced.

The above requirements have implications on the general design of the LURSOT system. From the point of view of the transmitter optics, it is better to have two lasers rather than three. That is, if a cw probe laser is used, it can perform both the surface orientation and surface motion detection. It will be much simpler to maintain the alignment between two lasers than it will be for three lasers. Also, a narrower spread of wavelengths between the various laser systems requires less exotic optical materials and makes the focusing of the beams onto the oil surface that much easier. The current system with wavelengths of 0.632 μm, 1.06 μm and 10.6 μm could not be worse in this respect.

Also, since the alignment of the beams is so critical to the proper functioning of the LURSOT system, a system to monitor this alignment would be very useful, particularly since under the influence of temperature changes, the pointing direction of the beams emerging from the lasers can change. If such misalignment cannot be avoided, a monitor of the beam alignment would be a very important diagnostic feature of the system.

Vibration is of considerable concern for another reason as well. If the steering mirrors in the transmitter optics path for the probe laser are vibrating, they will themselves introduce a time dependent Doppler shift into the transmitted beam. Such a shift could interfere with the detection of the shifts induced by the ultrasonic motion of the oil surface.

3.3.2 Focusing of Laser Beams at the Sea Surface

For a review of collimation and imaging of Gaussian beams see Appendix B. For the current investigation we wanted to calculate the limiting focal spot diameter, for various combinations of lasers and Galilean beam expanders which would be used to focus the beam at a distance of 100 m. As discussed in Appendix B, Gaussian beams can be focused to smaller spot diameters than beams possessing other higher-order modes. Thus we have assumed that Gaussian laser beams would be used in all of these studies. Furthermore, we have assumed the use of simple two-element Galilean beam expanders rather than those incorporating corrective elements. Slight departures of laser beams from the theoretical Gaussian power density distribution, as normally occurs in real lasers, would be somewhat compensated for by the use of beam expanders utilizing these more complicated designs.

We can make these assumptions without compromising the results, as long as we remember that we are calculating limiting cases; how closely an actual system approaches these limits depends on the matching of the beam expander to a particular laser source, which would only be performed as part of a detailed design study.

For the current studies we created a model which would, for a host of input parameters, calculate the final laser spot diameter at a given distance from the beam expander. A single case of the many performed during the study has been chosen for presentation here, in order to characterize the methodology and the format of the results; other cases are presented in Section 3.3.3.

Figure 42 shows a plot of modeled laser spot diameter as a function of the distance from the exit aperture of the optics. In this case, we assume an initial $1/e^2$ laser spot radius of 0.6 mm and a 25x collimator. The collimator is assumed to be optimized to produce the smallest beam spot size (beam waist) at 100 m, which in this case is 6.8 mm. In this case, the optical properties of the beam expander are fixed. In general, this plot shows that the spot size increases at a rate of about 1.1 cm for every 25 m to either side of the optimal 100 m range. If we wish to maintain the spot size to under 1 cm diameter, we are only allowed about 20 m offset from the nominal 100 m distance. This result suggests that having a fixed collimator may place strict limitations on how much the aircraft-to-surface distance can be allowed to vary.

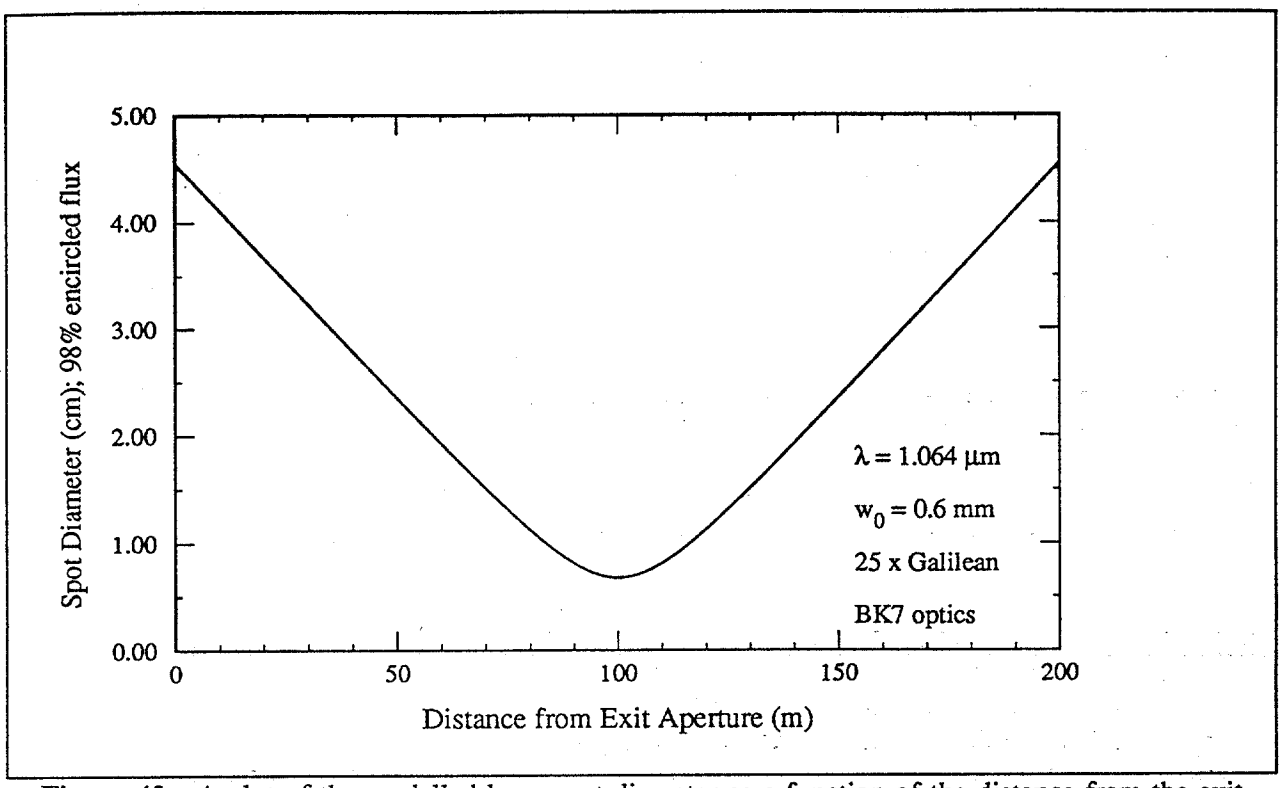

Figure 42 - A plot of the modelled laser spot diameter as a function of the distance from the exit aperture of the optics

The above result suggests that some form of dynamic focusing of the image in response to changes in the aircraft altitude may be necessary. In Figure 43, we have plotted the dependance of the beam waist position as a function of the separation between the two collimator lenses. Once again the system was optimized for a 100 m range. The offset plotted along the horizontal scale represents the change in the separation of the lens from its nominal 100 m setting. Decreasing the separation increases the range to the best focus. Conversely, increasing the separation decreases the range to best focus. We can see that there is a minimum range of 45 m for this particular modeled collimator. Also, as the separation is reduced we see the range of the minimum beam waste becomes increasingly sensitive to these changes, moving rapidly to very large values. The basic result that we wish to illustrate here is the fact that for very small changes in the lens separation, the beam waist range changes considerably. This lens adjustment could be used to try to compensate the laser spot size at the oil surface for changes in aircraft altitude. It would, however, have to be a very accurate mechanism as errors in the lens positioning on the order of a fraction of a millimeter can significantly affect the spot size. For example, a change in separation of only 120 μm moves the beam waist position from 200 m to 300 m.

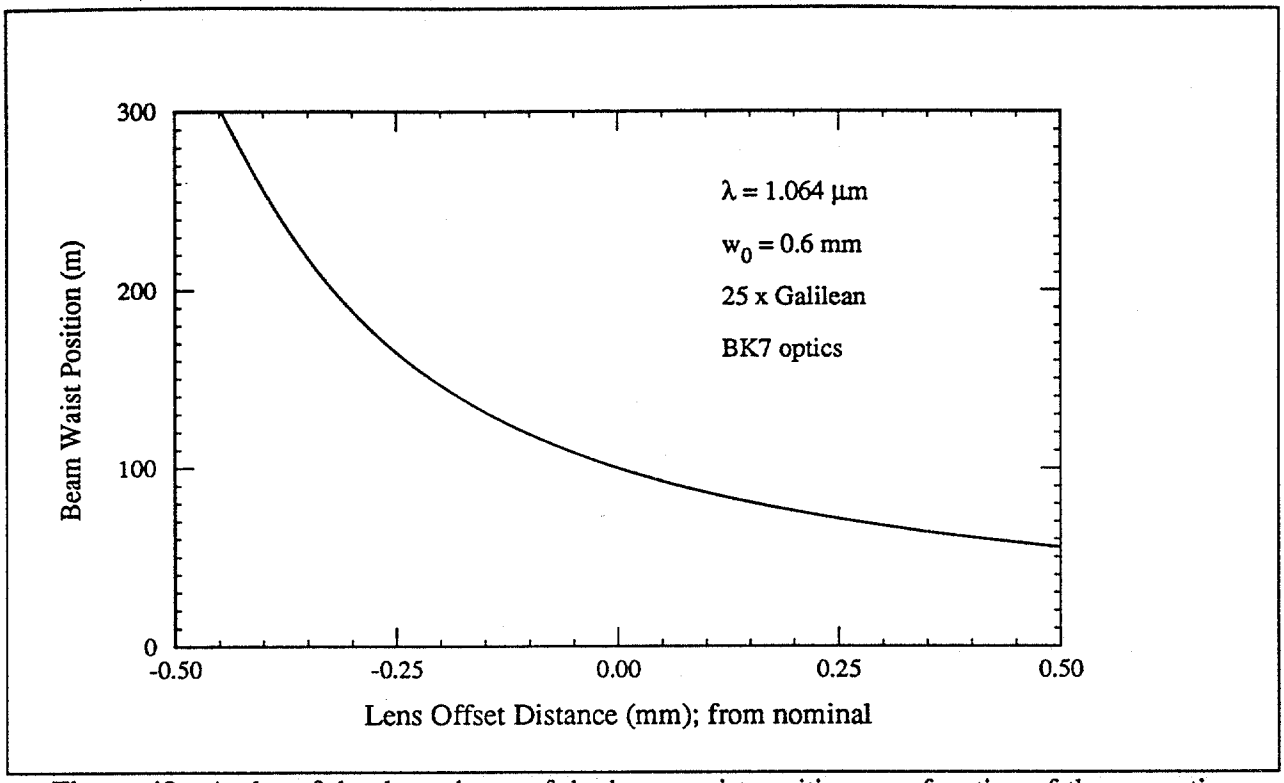

Figure 43 - A plot of the dependance of the beam waist position as a function of the separation between the two collimator lenses

In Figure 44 we further look at the effect of changes in collimator lens separation on the beam focusing at the oil surface. In this case we have plotted the beam waist size as a function of the change in the lens separation. The beam waist position changes with changes in the lens separation according to Figure 43. In general, the beam diameter is smallest for shorter focal distances (down to 0.35 cm at 60 m) and largest for long focal distances (up to 2.5 cm at 300 m). We see the same rapid change in values as the separation is reduced as we saw in Figure 43. At the left of this figure we see an extreme dependence of the beam waist size on lens separation. The same 120 μm change in lens separation mentioned in the previous paragraph could change the beam waist by almost a factor of 2 from 1.5 cm to 2.5 cm. This is equivalent to a factor of 3 change in the energy density delivered to the oil surface and thus can greatly affect the efficiency of the laser-ultrasonic interaction.

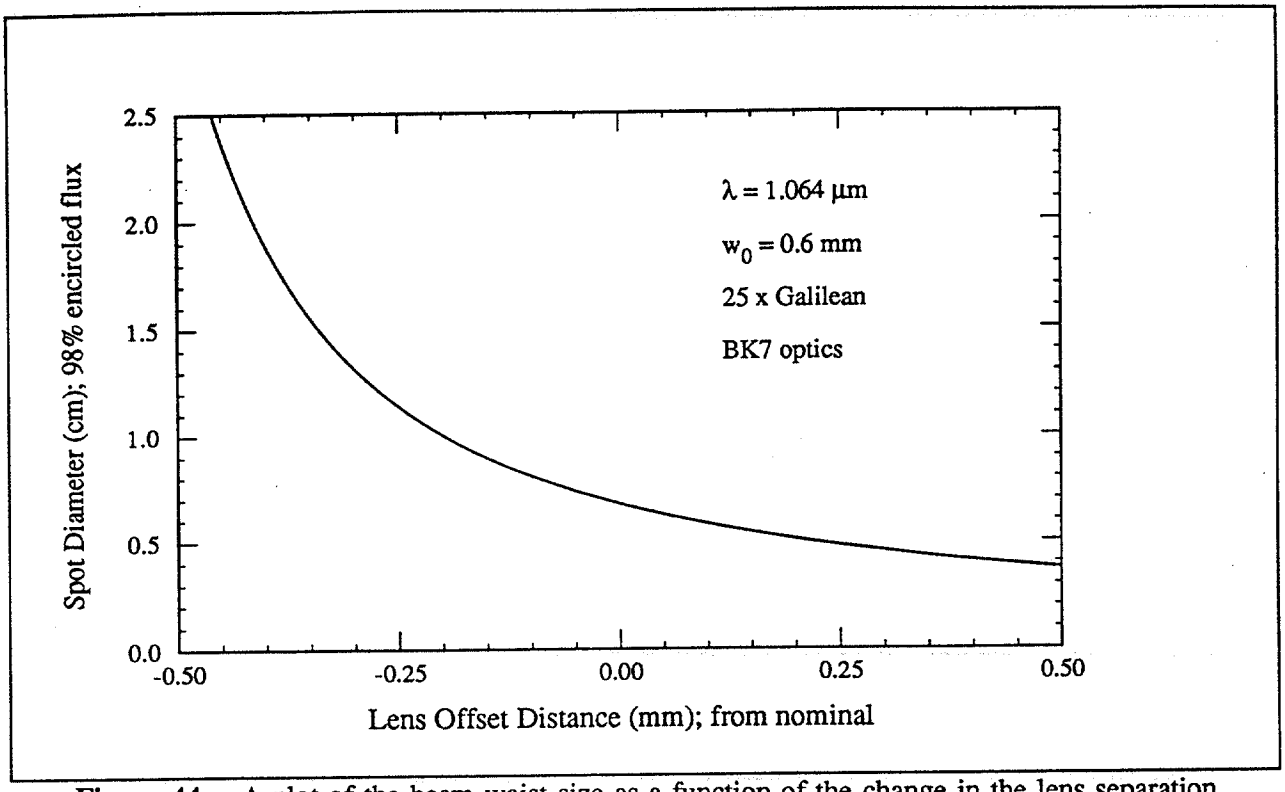

Figure 44 - A plot of the beam waist size as a function of the change in the lens separation

Figure 45 merely re-plots the previous results, showing beam waist diameter as a function of the position of that waist. Note that the lens separation is changing in order to move along this curve. This plot shows a nearly linear increase in beam waist diameter with increasing waist position for a given beam expander design. However, at the longest waist position, the beam waist diameter is an exponential function of focal position. This result demonstrates that for the particular beam expander design modeled in this analysis, there is a definite advantage to keeping the aircraft altitude at a minimum. For example, increasing the nominal altitude from 100 m to 200 m results in a best beam spot size which is a factor of 2 larger than in the 100 m case. This in turn results in a reduction in energy density at the surface by a factor of 4.

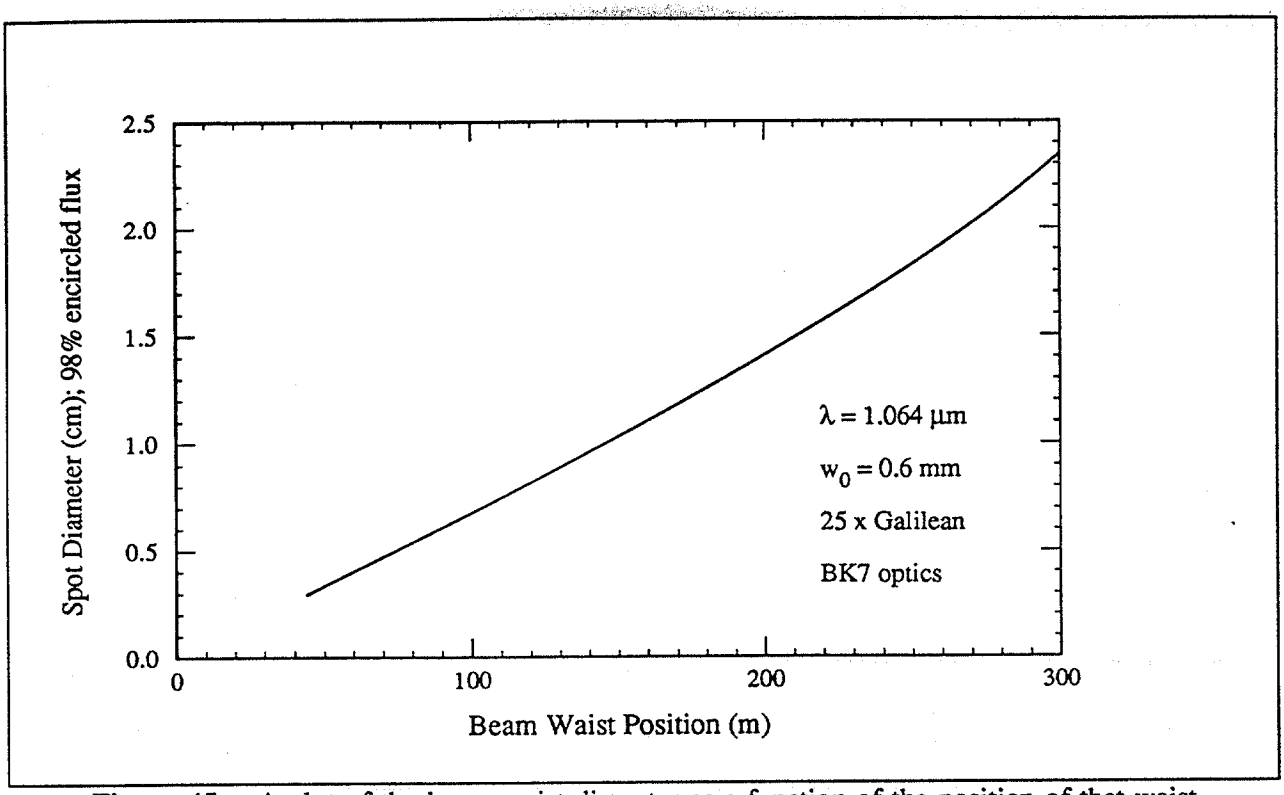

Figure 45 - A plot of the beam waist diameter as a function of the position of that waist

From these plots we can see that there is a minimal achievable beam waist size for a given initial laser beam and collimator design. Ideally, for LURSOT, we want a design that will provide minimal beam waist size at a range of about 100 m. Additionally, we would like this waist size to be weakly dependent on waist position and lens separation. In this way, the transmitter optics would be minimally susceptible to variations in aircraft altitude and vibrations which might cause variation in the lens separation. In the following section we look at the impact that changes in laser wavelength and the associated change in optical materials have on the collimator function.

3.3.3 System Considerations

Since at this point there are a number of options for laser systems for the generating and probe lasers, we have performed an analysis of possible transmitter optics for a number of selected wavelengths. The above case was for a wavelength of 1.064 μm for which we assumed BK7 optics. Other cases examined in the following include a wavelength of 355 nm with quartz optics, 1.65 μm with quartz optics, 2.3 μm with sapphire optics and 10.6 μm with ZnSe optics.

As a vehicle for the comparison of these various cases, we use the plot of beam waist diameter versus beam waist position used in Figure 45. At shorter wavelengths it is easier to obtain small beam waist diameters. For example in Figures 46 through 49 for 100 m waist positions, the waist diameter increases with wavelength from 0.1 cm at 355 nm to over 3.5 cm at 10.6 μm. For the longer wavelengths we also observe a turn in the plots indicating that it is not possible to obtain a focused spot of any diameter beyond certain ranges. For example, at 10.6 μm a beam waist cannot be generated beyond a range of 150 m for the assumed collimator characteristics.

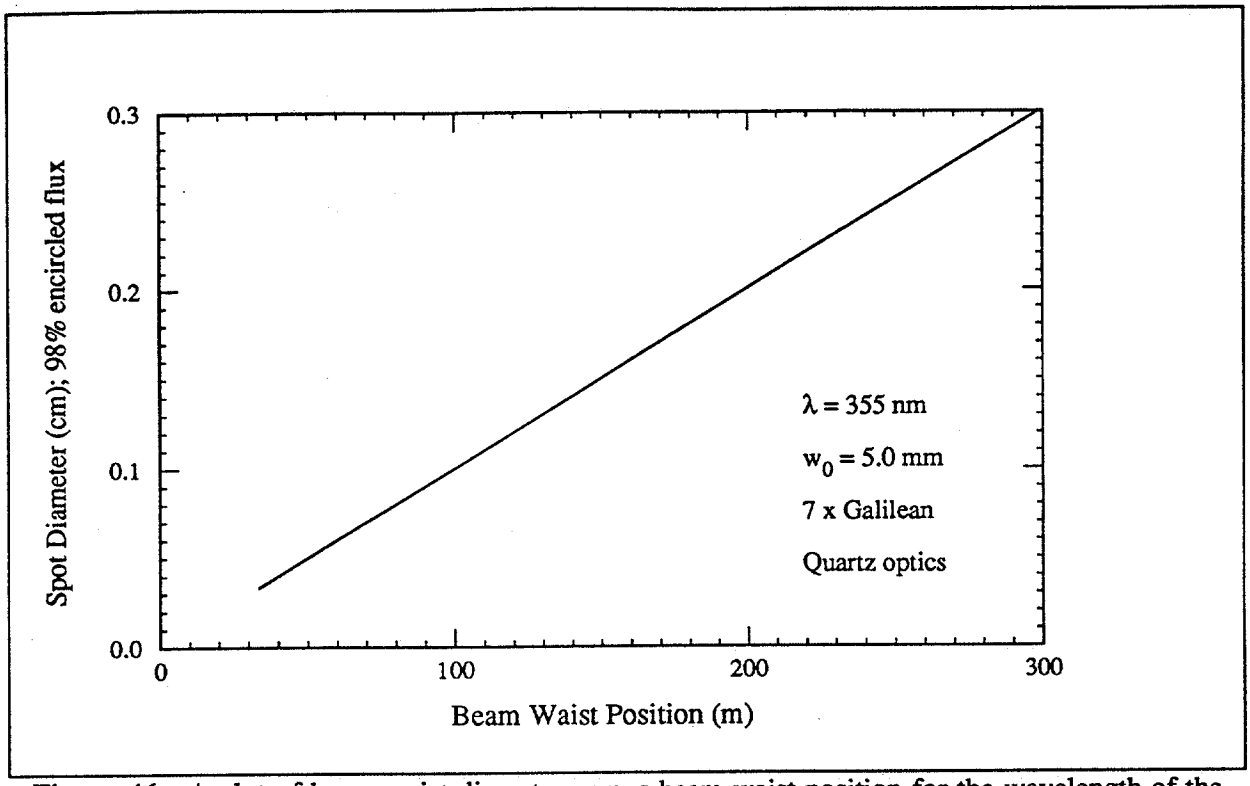

Figure 46 - A plot of beam waist diameter versus beam waist position for the wavelength of the generating laser at 355 nm

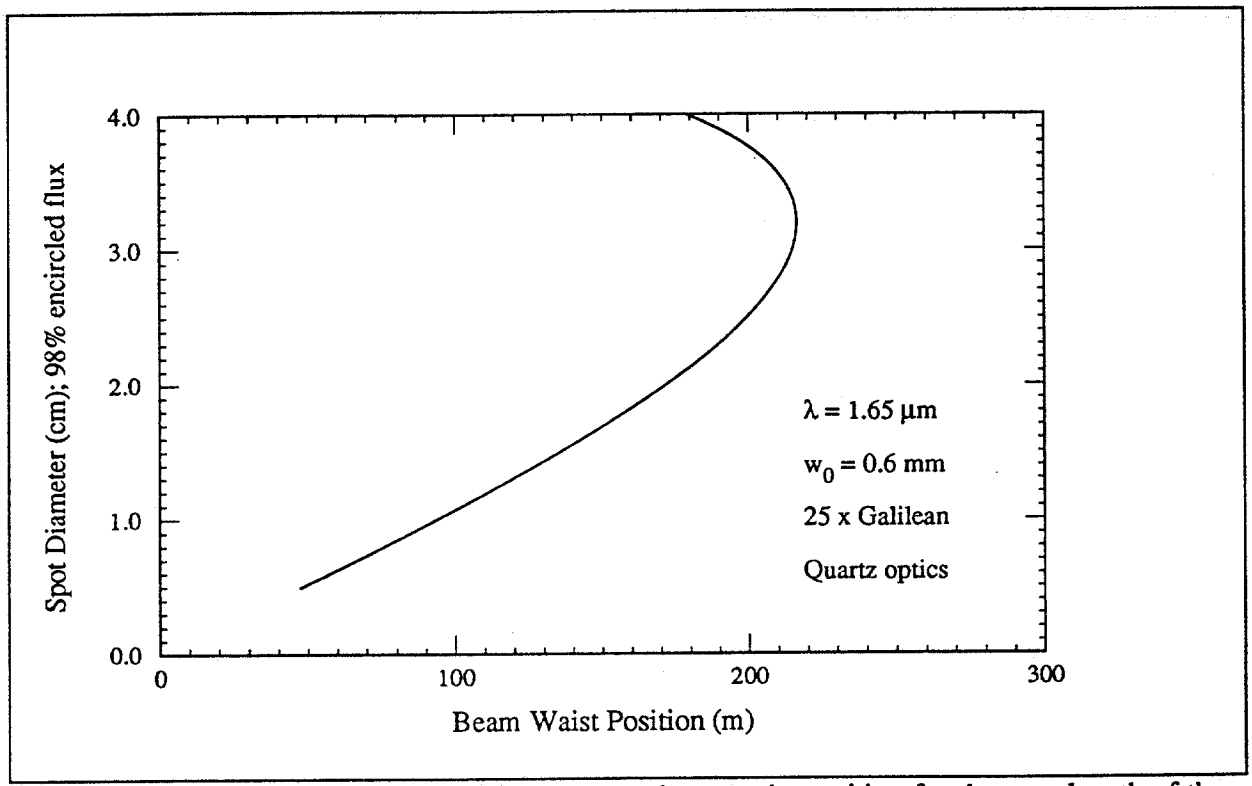

Figure 47 - A plot of beam waist diameter versus beam waist position for the wavelength of the generating laser at 1.65 µm

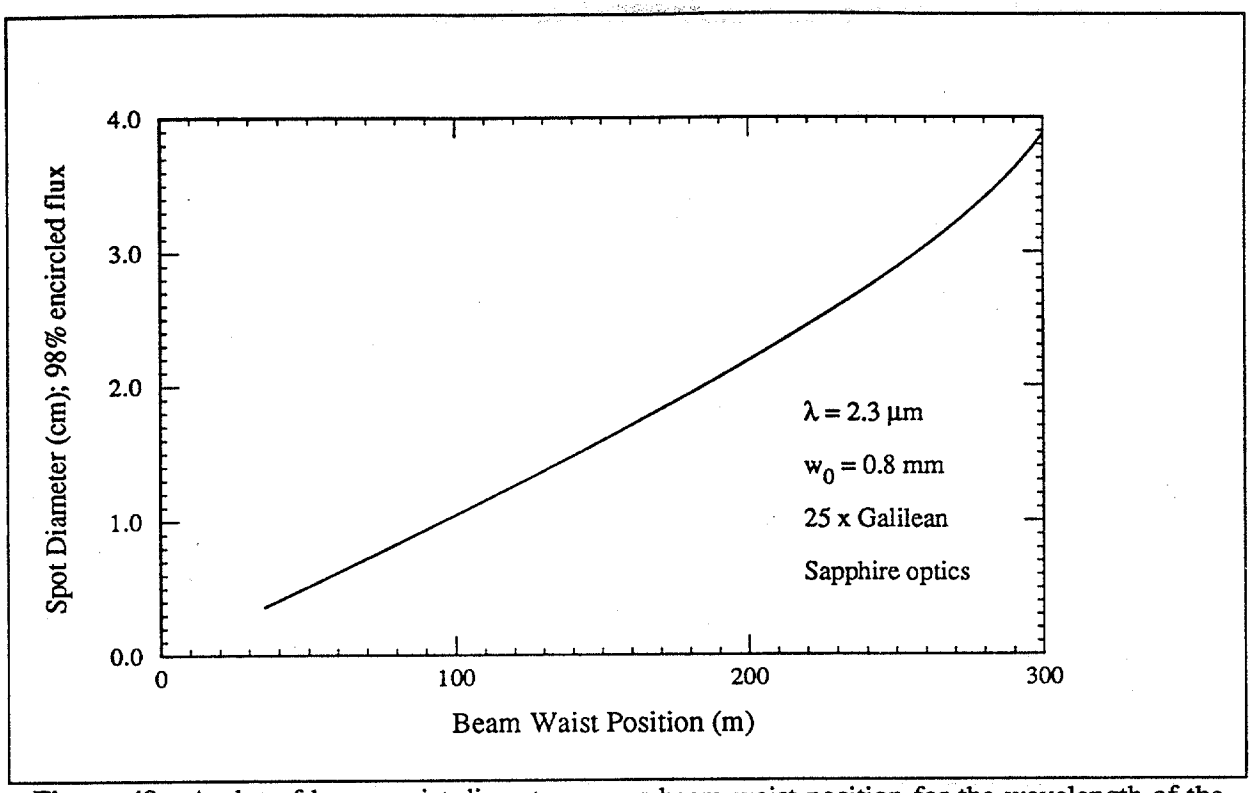

Figure 48 - A plot of beam waist diameter versus beam waist position for the wavelength of the generating laser at 2.3 μm

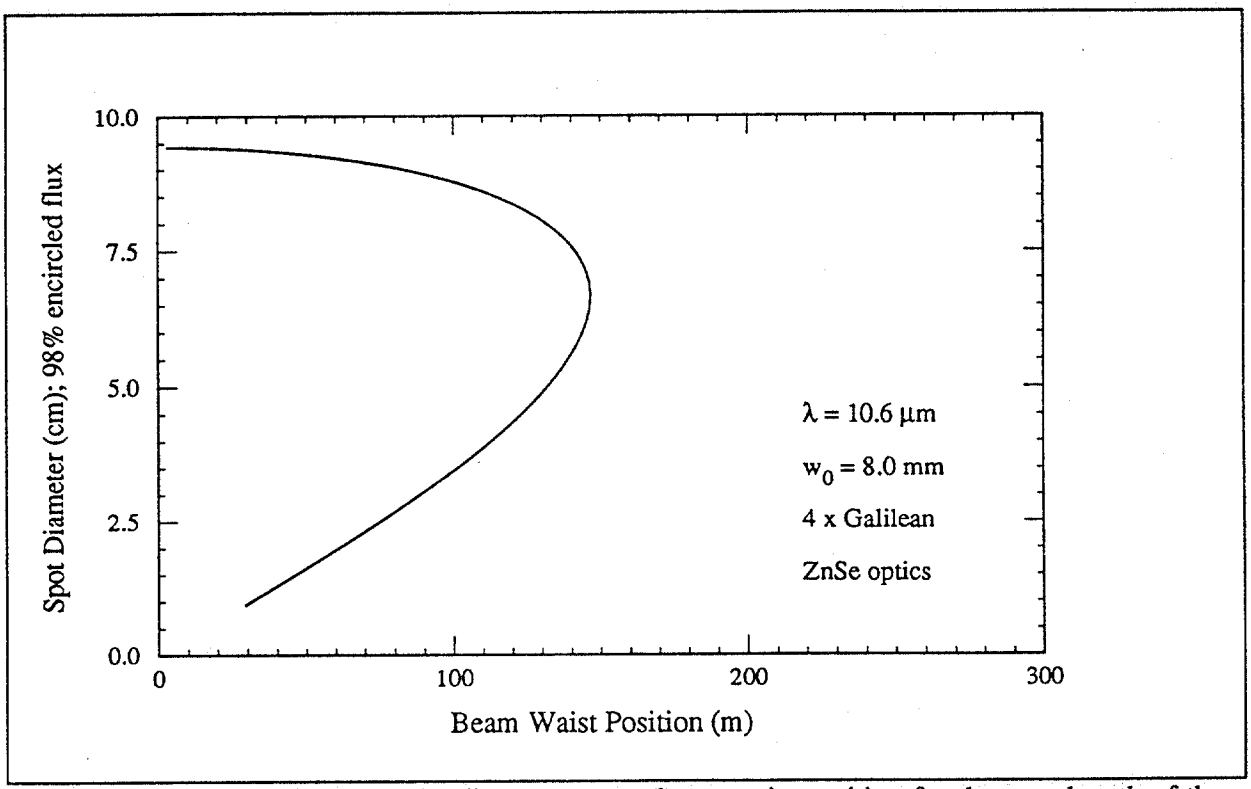

Figure 49 - A plot of beam waist diameter versus beam waist position for the wavelength of the generating laser at 10.6 μm

These results, along with other system performance-related requirements for the laser spot sizes, can be used to make general conclusions about the optimum spot sizes. The results of the above analysis show that the spot size at the water surface depends very strongly on the wavelength used. For example, the very short wavelengths in the UV can be focused to less than a millimeter while the 10.6 μm wavelength of the CO_2 laser exceeds 2.5 cm. For the generating laser we want to concentrate the laser light at the surface in order to generate a strong laser-ultrasonic interaction. This size is, however, influenced by the size of the probe laser as we require that the probe laser spot fit easily within the generating laser spot. This is necessary to ensure that the probe laser sees a uniform surface motion across its entire diameter. Otherwise, different portions of the probe beam will experience different Doppler shifts and the return signal will be smeared out over a wide frequency range. Additionally, we must account for the relative motion of the two beams due to the characteristic beam wander of the two laser systems. We expect that this wander will be on the order of 0.5 cm over the 100 m path from the aircraft to the water surface. These factors being considered, the generating laser pulse should have a diameter at the water surface of at least 1 cm. The probe beam must fit well within this, so a nominal value of 0.5 cm diameter would be acceptable. Thus, even though the shortest wavelengths can theoretically be focused to spot sizes much less than 1 cm, this cannot be considered to be a significant advantage for these shorter wavelength lasers.

3.4 Receiver System

The following sections will address the configuration of the receiver optics including potential design trade-offs, estimates of the receiver optical throughput including discussion of some of the limiting factors affecting it, and some preliminary signal-to-noise ratio (SNR) calculations.

3.4.1 Receiver Optics Configuration

The receiver optics have certain basic requirements which can be summarized as follows:

- Must collect the light from the orientation-sensing laser, after it has been reflected from the water surface, and focus it onto a suitable photodetector with the best optical throughput possible.
- Must collect light from the probe laser, after it has been reflected from the water surface, and collimate it to a beam of a suitable diameter and divergence for input to the confocal Fabry-Perot device.
- Must demodulate the reflected probe laser light using an appropriate confocal Fabry-Perot Interferometer.
- Must re-image the light beams exiting the confocal Fabry-Perot Interferometer onto a suitable photodetector.
- Must spectrally filter the light from the telescope so that background solar light does not reach the photodetectors, thus interfering with the intended measurements.

In its simplest form, the receiver optics would consist of a telescope, a field stop, collimating lenses, a beamsplitter, narrowband interference filters, a fiberoptic relay, a confocal Fabry-Perot Interferometer (c-FPI), and focusing lenses. There are many possible design arrangements, but the primary driving force behind any of them involves giving the c-FPI the incident light field which it requires.

The telescope collects the laser light reflected from the water surface and focuses it onto a field stop. The field stop is used to select the field of view of the telescope, and therefore to eliminate as much solar background light as possible. Since the laser spots at the sea surface are quite small, the required telescope field of view can be very small, thus maximizing the rejection of background light.

The first collimating lens is used to collimate the light passing through the field stop, and to produce a nearly-parallel ray bundle of a known diameter. The collimation is necessary since the efficiency of the beamsplitter and the narrowband interference filter(s) element is compromised otherwise.

The beamsplitter is used to split the light collected by the telescope; it directs the light from the orientation-sensing laser to one channel and the probe laser light to another channel. If two different wavelengths of light are used for the orientation-sensing laser and the probe laser, then the beamsplitter can be dichroic. This type of beamsplitter can efficiently separate an incident beam by transmitting one wavelength and reflecting the other. If the same cw laser is used for both the orientation-sensing and probe functions, then the beamsplitter must be a partially transparent plate used to divide the intensity between the two channels.

The narrowband interference filters are used to reduce the amount of background light which is focused onto the photodetectors. It would perhaps seem unnecessary to use a narrowband interference filter simultaneous with a c-FPI, in the same channel, but in fact the narrowband filter is required to filter out the contribution of background light which can be transmitted through the many fringes of the c-FPI.

The first focusing lens is used to focus the probe laser light onto the fiberoptic relay. The relay then transmits the probe laser light to the second collimation lens. The combination of focusing lens, fiberoptic relay and collimation lens serves to isolate the c-FPI from the rest of the receiver optics.

The c-FPI is used to detect small changes in the incident wavelength of the reflected probe laser beam, by causing these wavelength changes to be translated into intensity changes in the output beam of the device. The detailed optical properties of this device are discussed in Section 2.4, and illustrated in Figure 21.

The focusing lenses are used in each of the two channels to focus the collimated beams onto the appropriate photodetector.

3.4.2 Receiver Throughput

The following discussion is devoted almost entirely to the optical throughput of the confocal Fabry-Perot Interferometer. The reason for this is that it represents the most critical element within the receiver sub-system, and also the element over which we have the least design freedom.

Ideal c-FP Device Response

The c-FPI is a particular format of a group of Fabry-Perot interferometers utilizing spherical mirrors to effect a resonant cavity. In the confocal variation, the two end mirrors have equal radii of curvature which are also equal to their separation distance; thus, the centre of curvature of one mirror falls at the physical centre of the other (see Figure 50). In comparison with other demodulation devices, it has high light gathering capability and a relative insensitivity to vibration. We will examine the first of these two characteristics in this section.

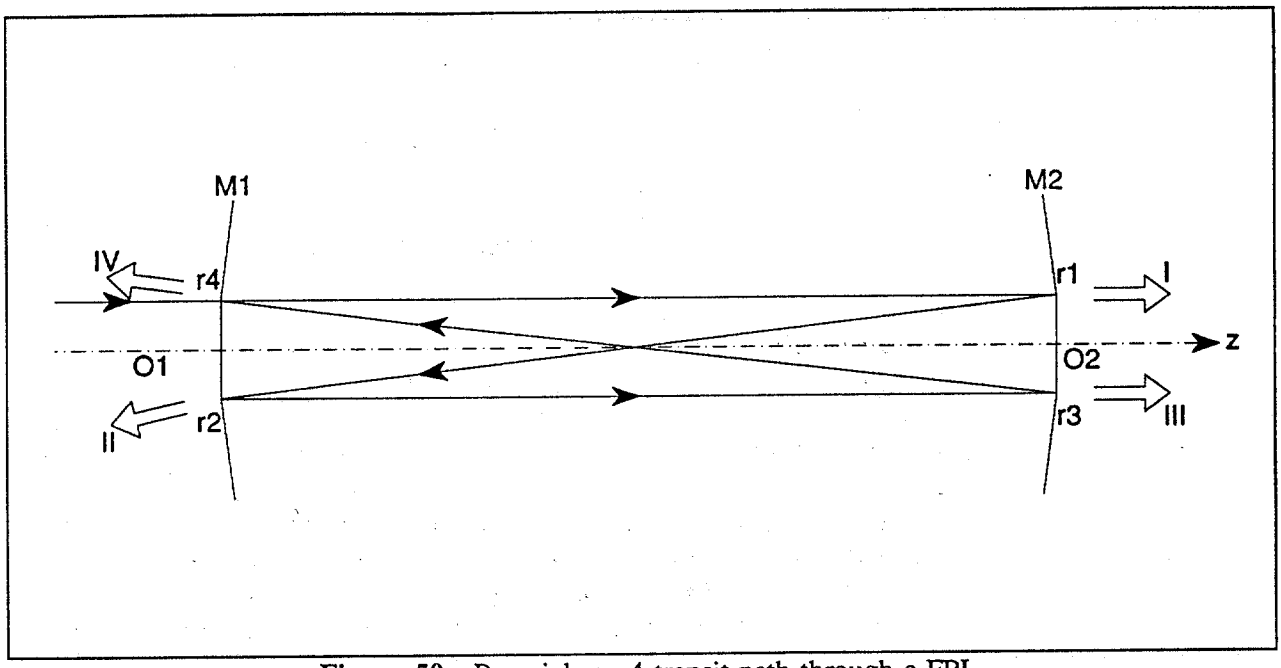

Figure 50 - Paraxial ray 4-transit path through c-FPI

Paraxial rays (i.e., those close to the optical axis of the device) which enter the device at small angles to the optical axis are termed re-entrant after four reflections from the end mirrors. This means that after two reflections from each of the two end mirrors, the ray path is overlaid with its original path as it entered the device. An incident ray entering at position r_4 on mirror M_1 undergoes four reflections (at points r_1 on M_2, r_2 on M_1, r_3 on M_2 and r_4 on M_1 respectively) before resuming its original path (see Figure 50). Obviously this also occurs after 8, 12, 16, ..., 4n reflections from the two mirrors. We will hereafter refer to a round trip of the cavity, involving four reflections from the end mirrors and rendering the ray re-entrant, as a four-transit path of the cavity.

Thus, at each of the points r_1 through r_4 there are many overlapping rays, each coming from successive four-transit paths of the cavity and thus having propagated through multiples of the four-transit pathlength. Each of these overlapping rays is essentially a replica of each other (except for the pathlength difference), and they all interfere. If the four-transit pathlength equals an integral number

of wavelengths of the incident ray there will be constructive interference at each of r_1 through r_4 and the resultant electromagnetic field will be maximized. Destructive interference will occur if the four-transit pathlength is a half-integer number of wavelengths of the incident ray, and the resultant electromagnetic field will be minimized. For other ratios of the four-transit pathlength and incident wavelength, partially constructive interference will result and the electromagnetic field will fall somewhere between the minimum and maximum value.

Thus, by changing either the wavelength of the incident light or the four-transit pathlength, the degree of interference, and hence the resultant electromagnetic field strength, can be varied between the minimum and maximum in a cyclic fashion. The demodulation capability of this optical instrument, for the LURSOT application, comes from its ability to interfere many versions of its incident light with each other.

Each of the end mirrors is highly reflective and partially transparent for the intended wavelength of light. Thus, a fraction of the light incident at each of points r_1 through r_4 is reflected and a smaller fraction is transmitted. This gives rise to four beams of light (labelled I through IV in Figure 50) which simultaneously exit the cavity. The intensity of beam I is dependent on the electromagnetic field strength at point r_1, and likewise for beams II through IV. The electromagnetic field strength at each of the points r_1 through r_4 is a complex summation of the phases of all contributing rays, and it takes into account the fact that each time the ray is reflected from a mirror, a little less intensity is available for interference at the next mirror (since the mirrors are semi-transparent).

Note that we refer to "beams" I through IV in the above discussion. However, the illustration in Figure 50 indicates that they are "rays". In actual fact, a single incident ray gives rise to four net resultant rays, which we may term ray I through ray IV. In practice, a large number of parallel incident rays (an input "beam") will give rise to four exit beams (beam I through IV), each consisting of an equal number of parallel rays. For convenience, in the following text we generally refer to incident rays and exit beams as corresponding entities, although strictly speaking they are not.

The intensity exiting the cavity for beam I (which is similar to that for the other three beams) can be related to the characteristics of the cavity and the wavelength of the incident ray by the following:

$$I(\phi) = \frac{I_0 T^2}{1 - 2R^2\cos\phi + R^4} \qquad (16)$$

$$\phi = \frac{2\pi(4\mu e)}{\lambda_0}$$

where

- I = the intensity of the beam exiting the cavity
- I_0 = the intensity of the beam incident on the cavity
- Φ = phase lag per four-transit path
- $_0$ = wavelength of the incident light ray
- e = radius of curvature of the end mirrors
  = separation distance of the end mirrors
- μ = refractive index of the medium between the mirrors
- R = intensity reflectance coefficient for mirrors
- T = intensity transmission coefficient for mirrors.

Assuming a fixed cavity design and a constant input intensity I_0 for the incident ray, the only variable term in the right side of Equation (16) above is the term in $cos\phi$, which itself varies only with the wavelength of the incident ray or the separation of the two end mirrors. We can also see that the intensity of beam I as it leaves the cavity is cyclic in either incident wavelength or mirror separation, because of the $cos\phi$ term. The maximum and minimum c-FP transmissions (considering beam I only) are given by

$$\tau_{max} = \frac{I_{max}}{I_0} = \frac{T^2}{[1 - R^2]^2}$$

$$\tau_{min} = \frac{I_{min}}{I_0} = \frac{T^2}{[1 + R^2]^2} \qquad (17)$$

where

τ_{max} = maximum value of c-FP transmission
τ_{min} = minimum value of c-FP transmission
I_{max} = maximum beam intensity exiting c-FP cavity
I_{min} = minimum beam intensity exiting c-FP cavity.

The equations shown above indicate that both the minimum and maximum intensity exiting the c-FP cavity are dependent on the reflectance and transmission coefficients for intensity; thus, the design properties of the c-FP can be changed not only by changing the radius of curvature of the end mirrors and their separation, but also by changing the reflectivity of these mirrors. In practice tailoring of the mirror reflectivity is quite readily accomplished by coating the end mirror substrates with a multi-layer dielectric coating which has the required properties.

Figure 51 illustrates the transmission for beam I exiting the c-FP cavity, for a 1 m long air-spaced device whose end mirrors have different reflectance coefficient values. The assumed nominal design wavelength is 1.064 μm. The differing mirror reflectivities are expressed in terms of the finesse parameter N_R, which is discussed below.

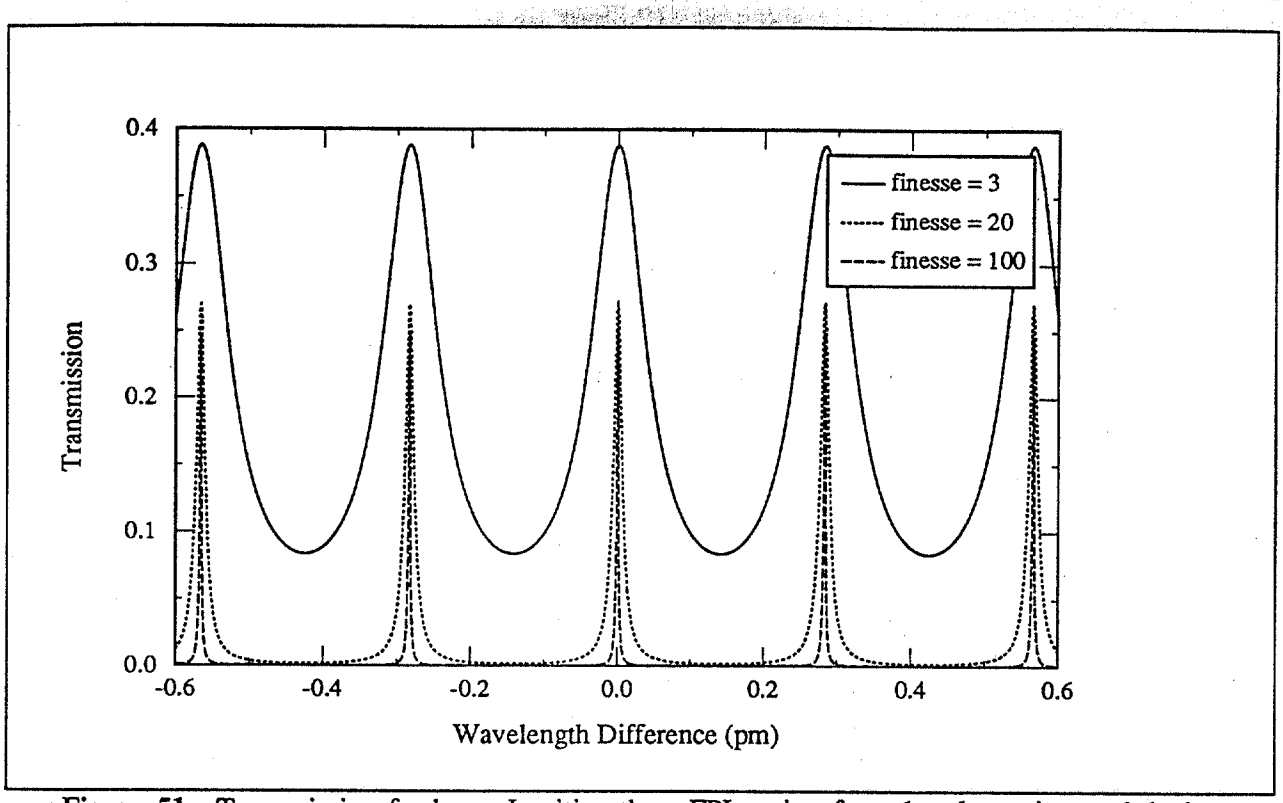

Figure 51 - Transmission for beam I exiting the c-FPI cavity, for a 1 m long air-speed device

It can be seen in Figure 51 that although the c-FP transmission cycles from a maximum to a minimum value with changing wavelength, it does not do so following a sine or cosine dependence; instead it follows a dependence termed an Airy function. When the finesse is low, then the transmission peaks are broad, the peak transmission is fairly large and the minimum transmission is also significant. When the finesse is large, then the transmission peaks are very sharp, the peak transmission is lower and the minimum transmission becomes virtually insignificant. In other words, the contrast (ratio between maximum and minimum transmission values) becomes larger as the finesse increases.

Note that the maximum transmission indicated from Figure 51 is only about 27%. This value is fairly low because we are dealing with only beam I from the cavity. If beams I and III are considered together, then the actual transmission becomes quite close to 50%. The other 50% of the incident light energy goes to beams II and IV. In practice, c-FP devices are often used in the transmission mode, where only beams I and III are monitored, since this generally provides the easiest packaging and access to the output beams. The LURSOT demonstration system employed such a c-FP device. Therefore, the use of a c-FP interferometer in the transmission mode automatically ensures that you will throw away 50% of your incident light, which is reflected back away from the input mirror M_1 in a divergent cone.

The design performance of the c-FP interferometer can be better characterized through the use of two other parameters, termed the free-spectral range (*FSR*) and the reflectivity finesse (N_R). These two parameters include the three design variables for a c-FP device: the radius of curvature of the mirrors (and their separation), the reflectivity of mirror M_1 and the reflectivity of mirror M_2. For this study we have considered only symmetric c-FP designs, where the reflectivity of both mirrors is equal. The two parameters *FSR* and N_R are defined as

$$FSR = \frac{1}{4 \mu e} \qquad (18\text{-}19)$$

$$N_R = \frac{\pi R}{[1 - R^2]}$$

where

FSR = wavenumber free spectral range for c-FP cavity
N_R = reflectivity finesse for c-FP cavity.

As previously discussed, a change in incident ray wavelength will cause the cF-P transmission to cycle between a maximum and minimum value. Successive transmission maxima are termed fringes. The free spectral range for a c-FP is defined as the difference in incident ray wavelength which tunes the device to the next fringe. In Figure 51, the *FSR* is about 0.0025 cm^{-1} (wavenumber units), or about 0.28 pm (wavelength units). In other words, successive transmission peaks are separated by about 1 part in four million with respect to the nominal design wavelength. This represents very high wavelength resolution, which is essential for the demodulation task in this application. The finesse, as discussed with regard to Figure 51, is a measure of the sharpness of the individual fringes. In mathematical terms, it is the ratio of the free spectral range to the fringe width at full-width-half-maximum (FWHM). The c-FP device from the LURSOT demonstration system had a cavity length of 1 m and a finesse of 10, so its spectral discrimination properties would be quite closely related to those of the middle curve in Figure 51, which represents a 1 m long c-FP with finesse of 20.

In Figure 51 a zero value of wavelength difference corresponds to one of the transmission peaks, meaning that the cavity has been tuned to provide a transmission peak for the design wavelength. The tuning is normally accomplished through small adjustments in the separation of the two end mirrors. As discussed elsewhere in this report, the c-FP interferometer for the LURSOT application will not be tuned to a transmission peak, but rather to the mid-point between maximum and minimum transmission, for the nominal probe laser wavelength. This point is termed the operating point for the device. It corresponds to an absolute transmission value near 25%, since the peak (beam I + beam III) transmission is about 50%. Changes in the wavelength incident on the c-FP device will then translate into changes in intensity output from the device, following the relationship shown by the curve in Figure 51.

At this point we have discussed axially related interferometer effects, but we have not considered spatial variations in the c-FP transmission which occur in the lateral directions, that is, in directions perpendicular to the optical axis. The previous theoretical analysis has no provision for these spatial variations, and thus it considers the transmission through a c-FP interferometer to be independent of lateral position. We know this is not the actual situation, since large diameter devices are not used. Therefore, some modifications to the previous simple model are necessary to describe more subtle optical properties of these devices.

Practical c-FP Device Response due to Optical Limitations

The preceding section has attempted to present the important theoretical concepts related to the use of a c-FP interferometer for this application. Taken within the limits of paraxial geometrical optics this discussion was perfectly valid, and the transmission of an actual c-FP device is quite close to the theoretical limit. However, the previous discussion does not discuss the limitations imposed by the assumption of paraxial geometrical optics. In this section we consider what these limitations are, and we place quantitative limits on the parameters which are affected by this assumption: maximum device diameter and maximum device acceptance angle. These quantitative limits also help us evaluate certain trade-offs which are encountered when a different c-FP cavity length, or a different operating wavelength, is considered.

From a flat oil-covered sea surface, the reflected probe laser beam at the aircraft position would be approximately the same size as that transmitted from the sensor towards the water surface, probably about 10 cm diameter at most. In this case a receiver of this aperture size would be sufficient to collect all of the reflected laser light, thus maximizing the detected signal. However, as we will show in Section 4, the nature of the sea surface under typical environmental conditions results in significant spreading of the laser beam as it is reflected from the sea surface. This would cause the reflected probe laser beam to over-fill a receiver with a 10 cm diameter entrance aperture, causing a loss of signal. To maximize the signal strength, then, we would like to utilize a receiver with a larger aperture diameter. It is at this point that we encounter the optical limitations of the c-FP (and other optical components) which have not yet been addressed.

The light-gathering capability of an optical device can be described most simply in terms of its étendue, which represents the maximum product of its entrance aperture diameter and its solid angle of acceptance. In order for the sensor receiver to make optimum use of its potential light gathering capability, the étendue of the c-FP interferometer must be matched to that of the receiver telescope. Thus, we encounter trade-offs in the acceptable size of our receiver optics. We would like a large diameter telescope in order to increase the light-gathering power of the receiver, and this necessitates a larger design for the c-FP device. On the other hand, we wish to package the receiver system in the smallest volume possible in order to facilitate airborne operation of the system, and we must consider the optical effects of aberrations present in the receiver optics.

The primary limitation on the étendue of a c-FP interferometer results from spherical aberration introduced by the two high reflectance mirrors which form the resonant cavity of the device. The spherical aberration causes rays which traverse the cavity not to become re-entrant unless they are paraxial (i.e., unless they follow shallow angle paths close to the optical axis of the device). Rays which are not re-entrant alter the delicate relationships for constructive and destructive interference which allow the cavity to function interferometrically. They cause mixing of the light from adjacent fringes, and thus reduce the demodulation capability of the device.

The spatial interference pattern of the c-FP interferometer, in the radial direction, can be determined by utilizing geometrical ray optics to trace the four-transit paths, and then utilizing the actual four-transit pathlengths in the equations presented previously instead of the pathlengths predicted by the simple theoretical model, which does not account for spherical aberration. We have referred to the radial direction, rather than the lateral direction mentioned in the previous section, since we will be making the (correct) assumption that the net optical properties of the c-FP are circularly symmetric with respect to its optical axis.

Vaughan[4] presents the four-transit pathlength in the following form:

$$l = 4(e + \epsilon) + \frac{\rho_1^2 \rho_2^2 \cos(2\theta)}{e^3} + \frac{2\epsilon(\rho_1^2 + \rho_2^2)}{e^2} \qquad (20)$$

where

l = four-transit pathlength
ϵ = c-FP offset from exact confocal spacing
ρ_1 = radius of ray intercept on mirror M_1
ρ_2 = radius of ray intercept on mirror M_2
θ = skew (twist) angle between intercept points.

The previous equation describes the actual four-transit pathlength for a real ray of arbitrary orientation which enters the c-FP cavity through the mirror M_1. This pathlength is shown to be dependent on the pathlength predicted by the simple theoretical model, $4(e+\epsilon)$, on the radius of the ray as it contacts the two mirrors, and on the skew angle through the cavity. Note that if one describes the position of points on both end mirrors in terms of their individual radius and azimuth angle values, then the skew angle is the difference in the azimuth angles for the two mirrors.

The equation above indicates that the four-transit pathlength is only approximately equal to the terms on the right hand side, because there are other higher-order spherical aberration terms which contribute to the four-transit pathlength, primarily for large radial distances. For the cases considered in our investigations, these other terms are negligible.

We can now replace the term $(4\mu e)$ in the expression for the exit beam intensity Equations 16a and 16b, with the expression above for the four-transit pathlength. This allows us to calculate, more realistically, the intensity transmitted through an air-spaced c-FP device for rays entering at any arbitrary point on the entrance mirror, and at an arbitrary angle.

Figure 52 illustrates the transmission of light through a c-FP interferometer, for rays at various distances from the optical axis. The design parameters of the c-FP for this example were selected to reflect those of the device used in the LURSOT demonstration system: cavity length 1 m, reflectivity finesse 10, nominal wavelength of the probe laser at 1.064 μm. The calculations were performed assuming that the 1.064 μm wavelength rays are incident parallel to the optical axis of the device, but at various radial distances from this axis. The curves shown in Figure 52 then indicate the transmission out of the device for these individual rays. In other words, for a collimated incident beam of constant unit intensity, the output beam would have a radial intensity pattern given by these curves.

[4] J.M. Vaughan, "The Fabry-Perot Interferometer: History, Theory, Practice and Applications", Adam Hilger Publishing, London, 1982.

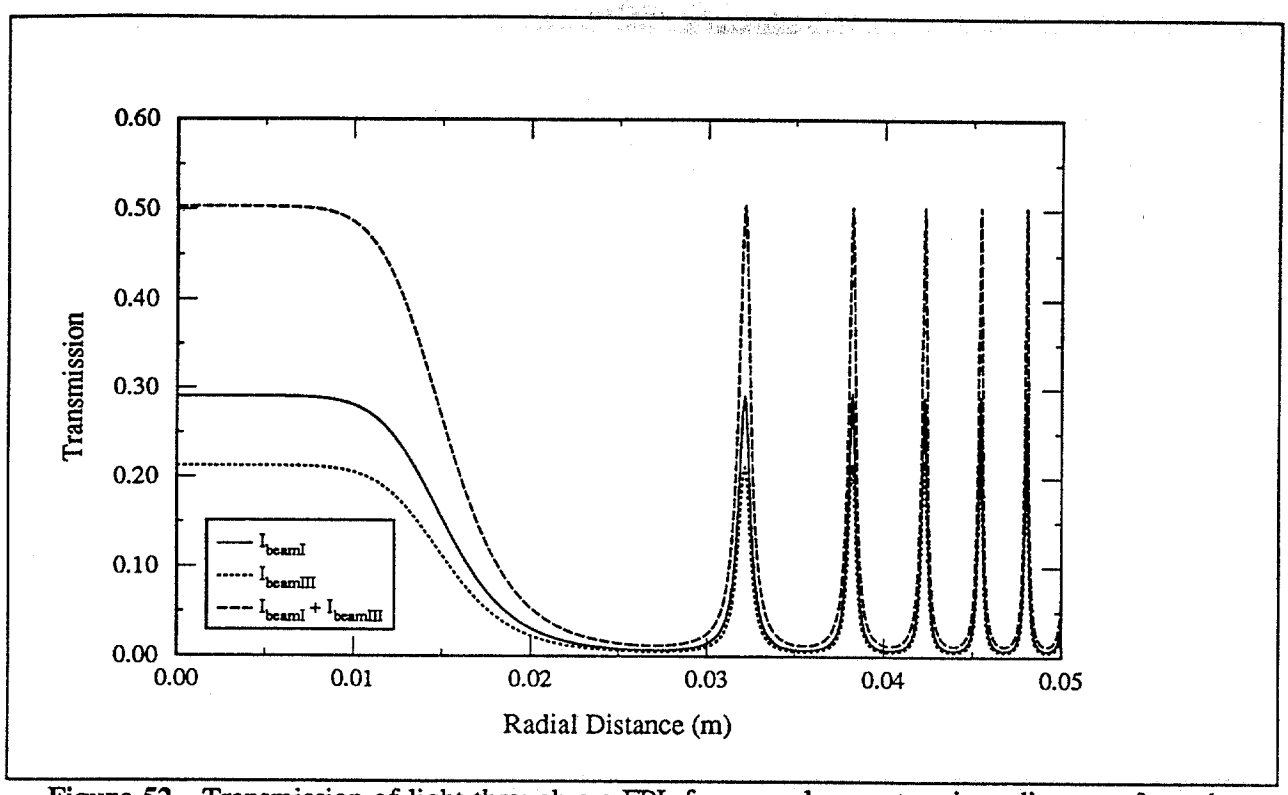

Figure 52 - Transmission of light through a c-FPI, for normal rays at various distances from the optical axis and for maximum transmission

Note also that the mirror spacing has been adjusted away from its exact confocal value, ***e***, by a small amount, ε, in order to tune the device for maximum transmission. For the c-FP design parameters listed above, and an incident light wavelength of 1.064 μm, this value is about -0.13 μm.

The solid curve from Figure 52 illustrates the transmission for beam I, the short dotted curve shows transmission for beam III, and the long dotted curve shows the transmission for the combination of beams I and III. As discussed earlier, the peak absolute transmission of the c-FP is about 50% for the two combined beams.

The nature of these curves is quite interesting. The transmission for both beams follows the same dependence. Between zero radial distance (i.e., at the optical axis of the c-FP device) and about 1.0 cm radius, the transmission is constant at its maximum value. It then decreases quickly with increasing radius, reaching a minimum near about 2.5 cm radius. This high transmission region is referred to as the primary disk of the device. Beyond 2.5 cm radius we see that there are regions where the transmission reaches its maximum in a small radial interval. These represent multiple rings, since the transmission is a maximum for a small radial distance, independent of the azimuthal angle. Five such rings are shown in Figure 52. It can also be seen that their thickness, as well as the radial distance between them, decreases with the outer rings.

We can now investigate what happens if we adjust the mirror spacing in order to tune the device for maximum transmission. If the mirror spacing is changed by about one wavelength, in either direction, then the c-FP transmission changes as indicated in Figure 53. In this case the primary disk disappears, but the rings do not!

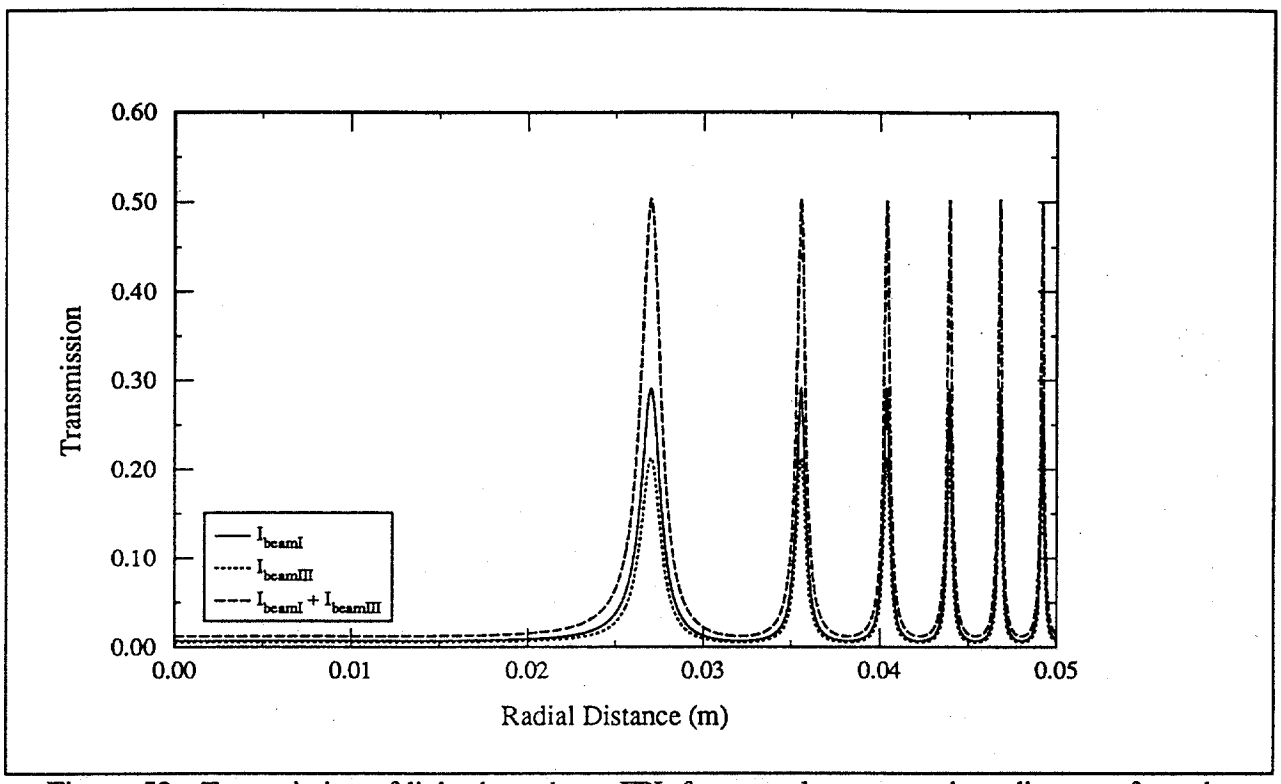

Figure 53 - Transmission of light through a c-FPI, for normal rays at various distances from the optical axis, and for minimum transmission

This is a graphic illustration of how spherical aberration limits the useable diameter of a c-FP interferometer. If the device diameter is chosen too large, then the discrimination or contrast in intensity, between minimum and maximum, is reduced. In the diagrams shown here this was accomplished by changing the mirror separation, but the same is true if the incident wavelength is changed. Therefore the demodulation capability of a c-FP interferometer is compromised if the device diameter exceeds a certain value. In this case, the highest contrast will be obtained if the c-FP diameter is kept below about 2.5 cm, or 1". Note that the c-FP used in the LURSOT demonstration system used 1" diameter mirrors.

We can also evaluate the effect of rays which enter the device at off-axis angles (i.e., rays which are not parallel to the optical axis) using the same analysis. In this case we again assume a fully collimated incident light beam, but which enters the c-FP device at an angle to its optical axis. We must be careful in how we specify the angle at which the beam enters the c-FP, however, because the tilt removes the symmetry of the output beam intensity: it is no longer circularly symmetric.

Assume that we choose the z-direction to represent the c-FP optical axis. Then we tilt the incoming beam in the x-direction by various small angles. We then look at the transmission in the radial direction of the cF-P interferometer, but at two specific azimuth angles: along the +ve x-axis (termed the parallel case) and along the +ve y-axis (termed the perpendicular case).

Figure 54 illustrates the results for the parallel case, in a fashion similar to that for Figures 52 and 53. Due to the complicated nature of the diagram, only the results for beam I will be shown, so the maximum transmission will not exceed about 28%. In addition, we have restricted the range of the radius variation so only the first ring is shown. The tilt angle between the incident light beam and the c-FP optical axis is varied between 0 and 70 mrad, in 10 mrad intervals. For zero tilt, the

transmission curve echoes that shown in Figure 52. As the tilt is increased, several things begin to happen to the transmission curve:

- The transmission in the central region of the primary disk decreases.
- The width of the primary disk increases
- The first ring becomes wider, and its position is shifted to a greater radius value.

When the tilt approaches 20 mrad, the primary disk actually begins to look like an annulus. As the tilt is increased further, the width and average radius of this annulus increase. When the tilt has reached about 30 mrad, the c-FP transmission is greatly reduced for rays at small distances from the c-FP optical axis. At 70 mrad tilt, extra rings are formed at small distances from the c-FP optical axis.

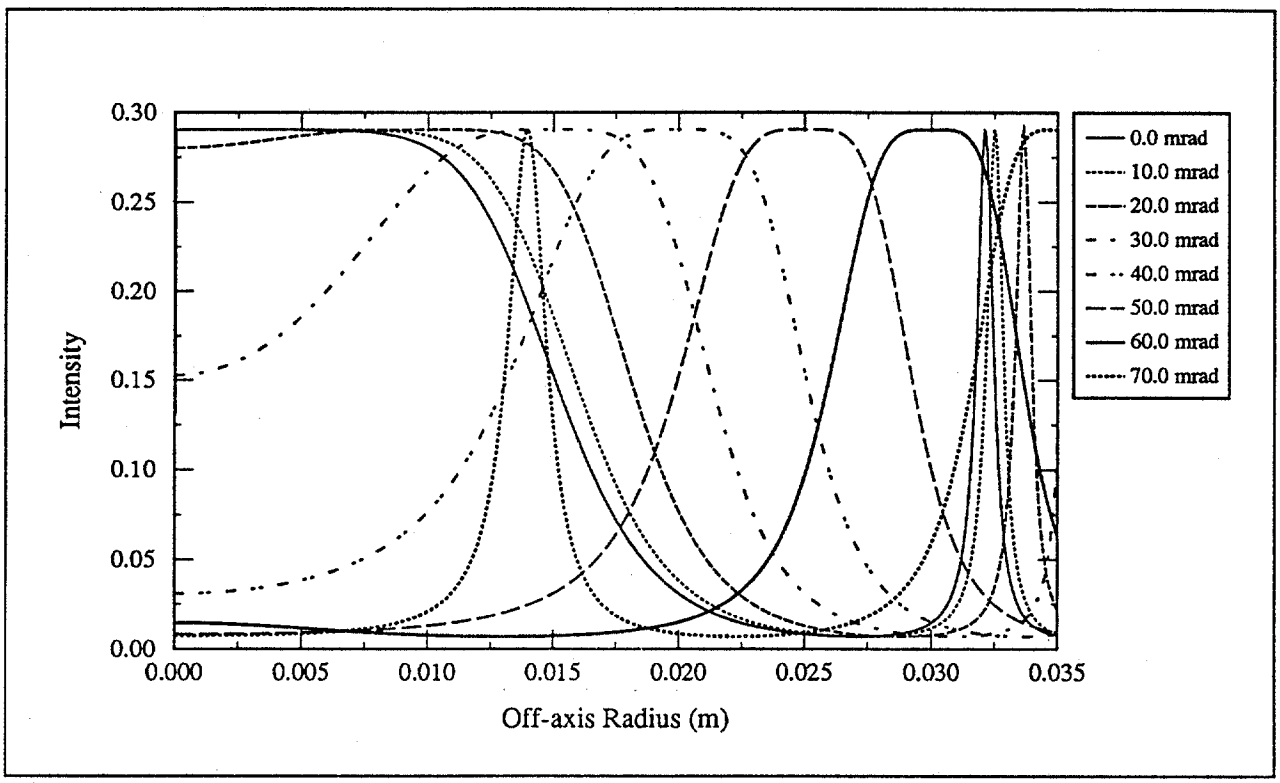

Figure 54 - Transmission of a tilted, collimated light beam through a c-FPI, viewed parallel to the tilt direction

Figure 55 illustrates a similar set of transmission curves for the perpendicular case. In this case the trends in the curves are somewhat different than for the parallel case, but the conclusions are the same: off-axis angles greater than about 10 mrad will significantly degrade the demodulation capability of the device, by distorting the intensity distribution of the output beam(s). The results in Figures 54 and 55 represent the situation where the c-FP device has been tuned for maximum transmission. Not shown are similar results for the case where the device is tuned for minimum transmission. It is also clear from these additional curves that very strange intensity distributions result when the off-axis (tilt) angles are increased.

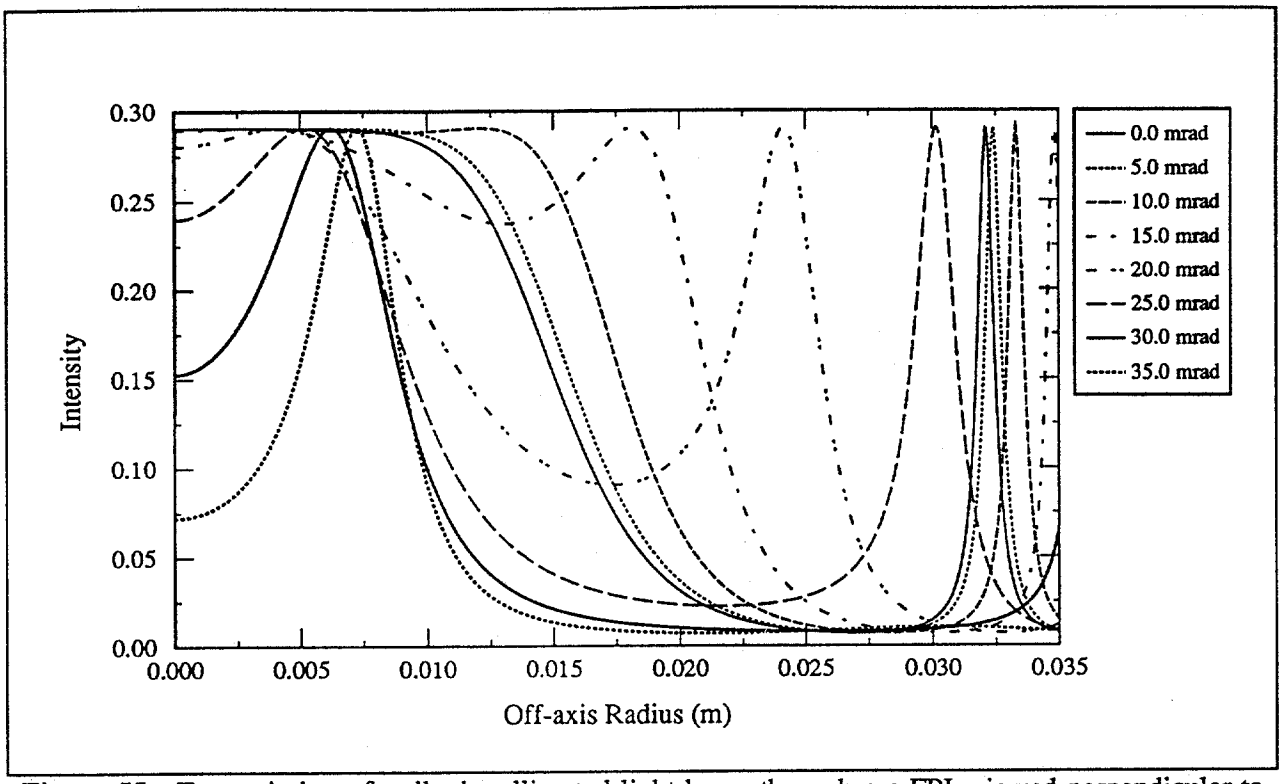

Figure 55 - Transmission of a tilted, collimated light beam through a c-FPI, viewed perpendicular to the tilt direction

In summary, we can state that practical limits for a 1 m long c-FP, intended for light of nominal wavelength 1.064 μm, are a 2.5 cm diameter and off-axis acceptance angles of not more than ~ 10 mrad.

Dimensional Considerations for c-FP Devices

The 1 m long c-FP utilized for the LURSOT demonstration system represents a rather unwieldy device which is heavy, large, hard to mount and hard to stabilize in an aircraft. The first three of these problems could be reduced by utilizing a shorter c-FP device. For this reason we have investigated the effect of different c-FP cavity lengths on the optical performance of the receiver system.

This investigation utilized much of the analysis we have discussed in the last section regarding practical c-FP response due to optical limitations. However, we have taken the methodology a step further. For this analysis we sum the contributions of beams I and III for each incident ray considered. Instead of considering light beams which are merely tilted with respect to the c-FP optical axis, we have simulated the actual situation more closely by treating the incident light beam as a quasi-collimated light source. That is, the net incident beam is assumed to consist of many collimated component beams, each with its own individual off-axis direction. We also considered the relative contribution (weight) of each component beam to decrease with increasing off-axis angle, following a Gaussian functional form. This would reflect the situation for an actual receiver, consisting of a c-FP interferometer linked to a telescope, which views an illuminated spot of Gaussian power density distribution from a large distance. As required, this simulates the actual viewing conditions quite closely.

Software was written which effectively convolved the components of the incident light beam with the appropriate transmission function for each one, in order to yield the output intensity profile. The overall transmission function is then calculated by ratioing the output and incident light intensity functions.

Figure 56 illustrates the results obtained by this technique for the case which closely relates to the LURSOT demonstration system: a 1 m c-FP interferometer of reflectivity finesse 10, illuminated with light at 1.064 μm wavelength. The data show how the effective transmission of the c-FP device changes as the diameter of the device is changed. The multiple curves show the effect of changing the rms acceptance angle which the c-FP interferometer sees. Note that we define the rms acceptance angle as the angle to which the weighting contribution has fallen to $1/e^2$ of its peak value. Curves designated by the term peak refer to those observed when the c-FP device is tuned for maximum transmission; those designated as min. correspond to tuning the device for minimum transmission.

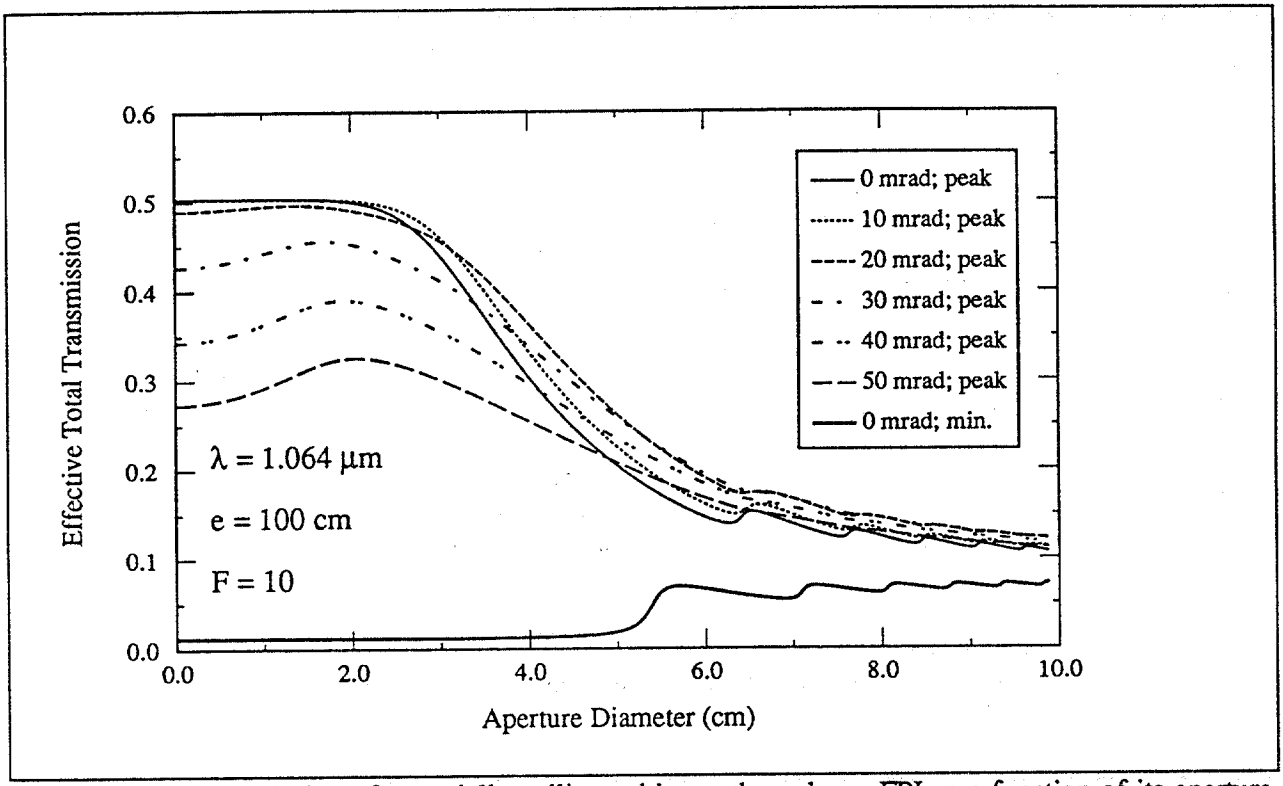

Figure 56 - Transmission of a partially collimated beam through a c-FPI as a function of its aperture diameter, for a 1 m cavity illuminated by 1.064 μm light

Note that we have changed the independent axis of this curve from radius to diameter, as compared to Figures 52 through 55. This is indicative of a critical difference in the meaning of the data. In Figures 52 through 55, the transmission was shown as a function of radial position. In other words, the transmission at a single point was shown, where the position of that point was allowed to vary. In Figure 56 the effective transmission for a device of a particular diameter is shown; this implies that we have integrated the transmission over all individual points which reside within that diameter. This is a subtle difference in terminology which represents a crucial difference in meaning.

There are several interesting points which can be made with regard to the results shown in Figure 56 for the 1 metre c-FPI:

- The effective transmission (when the device is tuned for maximum transmission) remains constant for device diameters up to about 2.5 cm, so the light-gathering power increases as the square of the diameter up to about 2.5 cm diameter, then levels off for larger diameters.
- The effective transmission (when the device is tuned for minimum transmission) remains constant for device diameters up to about 5.0 cm, so the light gathering power increases as the square of the diameter up to about 5 cm diameter.
- The greatest contrast is obtained when the diameter is not greater than about 2.5 cm.

In summary, the maximum useable device diameter for the 1 metre c-FPI appears to be about 2.5 cm, identical to the value indicated by the previous analysis. Increasing the diameter beyond this value will result in increased light-gathering capability, but decreased contrast. Thus, there is an optical performance trade-off with respect to the device diameter.

The maximum useable rms acceptance angle appears to be about 20 mrad. Increasing the rms acceptance angle beyond this value leads to both a reduction in light-gathering capability and a reduction in contrast. There is clearly no sensible optical performance trade-off with respect to the rms acceptance angle.

As discussed in Section 3.1.2 the optical bandwidth of the c-FP, which determines how sensitive the device will be to Doppler shifted laser light, is constant provided that the product of the cavity length and the reflectivity finesse of the device is constant. We also investigated the performance of a cF-P of 25 cm length and reflectivity finesse 40 (which has identical spectral bandwidth to the 1 metre cavity with reflectivity finesse 10) for use with light of 1.064 μm wavelength, to see how it compared with the larger device.

Figure 57 illustrates similar data to that shown in Figure 56, but corresponding to the shorter 25 cm device. It can be seen that the general character of the curves is similar to that shown in Figure 56. Both devices demonstrate a light-gathering capability, when tuned for maximum transmission, which increases quickly up to a certain diameter, and then levels off at greater diameters. Both devices also demonstrate reduced contrast beyond a certain diameter, and greatly reduced contrast when the rms acceptance angle exceeds a common threshold value.

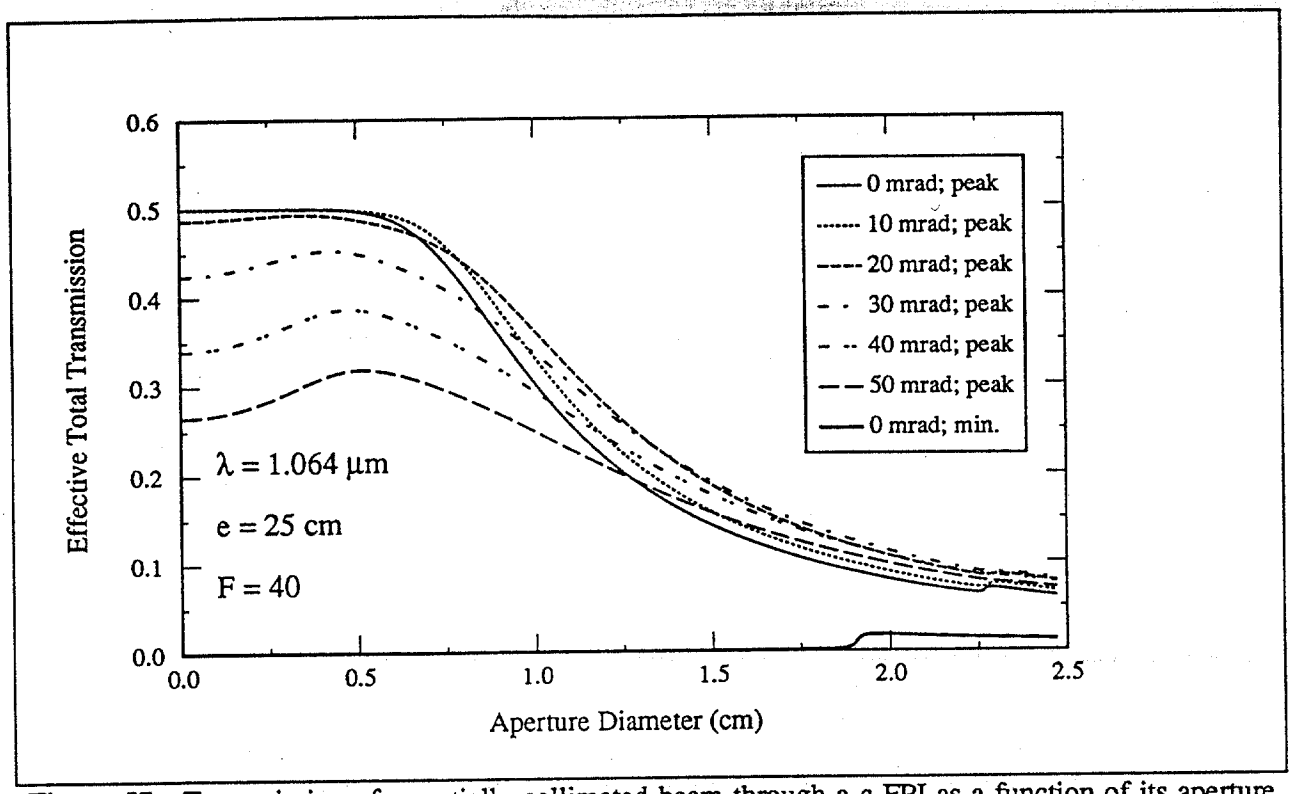

Figure 57 - Transmission of a partially collimated beam through a c-FPI as a function of its aperture diameter, for a 25 cm cavity illuminated by 1.064 μm light

The most striking differences between the shorter and longer cavities concern the absolute light-gathering capability. Both cavities demonstrate that about 20 mrad is the limit for rms acceptance angle. However, the longer cavity has a useable diameter up to 2.5 cm, while the useable diameter of the shorter cavity is only 0.7 cm, or about 30% of that for the longer cavity. This translates into a potential factor of ~ 12.5 increase in light-gathering capability for the longer cavity, which results in stronger laser-ultrasonic signals, which results in improved system performance.

One benefit of the shorter cavity, is a slight increase in contrast for smaller device diameters. This occurs primarily because of the low transmission of the shorter cavity when the device has been tuned for minimum transmission.

Incident Wavelength Considerations for c-FP Devices

Having investigated the effect of a different cavity length on the optical performance of the c-FP interferometer, we also wanted to study the effect of varying the nominal wavelength of the incident light. This would allow us to see if there were any potential benefits to be gained by changing the probe laser wavelength, solely from the perspective of the demodulation device.

We maintained the assumption of the shorter 25 cm cavity length, as done for the results shown in Figure 57. However, we also assumed that the nominal wavelength of the incident light was 1.65 μm. Figure 58 illustrates the results for these calculations. The results indicate that nearly all of the comments applicable to Figure 57 also apply here. This means that the 25 cm length c-FP device behaves almost identically to 1.064 and 1.65 μm incident light.

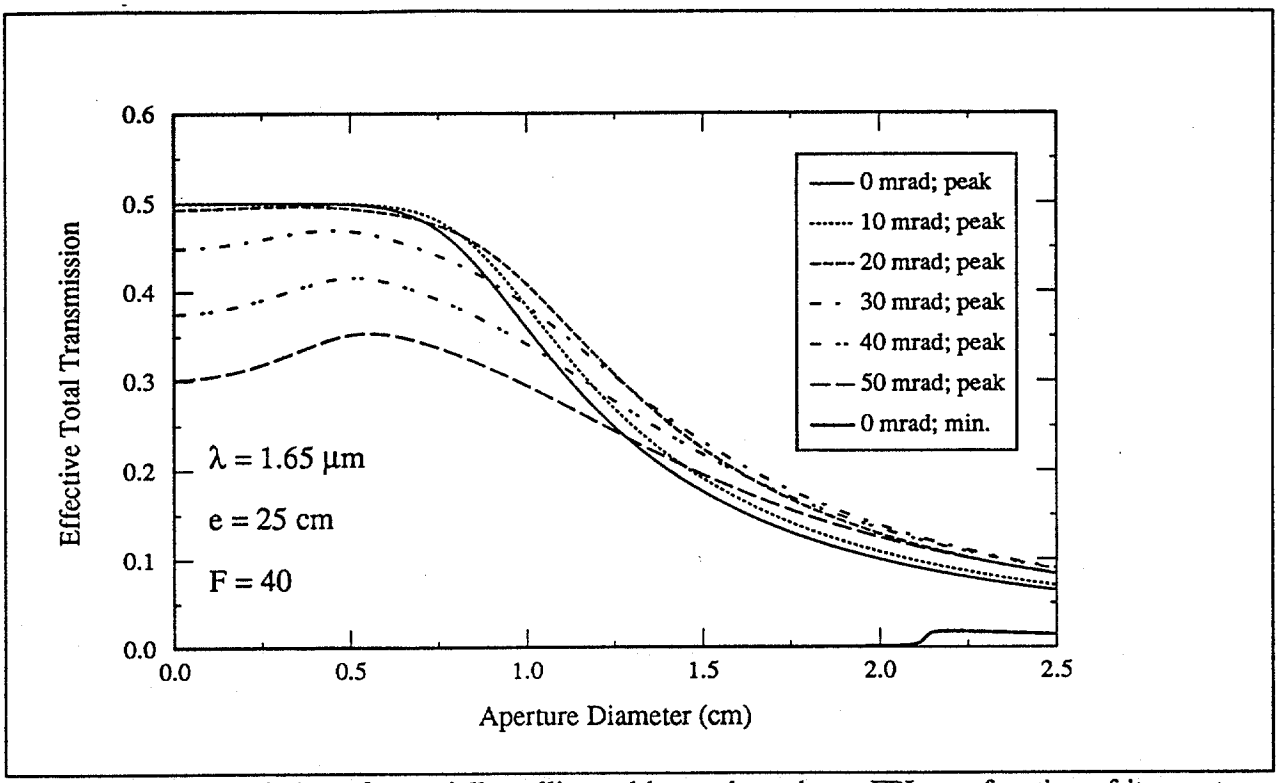

Figure 58 - Transmission of a partially collimated beam through a c-FPI as a function of its aperture diameter, for a 25 cm cavity illuminated by 1.65 μm light

The primary difference between the use of these two wavelengths is that the c-FP aperture diameter can be made somewhat larger (~ 10%) for the 1.65 μm wavelength, as compared to the 1.064 μm wavelength, without limiting the device optical performance.

Maximum Allowable Telescope Aperture Diameter

The restriction imposed by the optical limitations of the c-FP device, and the typical operating scenario for this application, act to impose a theoretical maximum size on the telescope aperture diameter.

We know from our other investigations that we want a probe laser spot on the sea surface which has a diameter of about 6 mm (depending on the specifications for both the probe and the generating lasers). For a nominal aircraft operating altitude of 100 m, this implies that light reflected into the telescope, from the edges of the laser spot, will have an off-axis angle of about 0.03 mrad relative to the sensor optical axis.

The conservation of étendue tells us that if the diameter of a beam is reduced by a certain amount, then the divergence of that beam (which is denoted by the off-axis angles of its rays) is increased by a similar amount. This means that if we can tolerate off-axis angles of magnitude ~ 20 mrad in the c-FP device, then the telescope diameter can be no larger than about (20/0.03 = 650) times greater than that of the c-FP diameter. This ratio is so large that it indicates there are no theoretical limits to telescope diameter, imposed by the usable diameter and useable acceptance angle of the c-FP device.

Conversely, packaging constraints within the aircraft dictate that the receiver telescope should not be significantly larger than the telescope used in the LURSOT demonstration system (20 cm diameter).

Furthermore, other optical aberrations within the telescope and transfer optics will cause distortion of the collimated light incident at the c-FP device, if too large a telescope aperture is utilized. Estimates of the maximum aperture size, and other parameters for the receiver optics layout, are beyond the scope of this feasibility study and must be performed as part of a detailed design process.

Total Optical Throughput

Keeping in mind the basic receiver optics configuration discussed previously, we can make some rather crude estimations of the total optical throughput for the receiver.

For a Newtonian telescope with only two reflective surfaces, we may have about 85% throughput for visible through near-IR wavelengths. Losses within the telescope are caused primarily by absorption at the metallic reflecting surfaces.

The collimating lenses can be anti-reflection coated to result in minimal optical losses; assume ~98% throughput.

The beamsplitter used to transmit the orientation-sensing optical signal to one photodetector, and the laser-ultrasonic optical signal to the c-FP interferometer, may transmit as little as ~ 40% or as much as ~ 95% to each channel, depending on the actual optical configuration (primarily if the splitting is merely wavelength discrimination, or an actual division of the incident intensity) chosen and the quality of the optics.

A narrowband interference filter should be used in conjunction with either of the two channels, in order to reduce solar background light levels from upwelling sky radiance as much as possible. These may transmit as little as 40% or as much as 60%, again depending on the actual optical design and execution.

As discussed earlier, the c-FP device will transmit a maximum of ~ 25% of the incident light when it is tuned to its operating point.

The focusing lens used to image the light from the beamsplitter (for the orientation-sensing channel) or the c-FP interferometer (for the laser-ultrasonic channel) can be anti-reflection coated to reduce losses; assume 98% transmission.

An optical fiber should be used to relay light between the main assembly of the receiver and the c-FPI collimating lens. This reduces the mechanical coupling between the sensitive c-FPI and the mechanically massive receiver assembly, thereby isolating the c-FPI to some extent. One should count on insertion losses on the order of 30%.

With these rather general calculations in mind, we find that the optical throughput for the orientation-sensing channel likely ranges between 13% and 45%. The laser-ultrasonic channel, at its operating point, likely has a throughput ranging between 2% and 8%.

3.4.3 SNR Calculations

The analyses for the determination of the LURSOT system performance essentially consist of two approaches: the specification of expected signal levels, and the calculation of SNR values applicable to these signal levels.

Signal Magnitude and SNR Models

The instantaneous laser power, reflected from the sea surface and then collected by the receiver telescope is given by a variation of the classic lidar equation for hard target reflectance,

$$P_s = P_0 \eta_t \eta_r \rho_0 \epsilon \exp [-2 \sigma_{ext} h] \quad (21)$$

where

P_s = signal power collected by the receiver
P_0 = instantaneous transmitted laser power
η_t = optical throughput for transmitter system
η_r = optical throughput for receiver system
ρ_0 = specular reflectance coefficient for sea surface
ϵ = optical loss factor for laser beam collection
σ_{ext} = atmospheric extinction coefficient
h = altitude of aircraft platform.

The optical loss factor from the equation above refers to the losses due to over-filling of the receiver telescope by the reflected laser beam. This over-filling is caused by curvature of the sea surface, and is dependent on many environmental parameters (see Section 4).

As well as backscattered laser light, the telescope receiver collects upwelling sky radiance which enters the telescope aperture within its FOV and spectral bandpass. Assuming that the sky radiance and telescope optical transmission can be regarded as constant within the spectral bandpass, the received power due to background sky radiance can be expressed as

$$P_b = \eta_r L_{sky} A_0 \Omega_r \Delta\lambda \quad (22)$$

where

P_b = optical power collected from background sources
η_r = optical throughput of receiver
L_{sky} = upwelling sky radiance (source strength)
A_0 = receiver entrance aperture area
Ω_r = receiver solid angle of acceptance
$\Delta\lambda$ = effective spectral bandwidth of receiver.

The effective spectral bandwidth of the receiver is a more complicated quantity to specify for this application, due to the comb-like transmission function of the c-FP interferometer. Likewise, the upwelling sky radiance may be a complicated parameter to specify, since it is quite dependent on environmental parameters and on the sensor viewing direction.

The optical power specified by the preceding two equations is assumed to be focused onto a suitable photodetector. The photodetector converts incident photons into an electrical current. The total current, comprised of contributions resulting from reflected laser light and collected sky radiance, that is generated in the detector output circuit can be expressed as

$$I_t = I_s + I_b = G\left[\frac{e_c \eta \lambda}{h_p c}\right](P_s + P_b) \tag{23}$$

where

I_t = total current developed in photodetector
I_s = photocurrent induced from signal power
I_b = photocurrent induced from background power
G = internal gain of photodetection circuit
e_c = electronic charge
η = quantum efficiency of photodetector
λ = wavelength of incident light
h_p = Planck's constant
c = speed of light.

The silicon avalanche photodiode (Si APD) and indium-gallium-arsenide avalanche photodiode (InGaAs APD) are important detector devices for, respectively, the 400 nm to 1.1 μm and 900 nm to 1.7 μm spectral regions since they represent the most sensitive practical photodetectors for these spectral regions. The SNR for these devices can be expressed by the following relations:

$$SNR = \frac{G_d R_d P_s}{\sqrt{I_a^2 + I_d^2}}$$

$$R_d = \left[\frac{e_c \eta \lambda}{h_p c}\right] \tag{24}$$

$$I_a^2 = \frac{\pi}{2} B i_{na}^2$$

$$I_d^2 = \pi e_c B\left(I_{ds} + F_d G_d^2\left[I_{db} + R_d(P_s + P_b)\right]\right)$$

where

SNR = signal-to-noise ratio for detector output
G_d = internal gain of photodetector
R_d = photodetector unity gain responsivity
I^2_a = noise component from amplifier
I^2_d = noise component from detector
F_d = photodetector excess noise factor
B = output circuit noise bandwidth
I_{ds} = photodetector surface dark current
I_{db} = photodetector bulk dark current
i_{na} = amplifier spectral noise current density.

Signal Magnitude and SNR Estimations

Using the signal magnitude and SNR models discussed in the previous section, we now wish to estimate signal magnitude and SNR values for a LURSOT-type sensor system.

To do this we require values for all of the input parameters defined in the signal magnitude and SNR models. Some of these parameter values are derived from a knowledge of commercially-available hardware, some from physical principles and some from well-established empirical relationships. Still others are the result of our own investigations, which are based in some cases upon experimental evidence which has been extrapolated from the study conditions to describe the current application. We must keep in mind the possible limitations of this process.

Since the optical channel which contains the c-FP interferometer has the lowest optical throughput, we will perform the signal magnitude and SNR calculations for it. Note that stability of the c-FP device must be assumed for these calculations.

We will make the following assumptions regarding the input parameters:

Parameters Required for Signal Power Estimation

- Probe laser instantaneous power is 10 mW
- Transmitter optical throughput is 90%
- Receiver optical throughput is either 2% or 8%
- Specular reflectance coefficient for sea surface is 3.3%
- Optical loss factor for beam collection is 1.6%
- Atmospheric extinction coefficient is 0.2 km^{-1}

Parameters Required for Background Power Estimation

- Upwelling sky radiance is 10 $W\text{-}m^{-2}\text{-}\mu m^{-1}\text{-}sr$
- Telescope entrance aperture diameter is 20 cm
- Telescope full-angle field of view (FOV) is 1.0 mrad
- Receiver spectral bandwidth is 0.2 nm

Parameters Required for SNR Estimation

- Electronic charge is 1.60×10^{-19} A-s
- Speed of light is 3.00×10^{8} m/s
- Planck's constant is 6.63×10^{-34} J-s
- Photodetector quantum efficiency is 30% (for 1.064 μm light)
- Photodetector current gain is 100
- Photodetector surface dark current is 40 nA
- Photodetector bulk dark current is 50 pA
- Amplifier spectral noise current density is 6.0 $pA\text{-}Hz^{-1/2}$
- Output circuit noise bandwidth is 50 MHz

The instantaneous probe laser power is essentially a lower limit for what is commercially-available with compact cw single-frequency sources (see laser discussion, Section 3.2.3). The transmitter optical throughput is a typical value for a multi-element beam expander which is anti-reflection coated for the particular output wavelength. The receiver optical throughput has been previously discussed.

The specular reflection coefficient for the sea surface represents an air-oil interface at which the laser beam is normally incident. This parameter typically varies between 2.5% and 4.0% for different oil types at different wavelengths, so we have assumed a median value.

The optical loss factor for beam collection actually represents the fraction of laser power collected by the receiver telescope with respect to the laser power which was reflected from the sea surface (see Section 4, Sea Surface Investigations). The value 1.6% is representative of an oil-covered surface whose radius of curvature is about 1.25 m, which our studies indicate may be expected for moderate wind speeds. However, this is the input parameter in which we have the lowest confidence for these calculations.

The atmospheric extinction coefficient is a typical value for about 10 km atmospheric visibility, at a wavelength of 1.064 μm. The value is actually estimated using the Koschmeider empirical relationship.

The value for upwelling sky radiance represents about 10% of the value of background sky radiance which would result from a sunlit cloud at this wavelength. This parameter is difficult to specify since the radiance is derived from many sources: reflection of skylight from the sea surface, multiple scattering within the atmosphere and upwelling radiance from the sea volume. The value we have assumed should probably be regarded as a conservative value, since the upwelling radiance is likely less than this.

However, we must also be careful with this parameter, since it merely specifies the strength of diffuse skylight. Sunlight glints, which are specular reflections from the sea surface, are also observed under certain conditions. The effective radiance of these glints may be many orders of magnitude greater than the diffuse value.

We have assumed a 20 cm diameter telescope for the receiver, which has a 1.0 mrad full-angle field of view. The diameter is thus the same as that of the telescope used for the LURSOT demonstration system. The telescope FOV is sufficient to allow full capture of the reflected laser light, since each point on the telescope entrance aperture will be capable of accepting light from a 10 cm diameter circle at the sea surface. The small telescope FOV also helps to reduce the background sky radiance which is collected by the telescope, and therefore will help make the receiver more immune to sun glints.

The narrowband interference filters are also used to reduce the intensity of the background skylight which is seen by the photodetectors. Without the use of such filters both channels of the receiver may be blinded by the background skylight which is especially intense in the visible spectral region. In addition, the combination of the narrowband interference filter and c-FP interferometer (in the demodulation channel) narrows the effective spectral bandwidth dramatically. The effective spectral bandwidth for this channel is approximately equal to the FWHM spectral bandwidth of the interference filter divided by the reflectivity finesse of the c-FP interferometer. For this case we have assumed a 2 nm interference filter and a reflectivity finesse of 10, yielding a 0.2 nm effective spectral bandwidth.

As mentioned earlier in this section, APDs are the detectors of choice in the 400 nm to μm spectral region where high sensitivity in a practical package are necessary. The Si APD can used up to about

1.1 μm, but has very low sensitivity at greater wavelengths. The InGaAs APD can be used at wavelengths between about 900 nm and 1.7 μm, although it has different characteristics than the Si APD.

For these SNR calculations, we have assumed the use of a Si APD to detect the 1.064 μm laser light. The device whose performance parameters are listed above is a commercially-available product with which Optech has had great success.

The output circuit for the detection electronics consists of the APD detector and a high bandwidth transimpedance amplifier. These elements essentially determine the SNR of the resultant signals. If needed, a low noise amplifier can also be used to boost the signal levels to aid in signal capture, without significantly affecting the calculated SNRs. The noise bandwidth for the transimpedance amplifier is 50 MHz, which implies that the detection circuitry can discriminate signal changes whose risetimes are as fast as 6 ns. This value was chosen as being appropriate for many of the surface displacement signatures which were studies for the oil surface displacement sensitivity analysis (see Section 2.2). The amplifier noise current spectral density is typical of these devices having such bandwidths.

Using these parameters we find that the instantaneous optical signal power onto the detector is about 91 nW if we assume the 2% receiver optical throughput, and about 0.37 μW if we assume the 8% receiver optical throughput. The background power is less than 1 pW for the low optical throughput case, and about 4 pW for the high optical throughput case. The relative magnitude of the signal and background power indicated by these results may indicate that the narrowband interference filters are not necessary. However, this is not true, since the filters also help to block the intense solar background light from the visible spectral region. They also allow some immunity of the system to the sun glints which would blind it without the filters.

The SNR calculations using the appropriate input parameters and the signal magnitudes given above result in SNR values of greater than 14 for the low optical throughput case, and greater than 30 for the high optical throughput case. In both cases the signals are signal-shot-noise-limited (neither the background shot noise nor the amplifier noise provides the dominant contribution).

Note that both of these values are calculated assuming that the signal is coming from the optical channel containing the c-FP interferometer, which has a smaller optical throughput than the orientation-sensing channel. The signal magnitude and SNR values for the orientation-sensing channel would thus be larger than the values indicated above.

We also wanted to assess the difficulty in signal detection if we were to use a 1.3 μm cw probe laser source instead of the 1.064 μm source. For the purposes of this calculation, we have assumed that the InGaAs APD detector sees equal signal and background powers as compared to the Si APD used for the previous calculations. In other words, we have merely simulated a change of detector, all other things being equal. The new parameter values which affect the SNR calculation are:

- Photodetector quantum efficiency is 75% (for 1.3 μm light)
- Photodetector current gain is 10
- Photodetector surface dark current is 100 nA
- Photodetector bulk dark current is 5 nA
- Amplifier spectral noise current density is 6.0 pA-$Hz^{-1/2}$
- Output circuit noise bandwidth is 50 MHz.

The results indicate an SNR of greater than 12 for the low optical throughput case, and greater than 40 for the high optical throughput case. These values are quite comparable to those calculated for the Si APD, even though the InGaAs APD characteristics are much different. The reason for this similar performance is that the InGaAs APD, while having a factor 10 less internal gain, also has a factor 2.5 greater quantum efficiency. The 1.064 μm wavelength actually falls on the long-wavelength tail of the Si APD responsivity curve, while the 1.3 μm wavelength is near the peak of the InGaAs APD responsivity curve.

The above results show that the performance of the receiver system, in both the orientation-sensing and demodulation capacities, should be adequate for the detection of the necessary signals. However, the methodology for processing the captured laser-ultrasonic signals has not been investigated sufficiently for us to draw any conclusions about whether these SNRs are adequate for this task. More work must be performed to determine the best methodology for processing these signals in order to derive information about the oil thickness.

Conclusions

Our investigations into the receiver configuration and performance lead us to state the following conclusions:

- The simple configuration for the receiver optics, discussed in Section 3.4.1, should provide sufficient performance to allow the detection of windows of opportunity (from the orientation-sensing channel of the receiver), and to allow the detection of laser-ultrasonic signals with good SNR.

- Not enough evidence exists for us to state what methodology should be utilized to process the laser-ultrasonic signals to derive oil thickness information, nor is there sufficient evidence for us to determine if the calculated SNR for the laser-ultrasonic signal is sufficient for this processing.

- The power levels attainable with commercially-available, compact, single-frequency cw laser sources seem to be of the right magnitude for this application. This will allow detection of laser-ultrasonic signals from oil surfaces of the correct orientation, but will not likely provide good signals when flying over normal wind-ruffled sea surfaces.

- Avalanche photodiode detectors should be utilized for both the orientation-sensing and laser-ultrasonic signal channels due to their better sensitivity than PIN photodiodes.

- The telescope aperture diameter is not limited by fundamental limitations of the c-FP interferometer. However, the need to package the receiver for airborne use and other optical distortion effects may act to limit its size. A 20 cm diameter telescope, as utilized in the LURSOT demonstration system, should be feasible, but a detailed design study must be performed to analyze all the trade-offs.

- The choice of a shorter c-FP interferometer necessitates decreasing its entrance aperture size to eliminate unwanted optical distortions. The use of such a smaller c-FP does not appear to place restrictions on the other receiver optical elements. However, of greater consequence will be the ability to stabilize a shorter cavity versus a longer one. This could not be evaluated in this feasibility study.

3.5 Time Delay Estimation Between Surface Pulse and Echo

The thickness of an oil layer on water is measured by first determining the time lag between the initial surface displacement and the echo displacement. Dividing the time lag by the acoustic velocity of oil yields an estimate of the thickness of the oil layer. Since the accuracy of the oil thickness measurement is limited by the uncertainty of the acoustic velocity of oil, it seems the estimation of the time lag between the initial surface displacement and the echo displacement is of less importance. However, the two pulses must be correctly identified and isolated before the cross-correlation technique can be applied to them. Incorrect identification of the two pulses can introduce larger error to the measurement of the oil thickness than the uncertainty of the acoustic velocity can. In this section, the time lag estimation using the cross-correlation technique is briefly discussed. Recommendations on this subject for the future development of LURSOT are outlined.

The time delay is determined by identifying the surface pulse and the echo within a window from the waveform of the detected c-FPI signal. It has been shown from the surface displacement model that the amplitude of the surface pulse is normally larger than that of the echo. Therefore, it would be more difficult to isolate the echo within a window when the SNR is low. Once the surface pulse and the echo are isolated, a simple cross-correlation technique is applied between the two signals to obtain an estimate of the time lag. It is well established that the error in the estimate of the time lag is inversely proportional to the bandwidth of the acoustic pulse and to the SNR of the two signals[5]. Generally, the cross-correlation technique provides a precise estimate of the time lag. Since the acoustic velocity of oil cannot be measured remotely, an assumed value is used. For the different types of oil and different environmental conditions, the variation of the acoustic velocity of oil can be as high as 25%. Therefore, the accuracy of the oil thickness measurement is limited by the uncertainty of the acoustic velocity of oil. Due to lack of time, we are unable to examine the performance of the cross-correlation technique in measuring the thickness of the oil layer in more details for various SNR expected under normal operations of the system.

Another issue which has not been addressed is how to identify and isolate the surface pulse and the echo pulse accurately. Although the accuracy of oil thickness measurement is not limited by the accuracy in estimating the time lag between the two pulse, this is only true if the two pulses can be correctly identified within a window. Therefore, the problem of selecting the window within which contains the surface pulse and the echo pulse should be treated more thoroughly. This is particularly important when measuring a very thin oil layer. It is recommended that more effort be spent in this area.

It has been suggested that a combination of linear filtering and deconvolution can be used to reduce the pulse length of the surface pulse and the echo to a series of spikes. However, the direct deconvolution technique requires *a priori* knowledge of a function which depends on the thermoelastic effect and the transmission response of the c-FPI. Blind deconvolution is a technique which does not require *a priori* knowledge of this function. The design of the deconvolution filter, also called the spiking filter, can also be obtained by optimizing various performance criteria. Simple quadratic filters have been used in seismic deconvolution and have shown very good performance against noise. Once

[5] C.H.Knapp and G.C.Carter, "The Generalized Correlation Method for Estimation of Time Delay", *IEEE Transactions on Acoustics, Speech, and Signal Processing*, Vol. ASSP-29, No.3, pp. 527-533, 1976.

the pulse length of the surface pulse and the echo is reduced, the task of identifying them would be more accurate. In fact, direct measurement of the time lag between the two spikes representing the surface pulse and the echo is possible.

The performance of the LURSOT system is also dependent on the accuracy in identifying the surface pulse and the echo from the output of the c-FPI. The techniques used to identify the two pulses need to be analyzed more rigorously in terms of the SNR. For the prototype system, it seems unclear how the two pulses were identified. It was uncertain whether the two pulses were identified manually by an operator or automatically by the computer. The optimal size of the window should also be investigated.

4.0 SEA SURFACE INVESTIGATIONS

In the course of the investigations into the effects of the sea surface on the laser-ultrasonic measurement technique, we have attempted to identify all of the critical parameters which are likely to adversely affect the technique, and to place some quantitative limits on their contributions. However, the number of unknowns involved, and the complicated nature of their interaction, lead us to believe that a significant, dedicated experimental investigation should be performed to remove some of the uncertainties and ambiguities before a second-generation system is developed. The reasons for our thinking thus will be discussed in detail in the following sections.

4.1 Background Considerations

The laser-ultrasonic technique assumes that the instrument and surface to be probed are stationary with respect to one another. This implies that there must be no spurious motion-induced Doppler effects to mask the desired interaction. The technique also relies on the reflection of the probe ("interrogation") beam back to the sensor receiver; thus, if the reflecting area is not oriented perpendicularly to the receiver optical axis, then there will be no measurable signal generated.

However, the ocean is not calm for nearly all conditions. Its surface changes both temporally and spatially in a complicated manner. Its surface roughness depends primarily on the current wind speed, but also on the time history of the weather conditions.

In addition, it is not easy to characterize the variations of its surface. The physics of its surface characteristics are very complicated due to the energy transfer between the wind and the water (or oil) volume. The naturally occurring water surface has been studied to a certain extent, but very little scientific literature is available concerning the surface dynamics and other optically-related properties of oil layers upon water. One fact is undisputed, however: oil on the surface of water tends to damp out the small-scale wave structure. This fact has implications for any experimental studies done regarding the LURSOT sensor development, since studies based on the characterization of normal sea surfaces may not be directly applicable to a typical LURSOT operational scenario.

One factor does work in the favour of studies undertaken to characterize the reflectance properties of the sea surface for this application. The air-water (or oil-water) interface at a particular point can be considered as a good specular surface, as long as there are no breaking waves. Therefore, the ocean surface can be confidently considered as a complicated, curved, tilted mirror-like surface so that geometrical optics can be utilized to predict the interaction between light and the air-water or air-oil interface.

For the LURSOT application, the nature of the ocean surface presents three different, but related, questions which must be answered before embarking on system development:

- What is the probability of observing a sea surface element which will directly reflect light from a sensor back to its receiver?
- How much de-focusing of an incident laser beam is incurred upon reflection by the sea surface?
- How important is the vertical motion of the sea to the highly motion-sensitive laser-ultrasonic technique?

The first of these questions relates to the statistical distribution of wave slopes. A sensor which is efficiently designed will couple as closely as possible to the wave slopes which appear with the greatest frequency.

The second of these questions relates to the curvature of the sea surface at the point of laser beam incidence. This is a problem quite unique to remote sensing of the sea surface using laser beams, since most applications involve a diverging laser beam (i.e., a large laser footprint on the sea surface, which "averages over" much of the fine-scale structure). For the LURSOT application we must focus the beam down to a small spot, which is of the same order as the fine-scale structure.

Elsewhere in this report, we have investigated the effects of aircraft vertical motion and vibration, and the effects of long-wavelength ocean swells, on the ability of the sensor system to measure laser-ultrasonic signals. Our studies show that "heaving" of the sea surface due to the passage of long-wavelength ocean swells may be sufficient to reduce the sensitivity of the demodulation technique, but time scales need to be considered. There will not be a problem if the passage of these swells also destroys the condition of perpendicularity to the sensor optical axis, since in this case the laser-ultrasonic signal would be interrupted and the measurement terminated. We also believe this effect is less likely to become a limiting factor for oil thickness measurements than either (1) or (2) from above.

We will address each of these questions in the following sections.

4.2 Physical Basis for Sea Surface Characteristics

For the "normal" sea surface, represented by an air-water interface, turbulent atmospheric winds deposit energy into the upper volume of the sea, and the interface becomes distorted due to this energy deposition. The amount of distortion, or surface movement, depends on the wind strength and on the ability of the water to dissipate the deposited energy.

Dissipation of the deposited energy occurs mainly due to the two restoring forces of gravity and surface tension. This gives rise to two different types of waves: gravity waves, whose primary restoring force is gravitational, and capillary waves, whose primary restoring force is surface tension.

Gravity waves form the basic character of the ocean surface, and are typically of longer wavelengths than capillary waves. They are the waves seen on the ocean surface when the wind has suddenly died down, and they give rise to the "rolling" nature of the sea surface. Gravity waves exhibit normal dispersion, since their propagation velocity increases with increasing wavelength.

Capillary waves, or "ripples", are the main mechanism by which energy is transmitted between the wind and the ocean. They also determine the fine scale roughness of ocean surface, and thus the reflection and refraction of light waves are primarily determined by the shape of capillary waves. Capillary waves can be seen commonly on lakes in the morning: a previously calm lake surface will suddenly show significant "ruffling" as the wind speed exceeds some threshold value. Capillary waves exhibit anomalous dispersion, since their propagation velocity decreases with increasing wavelength.

The boundary between the regimes of capillary waves and gravity waves is usually considered to be the boundary between normal and anomalous dispersion. At this point the wavelength is about 1.7 cm, and the propagation velocity is about 23 cm/s. At longer wavelengths, the velocity of the gravity

waves is greater than 23 cm/s; at shorter wavelengths, the velocity of the capillary waves is also greater than 23 cm/s.

Since the physical nature of gravity and capillary waves is so intrinsically different, it is not surprising that their presence (or absence) has such a profound effect on the fine-scale sea surface structure.

4.3 Review of Relevant Literature

The geometrical optics description for light interacting with the sea surface allows us to split the LURSOT detection problem into two essentially independent parts: How often does the surface become oriented normal to the beam direction, so that some laser light is reflected back to the sensor, and how much of the reflected light is broken up (and consequently not collected by the receiver telescope) due to the curvature of the water surface.

Every sea surface, for a given set of environmental conditions, will have an appropriate statistical formulation whereby its surface roughness can be described. Therefore for this application, we must deal in the realm of probability, rather than an area where macroscopic deterministic variables are employed, in order to characterize the important features of the sea surface. Unfortunately, the difficult part of the process involves obtaining the complete probabilistic formulation necessary to characterize the sea surface microstructure.

Some studies have been done on the microstructure of actual sea surfaces, but the majority of such investigations involve laboratory work. Laboratory studies are very useful to characterize the essential behaviour of the water surface under action by winds, but care must be taken in comparing their results directly to those determined from actual sea surfaces, for the following reasons:

- The fetch is different for the two cases. This is the effective distance along the water surface where the wind is allowed to interact with the surface. Obviously it is much shorter in the laboratory than in actual open ocean areas.
- Physical size constraints restrict the formation of rollers in the laboratory; long-wavelength swells that may develop over many kilometres of open ocean, and which may primarily provide a background sloping surface on which ride the many smaller-wavelength features.
- Allowing for the restricted fetch in the laboratory, it is even hard to get a uniform wind field across the surface of a wave tank.
- Care must be taken in the laboratory to ensure that waves generated in the downwind direction are not reflected from the tank end, and thereby allowed to cause significant interference with the primary wavefield.

Laser backscatter measurements from an ocean surface have been carried out for surface spot dimensions much larger than capillary wave wavelengths, as a function of off-nadir angle. Petrie[6] and Bufton *et al*[7] find that the backscatter energy decreases with angle and with increasing wind speed.

---

[6] K.J. Petrie, Laser Radar Reflectance of Chesapeake Bay Waters as Function of Wind Speed, IEEE Trans. on Geosci. Elect., GE-15(2): 87-96 (1977).

[7] J.L. Bufton, F.E. Hoge and R.N. Swift, Airborne Measurements of Laser Backscatter from the Ocean Surface, Appl. Opt., 22(7): 2603-2618 (1983).

The tilt of the gravity waves increases the backscatter variability more than does the density of specular surfaces (i.e., capillary wave facets) determined from the slope statistics. The measured results compare well with the theoretical treatments, including Bufton's calculation of the return signal from a given size footprint covering a particular slope distribution. However, the particular scenarios measured and modeled in these works are not directly applicable to the current application, since in both cases the laser beam spots at the sea surface were considerably larger than the capillary wave structure.

Wave Slope Statistics

The studies by Cox and Munk[8] on sea slope statistics, derived from photographs of ocean surface sunglint, form the basis for many subsequent models and experimental investigations. They analyzed data pertaining to both the normal sea surface, and to surfaces covered by artificial oil slicks. Their analysis was able to calculate the probability of occurrence for sea slopes as a function of wind speed. They found a near-Gaussian distribution of wave slopes over the range of windspeeds from 1 to 14 m/s. The ratio of upwind-to-crosswind mean square slopes was about 1.6 for normal sea surfaces, and about 1.0 for oil-covered surfaces. The mean square slope increased linearly with windspeed, in agreement with earlier work by Duntley[9]. They also found a small degree of skewness in the upwind distributions for normal sea surfaces; they were unable to determine whether the distribution was skewed for oil-covered water, due to limitations on the gathered data. There was no skewness in the crosswind direction. The following corrected results were obtained:

Table 8: Sea Surface Slope; Normal Surface, Upwind Direction

Wind Speed (m/s)	rms Slope (degrees)
1.0	3.2
2.0	4.5
3.0	5.6
5.0	7.2
10.0	10.1

[8] C. Cox and W. Munk, Measurement of the Roughness of the Sea Surface from Photographs of the Sun's Glitter, Journal of the Opt. Soc. of Amer., 44(11): 838-850 (1954).

[9] S.Q. Duntley, The Visibility of Submerged Objects, Part I, Optical Effects of Water Waves, Mass. Inst. Tech. Report, Dec. 15 1950 on U.S. Office of Naval Research Report NO N5.

Table 9: Sea Surface Slope; Oil-covered Surface, Upwind Direction

Wind Speed (m/s)	rms Slope (degrees)
1.0	1.6
2.0	2.3
3.0	2.8
5.0	3.6
10.0	5.0

The significance of these results can be summarized by the following comments:

- A Gaussian distribution of sea slopes indicates that the largest probability of occurrence for slope is a near-zero value, and the probability decreases quickly with increasing slope (either in the -ve or +ve direction, relative to the wind direction).
  The Gaussian distribution can be characterized by its mean square slope, which indicates the magnitude of the slope below which 67% of the data exists; the larger this value, the more frequently the wave slopes exist at higher values.

- It can be seen that the slopes for oil-covered water are considerably less, at all wind speeds, than those for the normal sea surface.

- The ratio of upwind-to-crosswind mean square slopes indicates whether there are larger slopes observed in the upwind direction than in the cross-wind direction. For normal sea surfaces the ratio is about 1.6, indicating that the water surface spends more time away from a level condition in the upwind direction. This may indicate that LURSOT-type measurements would be more productive if flown across-wind rather than upwind. In practice, however, the stability of the aircraft as flown in each of these directions must also be considered, as must the use of any gyro-stabilizing or pointing capability for the sensor viewing direction. For oil-covered surfaces, there seems to be little difference in which direction flights are flown, with respect to the wind direction.

- The linear dependence of the mean square slope on wind speed is as expected, since it implies that a lower wind speed results in a flatter ocean, which also implies a greater occurrence of the condition for perpendicularity.

- The skewness in the distributions implies that the maximum probability of occurrence does not occur for a zero slope; this might be an important consideration for an evaluation of whether gyro-stabilizing or active pointing might benefit the operation of the sensor. Cox and Munk observed that the degree of skewness increased with increasing wind speed.

In 1970, Wu[10] investigated the microstructure of the wind-disturbed water surface, using a laboratory-based wave tank. He used a conductivity probe for recording gravity wave heights, and an optical instrument for measuring the slope and curvature of the surface, on waves generated within a 1.5 x 1.5 x 14 m tank. The methodology used to obtain and evaluate the data resulted in a one-dimensional, rather than a two-dimensional, analysis of the surface wave characteristics. Wave height and wave slope measurements were taken for a range of wind speeds from less than 1 m/s to greater than 13 m/s.

It was found that the wave slopes for a particular wind speed were well represented by a Gaussian distribution with respect to angle. At medium wind velocities, the distributions are skewed so that the slope angle of maximum occurrence is positive (i.e., the vector normal to the water surface, on average, has a small component in the direction of the wind), but the distributions were not skewed at low or high wind speeds.

The standard deviation of the Gaussian slope distribution was also found to depend on wind speed. Up to about 2 m/s the standard deviation of the wave slopes is very small, meaning that the water surface is quite flat. Between about 2 m/s and 3.5 m/s (termed the "transition region"), the standard deviation of the wave slopes increases dramatically. This occurs because of the formation of capillary waves ("ripples"), whose appearance seems to be linked to some threshold wind speed where the wind changes from laminar to turbulent flow. The capillary waves are formed in order to facilitate energy exchange between the wind and the water surface. Above 5 m/s wind speed, the wave slope standard deviation increases slowly, and in fact appears to level off at a value near 17 degrees. Wave growth with wind speed ceases, and whitecaps begin to appear at most wave crests.

However, it should be noted here that while the trends in the data are applicable to both laboratory- and ocean-based studies, the absolute wind speeds corresponding to the different regimes are not. There is evidence to suggest that the formation of the capillary waves is likely to occur at higher wind speeds for actual sea surfaces, than for laboratory-generated surfaces.

By plotting the data, Wu was able to show that above the threshold point the standard deviation of the wave slope distributions essentially follows a logarithmic dependence on wind speed. Figure 59 illustrates the data calculated by Wu regarding the standard deviation of the surface slope as a function of (free-stream) wind velocity. Figure 59 also illustrates the average radius of surface curvature derived from these investigations, which will be referenced in the discussion of the next section.

[10] J. Wu, Slope and Curvature Distributions of Wind-disturbed Water Surface, Journal of the Opt. Soc. of Amer., 61(7): 852-858 (1971).

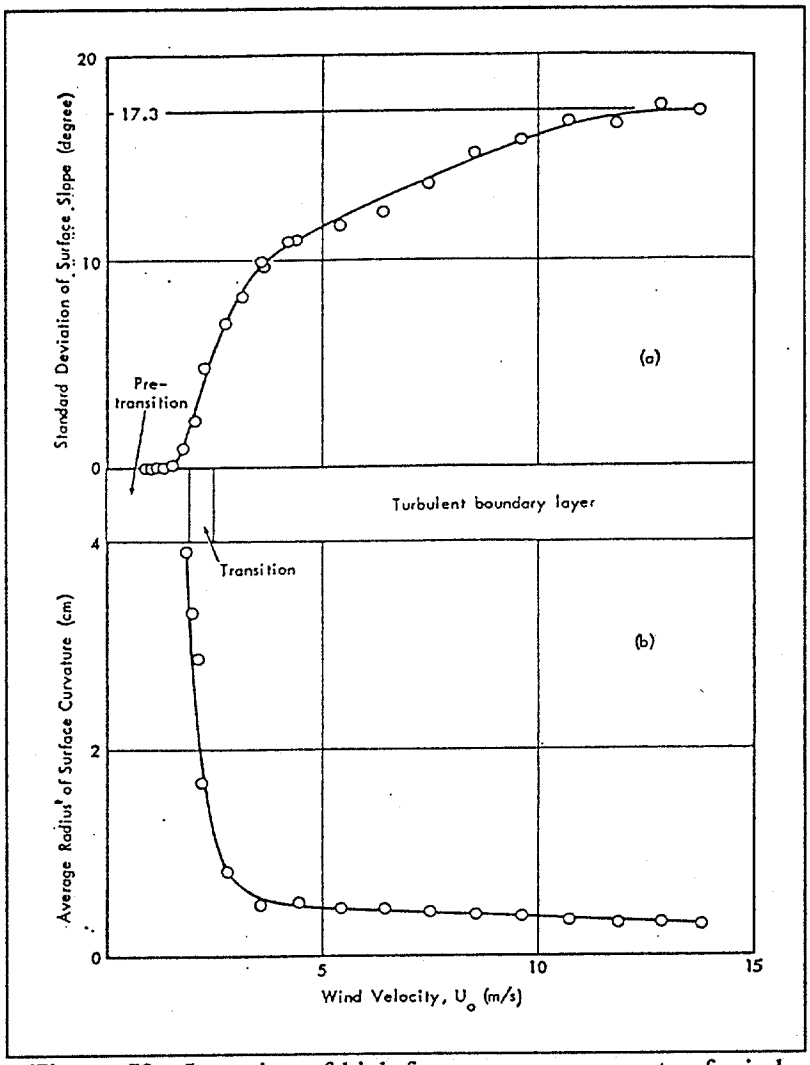

Figure 59 - Inception of high-frequency components of wind waves

Wu also performed a separate group of experiments to determine the source of the skewness in the wave slope distributions for medium wind speeds. He found that at these wind speeds the number of capillary waves present on the downwind faces of the basic (gravity) wave profile greatly outnumbered that on the upwind faces. It was this difference in the positioning of the capillary wave facets which was responsible for the skewness in the wave slope distributions. At higher wind velocities, the number of capillary waves on upwind and downwind faces of the basic wave profiles become more nearly equal, and the skewness decreases considerably. These results indicate that for the normal (i.e., non-oil-covered) sea surface, at medium wind speeds, a sensor would likely be better directed into the upwind faces of the basic wave profiles, in order to access a smaller fraction of capillary waves. This will reduce the detrimental effects of the capillary waves, manifest in a greater degree of surface curvature (see next section) and a higher wave slope standard deviation. However, it is not clear whether such an operational scenario would benefit a LURSOT-type sensor, since Wu's studies did not address the skewness for oil-covered water surfaces.

In additional work[11], where the statistics of actual wave slopes presented by Cox and Munk were re-analyzed, Wu was able to show that the logarithmic dependence of sea surface slope on wind velocity for laboratory data, also held for actual sea surface data. He also demonstrated that the wave slope statistics could be classified quite well according to whether the wind velocity was in the aerodynamically smooth or aerodynamically rough ("turbulent") regime. It was found that the sea surface slope increased with logarithmically-increasing wind velocity at a much slower rate in the aerodynamically smooth regime, than in the aerodynamically rough regime (see Figure 60, a reproduction from Wu's 1972 paper). Although there is some significant scatter in the data, particularly within the aerodynamically smooth regime, Wu argued that a double branch logarithmic curve properly fits these data. The data presented above, along with similar data representing wave slope statistics from oil-covered seas, convinced Wu that the grouping of the data into two classes was indicative of the very nature of the waves themselves: gravity or capillary. This association allowed Wu to proceed with a quantitative analysis of the sea surface characteristics which will be of benefit to this application, and which we will discuss below.

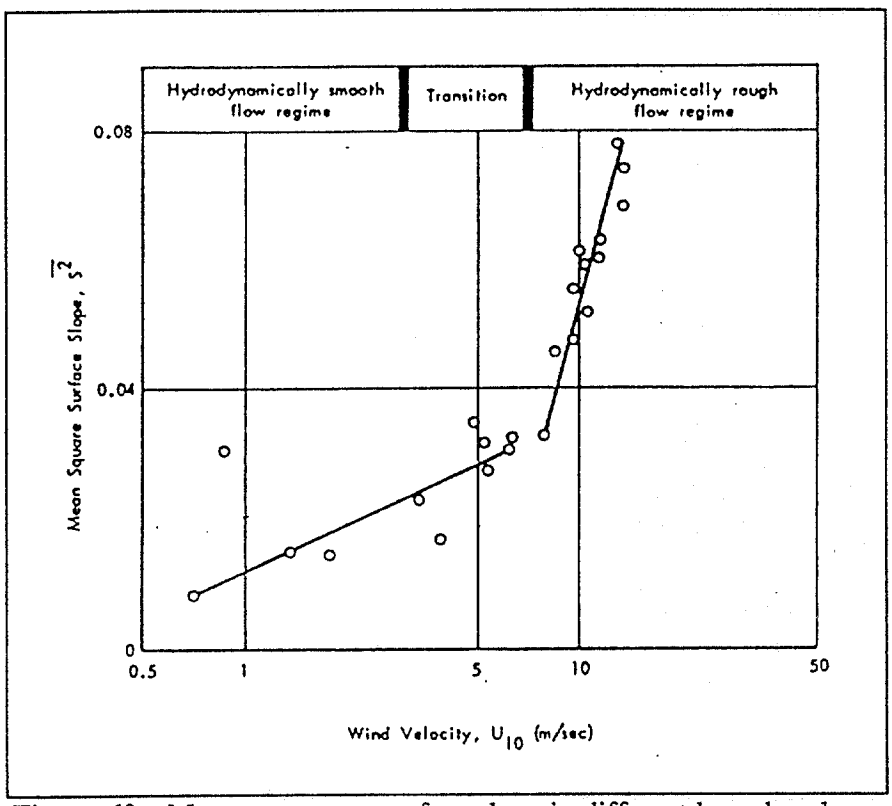

Figure 60 - Mean-square sea surface slope in different boundary-layer regimes of wind

[11] J. Wu, Sea-Surface Slope and Equilibrium Wind-Wave Spectra, The Physics of Fluids, 15(5): 741-747 (1972).

Cox[12] and Phillips[13] showed that the mean square slope of the sea surface can be expressed in terms of the ocean waveheight power spectral density (p.s.d.) function, as follows:

$$\overline{s^2} = \int k^2 \, \psi(k) \, dk$$

$$\begin{aligned} \overline{s^2} &= \textit{variance of sea surface slope} \\ k &= \textit{wavenumber of particular wave component} = \frac{2\pi}{\lambda} \\ \psi &= \textit{power spectral density function for waveheights} \\ \lambda &= \textit{wavelength of particular wave component} \end{aligned} \qquad (25)$$

The variance of the sea surface slope (the square of the rms slope) is then calculated from the integral of the square of the wavenumber times the waveheight power spectral density function, performed over all possible contributions of the wavenumber.

Phillips also proposed a very simple power spectral density function for the equilibrium range, where the growth of waves under the influence of the wind ceases. This power spectral density function would thus be applicable to higher wind speeds for gravity waves, and can be expressed as

$$\psi(k) = \frac{B}{k^3}, \qquad k_\delta > k > k_0 \qquad (26)$$

where

B = spectral coefficient to be determined
k_0 = wavenumber at the maximum of the p.s.d. function
k_0 = wavenumber at the gravity-capillary transition.

This formulation for the waveheight power spectral density function indicates that contributions for the sea surface waveheight decrease as the third power of the wavenumber, so short-wavelength wave components have little effect on the rms wave slope. The upper wavenumber limit represents the boundary between the regimes of capillary and gravity waves (see discussion earlier in this section), while the lower limit effectively represents the longest-wavelength wave components which can be supported on the sea surface, for a particular wind velocity. The Phillips power spectral density function has been supported by experimental investigations.

---

[12] C.S. Cox, Journal of Marine Research, 16: 241-256 (1958).

[13] O.M. Phillips, "The Dynamics of the Upper Ocean", Cambridge University Press, London, Chapter 4 (1966).

Wu and Phillips both have suggested that a similar power spectral density function may be applicable to the capillary wave regime, where a different spectral coefficient *B'* must be specified. In mathematical terms, the wave slope variance for the combined presence of gravity and capillary waves may then be expressed by

$$\overline{s^2} = B \int_{k_0}^{k_\delta} \frac{dk}{k} + B' \int_{k_\delta}^{k_\nu} \frac{dk}{k} \qquad (27)$$

where

B = spectral coefficient for gravity wave regime
B' = spectral coefficient for capillary wave regime
k_0 = wavenumber for gravity wave maximum
k_δ = wavenumber for gravity-capillary transition
k_ν = wavenumber for capillary wave maximum.

The upper wavenumber limit for the capillary wave regime is essentially the *neutrally stable wavenumber*, which represents the wavenumber at which energy input from the wind is balanced by energy dissipation due to viscosity. Thus, capillary waves of greater wavenumber (or smaller wavelength) do not exist on the sea surface. For sea water, this wavenumber limit ranges from about 12.6 cm^{-1} to 4.2 cm^{-1} depending on the wind speed. Thus, the short-wavelength limit ranges from about 1.5 cm (at low wind speeds) to about 0.5 cm or smaller (at high wind speeds). Interestingly, the transition point between gravity and capillary waves occurs for wavenumbers near 1.7 cm. This indicates that for lower wind speeds, the upper and lower limits of the second integral in the above equation become equal, and the contribution to rms wave slope from the capillary wave component disappears, as required to mirror the actual wave characteristics.

Given the two-component expression for the rms wave slope, Wu was able to utilize the data of Cox and Munk to evaluate the spectral coefficients *B* and *B'*. This was possible by making the assumption that the capillary wave component was not present for oil-covered seas, as supported by visual observations that indicated the absence of wavelengths less than about 30 cm. Thus, the wave slope distribution data observed for oil-covered seas was used to evaluate the constant *B* for the gravity wave component. It was found to be in good quantitative agreement with other previously-derived values. The wave slope distribution data for normal sea surfaces was then utilized to determine a value for the constant *B'*, for the capillary wave component. This process led to the specification of the following values for these constants:

$$B = 4.6 \times 10^{-3}$$
$$B' = 3.15 \times 10^{-2} \qquad (28)$$

The relative magnitude of these two constants confirms Wu's assertion that the capillary wave component becomes the dominant contributor to the wave slope standard deviation once the threshold wind speed for capillary wave formation has been reached.

The mathematical analysis related here will be augmented and discussed further in the next section relating to the wave curvature effects.

Surface Curvature Considerations

Wu also performed wave tank measurements to determine the radius of curvature of ripples. These measurements are important to the LURSOT problem, because they allow us to estimate the importance of sea surface curvature on the degradation of laser-ultrasonic signal strength.

Some degree of confusion exists with regard to studies of surface curvature because of the terminology utilized for its description. For our discussions, the radius of curvature represents the size of a sphere whose surface most closely matches that of the surface of interest. Thus, a large radius of curvature indicates a flatter surface, while a small radius of curvature indicates one which is highly curved. Alternatively we can refer to the degree of curvature (often abbreviated simply as the curvature) of a surface as a measure of how greatly curved the surface is. Numerically, it is equal to the reciprocal of the radius of curvature. Thus, a flat surface would have a small (degree of) curvature, while a highly curved surface would have a large (degree of) curvature.

The instrument used by Wu to measure the surface radius of curvature had a lower cut-off equal to 0.067 cm, and an upper cut-off equal to 4.0 cm. Occurrences of various wave curvature radii were counted, and statistics derived from this (see Figure 59 which illustrates the average radius of surface curvature as a function of the (free-stream) wind velocity). At the lowest wind speeds, there were few occurrences noted where the wave radius of curvature was smaller than the upper cut-off, 4.0 cm. For these low wind speeds the frequency of occurrence increased with increasing radius of curvature. Physically, this means that a flat surface is the norm, and deviations from flatness are rare.
As the wind speed approaches the threshold of capillary wave formation, the most probable radius of curvature remains close to the upper cut-off value (4.0 cm), but there are significant occurrences of radii down to the lower cut-off limit (0.067 cm). At about 2.8 m/s, near the mid-point of the transition region, the wave curvature probability distribution is nearly flat, meaning that all wave radii of curvature are equally likely. Above the transition region, the wave curvature probability distributions reverse their pre-transition trends. In this regime, the greatest probability occurs for wave radii of curvature near the lower cut-off limit (0.067 cm), and the probability becomes nearly zero for radii near the upper cut-off limit. This has the startling interpretation that for high wind speeds, where capillary waves are fully formed, virtually all of the wave structure has a radius of curvature less than 4.0 cm!

We can now appreciate the detrimental effects of a curved sea surface, if we remember that the interaction of laser light with it can be considered primarily as a specular reflection. A curved surface will act similarly to a spherical mirror of either concave or convex shape. A collimated beam of light incident at the surface will either become convergent (concave surface) or divergent (convex surface) upon reflection from it. The smaller the sea surface radius of curvature, the more strongly the beam will be made convergent or divergent.

For the LURSOT-type sensor, the incident laser beam is not completely collimated; it is slightly convergent in order to focus the laser spot at the sea surface, but the degree of convergence is so small that we can regard it simply as a collimated beam. This means that the reflected laser light will become divergent if reflected from a convex element of the sea surface, or convergent if reflected from a concave element.

Interestingly, the power density of the laser beam at the receiver after reflection from the curved sea surface is quite similar, independent of whether the sea surface element is of concave or convex shape. This effect seems in contradiction to experience, and hence a more detailed explanation is in order. A convex sea surface element will of course diverge a collimated beam upon reflection. A concave sea surface element will, on the other hand, cause a collimated beam to converge to a focus. After the

reflected rays are brought to a focus they subsequently begin to diverge. If the rays are collected at a large distance after the focus, then the power density will be quite low similar to the situation for light reflected from a convex surface. In fact, if the ratio of the sensor-to-sea-surface-distance and the surface-radius-of-curvature is large, then the received power density is insensitive to whether the curvature is concave or convex.

This is the situation for the LURSOT application. The nominal aircraft altitude is considered to be about 100 metres, while the sea surface radius of curvature for either normal or oil-covered seas is typically a small fraction of this value (see following discussions). The reflected laser beam is thus effectively diverging, as seen at the aircraft altitude, so a smaller fraction of it will be collected by the receiver telescope compared to that collected from a flat sea surface, resulting in a loss of signal strength. A more quantitative assessment of the amount of signal strength degradation is discussed in the following paragraphs.

We can take the analysis of the last section one step further, in order to derive certain quantitative information regarding the curvature of the sea surface. In agreement with the methodology for determining the rms wave slope, we can express the rms wave curvature as

$$\overline{c^2} = \int k^4 \, \psi(k) \, dk$$

$$\begin{aligned} \overline{c^2} &= \textit{variance of sea surface curvature} \\ k &= \textit{wavenumber of particular wave component} = \frac{2\pi}{\lambda} \\ \psi &= \textit{power spectral density function for waveheights} \\ \lambda &= \textit{wavelength of particular wave component} \end{aligned} \tag{29}$$

If we utilize the same formulation for the waveheight power spectral density function, then the wave curvature variance may be expressed by

$$\overline{c^2} = B \int_{k_0}^{k_s} k \cdot dk + B' \int_{k_s}^{k_v} k \cdot dk \tag{30}$$

where all parameters are as defined previously.

We must also remember that the radius of curvature of a surface is defined as the reciprocal of the (degree of) curvature. Therefore, the rms wave radius of curvature can be expressed as

$$R_c = \left[\overline{c^2} \right]^{-\frac{1}{2}} \tag{31}$$

where R_c is the rms radius of curvature of the sea surface.

If we utilize the formulae presented above, to determine the rms radius of curvature for the sea surface, then we obtain the results illustrated in Table 10.

Table 10: rms Radius of Curvature for Natural and Oil-Covered Sea Surface

Wind Speed (m/s)	rms Radius of Curvature (cm)	
	Natural Surface	Oil-covered Surface
0.8	n/a	340
1.0	n/a	160
7.75	5.7	125
8.0	4.1	125
9.0	2.2	125
10.0	1.6	125
11.0	1.2	125
12.0	1.0	125

The entries in Table 10 marked "n/a" indicate that the model does not yield results applicable for this regime.

The results shown in Table 10 are important for the following reasons:

- As also shown by the results of Wu's wave tank investigations (seen in Figure 60), the water surface radius of curvature experiences a rapid decrease beyond a certain wind speed, eventually levelling off at a certain asymptotic radius of curvature value.

- The asymptotic radius of curvature value is markedly different for the normal and oil-covered sea surfaces. In this case the radius of curvature is greater by a factor of more than 100 for the oil-covered surface, with respect to the normal surface. Note, however, that the absolute magnitudes of these curvature radii should be treated cautiously, due to the simplicity of the model and the inherent assumptions made for its application.

- Allowing for certain inaccuracies in the specification of the curvature radii, the levels of curvature indicated by the results above will lead to a substantial spreading of the reflected laser light, and hence a significant degradation of the laser backscatter power compared to that reflected from a flat water surface.

- The transition region (onset of capillary waves) for the normal sea surface, about 7.75 m/s, occurs at a significantly higher wind speed than that demonstrated for the laboratory water surface, about 2.0 m/s. As mentioned earlier, this is likely due to the difficulty in emulating all oceanic conditions within the laboratory.

We can utilize the calculated values for the rms wave radius of curvature to estimate the signal strength degradation due to the sea surface curvature. If we assume that the element of the sea surface from which the incident laser beam is reflected corresponds to a section of a sphere, then the fraction of laser power collected by the receiver telescope of the sensor can be approximated by

$$\epsilon = \left[\frac{d_{ap} R_c}{2 (h \pm \frac{R_c}{2}) d_s} \right]^2 \qquad (32)$$

where

ϵ = fraction of reflected laser power collected by receiver
d_{ap} = entrance aperture diameter of sensor receiver
R_c = radius of curvature of sea surface at incidence point
h = altitude of aircraft platform
d_s = spot diameter of laser beam at sea surface.

The fraction of laser power specified in the equation is the ratio of the reflected laser power which enters the sensor receiver to the total laser power reflected from the water surface. It can thus be regarded as the efficiency with which the reflected laser beam is collected by the sensor receiver.

This equation presumes a uniform power density distribution across the laser beam spot diameter, and hence a relatively uniform power density distribution at the altitude of the aircraft platform. This is sufficient for the purposes of this estimation, but probably represents a conservative calculation of the power returned to the sensor receiver. The choice of sign in the denominator is used to represent reflection from a concave (-ve sign) or convex (+ve sign) surface. As discussed earlier, the two variations of the formula yield virtually identical results when the aircraft altitude is significantly larger than the sea surface radius of curvature (i.e., $h >> R_c$).

Table 11 presents results obtained with the use of this equation to estimate the fraction of reflected laser power which is collected by the sensor receiver, for various sea surface curvature radii representing different environmental conditions. It was assumed that the altitude of the aircraft platform was 100 metres, the receiver entrance aperture diameter was 20 cm, the laser spot diameter at the water surface was 1.0 cm, and the sea surface reflection occurred at a wave trough (i.e., concave surface curvature).

Table 11: Fraction of Reflected Power Collected by Sensor Receiver

R_c (cm)	Fraction of Power Collected
0.4	1.6×10^{-7}
1.0	1.0×10^{-6}
6.0	9.0×10^{-6}
30	9.0×10^{-4}
125	0.016
340	0.12
1000	1.0

The results from Table 11 indicate several important ideas. As expected, the fraction of laser power collected by the sensor receiver increases as the sea surface radius of curvature increases; in effect, the divergence of the reflected laser beam is reduced, decreasing the beam diameter at the altitude of the aircraft platform.

The fraction of collected laser power varies from a low of ~ 1×10^{-7} for a 4.0 mm radius of curvature up to unity at 10 m radius of curvature. The 4.0 mm lower limit on radius of curvature probably represents the worst-case scenario for the normal (i.e., non-oil-covered) sea surface when capillary waves are fully formed. Taking into account the specular reflectance coefficient of ~ 2% from the water surface, we would thus expect about 3 nW of reflected laser power to be collected by the sensor receiver with a transmitted laser power of 1 W. This represents a tremendous loss of potential signal, and may indicate an additional reason why the LURSOT demonstration system had trouble collecting useable signal during actual flight tests. Even for the much larger 6.0 cm radius of curvature, which might be regarded as the upper limit for the presence of capillary waves, the collected laser power would be quite low.

In Table 11 the last four rows, for curvature radii ranging from 50 cm to 10 m, represent the regime where capillary waves have not been formed. This could result either from very calm conditions over the normal sea surface, or from the presence of oil upon it. The fraction of laser power collected varies from ~ 9×10^{-4} at the lower limit of curvature radius to unity at the upper limit. Given an average value of ~ 3.3% for the oil surface specular reflectance coefficient, this implies a minimum collected laser power of ~ 30 µW for a transmitted laser power of 1 W (without accounting for losses due to optical throughput in the sensor transceiver, or atmospheric transmission). Power levels of this magnitude are certainly detectable utilizing current receiver technology (see Section 3.4.3. regarding SNR Calculations), and hence the surface curvature for oil-covered seas does not appear to be a limiting factor for this application based on our interpretation of the sea surface effects.

Another point which deserves mention is whether there is any additional de-focusing due to the curvature induced at the water/oil surface by the thermoelastically-generated wave. With peak displacements of the order 0.1 µm, and spot diameters of the order 1 cm, we can expect induced curvature radii of the order 250 m. This value is about twice the nominal aircraft altitude, which means that we can expect some divergence of the laser beam beyond that from a flat surface, but the effects should be minimal. Furthermore, this effect will be totally masked, in almost all sensing conditions, due to the natural curvature of the sea surface caused by wind-generated waves.

Data Rate

At the outset of our investigations regarding sea surface effects, we fully expected that available data from the scientific literature, combined with knowledge of the system design and operational scenario, would allow us to derive some meaningful estimations of expected data rate using a relatively simple, straightforward analysis. This turned out not to be possible, due to a fundamental lack of critical information regarding the sea surface characteristics. The following section explains the methodology we pursued in our attempt to determine the data rate, and the reasons why this was not possible.

Before discussing the details of this process, it is important to define certain terminology which will be utilized later. The LURSOT sensor system is designed so that the pulsed generating laser is fired only when an accessible element of the sea surface is perpendicular to the sensor viewing direction. The statistical nature of the sea surface thus results in an aperiodic measurement cycle, that is, the events where the sea surface is aligned optimally with the sensor viewing direction come at irregular intervals. The expected data rate is then the reciprocal of the mean time between measurement events, and it must depend on the nature of the sea surface and how quickly the laser beams are swept over it.

The spatial and temporal variations in the sea surface are also responsible, along with the aircraft flight speed, for determining for how long the optimal alignment condition exists. This duration, termed the window of opportunity, places an upper limit on the time available to acquire the laser-ultrasonic wavefronts required for the oil thickness measurement. Conversely, this implies that there is an optimal aircraft flight speed, which satisfies the conflicting desires to fly slow so that laser-ultrasonic signals can be acquired for larger oil thicknesses, and to fly fast in order to increase the data rate.

If we know the wave slope probability distribution for the oceanic area of interest, then we can calculate the probability for optimal (i.e., perpendicular) alignment between a point on the ocean surface and the sensor viewing direction. This calculation is performed as follows, strictly for a nadir-pointing sensor:

$$P_{opt}(\theta_{rms},\theta_c) = \int_{-\theta_h}^{\theta_h} p(\theta_{rms},\theta_c;\theta')\, d\theta' \qquad (33)$$

where

P_{opt} = probability for optimum alignment
p = probability density distribution function
θ_{rms} = standard deviation of wave slope distribution
θ_c = wave slope value for distribution maximum
θ' = instantaneous wave slope value.

The equation presented above can be interpreted as follows. A given area of ocean will have a particular wave slope distribution function, which relates the probability per unit angle that a wave will be observed with a given slope. Therefore the actual probability for observing a wave element oriented "near-perpendicular" is the product of the probability density and the angular acceptance of the sensor receiver; if the acceptance angle of the sensor is large enough, or the wave slope probability distribution function is sharply peaked, then the process involves an integration, as shown in the formula above.

Both the wave slope probability density distribution function and the probability for optimal alignment are shown to be functions of the standard deviation (i.e., half-width) of the distribution function, and the location of the peak of the distribution function. Our survey of the scientific literature has shown that the standard deviation of the distribution function tends to increase logarithmically with wind speed, and the location of the peak of the distribution function is non-zero at medium wind speeds, thus indicating that these two parameters are dependent on the wind speed above the sea surface.

The limits on the integration are given by (again, strictly for a nadir-pointing sensor)

$$\theta_h = \tan^{-1}\left[\frac{d_{ap}}{2 \cdot h}\right] \tag{34}$$

where

h = altitude of aircraft
d_{ap} = entrance aperture diameter of sensor receiver
θ_h = half-angle of acceptance for sensor receiver.

The calculated probability value then indicates to us the expected fraction of time that we can expect optimal alignment between a single sea surface element and the (nadir-pointed) sensor viewing direction. In other words, the fraction of observation time for a fixed point in space. If we make the simplistic assumption that the sea surface demonstrates the same characteristics at different points in space, as well as at different times, then the calculated probability value will also tell us the expected fraction of flightline flown over which we observe optimal alignment, at a fixed time. In other words, if we could freeze time and then fly over the sea surface with a nadir-pointing sensor, the calculated value would indicate during what fraction of our flightline optimal alignment was expected.

The problem with the calculation of this value is that it tells us nothing about the data rate. The value gives us a flightline fraction during which we expect optimal alignment, but does not tell us an expected number of events for this alignment (or, similarly, the mean length of flightline during which a single event occurs). The result is a situation where one wants to solve one equation for two unknowns: any results will be meaningless unless ancillary data are supplied.

To properly evaluate the expected data rate of a LURSOT-type system, one must accurately specify the power spectral density distribution function for the waveheights (note that the Pierson spectrum referred to in our discussion of sea surface curvature, is one such theoretical distribution function) as a function of typical environmental conditions. A complicated mathematical modeling procedure, based on the generation of pseudo-random surfaces with known power spectra[14] must then be implemented in order to derive the desired data rate. We did not pursue this route since it would have required a considerable expenditure of the resources for this feasibility study, and the final results might depend critically on the accuracy with which we specified the sea surface microstructure, information whose accuracy, or lack of it, we cannot predict.

An alternative to modeling of the sea surface microstructure requires a detailed experimental investigation on natural waterbodies, rather than surfaces simulated in wave tanks. The literature survey we have performed indicates quite clearly that the water surface microstructure is different for natural and simulated sources. Since the relative success or failure of the remote laser-ultrasonic

[14] J.A. Borrego and M.A. Machado, Optical Analysis of a Simulated Image of the Sea Surface, Appl. Opt., 24(7): 1064-1072 (1985).

technique depends so critically on the true character of the water surface, we highly recommend that such a study be performed only outside the laboratory.

4.4 Conclusions

The survey of the scientific literature which we have performed, augmented by calculations of our own which are relevant for this application, have led us to certain conclusions regarding the effect of the sea surface on the laser-ultrasonic technique for oil measurements. These conclusions can be summarized as follows:

- Wu's results (see Figure 59) indicate that, except at a minimal wind speed, wave slope probability distributions with standard deviations greater than a few degrees are common, with greater standard deviations for increasing wind speeds. Thus, we expect a decreasing probability of achieving optimal alignment for higher wind speeds.

- Exactly how these results translate into an expected data rate is unclear. However, it seems clear to say that the data rate must depend on the following (for a non-scanning, nadir-pointing system):
  - Type of surface (normal or oil-covered)
  - Environmental conditions (primarily wind speed)
  - Sensor acceptance angle
  - Sensor platform altitude
  - Sensor platform flight speed.

- The presence of oil dampens out capillary wave action, to some degree, which allows a greater probability of optimal alignment than without oil. This manifests itself as a decrease in the standard deviation of the wave slope distribution.

- At medium wind speeds we expect an asymmetry of the slope distributions by up to several degrees. Since the system must be capable of operating in such conditions, it thus becomes advisable to design it with some form of alignment compensation capable of altering the sensor viewing direction by several degrees relative to nadir. This is to be considered as an additional requirement which is separate from any need to compensate the sensor viewing direction due to pitch and roll of the aircraft.

- Active scanning ("dithering") of the sensor viewing direction at angles close to nadir, in order to increase the probability of achieving optimal alignment and hence to increase the data rate, is a complex issue which we feel is impossible to model with any degree of reliability. Perhaps a more conclusive test of the benefits of such a technique could be realized through some specific experimental investigations (see Section 6, Conclusions and Recommendations).

- Curvature of the sea surface is likely to impose the following restrictions on the laser-ultrasonic technique for oil thickness measurement:
  - A significant restriction on the instantaneous output power necessary for the probe laser, since it will result in a diverging reflected beam. Given the radii of curvature estimated earlier in this section, it is quite likely that the reflected probe laser light from a normal, oil-free, wavy sea surface will be below the detection threshold of the sensor system. The extremely small curvature radii will result in a strongly diverging beam, and the power collected by the sensor receiver will be a very low fraction of the

total reflection. The much larger curvature radii from the oil-covered sea surface will still result in a lower signal power collected by the sensor receiver (as compared to a flat oil-covered surface), but it will be considerably greater than that from the oil-free water surface under typical wind conditions.

- A minimal problem for the generating laser, since we are interested only in transmitting the maximum fraction of laser light through the air-oil interface into the oil layer below. In fact, this will be a problem only in the sense that surface curvature may redirect the laser energy within the oil layer, thus altering the elastic wave generation to create propagation which is not completely normal to the sensor viewing direction. The net effect would likely be a slight decrease in the laser-ultrasonic generation efficiency.
- Insufficient reliable data exist for us to perform a meaningful analysis of the expected data rate for the sensor system, leaving us with two alternatives to characterize this parameter: perform detailed investigations utilizing modeling or experimental techniques. Modeling investigations have the disadvantage that they create much greater logistical problems, but they allow the study of actual measurement scenarios, and may be expected to produce results with less uncertainty.

5.0 LASER-ULTRASONIC TECHNIQUE SENSITIVITY ANALYSIS

The thermoelastic displacement of the oil surface is detected by a probe laser beam whose frequency is Doppler shifted due to the motion of the oil surface. The frequency of the probe laser beam can be demodulated by a c-FPI. The design and operation of the c-FPI is to lock the frequency of the transmitting probe laser at the 50% transmission response at which the c-FPI has good frequency discriminating capability. The Doppler-shifted frequency of the backscattered probe laser translates into intensity variations at the output of the c-FPI.

The amount of Doppler frequency induced on the probe laser beam is linearly proportional to the instantaneous velocity of the target. Therefore, demodulation of the probe laser beam is sensitive to the instantaneous velocity of the relative motion of the sensor and the target during the measurement periods. These sources of relative motion include the laser induced ultrasonic waves in the oil layer, which are the signals of interest, the sea wave motion and the aircraft motion. The effect of the vertical velocity of the aircraft and the vibrations inside the aircraft on the laser-ultrasonic detection must be fully evaluated. Another critical impact of the mechanical and acoustical vibrations within the aircraft is the maintenance of the separation of the two concave mirrors of the c-FPI. For successful operation of the c-FPI, the mirror separation must be accurately maintained to within a few hundredths of the probe laser wavelength. In this section, we report on the results of our investigations into the effect of aircraft vertical motion and vibration on the detection of the oil surface motion.

5.1 Sensitivity to Aircraft Vertical Motion

Numerical calculations of the output of the c-FPI were used to investigate the effect of the motion of the aircraft. The thermoelastic displacement of the oil surface was calculated using the IMI software and stored in an ASCII file. A computer program was written to model the effect of the vertical velocity and random vibrational motion of the aircraft. The power spectrum of the random vibrations of a typical aircraft from the RTCA/DO-160B document was used for the modeling. The relative motion between the sensor and the oil surface due to the aircraft motion was added to the true surface displacement. The resulting displacement was then fed to the model that implements the signal demodulation by a c-FPI.

Figure 61 shows the output of the c-FPI for various vertical velocities of the aircraft. The centre curve is the output of the c-FPI if the aircraft does not have any vertical motion during the measurement period. As the aircraft begins to have significant vertical velocity, the dc intensity at the output of the c-FPI is changed. But, more significantly, the magnitudes of the surface pulse and the echo are generally reduced depending on the magnitude of the vertical velocity. For a c-FPI with a bandwidth of 7.49481 MHz, a vertical velocity of -1.9861 m/s induces a Doppler frequency shift of half of the bandwidth of the c-FPI for the probe laser at the wavelength of 1.06 μm. As a result, the operating point at the transmission response of the c-FPI is shifted to the peak of the transmission response, at which the sensitivity of demodulation is poor.

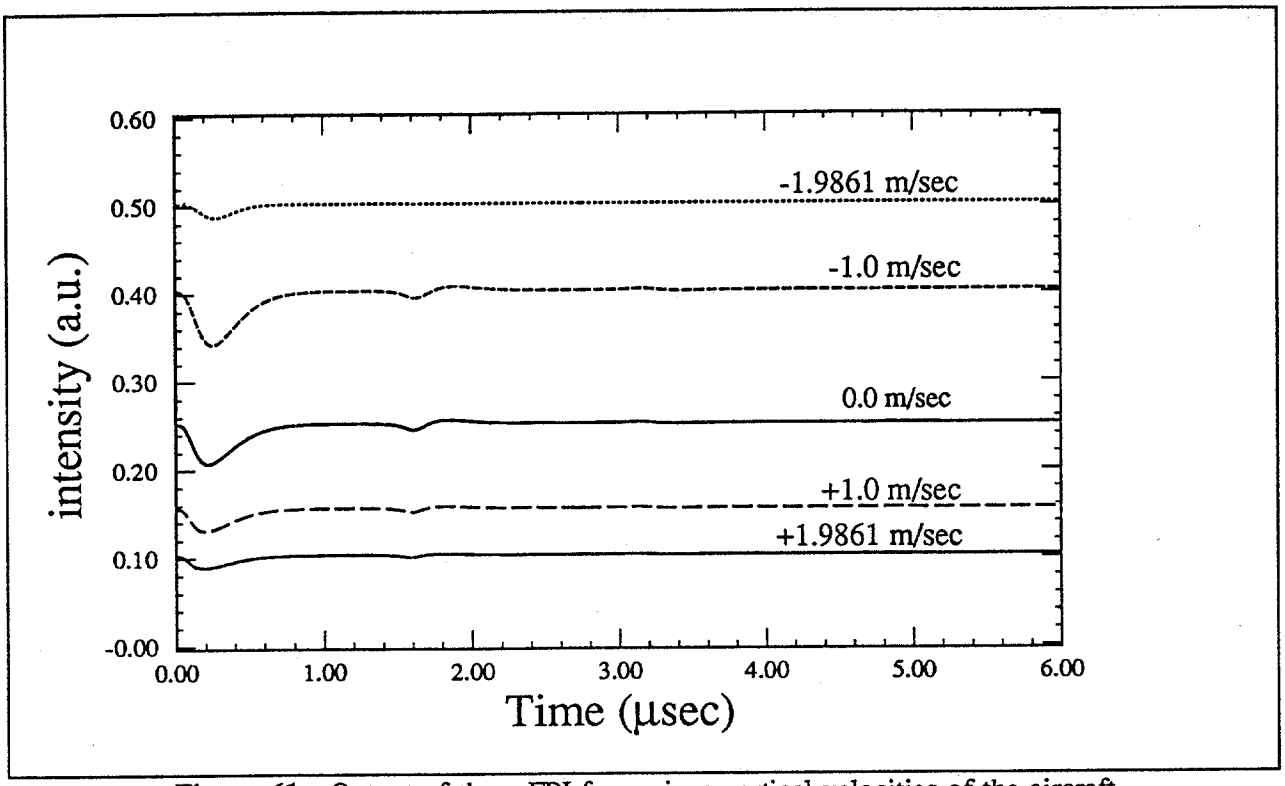

Figure 61 - Output of the c-FPI for various vertical velocities of the aircraft

5.2 Sensitivity to Aircraft Vibration

The effect of sinusoidal vibrations within the aircraft on the output of the c-FPI is demonstrated in Figure 62 and Figure 63 for low and high frequency vibrations. It can be seen that for high frequency vibrations, even a small amplitude of 0.005 μm will have a detrimental effect on the output of the c-FPI due to the large instantaneous vertical velocity. For low frequency vibrations, the motion of the aircraft can be considered as having constant velocity during the measurement period. Since the measurement periods are typically 10 μs to 50 μs, these are relatively short periods for the aircraft to have any drastic changes in motion. Hence, the vertical velocity distribution of a typical aircraft is of more concern.

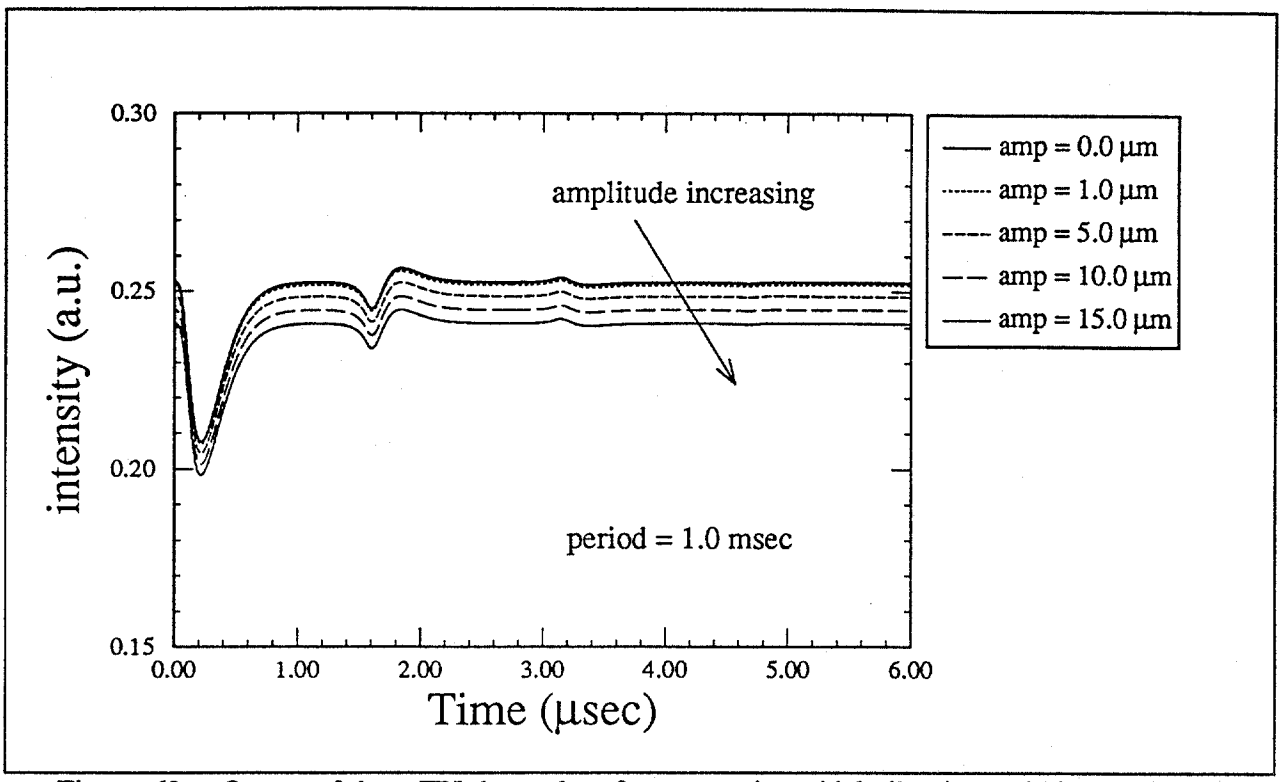

Figure 62 - Output of the c-FPI due to low frequency sinusoidal vibrations within the aircraft

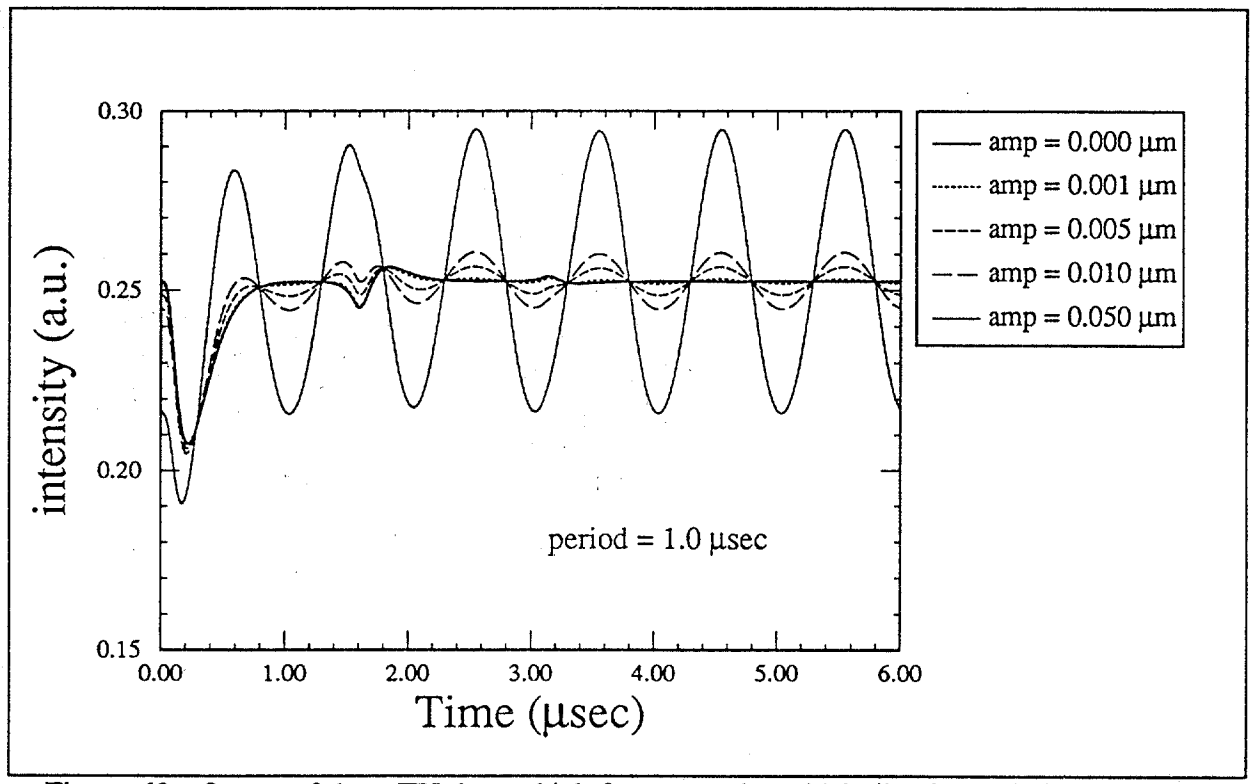

Figure 63 - Output of the c-FPI due to high frequency sinusoidal vibrations within the aircraft

The vibrational power spectral density from the RTCA/DO-160B document for a typical aircraft is shown in Figure 64. A typical time sample of the vibrational displacement of the aircraft based on the power spectral density shown in Figure 64 is plotted in Figure 65. The time sample is obtained by first generating a random Gaussian sequence with unity vibration power and then applying to it a time filter whose frequency response is the square root of the vibration power spectral density shown in Figure 64. The corresponding vibrational velocity is obtained in Figure 66. For an observation time interval of 10 ms, the vibrational displacement of the aircraft of within 10-50 μs, which is typical of the laser-ultrasonic events, can be shown to be very linear as demonstrated in Figure 67. Therefore, it is reasonable to assume the motion of the aircraft is linear with constant velocity during the measurement period. The vibrational velocity distribution of a typical aircraft is shown in Figure 68. It can be seen from this result that the aircraft has vibrational velocity larger than 1 m/s a significant portion of the time.

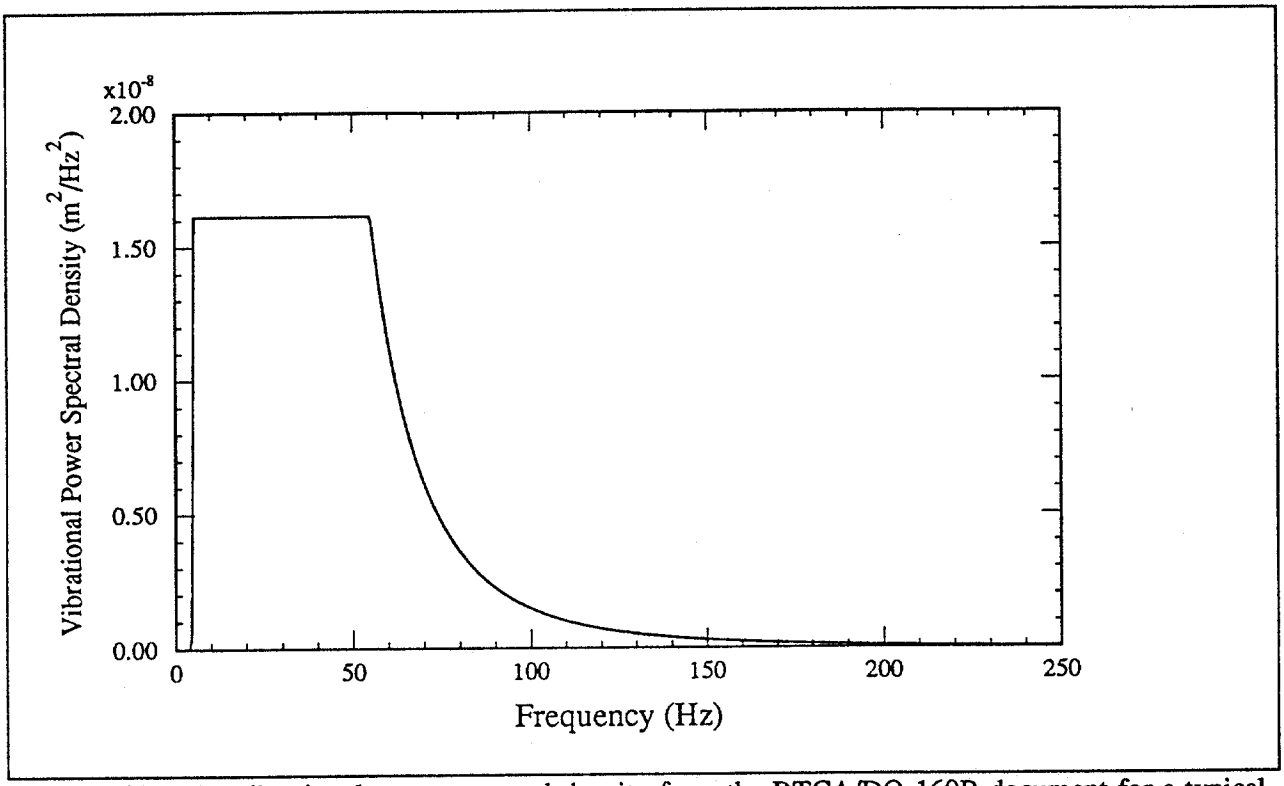

Figure 64 - The vibrational power spectral density from the RTCA/DO-160B document for a typical aircraft

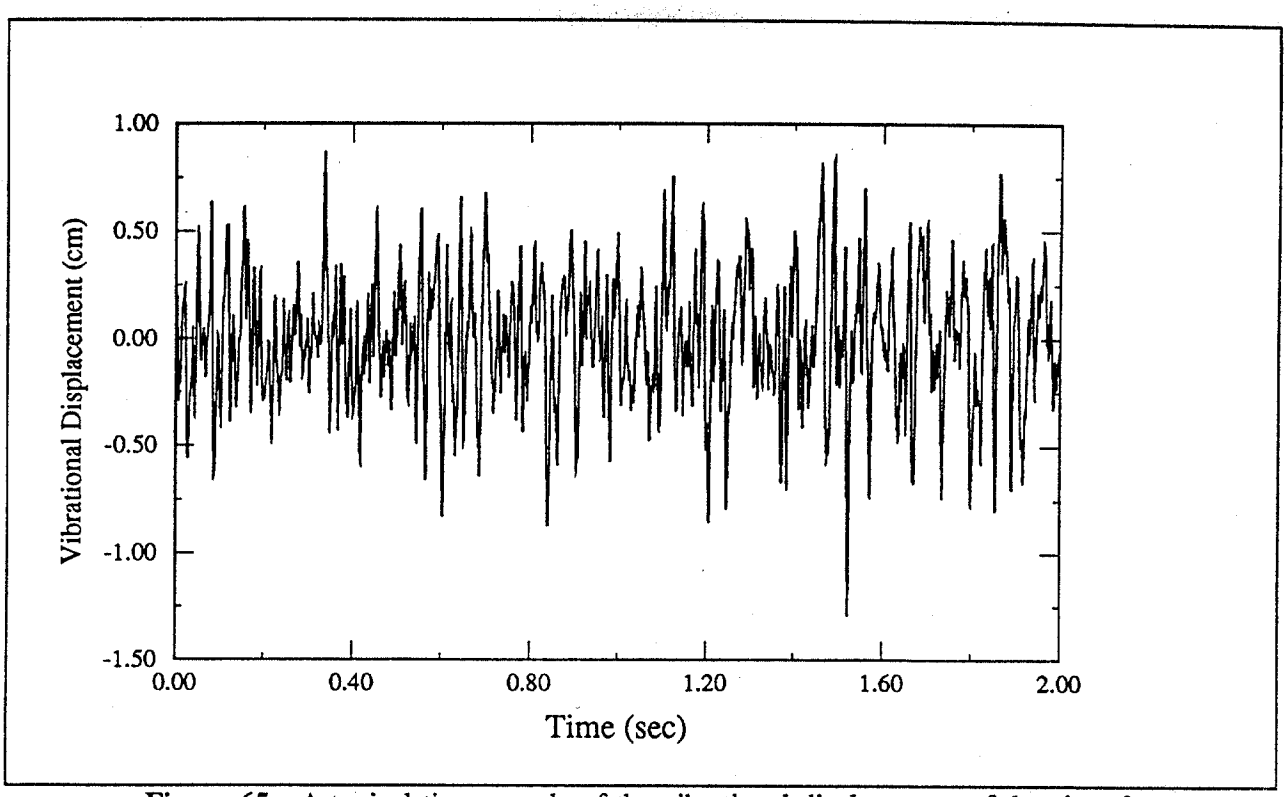

Figure 65 - A typical time sample of the vibrational displacement of the aircraft

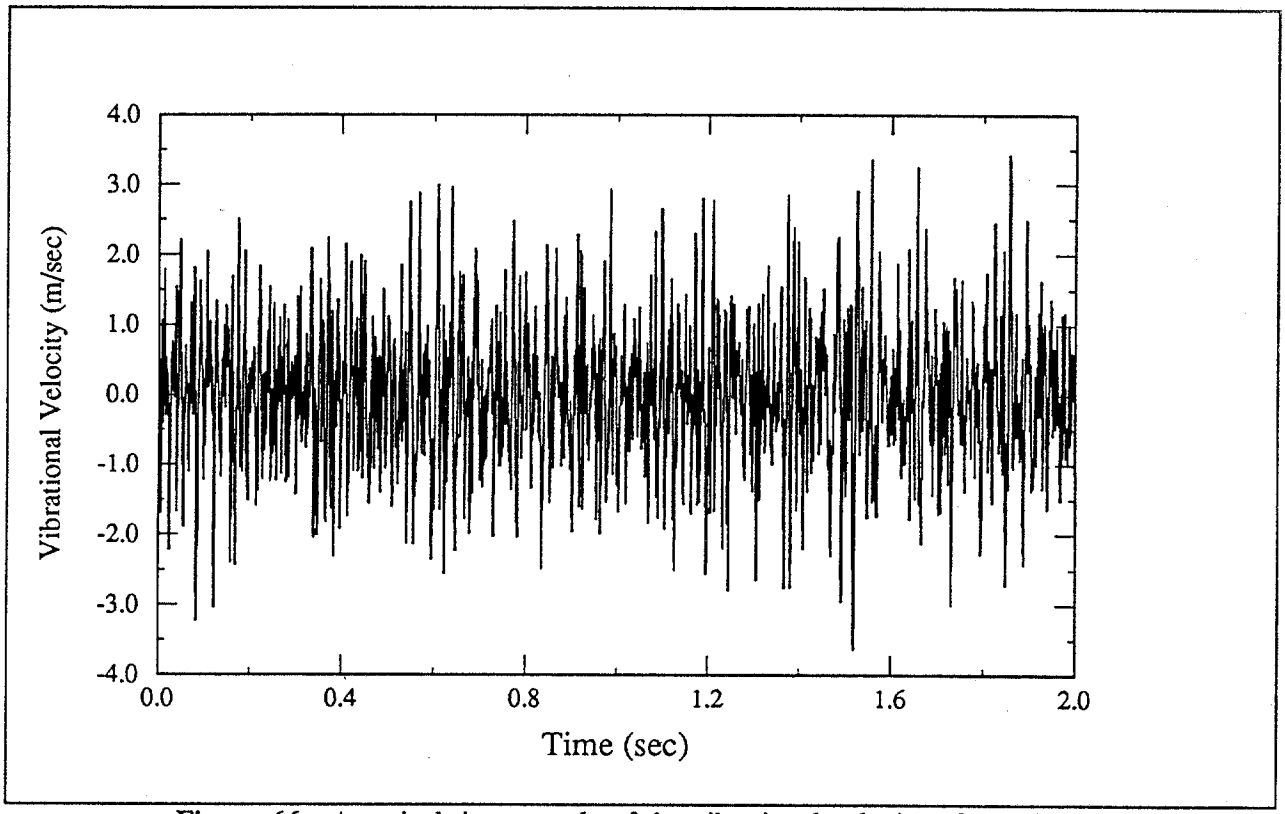

Figure 66 - A typical time sample of the vibrational velocity of the aircraft

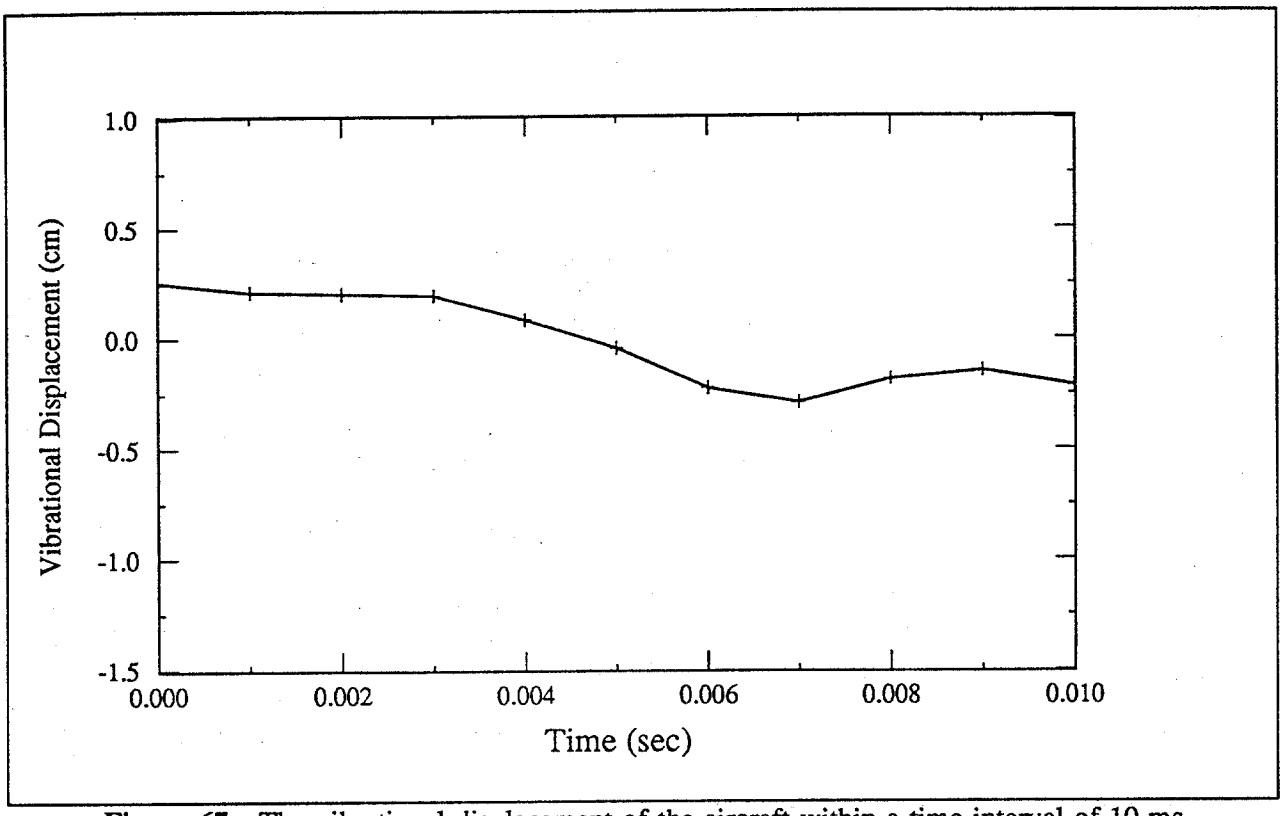

Figure 67 - The vibrational displacement of the aircraft within a time interval of 10 ms

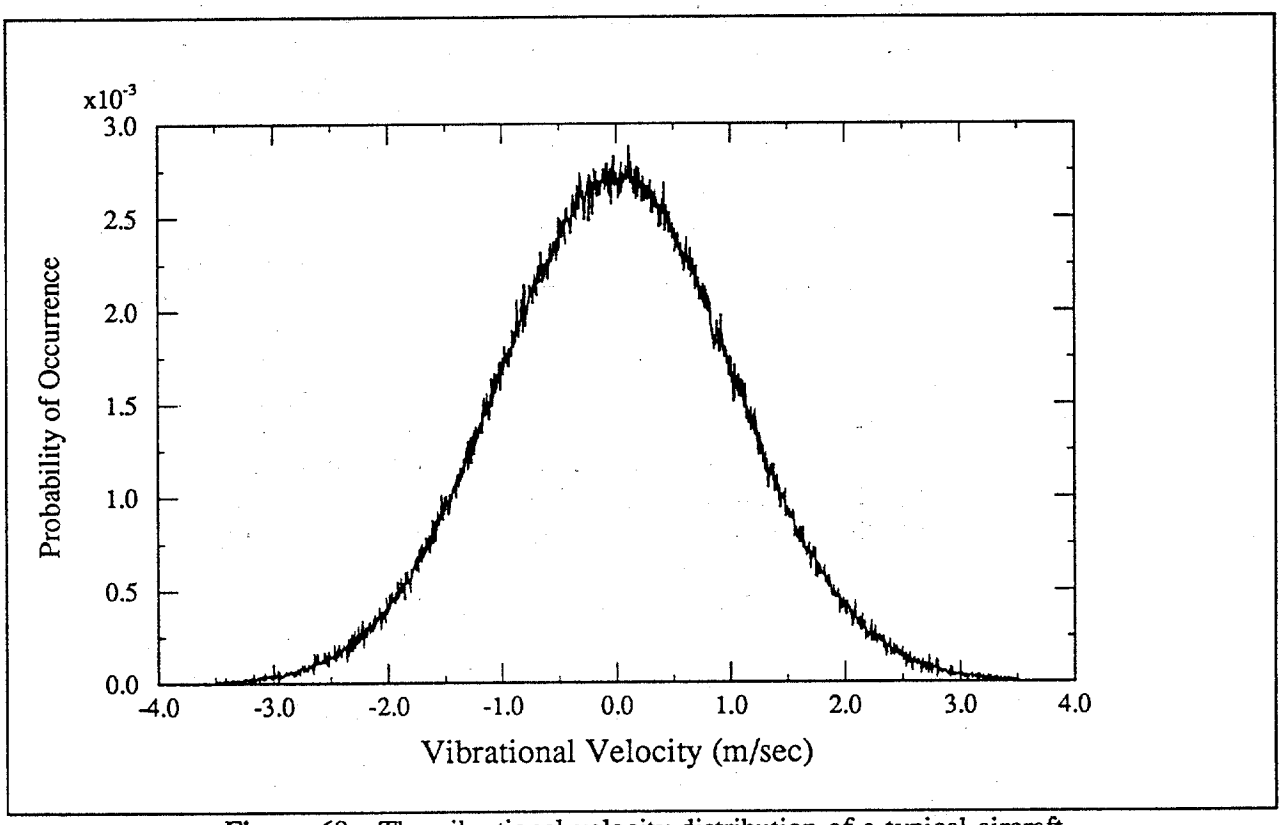

Figure 68 - The vibrational velocity distribution of a typical aircraft

Analysis of Real Altitude Data of a DC-3 Aircraft

Next, real altitude data of a DC-3 aircraft obtained during typical flight conditions were analyzed. The data were provided by Dr. Carl Brown of the Emergencies Science Division of Environment Canada. The data contained the altitude of the aircraft from three different flights over sea, each of which had a duration of 5 or 6 seconds. The data were obtained from a recent laser fluorosensor test flight. The raw time values were converted to time in seconds by dividing the raw time value by 100. The altitude in feet was obtained by dividing the raw altitude value by 2. The resolution of the data is ±0.5 feet RMS (single shot), with the accuracy being ±0.5-1.0 feet @ 25^0 (after calibration).

The raw altitude data for the three flights are shown in Figures 69-71. Because of the accuracy of the lidar data, the changes in altitude between any two laser shots (1 ms) appear to be significant. In addition, we are interested in the motion of the aircraft within a time span of a few tens of microseconds. It is necessary to interpolate the motion of the aircraft from the sampled data of 1 ms apart. As a result, the noisy altitude data were smoothed by linear regression using a polynomial of order up to eight. After the polynomial fit to the altitude data was found, it was used to obtain the instantaneous vertical velocity of the aircraft by differentiation.

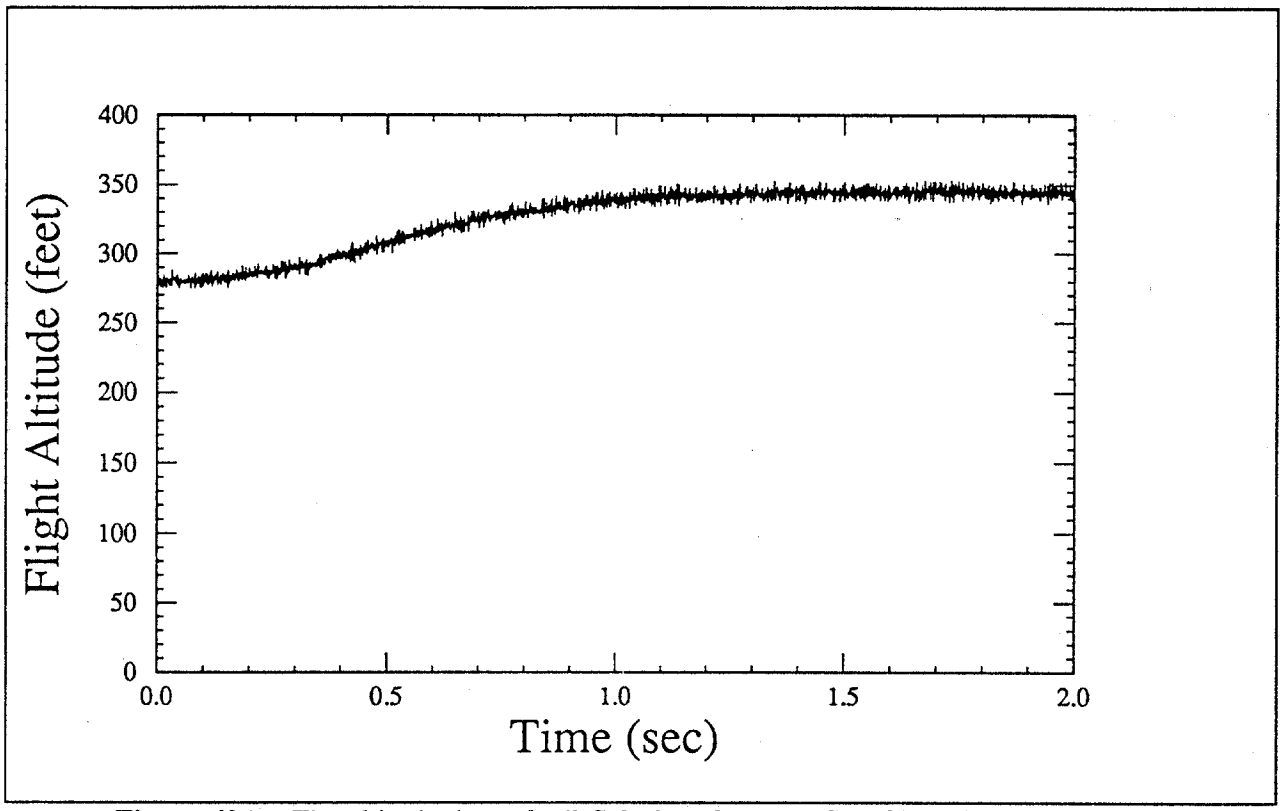

Figure 69A - The altitude data of a DC-3 aircraft on the first flight from 0.0 to 2.0 s

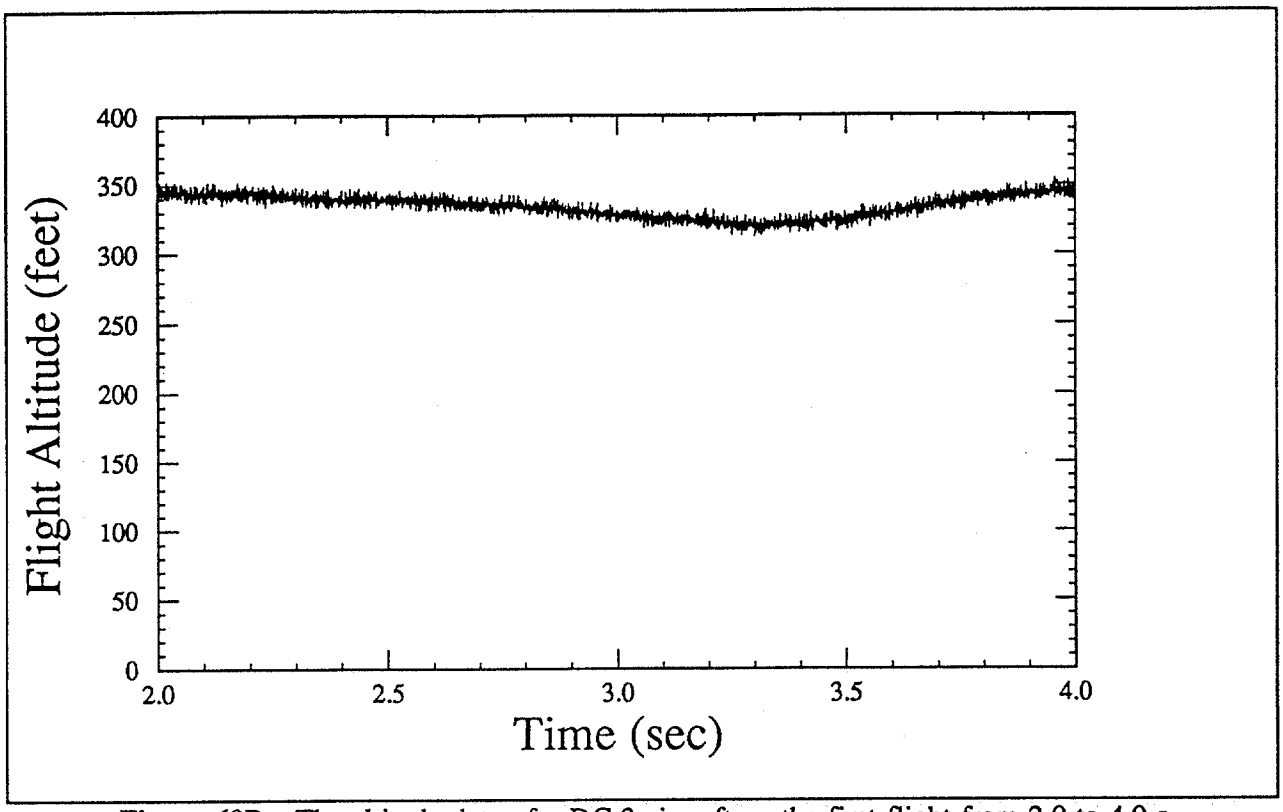

Figure 69B - The altitude data of a DC-3 aircraft on the first flight from 2.0 to 4.0 s

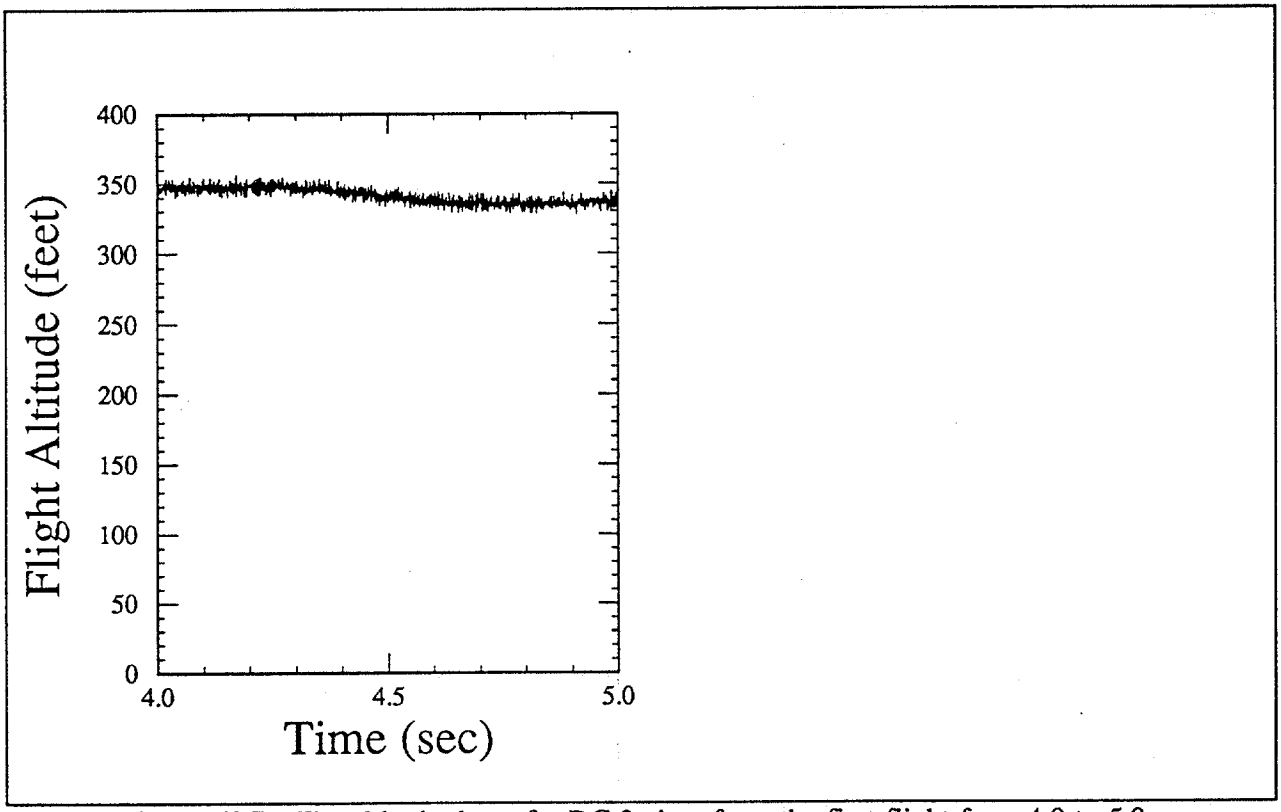

Figure 69C - The altitude data of a DC-3 aircraft on the first flight from 4.0 to 5.0 s

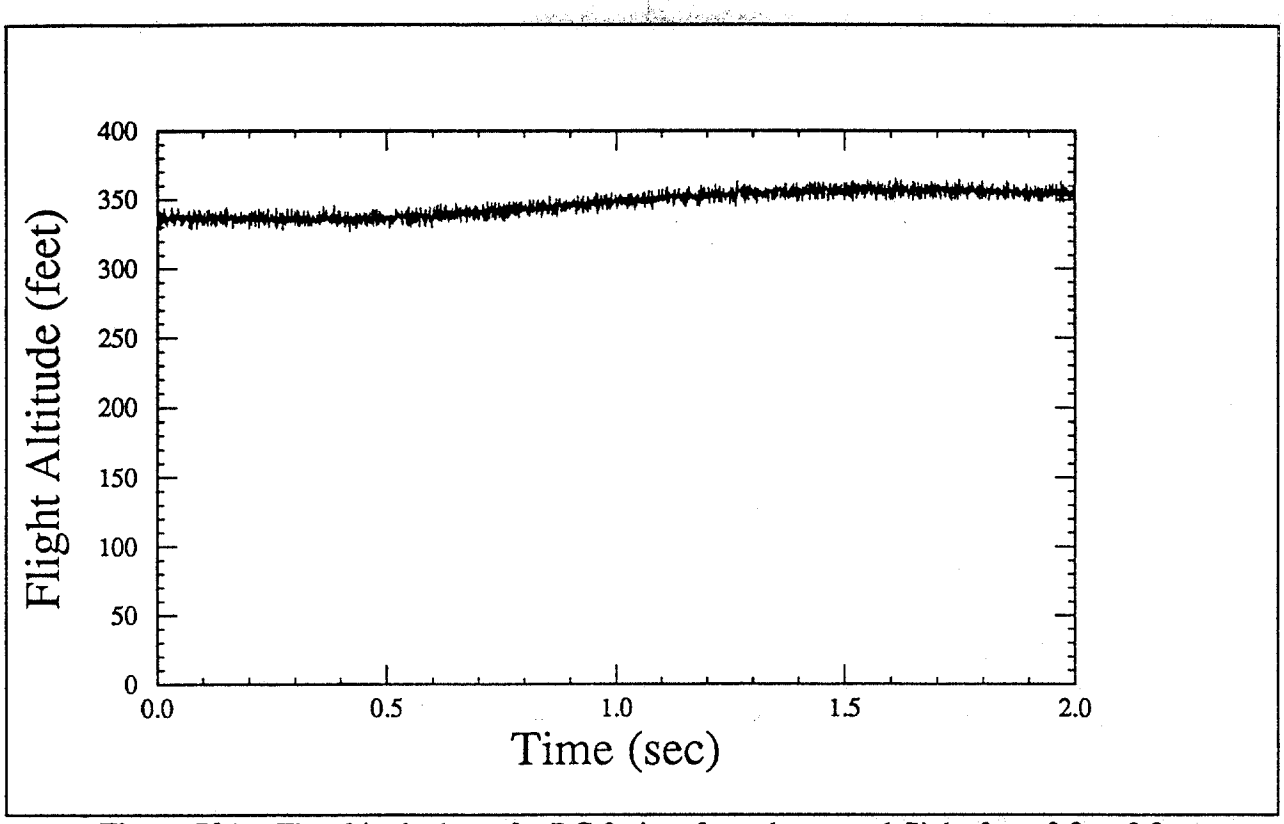

Figure 70A - The altitude data of a DC-3 aircraft on the second flight from 0.0 to 2.0 s

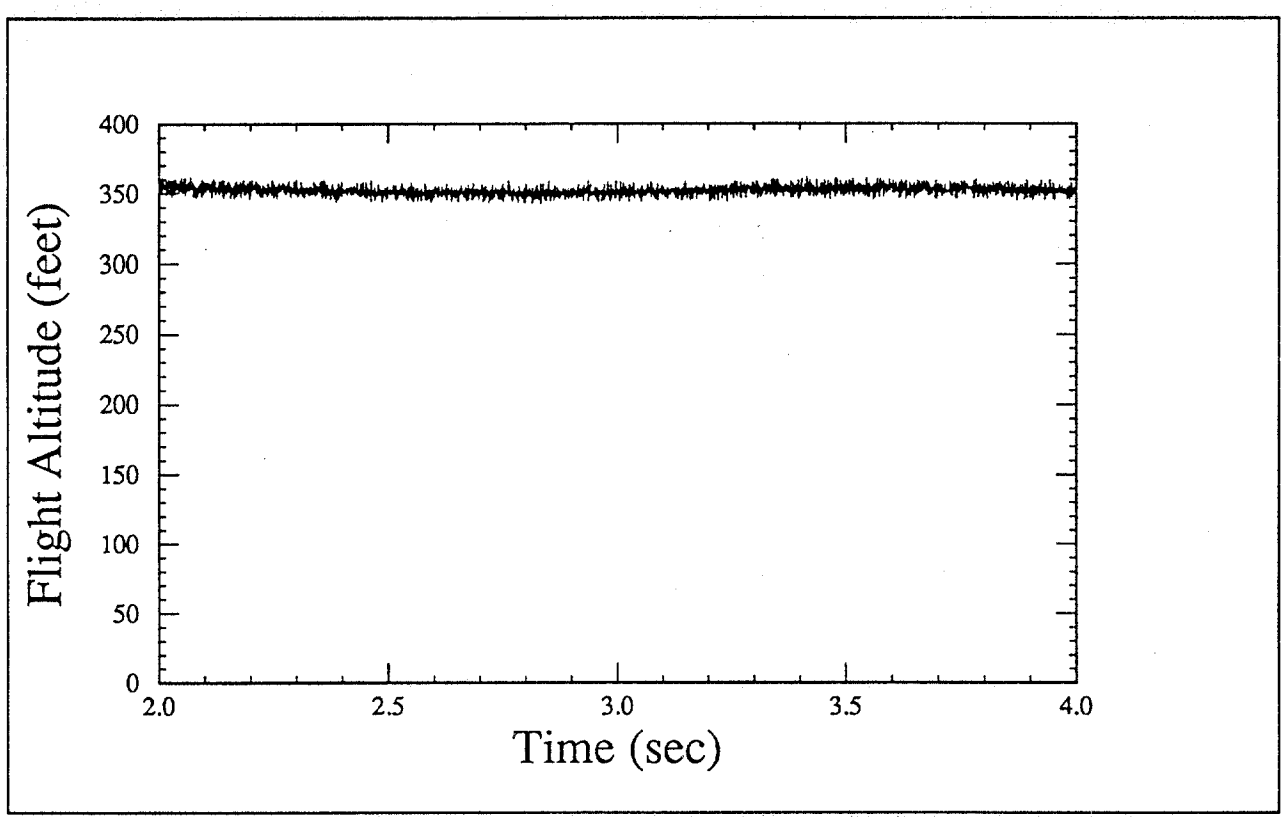

Figure 70B - The altitude data of a DC-3 aircraft on the second flight from 2.0 to 4.0 s

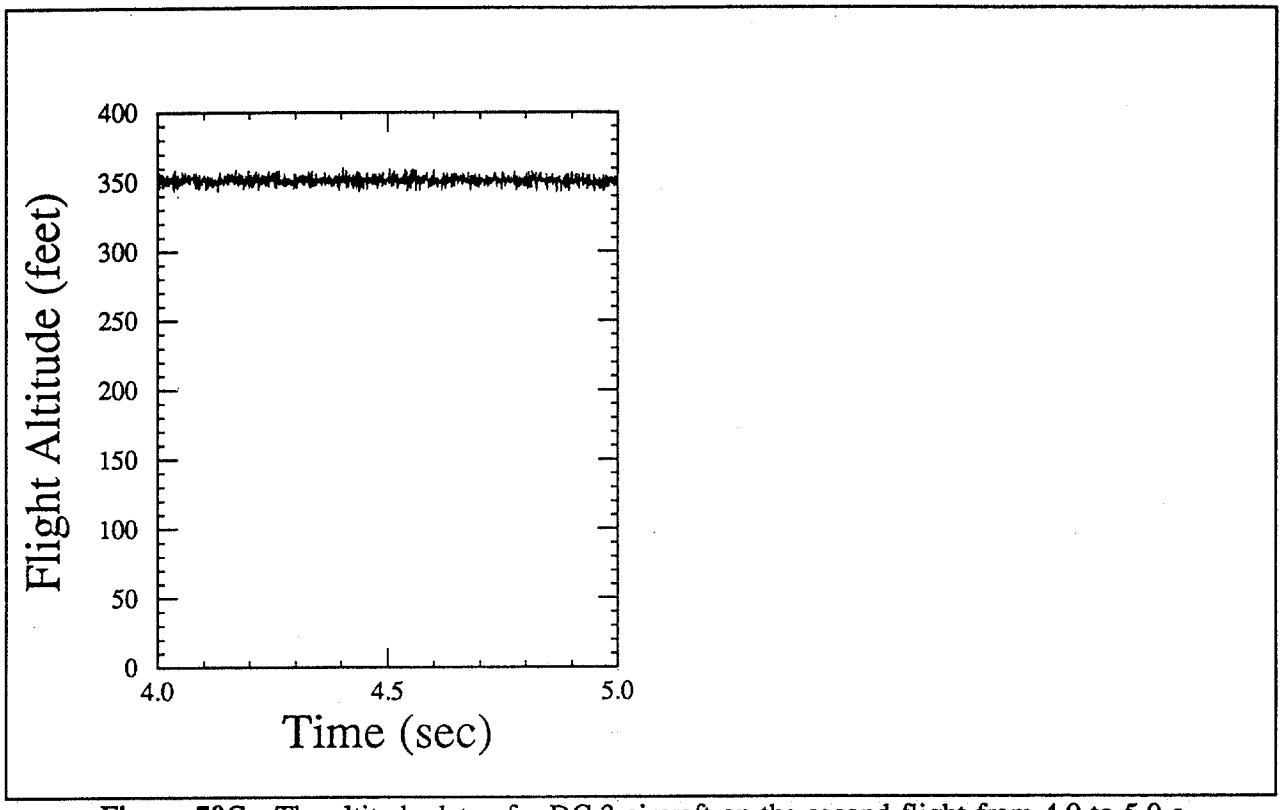

Figure 70C - The altitude data of a DC-3 aircraft on the second flight from 4.0 to 5.0 s

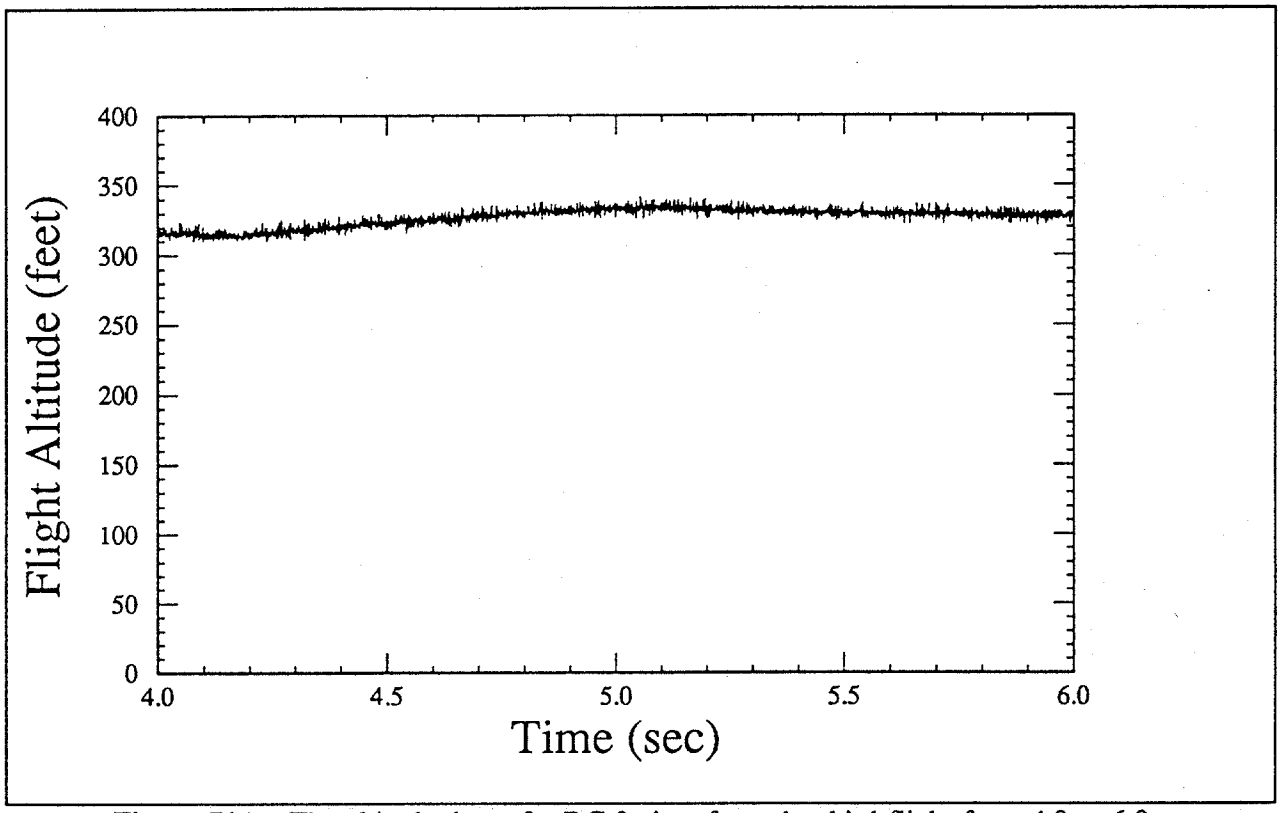

Figure 71A - The altitude data of a DC-3 aircraft on the third flight from 4.0 to 6.0 s

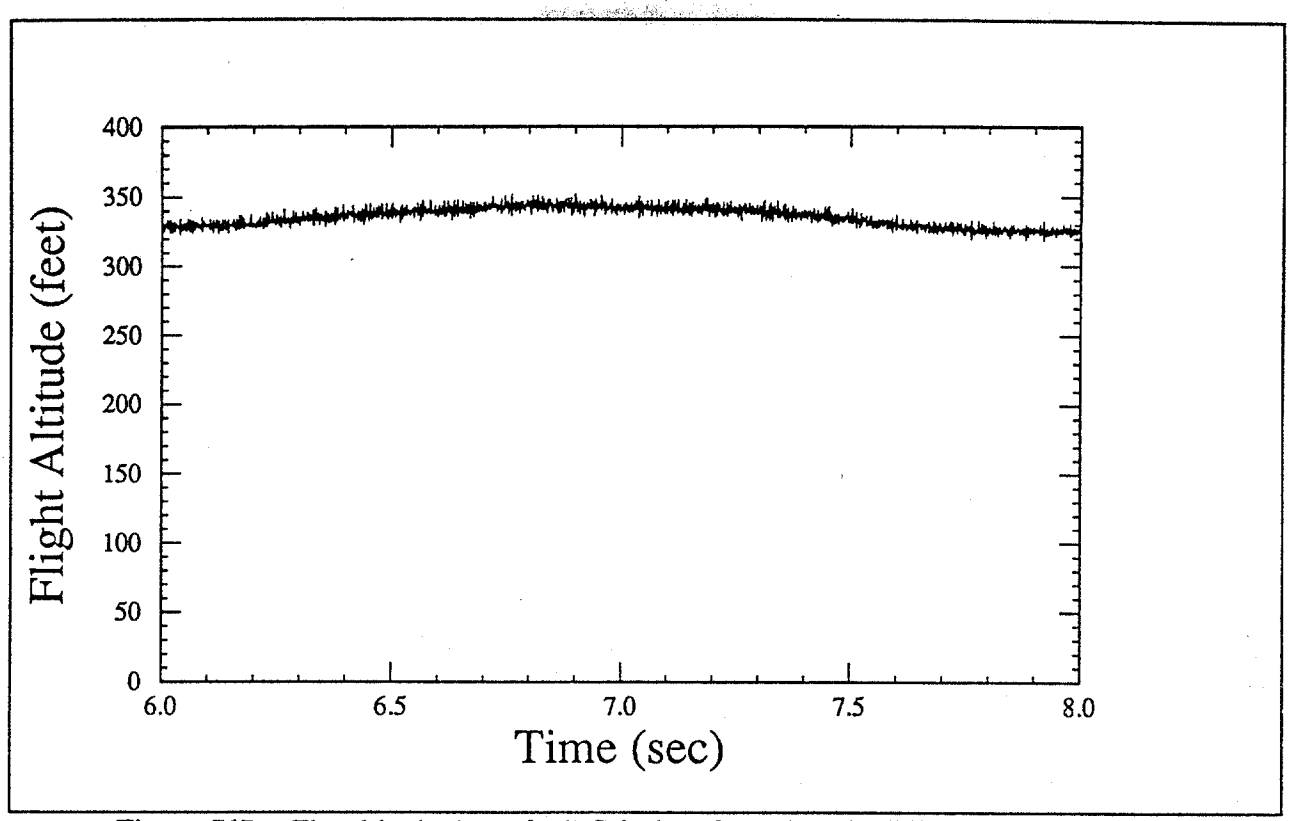

Figure 71B - The altitude data of a DC-3 aircraft on the third flight from 6.0 to 8.0 s

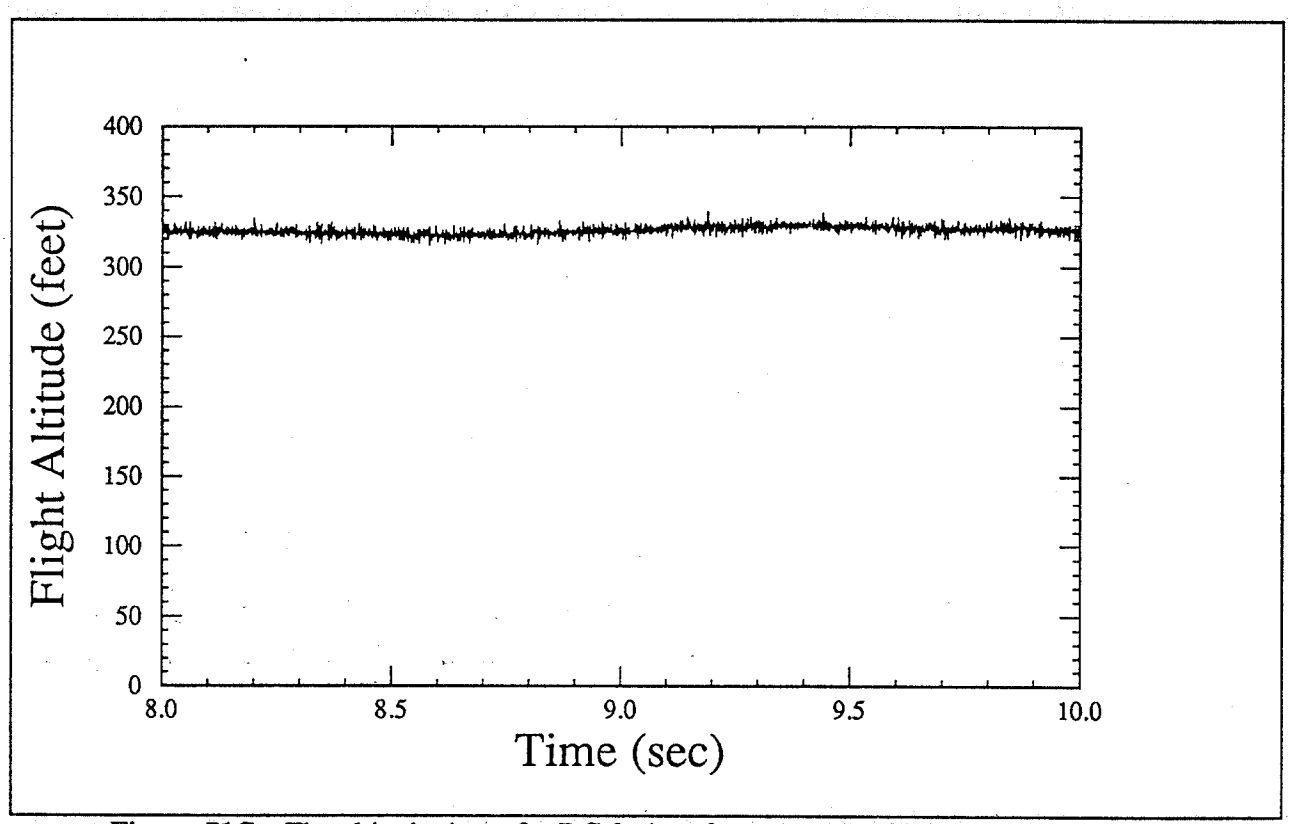

Figure 71C - The altitude data of a DC-3 aircraft on the third flight from 8.0 to 10.0 s

The distribution of the instantaneous vertical velocity is tabulated for each of the three flights in Figures 72-74. For LURSOT, the instantaneous vertical velocity of the aircraft is of importance because the ultrasonic displacement of the oil occurs within a time span of only a few microseconds. For IMI's design of the c-FPI and the wavelength of the probe laser, previous analysis and computer simulation on the sensitivity of the demodulation technique revealed that maximum vertical velocity of the aircraft allowed was limited to within ±2 m/s.

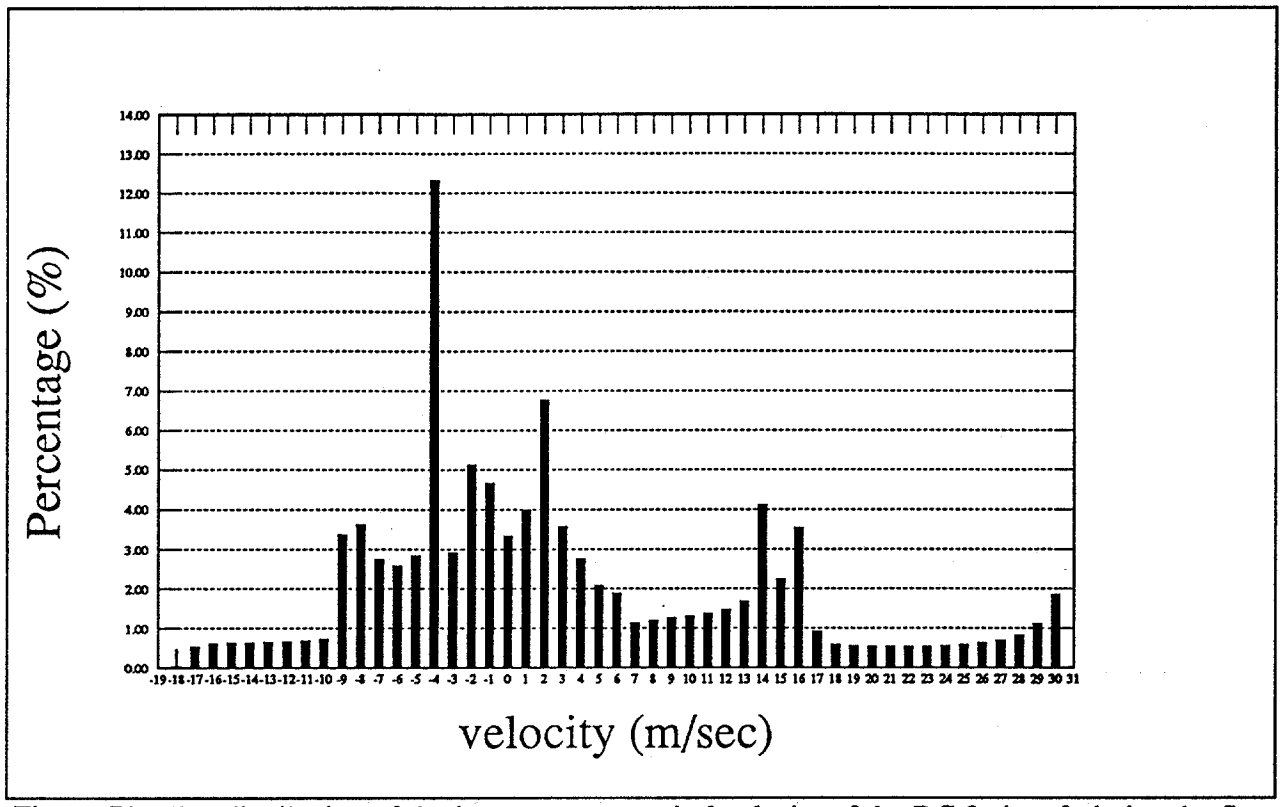

Figure 72 - The distribution of the instantaneous vertical velocity of the DC-3 aircraft during the first flight

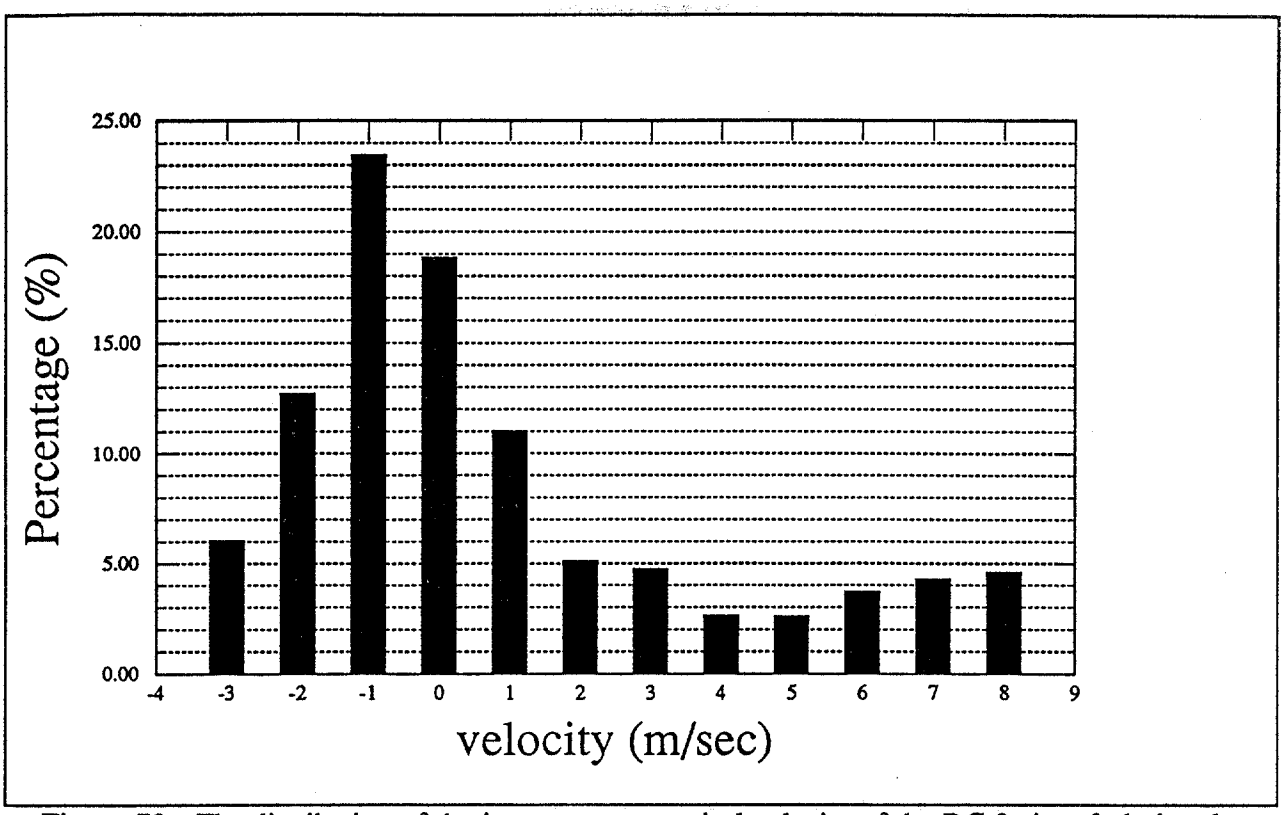

Figure 73 - The distribution of the instantaneous vertical velocity of the DC-3 aircraft during the second flight

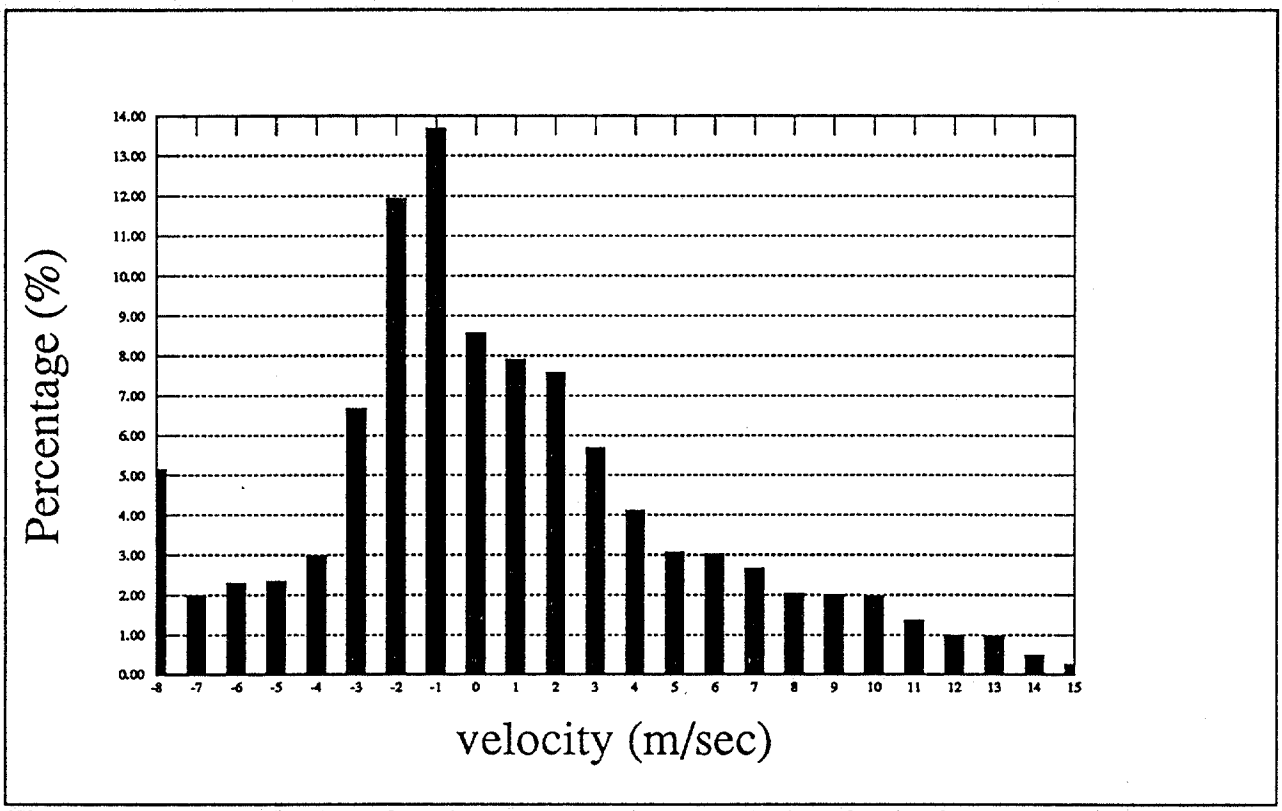

Figure 74 - The distribution of the instantaneous vertical velocity of the DC-3 aircraft during the third flight

Therefore, the proportion of the time that the instantaneous vertical velocity of the DC-3 was within ±2 m/s was evaluated for the three flights. The results are shown in the following table.

Table 12: Vertical Velocity Distribution of a DC-3 Aircraft

Flight	Proportion of Time within ±2 m/s	Minimum Velocity (m/s)	Maximum Velocity (m/s)
FLT1LD1.CSV	23.94 %	-17.62	30.16
FLT2LD1.CSV	71.26 %	- 3.50	8.49
FLT4LD1.CSV	49.72 %	- 8.36	15.09

Clearly, from the results shown in Table 12, the instantaneous vertical velocity of the aircraft presents a problem to the demodulation of the laser-ultrasonic signal. The magnitudes of the minimum and maximum vertical velocity are quite large, and the aircraft spends only a relatively small proportion of time within ±2 m/s. Consequently, the sensitivity of the demodulation receiver is significantly reduced if the vertical motion of the aircraft is not compensated for. The overall effect of this is to accept a lower data rate for the system..

5.3 Sensitivity to Sea Surface Motion

A preliminary investigation on the effect of wave motion on the sensitivity of the laser-ultrasonic remote sensing of oil thickness was performed. The investigation was done very briefly because of the unavailability of real wave height data and the lack of time. In spite of this, some wave property statistics were obtained from the Department of Fisheries and Oceans, via Environment Canada. In particular, the statistics of the wave properties were recorded as the number of occurrences of characteristic wave height and peak period at three different locations.

It was observed from these statistics that the frequency of occurrence for waves where the average velocity was 2 m/s or greater was quite small. However, the average velocity was taken over periods from 2 seconds to greater than 20 seconds. The magnitude of the instantaneous vertical velocity of the wave motion remains unclear. As a result, a thorough investigation of the characteristics of the sea surface motion is recommended.

5.4 Conclusions

The vertical velocity and vibration of an aircraft, and the motion of the sea surface, can both be considered as constant velocity offsets during the measurement periods. Effectively, this will shift the operating point of the c-FPI. Consequently, the sensitivity of the frequency demodulation is reduced and the output waveform of the c-FPI could also be distorted. For a c-FPI with a bandwidth of about 7.5 MHz, the analysis has shown that the combined vertical velocity of the aircraft and the sea surface motion within ±2 m/s seems tolerable, depending on the SNR of the output from the c-FPI. Otherwise, the operating point of the c-FPI with respect to the frequency of the probe laser is shifted to a point on the transmission response of the c-FPI at which the magnitude of the slope is very small.

If the effect of the vertical motion of the aircraft and the sea surface is left uncorrected, this could reduce the data rate of the LURSOT sensor. To evaluate the impact of the vertical motion of the aircraft and the sea surface, the signal-to-noise ratio of the c-FPI output signal must be considered. This is because the probability of correctly identifying the surface pulse and the echo pulse, and the accuracy of the time lag estimation, largely depend on the signal-to-noise ratio of the captured waveform.

6.0 GENERAL CONCLUSIONS AND RECOMMENDATIONS

We have reviewed, in considerable detail, the basic theory behind the LURSOT system and believe we have a good understanding of the requirements for a successful measurement. We have also used the IMI model and models developed by ourselves to examine the major system components. The results of this study leads us to two broad conclusions:

1) The mounting of the current prototype system in an aircraft is far too ambitious a step. Not enough is known about the behaviour of the system in this kind of environment.

2) Aside from the difficulties associated with the operation of the system in an aircraft, our analysis indicates that there is considerable room for improvement in the current system capability.

At this point, having successfully demonstrated the feasibility of the prototype system to measure oil thickness in controlled conditions, a thorough design review of the instrument is required. This seems especially sensible when one considers that the present prototype system is originally designed to measure steel sheets in a fixed geometrical configuration. A more fundamental understanding of the physics of the laser-ultrasonic interaction with a real sea surface is required. We also need to examine the system components from the points of view of achieving optimal system sensitivity and providing reliable operation from an aircraft. As a result, there remain a number of very fundamental issues that need to be examined before a new airborne system is developed.

Crucial to the success of the LURSOT technique is the probe system (probe laser and receiver) that detects the oil surface motion. Key to this system is the confocal Fabry-Perot Interferometer (c-FPI), which must be locked so that its operating point corresponds exactly to the probe laser wavelength. This highly precise tuning must be maintained subject to the aircraft conditions. This is the most critical issue for airborne use of the LURSOT system.

In this study we have examined alternatives to the c-FPI, but have concluded that it appears to be the best method for this application. We have also attempted to examine the current feedback mechanism that is supposed to lock the c-FPI to the probe laser frequency. We were hampered in this by a lack of detail on the part of UltraOptec, who consider this aspect of the system to be proprietary. In general, we suspect that the current feedback control is incapable of handling the broad spectrum of vibrational frequencies encountered in the aircraft.

Since we consider the c-FPI to be the most critical component in the system, it is of paramount importance that a proper, detailed analysis of this aspect of the system be done. This will require an analysis of the acoustical and vibrational spectra that the c-FPI encounters in the aircraft,to determine:

- Which components of these spectra are interfering with the oil surface motion measurement
- Which of these components can be eliminated through appropriate isolation of the c-FPI
- Which of these components can be compensated for by an active feedback loop.

This analysis will require simulation of the aircraft environment in a laboratory setting where the performance of the c-FPI can be carefully monitored.

The probe laser is another critical system component that needs to be thoroughly reviewed. Our analysis of the requirements for this laser suggests that a cw source would be more effective for a number of reasons. These include the following:

- The probe laser can also be used as the source for the surface orientation sensor, thereby saving on the complexity of introducing a third laser whose alignment must be maintained.

- Available cw lasers of appropriate power and spectral bandwidth are very compact and rugged, and of moderate cost. This is important from the standpoint of system reliability, simplicity of design and degree of technical risk.

- A portion of the cw output can be fed into the c-FPI to provide a reference signal to which the c-FPI can be locked, as was done for the LURSOT demonstration system. However, in the previous system the cw laser was used to injection-seed a pulsed laser, whose output was then used to probe the oil surface. Use of a cw probe laser will remove any potential problems with drift in the operating wavelength of the probe laser and c-FPI, and will also remove any uncertainties regarding the actual wavelength of the pulsed laser source.

The advantages and disadvantages of the choice of cw or pulsed probe laser need to be explored further.

The issue of eye-safety is also very important for the probe laser, since in either the pulsed or cw case this beam can be reflected in any direction by the changing water surface. Our assumption is that because of this, the probe laser must be eye-safe at the sea surface. This being the case, the probe laser may have to operate at 1.5 μm. This is not a problem for cw lasers, since suitable sources already exist. For pulsed lasers, however, it requires use of non-standard lasers further adding to the already complex requirements for long duration pulses, narrow spectral bandwidth and fire on command. This is not a recipe for a reliable laser source.

In any case, the probe laser will also have to be environmentally tested to ensure that it operates as expected under the conditions that will be encountered in the aircraft. This again will require simulation of the aircraft environment in the laboratory so that controlled tests of the laser performance can be done.

Associated with the probe laser requirements is an understanding of the sea surface topography and how this affects the reflected beam. Considerable uncertainty has been expressed on the part of Environment Canada regarding the frequency of occurrence and the quality of probe laser reflections from the sea surface. In short, there is considerable uncertainty about whether the aircraft-to-sea surface geometry would ever be suitable for generating usable laser-ultrasonic signals. Our investigation into this area met limited success due to the complexity of the sea surface topography and the limited amount of published data. Further investigation of this aspect of the system needs to be done as it plays a part in determining the requirements for the probe laser energy, receiver aperture size and sensor system mounting. Given the complexity of the problem, the only way to characterize the returns is to perform field tests in which statistics on the frequency and strength of the reflections from an oiled sea surface can be accumulated.

The generating laser is another critical component of the system. First, the requirements for eye-safe operation for this laser need to be reviewed. If eye-safety is required at the sea surface, then we are forced to change the generating laser to a system operating in the 2.3 μm region. This is the only wavelength region that will provide the required combination of efficient ultrasonic wave generation

and eye-safety. In this case, less common laser sources must be examined and evaluated to determine whether there is a source capable of meeting the generating laser requirements. A selected source must then be environmentally tested. If the eye-safety requirement can be relaxed, then we have an interesting choice between the present CO_2 laser and an excimer laser. In the case of the excimer laser, we need to more carefully examine the absorption features of the oils in the 308 nm region. In this study we had a very limited sample of low resolution absorption spectra for this wavelength region. Also, the miniature excimer laser that has many of the desired features has at present, marginal pulse energy. This issue needs to be more carefully addressed, perhaps with some tests of the actual oil reaction to pulses at UV wavelengths.

A more basic requirement for further development of the LURSOT concept is a better understanding of how the vertical motion of the aircraft and ocean waves affect the ability of the receiver to identify the ultrasonic-induced motion of the oil surface. Our analysis suggests that there may be a significant amount of interference with the Doppler measurements, which would essentially reduce the number of successful measurements. Moreover, it appears that some measurements will be lost outright while others will give erroneous values for the oil thickness. To further address this issue, we need to obtain better data on the motion of the aircraft and waves. If good statistical data on these quantities can be obtained, a theoretical model can provide analysis of the impact that these will have on the system data rate. Primarily, we want to be confident that these vertical motions will not reduce the rate of successful measurements to unusable levels. In parallel, laboratory tests could be performed to evaluate the impact of these motions through the controlled motions of a suitable, artificial target.

We also have concerns about the design of the transmitter optics and their behaviour under aircraft conditions. In particular we are concerned about their ability to maintain alignment of the two laser beams, and their potential to add Doppler shifts to the outgoing probe beam due to vibration along the beam axis. This is primarily a mechanical design problem that if done properly should not affect the data quality at all.

Finally, there is the question of system reliability, self diagnostics and performance monitoring. These are important features that are completely lacking in the current system. The LURSOT system is a particularly complex instrument with a large number of critical subsystems. Failure in any of these systems will result in a ***no measurement*** condition that could be misinterpreted as meaning that the geometry of the sea surface is not correct, or that there was not a measurable oil thickness. To be an operational system, LURSOT has to have enough self-monitoring capability that failures of any key system component will be reported to the system operator. Examples of sub-systems that should be monitored include:

- **Surface Orientation Receiver:** A record of the detection of correct surface orientation must be kept since this provides a record of the system triggering. Each trigger event should show that the generating laser has indeed fired and, if the aircraft is over oil, that a thickness measure has been acquired. From this basis, statistics on the success rate and quality of the oil thickness measurements can be generated.

- **Transmitter Optics Alignment:** The alignment of the probe, generating and surface orientation lasers is critical to the successful operation of the system. A system to monitor this alignment is required to help diagnose poor results.

- **System Timing:** The timing of the system is critical to its measurement function. Timing information on the initial trigger from the orientation sensor, the actual generating laser pulse emission, and the probe laser pulse emission if it is a pulsed source need to be correlated with

the temporal output of the c-FPI. This is required both for data analysis and for system diagnostics.

- **Fabry-Perot Interferometer Function:** As this is the critical system component, we need some diagnostics of its performance. We need to be able to monitor the locking of this device to the probe laser wavelength.

These monitoring functions will require additional sensing systems and data handing. They will, however, allow rapid system diagnostics, thereby aiding in the interpretation and analysis of the measurements.

The following provides a brief summary of our recommendations to develop the next generation of the LURSOT system, that is, an operational airborne system:

1) Develop a c-FPI capable of operating in an aircraft. This development requires testing the system under simulated conditions. Basic optical design, mechanical packaging, mounting and active feedback must all be examined to optimize the performance of this device.

2) Perform a detailed analysis of the pros and cons of cw versus pulsed probe laser.

3) Perform environmental testing of the probe laser. The goal is to establish a measure of the reliability of the laser, its maintenance requirements and the stability of its output in terms of beam quality, pulse duration and timing if pulsed, and wavelength.

4) Perform characterization measurements on the reflection of the probe beam from the sea surface. Intermediate steps involving simulated sea surfaces are both useful and desirable, but the most conclusive studies would be performed on oil-covered natural sea surfaces. The goal of such measurements is the characterization of statistics regarding the data rate, and statistics regarding the reflected signal strengths.

5) Re-examine eye-safety requirements for the generating laser. Will we be forced to consider 2.3 μm laser sources only, or do we have a choice of CO_2 or excimer lasers? In any case, careful specification of the laser needs to be done. As with the probe laser, environmental testing is necessary to determine laser reliability and stability under simulated aircraft conditions.

6) If any other laser type is to be considered as a replacement for the CO_2 laser, a more thorough examination of the oil absorption spectra in the applicable spectral region needs to be done, to confirm or refute the findings of our studies on low resolution absorption spectra. The primary purpose of these measurements would be to determine the spectra of selected oils at higher resolution, typical of laser spectral bandwidths, in order to avoid an erroneous choice of laser wavelength. This is particularly important for the UV spectral region. Experimental tests of the laser-ultrasonic interaction of oils with pulses from an excimer laser are also recommended if this option is considered.

7) Analyze further the effects of aircraft and wave motion on the data rate and data quality. This may require measurements of the aircraft vertical motion and characterization of the wave motion. Laboratory studies of artificially-induced solid target motion would help in the evaluation of motion impacts on these parameters.

8) Should all of the above efforts prove successful, a detailed system design is required to implement all of the above into a new instrument with self-test and self-diagnostic systems.

9) The integrated system then needs to be environmentally tested before being installed in the aircraft to ensure that it will operate reliably under simulated aircraft conditions.

10) Initial flight tests will then be required to obtain statistics on the field use of the system. This will require detailed analysis of the measurements with ground truthing to determine the accuracy of the LURSOT data.

APPENDIX A - EYE-SAFETY ANALYSIS

The last decade has brought about an increased awareness of the safety hazards associated with the operation of lasers, especially in uncontrolled (i.e., non-laboratory) environments. These hazards consist primarily of high voltage hazards, and radiation hazards to the skin and eyes. The first category of these hazards can be significantly reduced (or eliminated) through proper engineering, and is normally only an issue for maintenance personnel, not operators. Radiation hazards to the skin and eyes are by far the most common and serious problem likely to be encountered by those operating lasers, and by those intentionally or unintentionally observing them. Radiation injury to the eye and skin have similar injury thresholds, except in the retinal hazard region (400 nm to 1.4 μm) where the eye is considerably more vulnerable, yet eye-safety hazards are most often regarded as being the more important category due primarily to our dependence on eyesight for everyday activities. For these reasons we have considered eye-safety hazards only in this preliminary analysis.

The effects of optical radiation on the eye vary significantly with power density, energy density (temporally-integrated power density), spot size and wavelength. The dependence of the injury threshold on power and energy density are quite complex, because of the many mechanisms for eye damage and their complicated interactions. Injury to the eye may result from damage to the outer layers, where the incident laser beam is essentially a collimated beam, or from damage to the retina where imaging occurs. Damage to the retina depends also on the degree of accommodation of the eye, since this helps to determine the image size. Damage to the eye may occur from photochemical reaction, from thermal effects, or from photoacoustically-generated shocks. In the case of thermally-generated injuries, the important parameter is the time history of the laser-generated temperature elevation within the eye; thus both the instantaneous power level and the integrated power (energy) are important.

The laser spot size may be important depending on where the laser radiation is absorbed, before or after the iris. Optical radiation which passes through the iris may be reduced in power or energy purely by reduction of the spot size, if the incident laser spot is larger than the iris.

The wavelength is important for two reasons: it may determine an upper limit on the duration of the exposure, and it determines where within the eye the radiation is absorbed. In the former case, the natural aversion response ("blink reflex") of the eye limits the time spent looking at a bright visible source; however, an invisible optical radiation source may be viewed until actual eye pain or other effects are noticed.

In the latter case the optical radiation may be absorbed in the cornea (outer surface of the eye), the aqueous (interior volume of the eye, pre-lens), the lens, the vitreous (interior volume of the eye, post-lens), or the retina (back, "imaging" surface). Figure A1 illustrates[1] these regions of the eye conceptually. It is known that optical radiation in the retinal hazard region (400 nm to 1.4 μm) is transmitted throughout the volume of the eye where it becomes sharply focused onto the sensitive photoreceptors in the retina. This often leads to a blind spot (scotoma) on the retina surface within the illuminated region, which may become a severe visual impairment if it occurs within the central viewing area rather than within the peripheral field of vision. In addition, there may be more subtle effects on the microstructure of the eye, such as a reduction in dark adaptation. At short UV and long

[1] D. Sliney and M. Wolbarsht, "Safety with Lasers and Other Optical Sources: A Comprehensive Handbook", Plenum Press, New York (1980), Figure 3-1, page 66.

IR wavelengths most of the energy is absorbed in the cornea; this normally represents only a temporary injury because of the high cell regeneration level in the cornea. At near-UV and near-IR wavelengths (315 to 400 nm, and 770 nm to about 1.4 μm) there is great absorption in the lens, which may become a severe problem at projected future dates to the physiology of the lens tissue (damaged material is overgrown by new material, and kept within the interior of the lens structure). Wavelengths between about 1.4 and 1.8 μm are absorbed most evenly throughout the entirety of the eye structure, thus reducing the effects of localized damage. The aqueous and vitreous, being primarily composed of water, are less likely to be damaged compared to other structures within the eye.

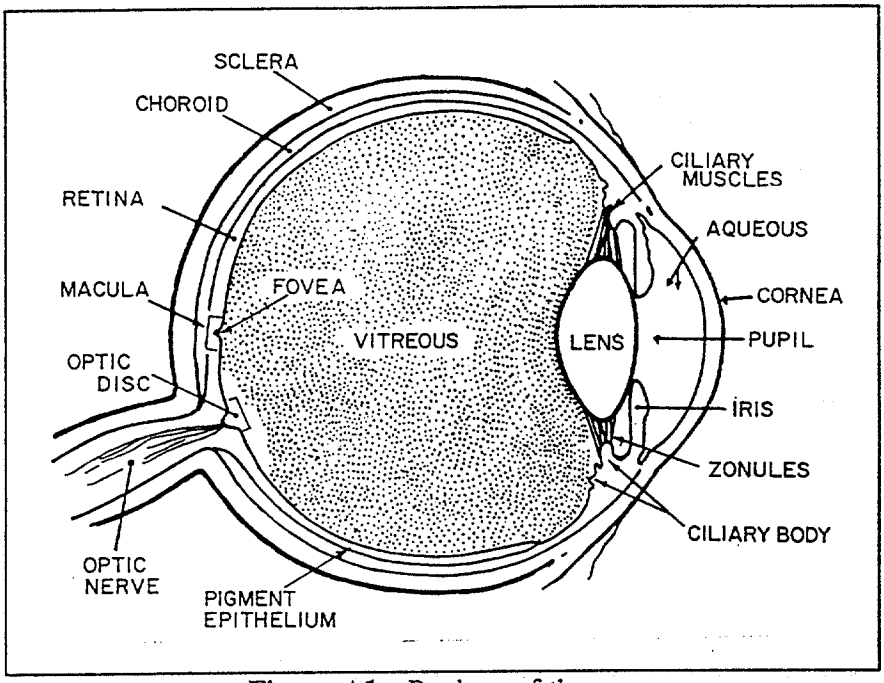

Figure A1 - Regions of the eye

To determine what level of laser output power/energy is eye-safe, we have adopted the guidelines of the American National Standards Institute [American National Standards Institute , ANSI z136.1-1993, American National Standard for Safe Use of Lasers, (New York, 1993). Compliance with these guidelines is sufficient for operating the particular laser system within Canada; however, if operation within the United States is required then the particular laser system must also comply with the guidelines of the FDA/CDRH (Federal Laser Product Performance Standard, 21CFR Part 1040), and if operation in other parts of the world is required then compliance with the IEC standards (IEC Standard on Radiation Safety of Laser Products, Equipment Classification Requirements and Users' Guide, Publications 825-1984 and 825-1990).

The evaluation of eye-safe laser power and energy levels for this application requires us to make some assumptions regarding the likely scenario whereby an observer would be irradiated by a laser beam from an overhead aircraft. As such we assume that the aircraft overflies an observer at an altitude of 100 m and a minimum speed of 100 knots (50 m/s). It is further assumed that the laser beam is nadir-directed (i.e., pointing vertically downwards from the aircraft), and that the beam is focused to a specific spot size where it then impinges directly on the observer's unaided eye (i.e., no binoculars or other optical aids). For simplicity in this preliminary analysis, we have assumed that only a single laser beam would be incident on the eye of the observer. In practice this would not be the case, since at least two and perhaps three coincident laser beams, at up to three different wavelengths and pulse

durations, may strike the observer's eye simultaneously. However, for the purposes of this analysis, we have tried not to overly complicate the situation.

The analysis was performed for several cases of different spot sizes (3 to 30 mm spot diameter) and laser pulse duration (10 ns to cw), for about 300 separate wavelengths between 180 nm and 10.6 μm. These cases were selected in order to bracket the expected values of these parameters for a LURSOT-type system. The assumption of a minimum aircraft speed of 50 m/s simplifies the analysis considerably, since then we can treat even the cw laser case as being pulsed. This occurs because a stationary observer on the ground will not be able to view the beam for extended periods of time. The effective pulse duration for laser illumination becomes the time required for the laser focal spot to sweep over the observer, unless the laser pulse duration is shorter than this time period. Because of the continuous horizontal motion of the aircraft, we assume that an observer witnesses only a single exposure.

The effective ocular exposures and limiting apertures for each case allow us to calculate the Maximum Permissible Exposure (MPE) for each wavelength in the desired range. Finally, the maximum eye-safe laser energy (for the pulsed cases) or laser power (for the cw case) can be calculated from the MPE. Note that there is a small, but non-negligible, margin of safety introduced by the fact that we do not assume any atmospheric attenuation of the laser radiation as it propagates from the aircraft to the observer. This margin of safety is a complicated function of the laser wavelength and the atmospheric conditions, but likely amounts to about 3-5% in the visible with more in the UV and IR.

Selected results from the eye-safety calculations are presented in Figures A2 to A6. In all cases the dependent variable (either maximum eye-safe laser pulse energy, for pulsed lasers, or maximum eye-safe laser power, for cw lasers) is shown as a function of wavelength. Multiple curves on the same set of axes show the effect of varying either the pulse duration or the beam spot size of the laser output. Note that the data presented in these graphs are for comparison purposes only. It is seldom possible to arbitrarily choose different laser sources (with different wavelengths) and maintain constant values of beam diameter and/or pulse length. The effect of real world parameters will be discussed in the trade-offs in a following section.

Figure A2 illustrates the maximum eye-safe laser pulse energy for relatively short laser pulse lengths (10, 30 and 100 ns), as might be utilized for the laser-ultrasonic generating laser. Immediately obvious is the tremendous range of eye-safe pulse energies over the spectral interval shown, 180 nm to 3.0 μm. There are approximately 6 orders of magnitude difference in eye-safe pulse energy between 400 nm and 1.5 μm.

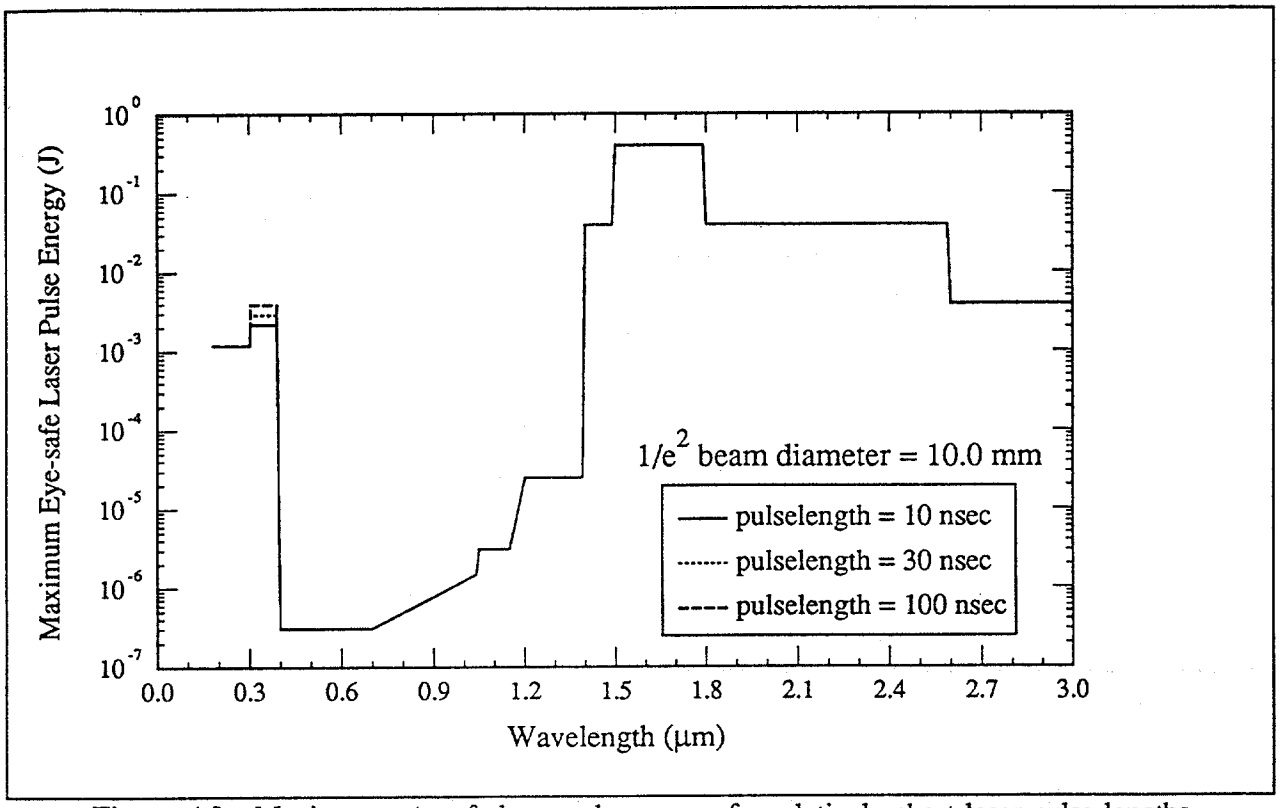

Figure A2 - Maximum eye-safe laser pulse energy for relatively short laser pulse lengths

The safest wavelength interval, usually referred to as the "eye-safe spectral region", extends from 1.5 to 1.8 μm (the shorter wavelengths of the IR-B spectral region). For the case shown where the $1/e^2$ beam diameter is 1.0 cm, about 400 mJ of pulse energy remains eye-safe to an observer. The next most eye-safe spectral regions are 1.4 to 1.5 μm and 1.8 to 2.6 μm, which allow similar levels of maximum laser pulse energy (about 40 mJ, or 10% of the values in the best eye-safe spectral region). The spectral range from 2.6 to greater than 10.6 μm represents the third best choice for eye-safety, where about 4 mJ of pulse energy is eye-safe, or approximately 1% of that acceptable in the best eye-safe spectral region. The graph has been shown only to 3.0 μm, but in fact the maximum eye-safe pulse energy is constant from about 2.6 to greater than 10.6 μm. The fourth best eye-safe region extends from about 305 to 390 nm, where between 2 and 4 mJ of pulse energy remains eye-safe, followed by the region from 180 to 300 nm, where about 1 mJ of pulse energy is eye-safe.

The most dangerous spectral region, as discussed earlier with regard to the physiology of the eye, is the "retinal hazard region" (about 400 nm to 1.4 μm). The least eye-safe portion of this region is at the visible wavelengths between 400 and 700 nm, where only about 0.3 μJ of pulse energy can be considered eye-safe. This value increases essentially logarithmically over the range from 700 nm to 1.2 μm, and then holds constant between 1.2 and 1.4 μm where only about 25 μJ of pulse energy is eye-safe.

One important aspect of the data shown by these curves is that there is very little dependence of the eye-safe laser pulse energy on pulse length, at least for the relatively short pulse lengths represented by these data. In fact, the current ANSI guidelines maintain this independence down to 1.0 ns pulse lengths, except for the near-UV spectral region where some variation of eye-safe pulse energy with pulse length has already been noted. This fact will have important consequences with regard to the optimal generation of laser-induced oil surface displacements, as we will demonstrate in a following section.

Figure A3 illustrates the maximum eye-safe laser pulse energy for a relatively short laser pulse length (30 ns), but for differing values of the $1/e^2$ beam diameter. In contrast to the previous graph, which showed little dependence of eye-safe pulse energy on pulse length, these data show that there is a very strong dependence of the eye-safe pulse energy on beam diameter. The results indicate that there is about one order of magnitude increase in eye-safe laser pulse energy for a factor 3 increase in beam diameter. Stated another way, the ratio of eye-safe pulse energies for two different beam diameters is dependent on the square of the ratio of the beam diameters. This indicates that the eye-safe energy density (the ratio of eye-safe pulse energy to $1/e^2$ beam diameter), is approximately a constant independent of the beam diameter. This too has important consequences for the optimal generation of laser-induced oil surface displacements, since the efficiency of surface displacement generation is directly related to the incident laser energy density. One proviso must be introduced at this point: the relative constancy of eye-safe energy density applies only to the more eye-safe wavelengths (i.e., less than 400 nm and greater than 1.4 μm). Within the retinal hazard region, the eye-safe energy density is actually a function of beam diameter for small beam diameters; thus, less energy density is eye-safe for small spot sizes than for larger spot sizes in this wavelength region.

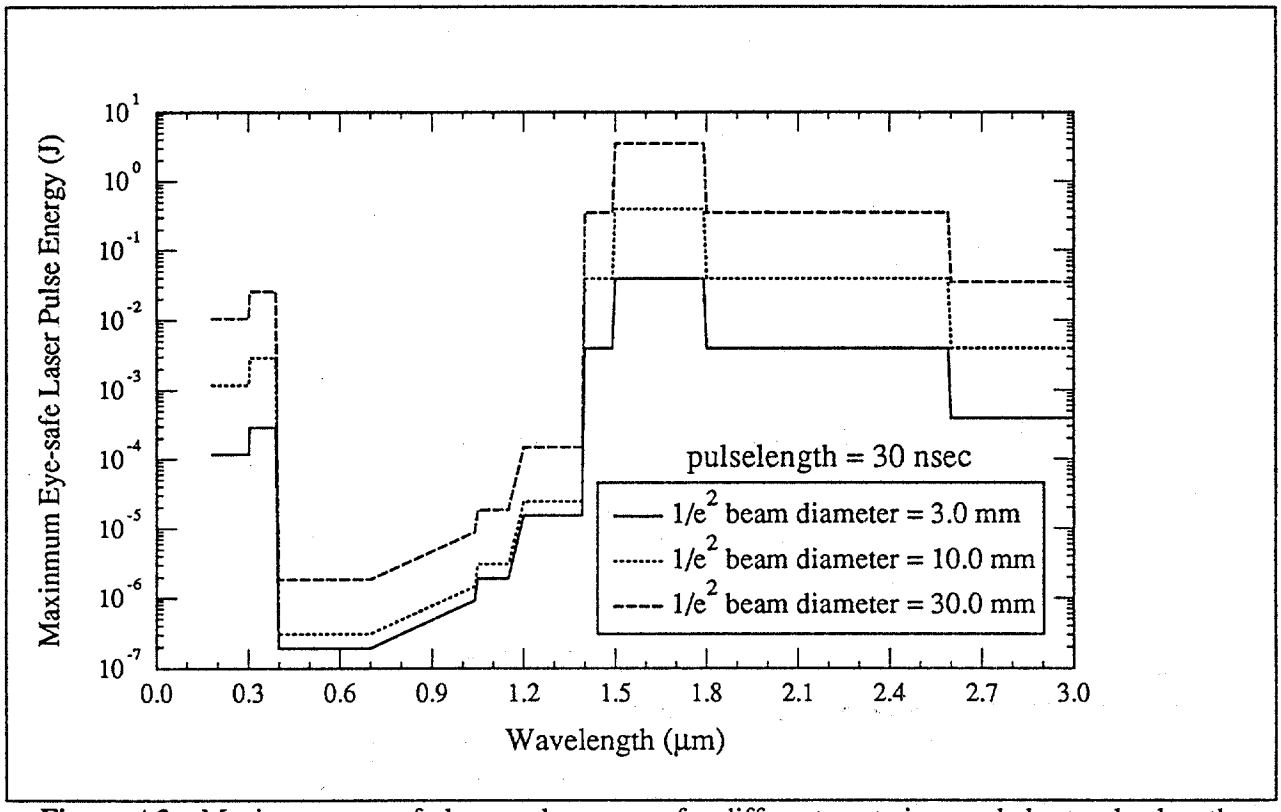

Figure A3 - Maximum eye-safe laser pulse energy for different spot sizes and short pulse lengths

Figure A4 illustrates the maximum eye-safe laser pulse energy for longer laser pulse lengths (50, 100 and 250 μs), such as might be used for the probe laser in a LURSOT-type system. For typical acoustic velocities of oil, the pulse lengths listed above would theoretically allow laser-ultrasonic measurement of oil layers with thicknesses of about 3, 6 and 16 cm, respectively. As with the results shown in Figure A2, the data represent a $1/e^2$ beam diameter of 1.0 cm. A comparison of the results presented in Figures A2 and A4 shows that the general characteristics of the corresponding curves in each of the two graphs are quite similar. Indeed, in many cases the magnitudes of the maximum eye-safe laser pulse energies for the same wavelengths are nearly equal. Differences are confined to the spectral regions 305 to 390 nm, 400 nm to 1.4 μm, and 2.6 to 10.6 μm.

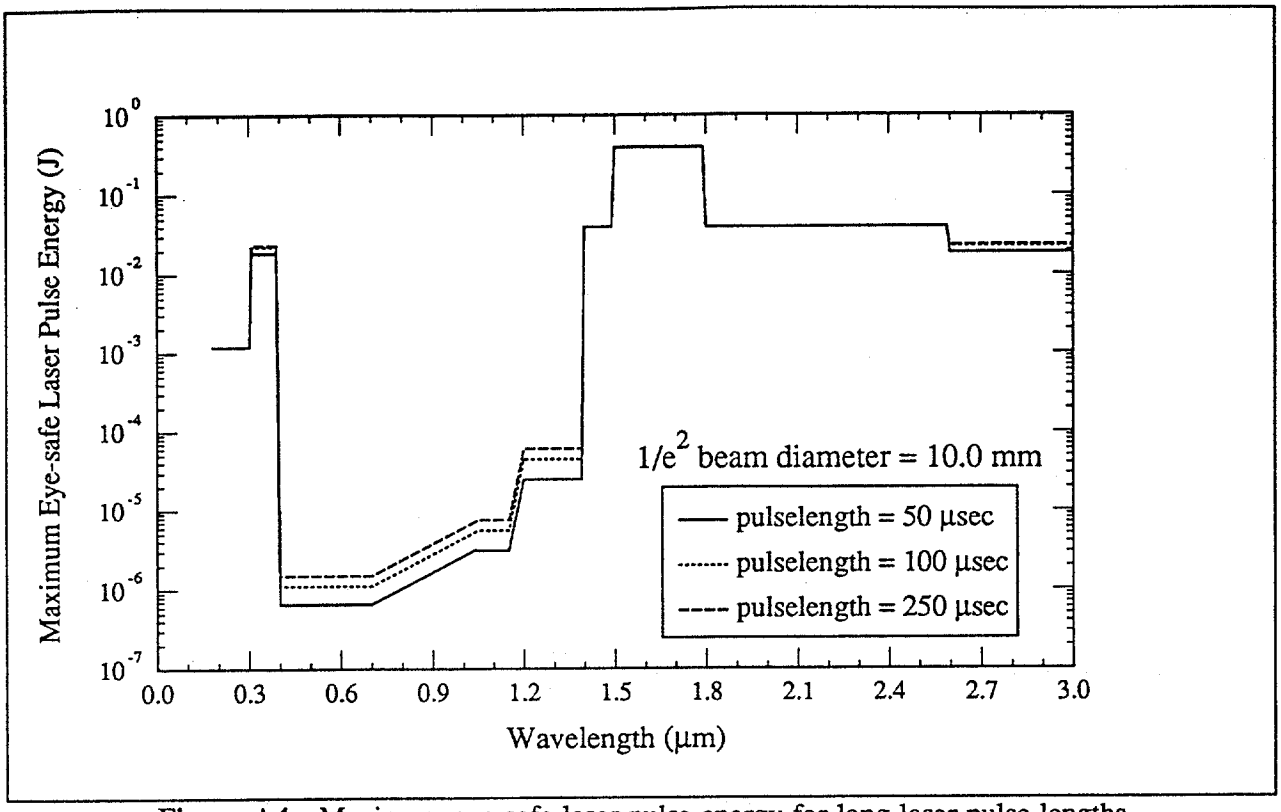

Figure A4 - Maximum eye-safe laser pulse energy for long laser pulse lengths

In the retinal hazard region, the longer laser pulse lengths allow the use of additional pulse energy between 400 nm and 1.05 μm. Furthermore, the eye-safe pulse energy increases with increasing pulse length in this regime, unlike that for the shorter pulse lengths shown in Figure A2. However, the gains in eye-safe pulse energy are not large (between a factor of 2 to 5, depending on the increase in pulse length), and they occur in a spectral region where the eye-safe laser pulse energy is very low. Thus, the utility of these wavelengths for the probe laser is in some doubt, at least from the perspective of eye-safety.

Interestingly, the increase in eye-safe laser pulse energy is not linear with the increase in laser pulse length. This means that, in general, the eye-safe instantaneous laser power (during the duration of the laser pulse) is actually lower for the longer pulse lengths than for the shorter ones. Since the detectibility of the laser-ultrasonic signal depends fundamentally on the instantaneous probe laser power, the use of longer probe laser pulse lengths in order to increase the maximum measurable oil thickness has a price in decreased detection sensitivity.

In the other two spectral regions which exhibit changes in eye-safe pulse energy between short and long pulse lengths (305 to 400 nm, and 2.6 to 10.6 μm), there is almost an order of magnitude increase in eye-safe pulse energy allowed when using the longer pulse lengths. Essentially, this brings the eye-safe pulse energy levels for these spectral regions almost on a par with the 1.4 to 1.5 μm and 1.8 to 2.6 μm spectral regions, which are still at least an order of magnitude less than the levels within the best eye-safe spectral region.

Figure A5 illustrates the maximum eye-safe laser pulse energy for a long pulse length, 100 μs, and for various values of $1/e^2$ beam diameter. The results can be compared to those shown in Figure A3, which represent a shorter pulse length of 30 ns. The characteristic of the results shown in Figure A5 is quite similar to that of Figure A3. The variation of maximum eye-safe pulse energy with increasing

beam diameter again illustrates that the eye-safe beam energy density is essentially conserved (except within the retinal hazard region, for small beam diameters).

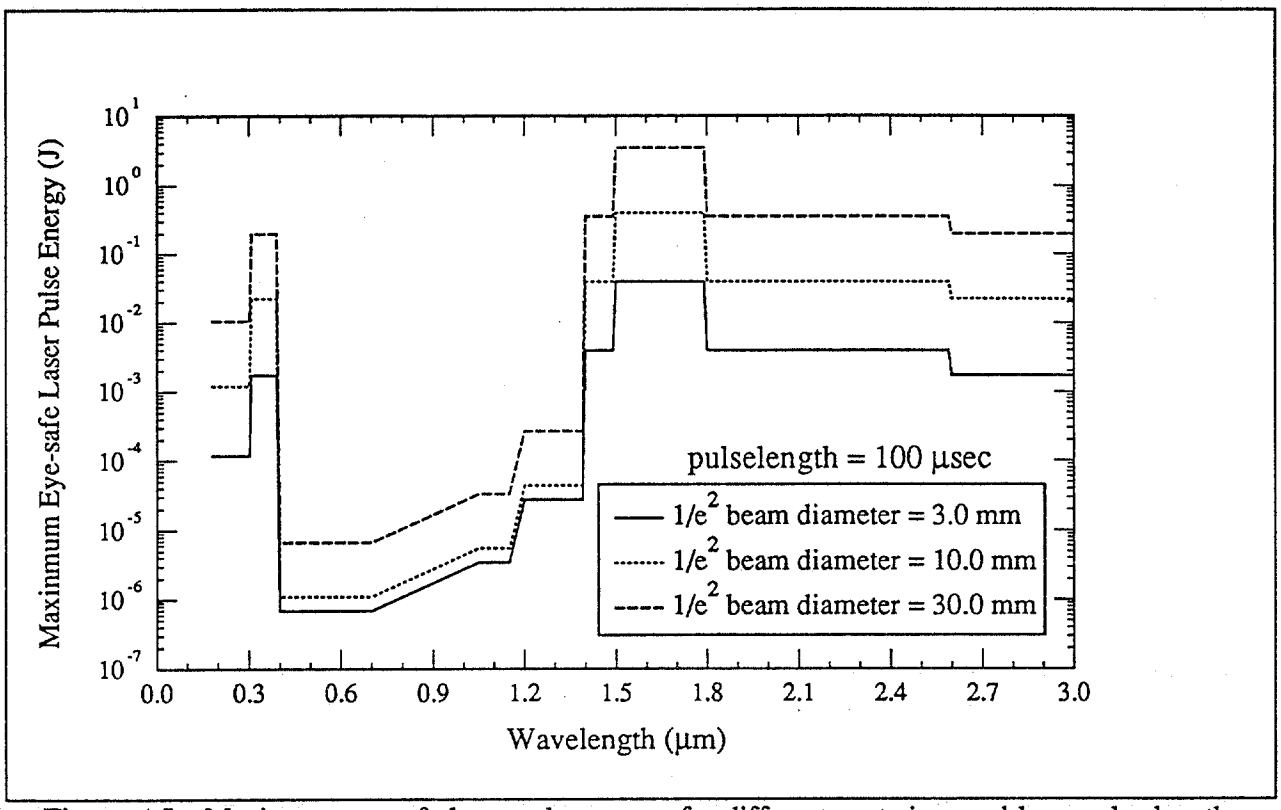

Figure A5 - Maximum eye-safe laser pulse energy for different spot sizes and long pulse lengths

The primary purpose of the probe laser is to illuminate the oil surface during the entire surface displacement period. Any variation in the probe laser intensity or optical frequency during this period acts to obscure the measurement of the true surface displacement. By nature then, a pulsed source used for the probe laser is itself a compromise, since it is difficult or impossible to produce laser pulses whose intensity cuts on sharply, remains constant over an extended interval and then drops sharply to define the end of the pulse. For this reason alone a cw (continuous wave) laser represents an attractive alternative to the long-pulse laser when used for a probe source.

Figure A6 illustrates the maximum eye-safe laser power for a cw laser whose beam sweeps across the eye of an observer at 50 m/s, and consistent with the other assumptions made for the pulsed laser eye-safety calculations. The calculations for this case were also done assuming $1/e^2$ beam diameter values of 3.0, 10.0 and 30.0 mm. The characteristic of the curves shown in Figure A6 is by now familiar, being very similar to that shown for the pulsed laser cases (this follows from the fact that the shape of the curves is determined, to a large extent, by the wavelength-dependent injury threshold of the eye which is similar for both pulsed and cw illumination).

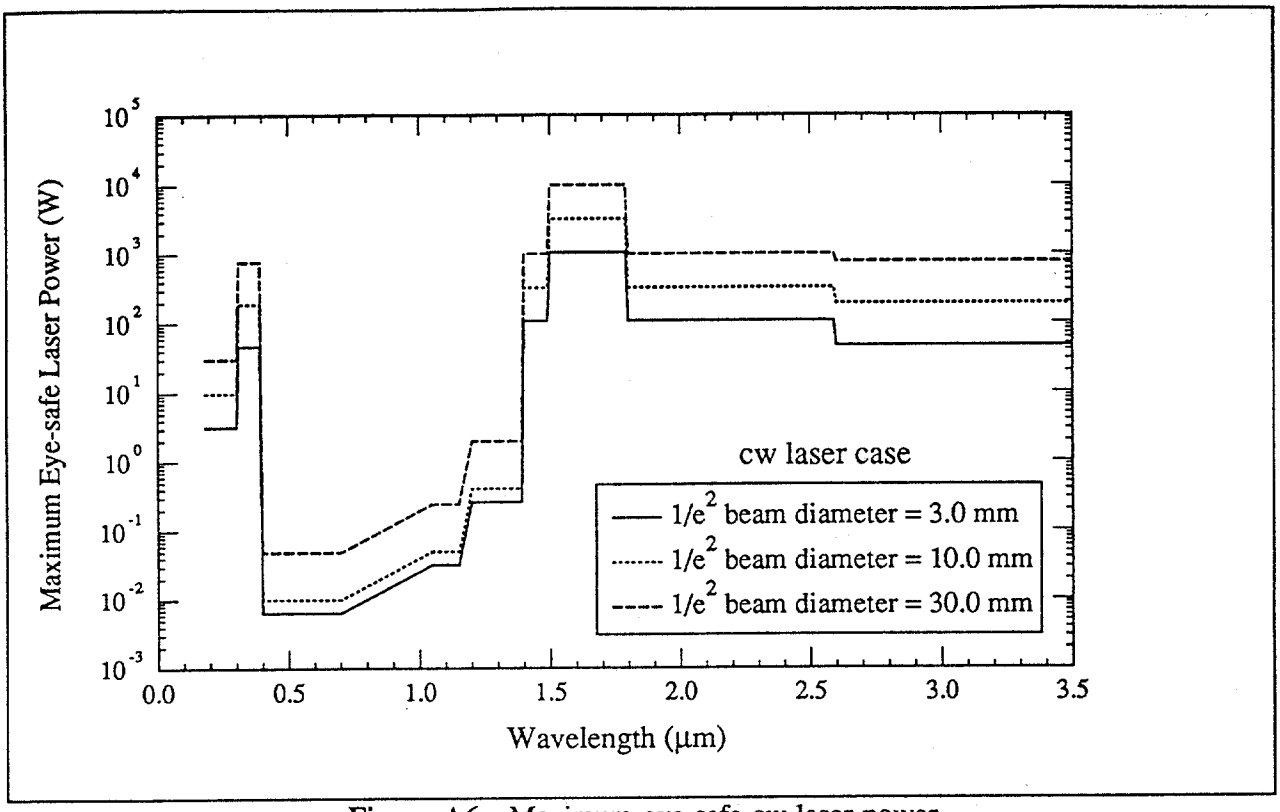

Figure A6 - Maximum eye-safe cw laser power

The best eye-safe spectral region allows laser power values up to the kilowatt range or more, depending on the extent to which the beam is spread (i.e., the beam diameter). For eye-safe laser power values of 50 W or greater, there is a good choice of spectral regions: 1.4 to 1.5 μm, 1.8 to 2.6 μm, 305 to 390 nm and 2.6 to greater than 10.6 μm. For these same spectral regions we may utilize eye-safe laser power values of at least 200 W if the spot diameter is 1.0 cm or greater. As with all other cases considered, the retinal hazard region represents the least eye-safe spectral region; between 400 and 700 nm only about 6 mW is eye-safe (depending on beam diameter), although this increases to more than 200 mW between 1.2 and 1.4 μm. Therefore, laser power values less than 100 mW are not out of the question for producing useful, detectable laser-ultrasonic signals.

APPENDIX B - FOCUSING OF LASER BEAMS AT THE SEA SURFACE

Laser Beam Properties

Those associated with the field of optics are familiar with the properties of object-image relationships, and how various optical elements affect them. In this case objects are considered to be collections of incoherent point sources, and the resulting images can be determined using the principles of aberration theory and superposition. The images resulting from multiple elements can be determined by a successive application of these techniques.

However, the handling of laser light by optical components is described differently. Laser light is generated coherently throughout the relatively large volume of the laser cavity, and the emergent beam acts as if it all originated from the same point. The emergent wavefront is thus well defined, and the laser beam is not subject to certain of the limitations of incoherent beams. As such, the beam can be focused to a much greater degree than is possible with incoherent light sources. The coherence of the emergent laser beam requires that aberration and diffraction theory be applied when considering the handling of these beams.

Before discussing how laser beams are focused, we must briefly describe some of the fundamental properties of these beams. Laser output is created when stimulated emission occurs within a resonant cavity, the laser cavity. The laser cavity may be resonant along its optical axis (the "longitudinal" direction) or across a plane perpendicular to this axis (the "transverse" direction). The resonant condition within the laser cavity is thus described in terms of both longitudinal and transverse modes. The spectral (wavelength) characteristics of a laser, such as the spectral bandwidth, are primarily determined by the longitudinal modes; beam properties such as the beam diameter and divergence and the energy distribution within the beam are primarily determined by the transverse modes. For our investigation of the limitations concerning the focusing of laser beams at large distances, the transverse modes of the laser are the most important.

Gaussian Laser Beams

Laser transverse modes are described mathematically by a well-known set of functions, and defined by the designation $TEM_{m,n}$ ("Transverse ElectroMagnetic waves") where m and n are integers used to describe nodes in the distribution. As m and n take on larger values, the power density distribution within the beam becomes more and more complicated. The power density distribution, or transverse mode, termed $TEM_{0,0}$ has a special significance and is also referred to as the "Gaussian" intensity distribution. As the name implies, the power density is described by the Gaussian function

$$E(r) = E_0 \, e^{[-2\,r^2 / w^2]} = \frac{2\,P_0}{\pi\,w^2} \, e^{[-2\,r^2 / w^2]} \qquad \text{(B1)}$$

where

E (r) = power density at radial distance r
E_0 = power density at distribution centre
P_0 = total power within laser beam
r = radial distance from distribution centre
w = beam radius to $1/e^2$ point.

This circularly symmetric power density distribution has a maximum at its centre, and it decreases according to the Gaussian function in the radial direction away from its centre. It is the simplest of the power density distributions emergent from a laser cavity, and it has some unique properties.

Firstly and perhaps most importantly for this application, it has the capability to be focused to the smallest spot size of all the laser transverse modes.

Secondly, at a particular plane perpendicular to the laser optical axis, termed the *beam waist*, the beam diameter reaches its minimum value and the radius of curvature of the wavefront is infinite (i.e., the beam can be pictured as a small circular section of a plane wave, with a Gaussian power density distribution). For many lasers, the beam waist is located at or close to the exit aperture from which the beam emerges. The fundamental optical mechanism of diffraction ensures that the beam must spread transversely as it propagates through free space, so that the beam diameter must always increase beyond the beam waist position. The wavefront also acquires curvature as the beam propagates. The relations describing the beam radius and the wavefront radius of curvature are

$$w(z) = w_0 \left[1 + \left(\frac{\lambda z}{\pi w_0^2} \right)^2 \right]^{1/2}$$

$$R(z) = z \left[1 + \left(\frac{\pi w_0^2}{\lambda z} \right)^2 \right] \qquad \text{(B2-B3)}$$

where

$w(z)$ = beam radius to $1/e^2$ point at distance z
w_0 = beam radius to $1/e^2$ point at beam waist
$R(z)$ = wavefront radius of curvature at distance z
λ = wavelength of laser light
z = distance along optical axis from beam waist.

The mechanism of diffraction for a Gaussian beam ensures that its diffraction pattern is also given by a Gaussian power density distribution. In fact, Equation B1 for the Gaussian power density is valid for any point along the optical axis from the beam waist, provided that the appropriate value for the instantaneous beam radius, $w(z)$, is used. Inspection of the relations for the beam radius and the wavefront radius of curvature show that the beam is essentially a section of a plane wave at the beam waist; at large values of z (the "far field"), the beam is essentially a section of a spherical wave; in between these extremes (the "near field") both the beam radius and the wavefront radius of curvature change non-linearly with distance z. In the far field, the beam divergence is uniquely related to the beam radius by the following relation

$$\theta = \frac{w(z)}{z} = \frac{\lambda}{\pi w_0} \qquad \text{(B4)}$$

where θ is the half-angle beam divergence in the far-field.

Thus we see that the properties of Gaussian laser beams lead to the following:

- A Gaussian beam experiences diffraction, but remains a Gaussian beam, as it propagates.
- In the far-field, a Gaussian beam appears as a section of a spherical wave; it thus behaves as if it comes from a point source, and its imaging by optics can be treated with the classical optics methods.
- In the far-field, the divergence of a Gaussian beam is directly proportional to its wavelength, and inversely proportional to its beam waist radius. Thus, identically-sized Gaussian beams of different wavelengths will diverge at different angles. Furthermore, a Gaussian beam's divergence may be reduced by increasing its diameter (laser beam expanders make use of this principle).
- In the near-field a Gaussian beam behaves quite differently from a classical point source, and its imaging by optics must be treated using a specialized methodology which has been specifically developed for Gaussian beams[2] (see below).
- From the power density distribution function for Gaussian beams, an integration over a circular area leads to the result that somewhat more than 98% of the beam energy is contained within a circular area whose radius is 1.5 times the beam waist radius. This has consequences for the sizing of any optical elements used for the handling of Gaussian laser beams.

Gaussian Laser Beam Handling by Optical Elements

The methodology[3] used to treat the effects, on Gaussian laser beams, of optical elements such as lenses and mirrors is to assume that the laser beam waist is the "object" point; the new beam waist created by the optical element is then associated with the "image" point. Utilizing the properties of Gaussian beams then the properties of the object and image are related by the following:

$$\frac{1}{s + \dfrac{z_r^2}{(s - f)}} + \frac{1}{s''} = \frac{1}{f}$$

$$m = \frac{w_0''}{w_0} = \left\{ \left[1 - \left(\frac{s}{f} \right) \right]^2 + \left(\frac{z_r}{f} \right)^2 \right\}^{-1/2} \qquad \text{(B5-B8)}$$

$$z_r = \frac{\pi w_0^2}{\lambda}$$

$$z_r'' = m^2 z_r$$

where

s = distance from "object" waist to optical element
s'' = distance from "image" waist to optical element
f = focal length of optical element
w_0 = "object" beam waist radius

[2] S.A. Self, Focusing of Spherical Gaussian Beams, Applied Optics, 22 (5): 658 (1983).

w_0'' = "image" beam waist radius
m = beam waist radius magnification ratio
z_r = Rayleigh range for "object"
z_r'' = Rayleigh range for "image".

The relations shown above allow one to calculate the position and size of an "image" beam waist, given the position and size of an "object" beam waist, and the focal length of the optical element. The object and the image may either be real or virtual, in accordance with the classical object-image relations for incoherent point sources. The usual conventions[3] regarding the sign of these various quantities has been made. Note that these relations can be cascaded together in order to predict the position and size of a Gaussian laser beam which has traversed multiple optical elements. Note also that as the Rayleigh range tends toward zero (i.e., for either very small "object" beam radii, or very large wavelengths), the above relations become identical to those for the classical object-image relations for incoherent point sources.

As an example, we consider the case whereby a CO_2 laser (10.6 μm wavelength) with a Gaussian beam diameter of 8.0 mm (to the $1/e^2$ power density points) is focused by a lens of focal length +80 cm. The lens is positioned so that the distance between the laser beam waist and the lens is 90.0 cm. In this case the Rayleigh range is about 4.74 m; the "object" beam waist is real, is located at 80.3 cm from the lens, and has a $1/e^2$ waist diameter of about 2.7 mm. In order to allow all significant portions of the beam through the lens, it must have a diameter of at least 12.0 mm. The beam as it passes through the lens has a $1/e^2$ diameter of 8.0 mm; this decreases over the next 80.3 cm until the beam reaches its minimum diameter of 2.7 mm; the beam diameter then increases with increasing distance thereafter.

Beam Expander Characteristics

In our discussion of the properties of Gaussian laser beams, we mentioned that a beam expander may be used to reduce the divergence of a beam by first expanding it to a larger diameter. In its simplest configuration, a beam expander consists of two lenses. The input lens creates either a real (Keplerian design) or a virtual (Galilean design) image; the output lens is positioned so that its focal point essentially coincides with the image of the first lens.

For a properly designed unit, this configuration results in a highly collimated laser beam which is of larger diameter than the initial laser beam diameter. Slight adjustment of the separation distance between the two lens elements results in "defocusing" of the output laser beam, so that the output laser beam can be made to diverge or converge somewhat from its optimum collimation condition; this then provides for the ability of a beam expander to focus the laser beam at large distances. However, the degree to which a laser beam can be focused at a certain distance depends on a host of parameters regarding the wavelength, diameter and positioning of the laser source with respect to the beam expander, as well as the design of the beam expander itself.

For many situations involving the use of beam expanders with lasers, and for all situations where high power lasers are expanded, a beam expander of Galilean design is appropriate. The input lens is a

[3] E. Hecht and A. Zajac, "Optics", Addison-Wesley Publishing Company, Massachusetts (1974), Chapter 5.

negative lens (i.e., it results in a virtual rather than a real image) which diverges the input beam; the diverging laser beam is then collected and collimated by the positive output lens. This design is preferred over the Keplerian one, since the laser beam is not focused internally (which could lead to spurious undesirable effects especially with high power laser sources). In actual practice, the output lens element is somewhat more complicated than a simple bi-convex lens, in order to correct for certain aberration effects.

100 WILDCAT ROAD, NORTH YORK, ONTARIO, CANADA M3J 2Z9 TELEPHONE (416) 661-5904 FAX (416) 661-4168